

Stochastic dynamics in olfactory signal transduction and development

Dissertation

zur Erlangung des akademischen Grades
Doctor rerum naturalium (Dr.rer.nat.)

vorgelegt der

Fakultät Mathematik und Naturwissenschaften
der Technischen Universität Dresden

von

Peter Borowski

Max-Planck-Institut für Physik komplexer Systeme, Dresden

28. September 2006

Abstract

The purpose of the senses of animals (and humans) is to translate information available in the external environment into internal information that can be processed by the brain. In the case of the olfactory sense – the sense of smell – this is information about the type and concentration of odourants. In the last 15 years major progress has been made in the experimental understanding of the first two stages of the olfactory sense: the signal transduction inside the cilia of the olfactory receptor neurons and the first 'relay station' in the brain, the olfactory bulb, as well as the connection between these two. Theoretical studies that classify the experimentally achieved knowledge or help in testing different biological hypotheses are only starting to be developed. The present work aims to contribute to the theoretical understanding of the first two stages of the olfactory sense.

The first processing of the olfactory information, the olfactory signal transduction, is accomplished by a complex chemical network in the sensory cells with the task of coding the available information reliably over a wide range of stimulus strength. In the present work, methods from nonlinear dynamics combined with network theory (namely stoichiometric network analysis) are used to identify a specific negative feedback mechanism that accounts for a number of recently measured experimental results, e.g. oscillations in calcium concentration or the adaptation of the cell towards strong stimuli. This feedback is an experimentally well-established inhibition of cationic channels by the calcium-loaded form of the protein calmodulin. The results of the set of coupled nonlinear deterministic differential equations describing these dynamics agree quantitatively with experimental data. A bifurcation analysis of the system considered shows the robustness of the oscillatory solution against changes in parameters used. It also gives predictions that could serve as an experimental test of the proposed mechanism.

Further abstraction and simplification of this specific signal transduction unit leads to a stochastic two-level system with negative feedback, that can not only be found in signalling systems but also in other branches of cell biology, e.g. regulated enzyme activity or in transcription dynamics. Whereas the description outlined above is fully deterministic, here the model system is intrinsically noisy. The influence of the feedback on the intrinsic noise as well as on the signalling properties of the module are analysed in detail by computing mean values, correlation and response functions of the two dynamical system variables using different analytical approaches. Common to all of them is that the intrinsic noise of the system is calculated from its dynamics rather than being introduced by hand. A master equation is used to get generally valid expressions for the mean values. Correlation and response functions for weak feedback are calculated within a path-integral description, and an easier self-consistent method with restricted validity is developed for future extensions of the module such as, e.g., the inclusion of diffusion. The results of the analytical methods are compared to each other and to the results of extended numerical simulations. The considered quantities allow for statements regarding the quality of the signal transduction properties of this module and the positive and negative effects of feedback on it.

Going one step up in the information processing in the olfactory sense, another system is found that shows interesting dynamics during development and is influenced by stochastic effects: the formation of the neural map on the surface of the olfactory bulb – stage two in the olfactory system. The dynamics of this very complex biological pattern formation process is studied mostly numerically focusing on three different aspects of axonal growth. Possible chemical guidance cues and the reaction of axonal growth cones to them are described using different levels of detail. There is strong experimental evidence for interactions among growing axons which is implemented in different ways into models. Finally, axon turnover is considered and used in the most promising simulation approach, where many axons grow as interacting directed random walkers. For each of these aspects, qualitative features of respective experiments are reproduced.

Zusammenfassung

Die Sinne der Tiere (und Menschen) dienen dazu, Informationen über die Außenwelt in neuronale, 'interne' Information zu 'übersetzen'. Im Falle des Geruchssinns sind dies Informationen über die Art und Konzentration von Geruchsstoffen. In den letzten 15 Jahren wurden große Fortschritte im experimentellen Verständnis der ersten beiden Stufen des Geruchssinns gemacht, sowohl was die Signaltransduktion in den Zilien der Geruchszellen betrifft, als auch bezüglich der ersten 'Schaltstelle' im Gehirn, dem olfaktorischen Bulbus (sowie in der Verbindung dieser beiden Stufen). Die Entwicklung theoretischer Studien, die die experimentell gewonnenen Daten klassifizieren können, befindet sich dagegen erst am Anfang. Ziel der vorliegenden Arbeit ist es, zum theoretischen Verständnis dieser ersten beiden Stufen beizutragen.

Die erste Verarbeitung der olfaktorischen Information, die olfaktorische Signaltransduktion, wird durch ein komplexes chemisches Netzwerk in den Sinneszellen bewerkstelligt. In dieser Dissertation werden Methoden der nichtlinearen Dynamik, kombiniert mit Netzwerktheorie (stöchiometrische Netzwerkanalyse) benutzt, um einen negativen Rückkopplungsmechanismus zu identifizieren, der einige in neuerer Zeit gewonnene experimentelle Ergebnisse erklären kann, u.a. Oszillationen der Kalziumkonzentration oder die Anpassung der Zelle an starke Reize. Bei dieser Rückkopplung handelt es sich um eine experimentell gut bestätigte Hemmung eines Kationenkanals durch den Kalziumkomplex des Proteins Calmodulin. Das Ergebnis der vier gekoppelten nichtlinearen deterministischen Differenzialgleichungen, die das dynamische Verhalten des Systems beschreiben, stimmt quantitativ mit experimentellen Daten überein. Eine Bifurkationsanalyse zeigt die Robustheit der oszillierenden Lösung gegenüber Veränderungen der verwendeten Parameter und macht Vorhersagen möglich, die als experimentelle Tests des vorgeschlagenen Mechanismus dienen können.

Eine weitere Abstrahierung der oben beschriebenen Signaltransduktionseinheit führt zu einem stochastischen Zweiniveausystem mit negativer Rückkopplung, das nicht nur in Signalsystemen gefunden werden kann, sondern auch in anderen Bereichen der Zellbiologie. Im Gegensatz zu der oben beschriebenen, komplett deterministischen Beschreibung zeigt das hier betrachtete Modellsystem intrinsisches Rauschen. Der Einfluss der Rückkopplung auf das Rauschen sowie auf die Signalübertragungseigenschaften des Moduls werden detailliert analysiert, indem mit Hilfe verschiedener analytischer Methoden Mittelwerte, Korrelations- und Antwortfunktionen des Systems ausgerechnet werden. Diese Methoden haben alle gemein, dass das intrinsische Rauschen des Systems aus der Dynamik selbst berechnet wird und nicht 'von Hand' eingefügt wird. Um allgemeingültige Ausdrücke für die Mittelwerte zu bekommen, wird eine Mastergleichung aufgestellt und gelöst. Die Korrelations- und Antwortfunktionen werden für schwache Rückkopplung mit Hilfe einer Pfadintegralmethode ausgerechnet, und eine einfachere, selbstkonsistente Methode begrenzter Gültigkeit wird für mögliche Erweiterungen des Systems, z.B. die Berücksichtigung von Diffusion, entwickelt. Die Ergebnisse der verschiedenen analytischen Methoden werden miteinander und mit den Ergebnissen ausführlicher numerischer Simulationen verglichen. Die betrachteten Größen ermöglichen Aussagen über die Qualität der Signaltransduktion dieses Moduls sowie über die positiven und negativen Effekte der Rückkopplung auf diese.

Ein weiteres Beispiel für interessante und von stochastischen Effekten beeinflusste Dynamik findet man einen Schritt weiter in der olfaktorischen Signalverarbeitung: Die während der Entwicklung stattfindende Ausbildung der neuronalen Karte auf der Oberfläche des olfaktorischen Bulbus, der zweiten Stufe des olfaktorischen Systems. Die Dynamik dieser sehr komplexen biologischen Musterbildung wird mittels numerischer Simulationen untersucht, wobei der Schwerpunkt auf drei verschiedene Aspekte axonalen Wachstums gesetzt wird. Die Reaktion axonaler Wachstumskegel auf mögliche chemische Signale wird verschieden detailliert beschrieben. Es gibt deutliche experimentelle Hinweise auf Wechselwirkung zwischen Axonen, was in den Modellen auf verschiedene Arten implementiert wird. Schließlich wird die Erneuerung der Axone betrachtet und im vielversprechendsten Modell, in dem viele Axone als wechselwirkende gerichtete random walkers simuliert werden, berücksichtigt und analysiert. Für jeden dieser drei Aspekte können entsprechende experimentelle Ergebnisse qualitativ reproduziert werden.

Contents

1	Introduction	1
1.1	Motivation	1
1.2	The olfactory system	2
1.2.1	The olfactory receptor neuron (ORN)	2
1.2.2	The olfactory bulb (OB)	4
1.2.3	The olfactory system in insects	4
1.2.4	The vomeronasal organ – pheromone detection	5
1.3	Performance of the olfactory sense and interesting questions	6
2	Signal Transduction in the Olfactory Receptor Neuron	9
2.1	Experimental background	9
2.1.1	The cAMP-mediated signal transduction pathway	10
2.1.2	Experimental findings from whole cell measurements	12
2.2	Oscillations and short time adaptation from negative feedback	17
2.2.1	Chemical reactions and kinetics	17
2.2.2	Stoichiometric network analysis	19
2.2.3	Numerical solution, comparison to experiments	22
2.2.4	Explicit bifurcation analysis	27
2.2.5	Synchronisation between the cilia of an ORN	30
2.3	Summary and comparison to other theoretical approaches	31
3	Ion Channel Dynamics in Olfactory Signal Transduction: A Stochastic Signalling Module	33
3.1	From a deterministic to a stochastic description	33
3.2	A two-state signalling module with negative feedback	35
3.2.1	Definition of the relevant quantities	37
3.3	Channel open probability in the steady state	38
3.3.1	Solution using a master equation	39
3.4	Correlation and response functions	41
3.4.1	Path-integral formalism	41
3.4.2	Self-consistent feedback model	52
3.5	Numerical results	56
3.5.1	Weak feedback	57
3.5.2	Strong feedback	62
3.6	Extensions and outlook	68
3.6.1	Coupling of channels in a cilium	68
3.6.2	Further extensions and modifications	71
3.7	The module aspect and other systems where this analysis may apply	71
3.8	Summary	73

4	Axon Guidance in the Development of the Olfactory System	75
4.1	The olfactory map – a remarkable example of pattern formation	75
4.2	The biology of the formation of the olfactory map	77
4.2.1	How axons grow	77
4.2.2	Chemical guidance cues	77
4.2.3	Axon-axon interactions	79
4.2.4	Axon turnover	81
4.2.5	Other possible mechanisms	82
4.3	Theoretical approaches to axon sorting and guidance	82
4.3.1	Axon sorting through interacting growth cones – a generalised Potts model	83
4.3.2	Detailed model of the turning of axons in response to guidance cues	87
4.3.3	Advancing axons as interacting directed random walks	91
4.4	Summary and discussion	97
5	Conclusions and Perspective	101
	Appendix	103
A.1	The reaction of calcium and calmodulin	103
B.1	Calculation of the integrals $\hat{I}_0, \hat{I}_1, \hat{I}_2$	106
B.1.1	Generalised convolution theorem	106
B.1.2	Calculation of \hat{I}_0	106
B.1.3	Calculation of \hat{I}_1	106
B.1.4	Calculation of \hat{I}_2	108
B.2	Solution of the rate equation: $f(t), f_2(t)$	109
B.3	Relation between G_{11} and G_{00}	110
B.4	Calculation of $\langle c(t) \rangle_0$ and $\langle c(t) \rangle_1$	111
B.5	Additional expressions	113
B.6	Coefficients of the correlation and response functions	113
B.7	Computation of the linear response to a sinusoidal stimulus	115
C.1	Axon sorting and guidance through interacting growth cones – a continuum model	116
C.2	Additional figures for chapter 4	120
C.2.1	Further plots from the generalised Potts model	120
C.2.2	Flowchart for the detailed turning-model including axon-axon interaction	120
C.2.3	Further configurations of the interacting directed random walks	121
	Bibliography	123
	Index	130

Chapter 1

Introduction

1.1 Motivation

Physics as the most fundamental of the natural sciences not only investigates the very elementary constituents and dynamics of matter but also provides experimental techniques as well as theoretical models and concepts for other branches of science. Regarding biology, this interaction has a long tradition [135] but in recent times, cooperation has increased intensely and theoretical concepts borrowed from statistical physics of complex systems gain more and more influence in the science of the living matter. This interaction, however, is not unilateral. Theoretical physics has also profited a lot from the consideration of living systems, even if it is only the realisation of the fact that often, simple, linear descriptions do not suffice.

It is the conviction of many scientists [15, 17, 87] that the description of complex biological systems in terms of quantitative theoretical models rather than purely qualitative arguments can contribute a lot to the understanding of both the functioning and the purpose of these systems. A more structured and possibly more abstract framework might lead to more effective research and provide a way to classify the vast amount of results from experimental biological studies (e.g. [34, 104]). This way of dealing with complex systems (e.g. by introducing a new language of description) has proven before to be very fruitful in other fields, e.g. in electronics or traffic science. As a step in this direction, the present dissertation deals with the theoretical description of complex processes at the interface between living matter and the outer, inanimate world, which is the working area of the senses.

A vital task organisms have to fulfil and that is naturally connected to physics, is the perception of the outer, 'physical' world and the transduction of the information available into information that the organism can process internally. A specific example where this task is accomplished in animals are the senses. For the visual sense, physics has contributed a lot to the understanding of both the signal transduction in the sensory cells in the eyes (e.g. [37]) as well as the neural processing and the way information is encoded in the different stages of vision (e.g. [8]). Physics seems appropriate, since light, the subject of visual perception, is well described in physical terms. The same holds for the auditory sense, although it is not as well understood as vision, yet. For the chemical senses, particularly the olfactory sense – the sense of smell, a deeper understanding of the underlying biology emerged only in the last 10–15 years. Quantitative modelling and analysis have not yet contributed much to the understanding of this sense, partly, certainly, because of the nature of the stimulus which is chemical and not as easily classifiable as in vision and hearing. Whereas, e.g. the information encoded in the frequency and amplitude of an electromagnetic or air pressure wave is easily quantifiable, this is a tougher task for the stimulus of the olfactory sense – type and concentration of a huge number of

odourants. However, physics is still ubiquitous in all stages of olfactory transduction: There are chemical networks showing complex nonlinear dynamics, there is information being transferred from one form to another, there are complicated patterns formed during the development and at the end there are electrical signals, that propagate and are used for inter-cell communication within complicated neural networks.

The work presented in this dissertation is meant as a contribution to the rapidly evolving field of olfactory research from the perspective of theoretical physics. Its purpose is twofold: On the one hand, tools and models mainly from statistical physics are used for a deeper understanding of experimental data that is available only since a few years. Models quite close to the actual biological system are set up and analysed in order to provide explanations, check hypotheses or propose specific mechanisms and experiments that might contribute to a more quantitative understanding of the biological system. On the other hand, parts of the olfactory system are seen and described from a more abstract viewpoint and their properties are analysed using methods again mainly from statistical physics. Results are obtained that are not restricted to the olfactory system but might be applied to signalling systems in general, as well as to other systems within cell biology.

The following brief introduction into the biology of the olfactory system also serves as an overview over the contents of this thesis.

1.2 The olfactory system

The olfactory sense – the sense of smell – is, according to the classical [3] definition, one of the five senses and forms together with the gustatory sense the group of chemical senses. It transduces the information about the type and concentration of a wide variety of different volatile chemicals that are inhaled during respiration into the recognition of different smells that can be named (e.g. [50]), classified and remembered. The olfactory sense in vertebrates consists roughly of three stages:

- I) Transduction of chemical signals into electrical signals.
- II) Convergence, amplification and correlation of electrical signals.
- III) Recognition and other higher brain functions; connection to memory.

Stage I) takes place completely in the receptor cell of the olfactory sense, the olfactory receptor neuron (ORN). Stage II) happens in a part of the brain, the olfactory bulb (OB), which then sends signals to several brain regions (piriform cortex and amygdala, among others (stage III)). This thesis mainly deals with stage I) as well as the connection between stages I) and II). The biology of both of these stages will be briefly introduced in the following subsections, more detailed descriptions follow in the introductions of the relevant chapters. Fig. 1.1 shows the areas in the heads of a rat and a human where the three different stages are situated.

1.2.1 The olfactory receptor neuron (ORN)

Situated in the roof of the nasal cavity (Fig. 1.1) lies the olfactory epithelium, sensory tissue that contains the olfactory receptor neurons (ORNs). They are embedded into a layer of other cell types (supporting cells, basal cells and microvillar cells) and are distributed over the surface of the epithelium [110]. Fig. 1.2 shows a schematic section through the olfactory epithelium as well as a microscopic picture of an ORN from a frog.

As can be seen in Fig. 1.2, the ORNs extend long cylindrical shaped structures, the cilia, from the so-called dendritic knob at the end of the dendrite into a liquid layer on top of the cell surface, the mucus. These cilia are the sites where the receptor proteins of the sense of smell, the olfactory receptors (ORs), are situated and where the main part of the signal transduction takes place. Odourants are inhaled with the respiratory air into the nose,

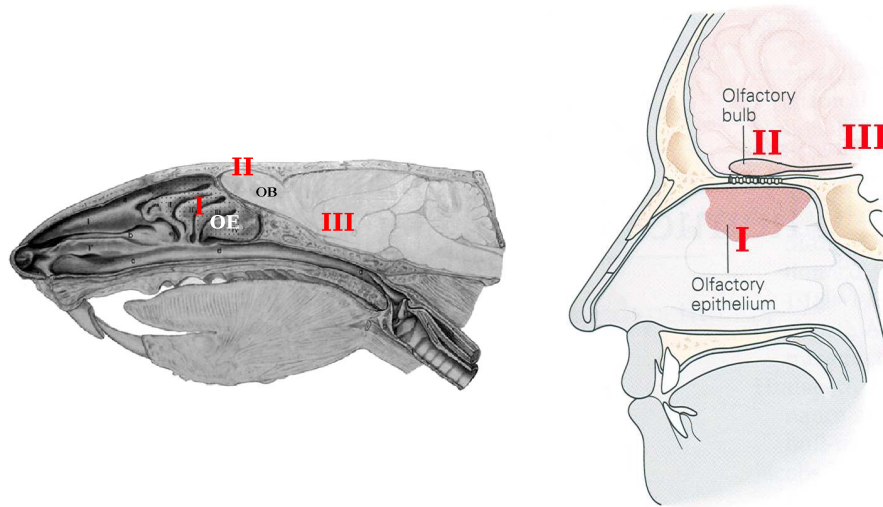


Fig. 1.1: **Left:** Section through the head of a rat (modified from [42], see also [150]). **Right:** Schematic section through a human head (modified from [72]). Indicated with roman numbers are the three stages of the olfactory system as described in the text (OE: olfactory epithelium; OB: olfactory bulb).

diffuse into the mucus layer (probably bound to odourant-binding proteins) and might finally bind to a receptor on the membrane of the cilium of an ORN. This starts the signal transduction cascade, a series of chemical reactions between a variety of different molecules and ions, whose main effect is an increase in the calcium concentration inside the cilia and a reduction of the transmembrane potential of the cell. The introduction of chapter 2 describes this process in greater detail and later in that chapter, a theoretical description for the dynamics of the signal transduction in the ORNs is presented. Chapter 3 seizes this description and by further reducing the complexity of the model system, presents analytical results that are generally applicable to signalling systems.

In the olfactory epithelium of mice there are a few million ORNs [107]. It is known from the study of the genome of mouse that there are about 1000 [113] different functional genes for different olfactory receptors (ORs) (in human ~ 400 [113]). Through a number of different experiments it was possible to conclude, that most likely in each ORN there is only one (of the approximately 1000) type of OR expressed¹ [108]. Each OR responds differently to different odourants and most of the receptors have a broad reception range, meaning that they respond to quite a few different odourants with different response strengths. However, there seem to be a few highly specified receptors (cf. also Subsec. 1.2.4). Fig. 1.3 shows a schematic representation of this fact for a small set of ORs.

ORNs are neurons and therefore able to fire action potentials through their axon. These action potentials are generated in a region of the soma – the axon hillock – after a sufficiently strong stimulus in the cilia reduced the transmembrane potential below some threshold. How the information about the types and concentrations of odourants is encoded in the series of action potentials (the spike train), is largely unknown (see Subsec. 2.1.2). ORNs react differently depending on the OR they express and on the stimulus type and strength (Fig. 1.4).

The action potential (or the whole spike train) then travels along the axon towards the brain, more specifically, to the olfactory bulb described in the next subsection.

¹A possible exception of this one receptor-one neuron hypothesis has been reported in drosophila [59].

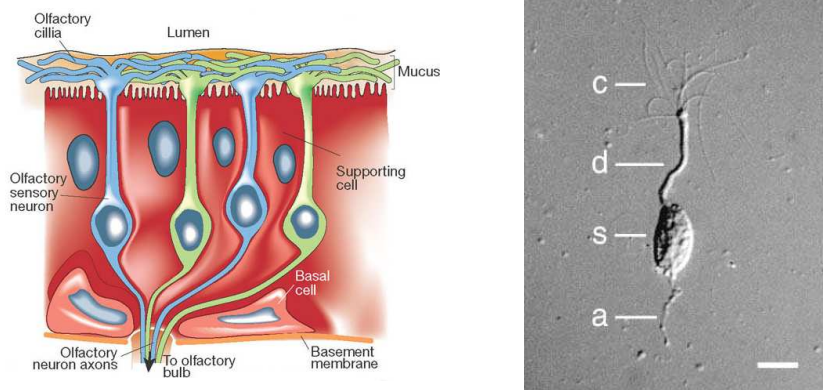


Fig. 1.2: **Left:** Schematic section through the olfactory epithelium in a mammal (modified from [48]); **Right:** Microscopic picture of an ORN from a frog with the axon cut (from [78]). c: cilia, d: dendrite, s: soma, a: axon; scale bar: $10\mu\text{m}$.

1.2.2 The olfactory bulb (OB)

The olfactory bulb (OB) gathers all the information from the ORNs and pre-processes it. It is a part of the brain situated near the nose (Fig. 1.1) and the axons of all ORNs end on it, connecting to secondary neurons through synapses. Fig. 1.5 shows pictures of the OB from both mouse and human.

The olfactory bulb as seen under the microscope has a structure that resembles a raspberry (left panel of Fig. 1.5): its surface is covered with a high number of small, ball-like structures, the so-called glomeruli, consisting of axons, dendrites and synapses between them. Through genetic labelling techniques [107], it was possible to show that the axons reaching one specific glomerulus all extend from ORNs that express a specific type of OR. The dendrites in the glomeruli stem from secondary neurons (mitral and tufted cells) that the axons of the ORNs synapse to. The axons of all ORNs of a specific type are mostly found to converge into one or two glomeruli, resulting in ~ 1800 glomeruli in the OB of mouse [107]. Since each secondary neuron connects to a large number of axons from the ORNs, the glomeruli therefore collect information available from one specific type of OR, which can be seen as an amplification step.

The main purpose of the OB is the convergence and discrimination of information from ORNs of different types. This is achieved both through spatial organisation on the surface of the OB as well as inter-neural connections on the secondary level. The establishment of this spatial organisation during the ontogenetic development of an animal is the subject of chapter 4. In the introduction to this chapter, the detailed structure and purpose of the OB will be explained in greater detail.

Since almost all ORNs that express a specific OR (and therefore respond similarly to a specific odourant) project their axons on one specific glomerulus, the response pattern of the ORNs (Fig. 1.3) translates into a spatial activity pattern on the surface of the OB. Fig. 1.6 shows examples of such patterns for three different odourants.

1.2.3 The olfactory system in insects

In insects (non-vertebrates), the general structure of the olfactory system is quite similar to the one described so far, although the number of genes coding for olfactory receptors is much lower (~ 50 – 100). Olfactory receptor neurons of insects usually appear in groups of one to four in so-called sensillia, small hair-like structures situated on sensory bristles on the animal's head. In drosophila, e.g., sensory bristles are located on special antennae as well as on a separate structure called the maxillary palp [45]. The ORNs in insects have

ORs	S 1	S 3	S 6	S 18	S 19	S 25	S 41	S 46	S 50	S 51	S 79	S 83	S 85	S 86
odorants														
butanoic acid														
pentanoic acid														
hexanoic acid					●									
heptanoic acid	●			●	●		●	●		●	●			
octanoic acid	●			●	●		●	●		●	●	●		
nonanoic acid	●			●	●		●	●		●	●	●		●
pentanol	a	●	a						b					
hexanol	b	●	a				●		b					
heptanol	b	●			●	●			b					
octanol	b			●	●		●	●	b	●				
nonanol	b			●	●		●	●	b	●	●			
bromobutanoic acid														●
bromopentanoic acid														●
bromohexanoic acid					●		●							●
bromooctanoic acid	●			●	●		●	●		●	●	●		●
hexanedioic acid														●
heptanedioic acid														●
octanedioic acid			●								●			●
nonanedioic acid			●						●	●				●

Fig. 1.3: Schematic picture of response strengths of different olfactory receptors (ORs – top row) to different odourants (left column) (from [97]). Big filled circles indicate strong response, smaller circles weaker response. Activity was measured as fluorescence of ORNs that were loaded with a Ca^{2+} sensitive dye (for details, see [97]). Most of the receptors respond to several odourants, whereas, e.g. the ORs S50 and S86 are highly specified within this specific set of odourants.

a single dendrite instead of a number of cilia, which is bathed in a fluid, the sensillum liquor, containing odourant binding proteins and most probably serving similar tasks as the mucus in vertebrate olfaction. The signal transduction mechanism taking place in the sensillia of insect ORNs is similar to the one in the cilia of vertebrate ORNs [60], which will be described in Sec. 2.1. Very much like in the case of vertebrates, the axons of the ORNs in insects connect to a part of the brain, the antennal lobe (e.g. [68, 80]), which is the equivalent of the olfactory bulb. Structures in insects are much smaller and less complex and often also more specified than in vertebrates or mammals [45].

1.2.4 The vomeronasal organ – pheromone detection

In insects and many vertebrates, there is a second and spatially separate organ dedicated to the detection of smell, called (in vertebrates) the vomeronasal organ. Also situated in the nasal cavity [48], it has many similarities to the olfactory system and some of the results to be presented in the later chapters might be applicable. The detailed mechanism of signal transduction in the receptor cells of the vomeronasal organ is not yet completely discovered [45]. It is known, however, that those receptor neurons are much more sensitive as well as more specific than the receptor neurons in the ORNs. The apparent main purpose of the vomeronasal organ is the detection of species-specific messenger chemicals, i.e. pheromones, that influence, e.g. sexual behaviour, nursing or aggressiveness [141]. The receptor neurons of the vomeronasal organ project their axons to the accessory olfactory bulb, showing convergence and sorting very similar to the axons of the ORNs [20]. A difference persists in the further connections to higher brain regions, where the neurons from the vomeronasal pathway do not send information to the cortex but only to brain regions that are connected to unconscious response like the amygdala. In humans, the remains of a vomeronasal organ are most probably not functional [161].

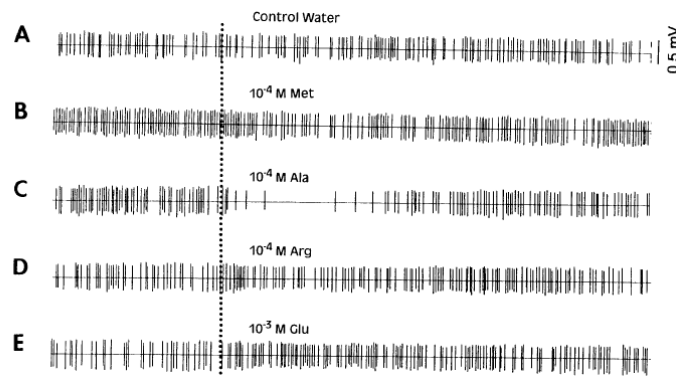


Fig. 1.4: Typical spike trains produced by ORNs after stimulation with different odourants (the amino acids Met, Ala, Arg and Glu; ORNs from catfish; from [133]). Note, that the contact with odourants can both increase and decrease the spontaneous spiking rate.

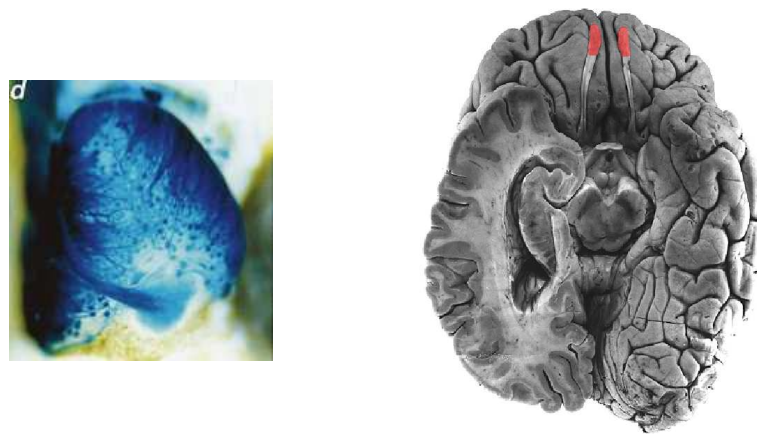


Fig. 1.5: Olfactory bulb in mouse (left (from [109])); the diameter of the OB in adult mice is 2–3 mm [115] and human (right (human brain seen from below, OB marked in red); modified from [148]). Note on the left picture the long thin fibers terminating in small, ball-like structures. These are the genetically labelled axons of the ORNs and the regions where they build synapses to secondary neurons, the glomeruli.

1.3 Performance of the olfactory sense and interesting questions

Although the sense of smell is certainly not the most important sense for human survival, it still accomplishes an incredible task that so far no 'electronic nose' [114] is able to imitate or substitute in a comparable manner as cameras, microphones or hearing aids do with respect to the visual or the auditory sense. Most of the approximately 1000 different olfactory receptor (OR) proteins have a huge reception range of many hundred molecules that they respond to. Since reception ranges of different ORs often overlap and coding (and perception) of olfactory information depends further on concentration, a practically infinite number of different olfactory impressions can be perceived, the limiting entity not being the olfactory sense itself but rather the brain that just cannot remember (and certainly not name) such a huge amount of qualitatively different impressions. Concerning quantitative sensitivity, the covered reception range is comparably large as in the other senses. Like photoreceptor cells that are able to detect single photons [45], specific olfactory receptor neurons (ORNs) are also known to operate at the physical limit, i.e. they can detect single

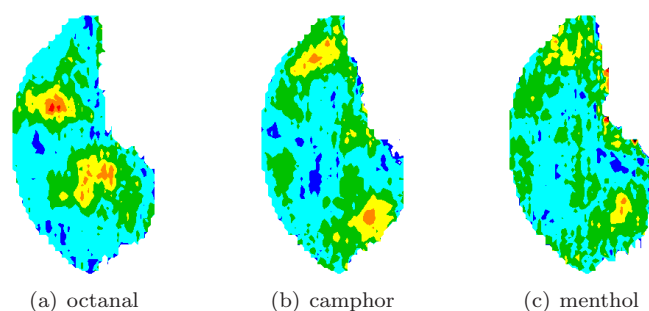


Fig. 1.6: Activity patterns of a rat OB after stimulation with the respective odourant (from [57]). Activity is measured in terms of uptake of a special radioactively labelled form of glucose. Red represents high, blue low neural activity and a special projection technique is used to display the surface of the whole OB. For each odourant such a map can be measured and catalogued [57].

odourant molecules². On the other hand, adaptation to higher concentrations of odourants works almost perfectly in all concentration ranges, a property of the olfactory sense that one appreciates when spending a few minutes in an unpleasantly smelling surrounding [10].

There are several questions raised from a more general perspective when considering this technically so far unrivalled performance of the olfactory sense (or the senses in general). First of all, there is the question of how information is encoded, transmitted and processed using molecules and ions. Which types of molecules are used at which state and are there certain universal design principles being applied and maybe also being found in other instances of cellular information processing? Since the reaction enthalpies of biochemical reactions involved in cellular processes usually are in the range of thermal energies, fluctuations of molecule numbers and 'false alarms' in the detection units will be important and quite common. Further, the often very low numbers of molecules of a given species within the small compartments where detection and transduction of signals takes place, contributes to the ubiquitousness of chemical noise. How does the cell suppress (or use [63]?) noise in order to reliably detect very weak stimuli and transmit this information in such a random environment? Another intriguing question is that of how receptor cells achieve their often almost perfect adaptation over large ranges of stimuli strengths. On which level do the necessary feedback loops operate and how do they cooperate?

Going a step further in the sensory systems, information is coded in more easily quantifiable electrical impulses. Questions arising on this higher level of perception include that of the purpose of a (spatial) neural map or how information from different channels is correlated and co-processed. How the brain makes sense of this information in terms of cognition and remembrance is a question that is clearly out of scope, yet. The same holds (at least for the present work) for the very interesting question of how sensory systems evolved and why certain reappearing structures and design principles prevailed against others.

The aim of the present work is to shed some light on answers to a few of the aforementioned questions taking the perspective from theoretical physics. Throughout this thesis, the system of interest is the olfactory sense, however, some concepts and ideas (especially from chapter 3) are abstract enough to be applicable to other (sensory) systems, as well. Additionally, this thesis provides an example of how (three) substantially different theoretical approaches can be utilised to tackle the complexity of living systems.

²Olfactory receptor neurons in the antennae of moths were shown experimentally to be able to sense single pheromone molecules [71, 134].

Chapter 2

Signal Transduction in the Olfactory Receptor Neuron

2.1 Experimental background

The signal transduction in the olfactory system – as in all other senses – makes information about the outside world accessible to the brain. In the case of the sense of smell, this information is about the type and concentrations of different volatile (and therefore usually small) molecules that pass by the olfactory epithelium in the nasal cavity during respiration. The 'language' of the brain, on the other hand, is the language of spike trains – series of action potentials that are communicated between the neurons through axons, dendrites and synapses. The 'translation' between these two different forms of information encodings is accomplished by the signal transduction mechanism of the olfactory receptor neuron (ORN). The main part of this transduction – and also the part covered in this thesis – happens in the cilia of the ORNs, long and thin tubes of membrane that extend into the mucus layer from the dendritic knob of the ORN. Fig. 2.1 shows a closeup view on the cilia of an ORN embedded in the olfactory epithelium.

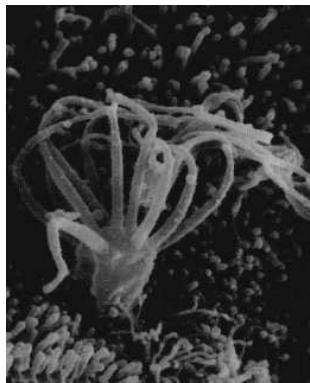


Fig. 2.1: A scanning electron micrograph of the dendritic knob and the cilia of a human ORN with surrounding epithelium (from [110]). The dendritic knob has typically a diameter of 1–2 μm , cilia vary in length from 1 μm to over 30 μm [110] (species-dependent up to 250 μm [133]) and have a diameter of about 0.1–0.3 μm (cf. also Fig. 1.2).

Two main signal transduction pathways have been discovered in ORNs [133, 136]:

1. A cyclic adenosine monophosphate (cAMP) mediated pathway through cyclic-nucleotide-gated (CNG) channels.

2. A pathway mediated through inositol triphosphate (IP_3) that gates until now [48] unidentified cationic channels.

In vertebrates, the cAMP mediated pathway seems to be the predominant one. The role of the second pathway is not clear [42], not even if it is a separate pathway on its own (e.g. in specific cells) or if it coexists with the first one in the same cells and both are coupled through some link.

Since the cAMP-mediated pathway in vertebrates is much better understood and since there is much more experimental data available for it, this work deals only with the first of the two pathways. The involved chemical species and the transduction through it will be described in more detail in the following subsection.

2.1.1 The cAMP-mediated signal transduction pathway

Fig. 2.2 shows a schematic section through a cilium of an ORN with the main chemicals involved in the cAMP-mediated olfactory signal transduction pathway¹.

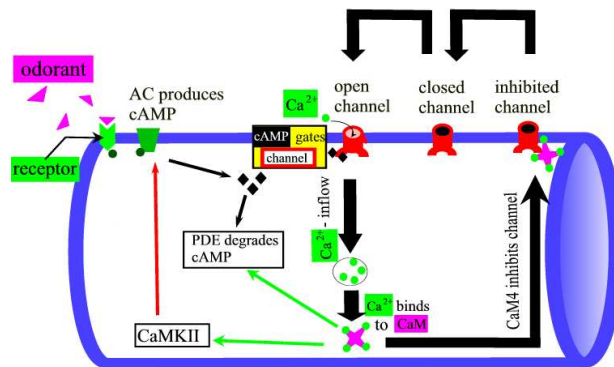


Fig. 2.2: Schematic drawing of a part of the cAMP-mediated signal transduction in a cilium of an ORN focusing on the negative feedback calcium-loaded calmodulin (CaM4) exerts on the ion channels. Black arrows indicate negative feedback reactions or transitions, green arrows enhancement and red arrows inhibition of enzymatic activity. The main forward-path is: Binding of an odourant molecule to a receptor which activates the enzyme adenylyl cyclase (AC). This leads to an increase in cAMP which gates specific cationic channels. Calcium flows in and depolarises the cell. See text for a more detailed description.

The starting event of the signal transduction pathway is the binding of an odourant molecule (possibly attached to an odourant binding protein) to an olfactory receptor (OR), of which there are many different types. Common to all of them is their tertiary structure: They are all 7-transmembrane G-protein coupled receptor molecules, that means, they are proteins located in the cell membrane with parts extending outside the cell (the odourant-binding regions) and parts reaching inside the cell (the coupling region for the G-protein). Upon binding of a ligand (odourant) to the outer part of the OR, the protein changes conformation and by that sets off a smaller protein inside the cell, the G_α -subunit of the G-protein, that diffuses in the cytosol of the cilium. If by chance such a G-protein hits a specific enzyme anchored in the membrane of the cilia, the adenylyl cyclase (AC), it can bind, change the conformation of the AC and by that 'activate' it (enhance its catalytic power). The reaction catalysed by the AC is a cyclisation reaction of the 'energy carrier' of the cells, adenosine triphosphate (ATP), that is abundant in cells, into a small

¹A closely related pathway is operating in cone photo-receptors in the retina.

molecule called cyclic adenosine monophosphate (cAMP) (Fig. 2.3). cAMP is called the second messenger molecule of the signal transduction cascade (the first being the odourant itself) and due to its small size diffuses rapidly through the cytosol (diffusion constant $D \approx 300 \frac{\mu\text{m}^2}{\text{s}}$ [24]).

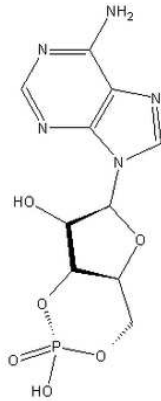


Fig. 2.3: Chemical structure of cAMP (from [159]).

In ORNs, a special kind of chemically gated ion channels has been found, the cyclic-nucleotide-gated (CNG) channels. The ligand for these channels is cAMP (or cyclic guanosine monophosphate (cGMP)) and two to four² of these second messenger molecules are needed to gate one CNG channel. These channels are specific for positively charged ions, mainly sodium (Na^+) and calcium (Ca^{2+}) that passively flow through the channels into the cell – the direction determined by the transmembrane voltage and their respective Nernst potentials. This provides a first electrical signal: the transmembrane potential is raised. The main change in the potential results from the current of chloride ions that flow, also passively according to their Nernst potential, out of the cilium through specific chloride channels gated by calcium ions [121]. The change in transmembrane potential spreads very quickly (in the range of $10^7 \frac{\mu\text{m}}{\text{s}}$ [70]) and when a specific threshold value is reached in the soma (Fig. 1.2), an action potential is generated in a region called axon hillock and subsequently travels along the axon towards the olfactory bulb.

Independent of the stimulus (odourants binding to the receptors), active elements in the membrane of the cilia maintain the concentration differences needed for the transduction of a stimulus as described above. There is evidence for sodium-calcium exchangers [122] that, by letting in three Na^+ ions, pump out one Ca^{2+} ion per cycle [92]. Active, i.e. energy-consuming ionic pumps might be present, evidence exists, e.g. for an active chloride pump [73].

As in all signalling systems, mechanisms are needed, that regulate the dynamics of the transduction, e.g. adapt the system to different input strengths and provide a way to shut down the input and reinitialise the system to make it ready for new inputs. Commonly, those mechanisms are negative feedback loops, of which there are several working inside the cilia of the ORN on the level of chemistry (for an overview, see [170]). Fig. 2.2 schematically shows three of them that go through a calcium-binding protein abundant in ORNs (and other cells), calmodulin (CaM). CaM has four binding sites for calcium ions and the fully calcium-loaded complex (abbreviated CaM4) is able to regulate different stages of the signal transduction pathway:

1. CaM4 enhances the activity of the enzyme phosphodiesterase (PDE) that catalyses the degradation of cAMP to AMP [12, 165].
2. CaM4 enhances the activity of the enzyme calcium kinase II (CaMKII) that down-regulates the activity of AC and therefore reduces the production of the second messenger cAMP [89].
3. By binding to the CNG channels, CaM4 can directly decrease the current through these channels [13, 81].

The last mechanism will be identified later in this chapter to be of high importance for the dynamics of the signalling on intermediate time scales of a few seconds.

There might be several other feedback mechanisms operating in the described signal transduction pathway, that are not mediated by calmodulin [170], e.g. a cAMP-activated

²Reported Hill coefficients for the activation of CNG channels by cAMP lie between 1.5 and 3.5 [25, 74]. The tetrameric structure of the CNG channel suggests a maximum number of four cAMP binding sites.

protein kinase A that deactivates the receptor.

All the chemical species present in the cilium (the reaction compartment) interact with different kinetics and therefore together represent a chemical network whose main purpose can be seen as a transducer from an input signal (the odourant type and concentration) to an output signal (the number, timing and correlations between the action potentials sent out on the axon). The nodes of this network are the chemical species, the links the possible reactions³. Different subnetworks can – as approximations – be separated and analysed independently with newly defined inputs and outputs.

In the following, some experimental findings of single cell measurements are presented and Sec. 2.2 provides a theoretical treatment of a specific chemical subnetwork, the results of which are later compared to some of these experimental data.

2.1.2 Experimental findings from whole cell measurements

For the analysis of the signal transduction pathway and its dynamics, ORNs are usually dissociated from the olfactory epithelium of animals (mice, rats, frogs, salamanders, newts, trouts, ...), so single cells and their response to different kinds of stimuli can be looked at. Cells can be kept alive (show unchanging response behaviour) for several hours [95] in an ionic solution with physiological condition (usually Ringer solution [5]). When removing the ORNs from the surrounding tissue, their comparably long axons have to be cut (cf. right panel of Fig. 1.2). Apparently, the effect of this 'opening' of the cell membrane on the physiological properties of the cell can be neglected (the cell is still able to perform its tasks after this cut, e.g. maintains concentration gradients across its membrane).

As described earlier in this section, the 'output' of the system, i.e. the response of the ORN to a stimulus is a spike pattern that is conducted towards the brain. Different to the visual system [9], not much is known about the way information is encoded in spike trains produced by an ORN. Whether it is the spike rate, the onset time of a group of spikes or temporal correlations between spikes that carries the information transduced in the signal transduction in the cilia is not clear⁴. E.g., an ORN can react to a stimulus with an increase or a decrease in the spiking rate, depending on the type and concentration of odourant presented (Fig. 1.4). In terms of more general and conserved features of the signal transduction in ORNs, it is best to go one step upwards the signalling pathway and treat the transmembrane potential or the transmembrane current as the output of the signalling process. This not only shows much more reproducible properties, it also simplifies the possible dynamics by leaving out the complex generation of action potentials in the soma of the cell [112].

Measurements – techniques

Several techniques are available for measuring the electrical properties of a cell. The electrical potential inside a cell is measured by sticking a microelectrode (usually a micropipette filled with a conducting ionic solution) into the cell. The most interesting technique for measuring the transmembrane current is the suction pipette technique [95, 126]. Here, the whole ORN is sucked into a pipette such that only the dendrite and the cilia stick out of it and are surrounded by the physiological solution and therefore are exposed to the odourants (Fig. 2.4). Assuming a tight attachment of the cell membrane to the glass walls of the pipette (and therefore a negligible leak current), the current measured to flow between the inside of the pipette and the outside must be the transmembrane current through the ion channels, pores and active elements in the membrane of the cell.

Measuring concentrations of intermediate products of the signalling pathway is quite difficult, partly due to the extremely small volume of the cilia. The only involved chem-

³Biochemical measurements of the kinetics of the reactions are often hard to obtain and difficult to relate to the mechanisms in the cell. For some examples, see [11, 16, 69] and references in Tab. 2.1.

⁴Only recently, attempts of a classification have been made [129].

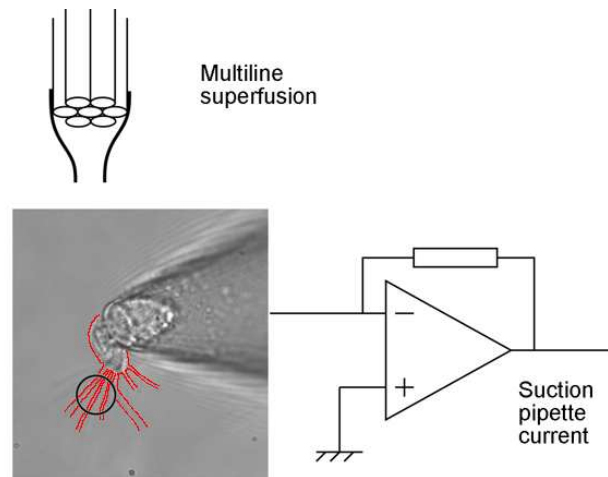


Fig. 2.4: The suction pipette technique for measuring the transmembrane current (modified from [126]). The ORN (bordered by the red line – in this case from salamander) is sucked into a micropipette and held in a constant stream of physiological solution to which odourants can be added. The current between the inside of the pipette and the outside is recorded ('suction pipette current'). The black circle in the microscopic figure (diameter $\sim 10\mu\text{m}$) is the laser spot of the fluorescence measurement (see text).

ical where this is possible quantitatively at least to some extent, is calcium. There are a number of organic molecules that strongly increase fluorescence in the presence of calcium, so-called calcium-sensitive dyes (e.g. Fluo-3). The cell can be loaded from outside with these molecules and by using a laser, the fluorescence intensity of the dye can be measured and related to the calcium concentration (e.g. [126]). This can even be done spatially resolved (fractions of micrometres) to reveal spatial inhomogeneities in the calcium concentration [90]. The typical time scale of the reaction between dye and calcium is a few milliseconds [21] and therefore well below the timescales typically studied in the experiments described below.

ORNs can be stimulated in various ways. Direct stimulation with an odourant activates the full signal transduction pathway. For that, the cells are usually kept in a steady flow of a physiological solution. With a micropipette, various water-soluble odourants in different concentrations can be added to the steady flow and pass by the cilia of the ORN. Instead of an odourant, a chemical called IBMX (3-isobutyl-1-methylxanthine) can be applied to the cilia. IBMX inhibits PDE (see Subsec. 2.1.1) and therefore increases the cAMP concentration (e.g. [90]). Another technique to excite the signalling pathway of the ORN is the photolysis of so-called caged cAMP [74, 145]. The second messenger cAMP can be chemically coupled to different organic molecules such that the bond between these two parts can be broken (and therefore cAMP released into the cytosol) when the probe is illuminated with UV light. By this, only the signal transduction pathway downwards from cAMP is excited, i.e. the dynamics of the receptors, G-proteins and the cyclases do not contribute to the overall dynamics.

Using different time patterns of stimuli (odourant or IBMX concentration, length and intensity of UV light), different response properties of the system can be tested. The simplest time pattern is just a single short pulse. Short time adaptation can be tested by applying two short consecutive pulses with varying waiting time between those. Applying a single, long (compared to the timescales in the system) pulse is practically the same as applying a step pulse. Another way of testing the adaptation behaviour is a step pulse on top of a baseline concentration ('step-step'). Table 2.1 lists some of the experiments available in the literature.

pattern	stimulus	duration	animal	ref.
short pulse	cineole	1 s	salamander	[126]
	cineole	0.025 s	frog	[6]
	cineole	1 s	mouse	[124]
	cineole	1 s	salamander	[88]
	menthone	90 ms	rat	[96]
	amino acid mixture	25 ms/1 s	trout	[144]
	odourant mixture	20 ms	salamander	[95]
	IBMX/K ⁺	1 s	salamander	[90]
	cineole/caged cAMP	0.1–3 s	newt	[146]
caged cAMP	0.2–0.5 s	newt	[145]	
long pulse	cineole	30 s	salamander	[126]
	cineole	30 s	mouse	[124]
	cineole	40 s	salamander	[103]
	cineole	30/60 s	frog	[125]
	amino acid mixture	3/5 s	trout	[144]
	menthone/2-isob.-3methoxy pyr.	13/30/∞/22 s	rat	[96]
	menthone/IBMX/caged cAMP	4/8/15 s	rat	[96]
step	IBMX		salamander	[90]
	caged cAMP		newt	[145]
double pulse	cineole	2×0.1 s	salamander	[88]
	cineole	2×1 s	mouse	[124]
	cineole	2×8 s/4×0.1 s	salamander	[170]
	amyl acetate	2×0.2 s	newt	[84]
step-step	cineole	4/1 s	frog	[123]

Tab. 2.1: Experiments conducted with whole cell ORNs found in the literature.

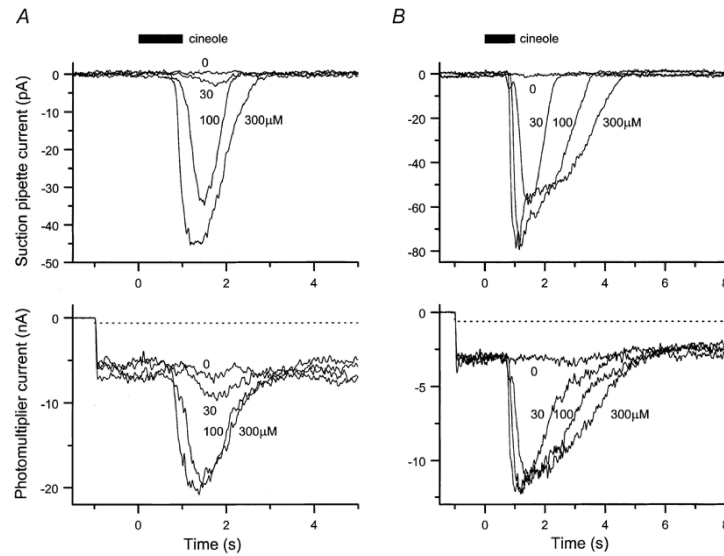


Fig. 2.5: Transmembrane current (upper row) and calcium-sensitive fluorescence intensity (lower row) as response to a one second stimulation (black horizontal bars) with different concentrations of the odourant cineole (experimental setup as in Fig. 2.4). Two different ORNs from salamander were used: one with low (A) and one with high (B) sensitivity to cineole. Each curve is an average over two measurements (modified from [126]).

Measurements – results

Fig. 2.5 shows the response (transmembrane current and fluorescence of a calcium-sensitive dye) of two ORNs to a stimulation with a one second pulse of the odourant cineole. After a short latency time (including effects that strongly depend on the experimental setup), both the current signal and the fluorescence show pulses with a quick rising phase and a slower falling phase (the sign of the curves depend on the current definition and the polarity of the photomultiplier of the fluorescence measuring device, respectively). Looking only at the current and the calcium, the cell needs about 2–5 s to recover from the stimulus, depending on the odourant concentration and the sensitivity of the cell. The ORN with high sensitivity (B in Fig. 2.5), especially for the current response, shows a shoulder in the curves for high stimuli (also seen, e.g. in [88]).

If the duration of stimulus presentation is prolonged (several seconds), different behaviours are reported in the literature. Fig. 2.6 shows an example of a measurement with oscillatory response, both in transmembrane current and in calcium concentration. Similar behaviour was observed in [124, 125, 144]. Other sources report different response shapes, namely one similar to the case of a short stimulus pulse [96, 103], partly with strong fluctuations but no pronounced oscillatory pattern. In most experiments, oscillatory response was found only for intermediate concentrations of odourant, the response to low or high concentrations looks similar in shape to the measurements of a short pulse.

An important functional ingredient of signalling systems is adaptation. A distinction has to be made between short time adaptation and adaptation on longer timescales (minutes). Fig. 2.7 shows a typical result of a double pulse experiment to investigate short time adaptation. Here, two short but strong pulses are presented to the system and the magnitude of the response to the second pulse is measured and related to the waiting time between the two pulses. For short waiting times ($\lesssim 10$ s), the cell has not completely recovered its signalling apparatus from the first pulse, which leads to a diminished response to the second pulse.

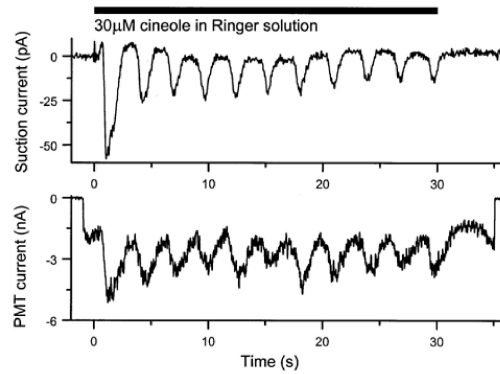


Fig. 2.6: Transmembrane current (upper row) and calcium sensitive fluorescence intensity (lower row) of a salamander ORN as response to a prolonged stimulation (30 s) with an intermediate concentration of the odourant cineole (black horizontal bar) (modified from [126]).

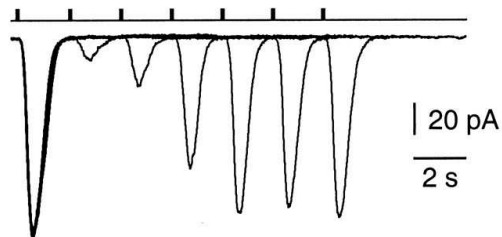


Fig. 2.7: Transmembrane current (voltage clamped to -60 mV) of a salamander ORN as response to two consecutive short and strong odourant pulses ($300 \mu\text{M}$ cineole for two times 0.1 s – upper row). Six different experiments with inter-pulse intervals of 2 s, 4 s, 6 s, 8 s, 10 s and 12 s are superimposed in this figure (from [88]). Waiting time for full recovery of the cell between two double-pulse experiments was 40 s.

2.2 Oscillations and short time adaptation from negative feedback

The aim of this part of the present thesis is to analyse the chemical kinetics in the signal transduction of the olfactory receptor neurons and to find a minimal model that qualitatively (and to some extent also quantitatively) captures some of the experimental findings described in the last section, most importantly the oscillations and the short time adaptation behaviour. In the first subsection below, this minimal model is introduced and explained. The model is analysed using a powerful analytical method, the stoichiometric network analysis (SNA), briefly described in the second subsection. The model as described in the following has to be seen as the outcome of the analysis of many possible chemical networks, using SNA. After it was proven by SNA that the system can show the desired dynamics, the four coupled differential equations describing it are analysed numerically and the results are compared to the experimental findings described in the preceding section. An explicit bifurcation analysis using relevant experimental parameters of the model is added, both serving as a test of the robustness of the presented model as well as giving predictions for possible future experiments.

2.2.1 Chemical reactions and kinetics

The interesting dynamics of the experiments presented in the preceding section happens on time scales of tens of milliseconds to seconds. Since the dimensions of a single cilium are so small, diffusion within a cilium happens on timescales of millisecond (the diffusion constant, e.g. of cAMP is around $3 \cdot 10^{-10} \frac{\text{m}^2}{\text{s}}$ [24]). It is assumed that the involved chemical species are homogeneously distributed along a cilium⁵ and that odourant concentrations are high enough for a spatially homogeneous excitation. Therefore, in the following, the system is treated as a well-mixed compartment with uniform spatial distribution of the relevant chemicals and no diffusion terms will be considered.

Analysing many of the possible reaction networks built from the reactions mentioned in Subsec. 2.1.1 using SNA (see next subsection), the following four reactions proved to be the ones that can reproduce the experimental findings described in Subsec. 2.1.2:

1. The switch between the open ('o') and the closed ('c') form of the cyclic-nucleotide-gated channel (CNG) is described as a chemical reaction with the opening rate k_{act}^+ used as a stimulus to the system and the closing rate $k_{\text{CNG}^\circ}^-$:



2. In the cytoplasm of the cilium, the protein calmodulin (CaM) binds four calcium ions. No intermediate calcified forms of CaM are considered, only the fully loaded CaM4:



3. The fully calcium-loaded calmodulin binds irreversibly to the open channel and turns it into an 'inhibited' ('i') channel that prevents the entry of ions into the cilium:



⁵For the CNG channel, the distribution along a cilium has been studied experimentally but led to contradictory results [49, 121].

4. The channel-calmodulin complex can reversibly dissociate, leaving the channel in the closed form:



Two conservation constraints for the concentrations of the channel and calmodulin reduce the number of independent species in this reaction scheme to four. Volume concentrations are denoted by the according species put into rectangular brackets, for surface species, a subscript s is appended to the bracket. The factor σ converts between both concentration measures (σ is the volume/surface ratio of the cilium):

$$[\text{CNG}^{\text{tot}}]_s = [\text{CNG}^c]_s + [\text{CNG}^o]_s + [\text{CNG}^i]_s, \quad (2.5)$$

$$[\text{CaM}^{\text{tot}}] = [\text{CaM}] + [\text{CaM4}] + \frac{1}{\sigma}[\text{CNG}^i]_s. \quad (2.6)$$

The four independent quantities chosen for the further analysis are the surface concentration of the open form of the channel $[\text{CNG}^o]_s$, the intraciliary calcium concentration $[\text{Ca}^{2+}]$, the concentration of the fully calcium-loaded calmodulin $[\text{CaM4}]$, and the surface concentration of the channel-calmodulin complex (the 'inhibited' channel) $[\text{CNG}^i]_s$. The according dynamic equations for these four species are again partly a result of the stoichiometric network analysis presented later in this section. Most of the terms in the following kinetic equations are results of the law of mass action. The cases where another kinetics is used are detailed below.

1. An external stimulus enhances the rate k_{act}^+ and leads to an opening of the channels. $k_{\text{act}}^+(t)$ captures the whole dynamics of the signal transduction starting with the binding of an odourant to the receptor to the point when cAMP binds to the CNG channel. Open channels can spontaneously close or turn into the inhibited form through reaction with CaM4:

$$\begin{aligned} \frac{d}{dt}[\text{CNG}^o]_s = & k_{\text{act}}^+([\text{CNG}^{\text{tot}}]_s - [\text{CNG}^o]_s - [\text{CNG}^i]_s) \\ & - k_{\text{CNG}^o}^-[\text{CNG}^o]_s - k_{\text{CNG}^i}^+[\text{CNG}^o]_s[\text{CaM4}]. \end{aligned} \quad (2.7)$$

2. Calcium ions flow through the open channels into the cilium with a constant current i_{Ca} , which is the most simple way of modelling ionic currents⁶. For the active extrusion of calcium ions from the cytoplasm of the cilium, a first order approximation is used, a Hill-type equation [156] with the 'dissociation' constant K_{Ca} . Further, free intraciliary calcium disappears when bound to CaM and reappears, when CaM4 dissociates:

$$\begin{aligned} \frac{d}{dt}[\text{Ca}^{2+}] = & \frac{1}{\sigma}i_{\text{Ca}}[\text{CNG}^o]_s - \frac{1}{\sigma}k_{\text{Ca}}\frac{[\text{Ca}^{2+}]}{[\text{Ca}^{2+}] + K_{\text{Ca}}} \\ & - 4k_{\text{CaM4}}^+[\text{Ca}^{2+}]^2 \left([\text{CaM}^{\text{tot}}] - [\text{CaM4}] - \frac{1}{\sigma}[\text{CNG}^i]_s \right) \\ & + 4k_{\text{CaM4}}^-[\text{CaM4}]. \end{aligned} \quad (2.8)$$

⁶This simplification neglects the dependence of the ionic current on both transmembrane voltage (V_m) and concentrations inside (c^{in}) and outside (c^{out}) the cell. A more involved study would include the voltage as a dynamical variable and use the Goldman-Hodgkin-Katz current equation [158] for the transmembrane current of the ion species n : $i_n = z_n^2 F P_n \beta V_m \left(\frac{c_n^{\text{out}} - c_n^{\text{in}} e^{z_n \beta V_m}}{1 - e^{z_n \beta V_m}} \right)$, where z is the valence of the ion, F the Faraday constant, P the permeability and $\beta = \frac{1}{k_B T}$ with the Boltzmann constant k_B and the temperature T .

3. The fully calcium-loaded form of calmodulin is produced from its calcium-free form in a reaction which is of second order in the calcium concentration⁷. CaM4 spontaneously dissociates and it also takes part in the dynamics of the 'inhibited' form of the channel:

$$\begin{aligned} \frac{d}{dt}[\text{CaM4}] = & k_{\text{CaM4}}^+ [\text{Ca}^{2+}]^2 \left([\text{CaM}^{\text{tot}}] - [\text{CaM4}] - \frac{1}{\sigma} [\text{CNG}^{\text{i}}]_s \right) \\ & - k_{\text{CaM4}}^- [\text{CaM4}] \\ & - \frac{1}{\sigma} k_{\text{CNG}_1}^+ [\text{CaM4}] \left([\text{CNG}^{\text{tot}}]_s - [\text{CNG}^{\text{o}}]_s - [\text{CNG}^{\text{i}}]_s \right) \\ & + \frac{1}{\sigma} k_{\text{CNG}_1}^- [\text{CNG}^{\text{i}}]_s - \frac{1}{\sigma} k_{\text{CNG}_2}^+ [\text{CaM4}] [\text{CNG}^{\text{o}}]_s. \end{aligned} \quad (2.9)$$

4. The calmodulin-channel complex is formed with the fully calcium-loaded form of calmodulin from both open and closed channels. It spontaneously dissociates:

$$\begin{aligned} \frac{d}{dt}[\text{CNG}^{\text{i}}]_s = & k_{\text{CNG}_1}^+ [\text{CaM4}] \left([\text{CNG}^{\text{tot}}]_s - [\text{CNG}^{\text{o}}]_s - [\text{CNG}^{\text{i}}]_s \right) \\ & - k_{\text{CNG}_1}^- [\text{CNG}^{\text{i}}]_s + k_{\text{CNG}_2}^+ [\text{CaM4}] [\text{CNG}^{\text{o}}]_s. \end{aligned} \quad (2.10)$$

Eqs. (2.7)–(2.10) provide a set of four coupled nonlinear ordinary differential equations. For most of the parameters of this reaction network (the reaction rates and constants as well as the total concentrations of CNG and CaM), only rough estimates are available from experiments. Therefore, not only a detailed numerical analysis of the network (Subsec. 2.2.3) is desirable but also an analysis of the robustness of the numerically obtained results (Subsec. 2.2.4) as well as a general, parameter-independent analysis of the capabilities of this network (Subsec. 2.2.2).

2.2.2 Stoichiometric network analysis

Stoichiometric network analysis (SNA) [27] is a tool that helps judging qualitatively, whether a given set of chemical reactions (the stoichiometric network) is able to show specific dynamical behaviour, merely from its topology, i.e. the way in which the different components of the network are connected. It is an analysis of the capability of a given network to produce, e.g. oscillations or show instabilities, and as this it works independent of a specific choice of the kinetic parameters \vec{k} of the chemical reactions. SNA can therefore be used to 'design' a minimal reaction network from a larger pool of (chemically) possible reactions that – just from its topology – might show a desired dynamical behaviour. By using SNA, specific conditions (e.g. relations between the fluxes through different reactions) can be derived that must be met in order to find, e.g. an oscillating state. However, for actually checking, if this oscillating state occurs within experimentally reasonable kinetic parameters, direct numerical simulations (Subsec. 2.2.3) or an explicit bifurcation analysis considering the relevant kinetic constants (Subsec. 2.2.4) must be performed. The reactions described in the preceding subsection have to be seen as the outcome of an SNA of a number of different (chemically) possible networks with other species involved or with different kinetics. The criterion for this choice was the ability of the network to produce oscillating solutions and therefore being able to reproduce at least qualitatively the experimental measurements shown in Fig. 2.6. In the following, SNA⁸ will be applied to the network detailed in Subsec. 2.2.1 and conditions for an oscillatory solution of it will be derived.

⁷The relevance as well as the experimental validity of the order of this reaction will be discussed later in Subsec. 2.2.2 and Appendix A.1.

⁸The formalism of SNA is derived in [27], more accessible introductions can be found in [29, 40, 43, 130] and applications of SNA to real chemical networks in [30, 31, 41, 142]. A related mechanism is presented in [157].

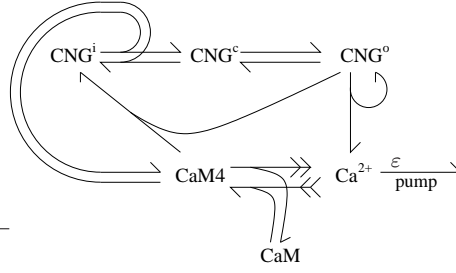


Fig. 2.8: Network diagram of the reactions from Eqs. (2.1)–(2.4) including the influx and the removal of calcium ions. The (positive) stoichiometric coefficients of the products are encoded as the number of barbs on the respective reaction arrows, the (negative) ones of the reactants by the number of feathers. The kinetic exponent of a reactant is symbolised by the number of left feathers (e.g. the formation of CaM4 requires four calcium ions and the kinetics is assumed to be of second order, so two out of four feathers are put on the left). By convention, no feathers are drawn, if both stoichiometric and kinetic coefficient are one. Non-integer kinetic coefficients are written as a number next to the arrow (ε in case of the pump – see text).

One advantage of SNA is, that to a great extent it can be done using diagrams. The stoichiometry as well as the kinetics of reaction networks is encoded in these network diagrams which is explained for the reactions from Eqs. (2.1)–(2.4) in Fig. 2.8.

A simplified version of the network in Fig. 2.8, can be drawn based on the following assumptions:

1. CaM4 dissociates quickly from the inhibited channel, i.e. CNG^i can be eliminated from the network.
2. Considering only the weak stimulus regime, most channels will be in the closed state and changes in $[\text{CNG}^c]$ will be negligible, i.e. CNG^c is also eliminated.
3. The same holds for the concentration of calcium-free calmodulin which is assumed to be constant and therefore not considered as a dynamical variable.

Denoting the open channels as X , calcium as Y and CaM4 as Z (with the respective concentrations x, y, z), the simplified network diagram is given in Fig. 2.9(a). The corresponding kinetic equations are

$$\frac{d}{dt}x = k_1 - k_5xz, \quad (2.11)$$

$$\frac{d}{dt}y = k_2x - 4k_3y^2 + 4k_4z - k_6y^\varepsilon, \quad (2.12)$$

$$\frac{d}{dt}z = k_3y^2 - k_4z. \quad (2.13)$$

Here, instead of the Hill-type equation for the removal of calcium in Eq. (2.8), a power-law dynamics with exponent ε is assumed, which will be related to the modelling in Eq. (2.8) later. Eqs. (2.11)–(2.13) can be written with the concentration-vector $\vec{x} = (x, y, z)^T$ in matrix notation as

$$\frac{d}{dt}\vec{x} = \nu\vec{v}, \quad (2.14)$$

with the stoichiometric matrix

$$\nu = \begin{pmatrix} 1 & 0 & 0 & 0 & -1 & 0 \\ 0 & 1 & -4 & 4 & 0 & -1 \\ 0 & 0 & 1 & -1 & 0 & 0 \end{pmatrix} \quad (2.15)$$

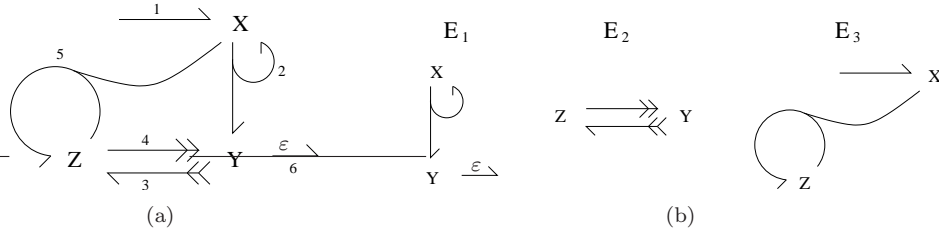


Fig. 2.9: (a) The simplified reaction network considered. X denotes the open channels, Y CaM4 and Z calcium. (b) The three extreme currents into which the simplified reaction network can be decomposed.

and the velocity-vector $\vec{v} = (k_1, k_2x, k_3y^2, k_4z, k_5xz, k_6y^\varepsilon)^T$. Since mass action kinetics is assumed, the elements of \vec{v} can be written as $v_j = k_j \prod_i x_i^{\kappa_{ij}}$ with the matrix of the kinetic exponents

$$\kappa = (\kappa_{ij}) = \begin{pmatrix} 0 & 1 & 0 & 0 & 1 & 0 \\ 0 & 0 & 2 & 0 & 0 & \varepsilon \\ 0 & 0 & 0 & 1 & 1 & 0 \end{pmatrix}. \quad (2.16)$$

Due to specific properties of stoichiometric matrices, the complete set of steady states \vec{v}_{ss} ($\nu \vec{v}_{ss} = 0$) can be written down in closed form in SNA as linear combinations of a certain number of undecomposable subnetworks \vec{E}_i , the extreme currents [28]:

$$\vec{v}_{ss} = \sum_i j_i \vec{E}_i \equiv \mathbf{E} \vec{j}, \quad j_i \geq 0. \quad (2.17)$$

\mathbf{E} is the matrix containing the vectors \vec{E}_i as columns. Each of these undecomposable subnetworks must fulfil the stationary state condition, i.e. the number of (incoming) barbs must be the same as the number of (outgoing) feathers for all species (cf. caption of Fig. 2.8). For the six reactions among three species (Fig. 2.9(a)) there are three [40] extreme currents that can be found by successively taking out reactions from the network as long as the stationarity condition is still fulfilled⁹. Fig. 2.9(b) shows the three extreme currents for the simplified network. Numbering the reactions as in Fig. 2.9(a), the extreme currents can be written as

$$\vec{E}_1 = \begin{pmatrix} 0 \\ 1 \\ 0 \\ 0 \\ 0 \\ 1 \end{pmatrix}, \quad \vec{E}_2 = \begin{pmatrix} 0 \\ 0 \\ 1 \\ 1 \\ 0 \\ 0 \end{pmatrix}, \quad \vec{E}_3 = \begin{pmatrix} 1 \\ 0 \\ 0 \\ 0 \\ 1 \\ 0 \end{pmatrix}. \quad (2.18)$$

A transformation can now be found from the set of kinetic constants \vec{k} to the set of fluxes through all extreme currents \vec{j} and with that the Jacobian of the dynamical system (Eq. (2.14)) can be written as

$$J = \nu \text{diag} \left(\sum_k j_k \vec{E}_k \right) \kappa^T \text{diag}(\vec{x}_0)^{-1}, \quad (2.19)$$

where $\text{diag}(\vec{u})$ is defined as the matrix that has the components of \vec{u} as its diagonal elements and \vec{x}_0 is the vector of steady state concentrations. Often – as in the case presented here – it is sufficient to analyse the stability properties of the reduced Jacobian [27]

⁹The extreme currents can also be found using specifically designed algorithms [22, 77].

$\tilde{J} = -\nu \text{diag} \left(\sum_k j_k \vec{E}_k \right) \kappa^T$, which reduces the number of independent parameters for the bifurcation analysis from six kinetic constants k_i to three flux constants j_k . Since the stability of the system does not depend on the actual numbers of the j_k but only on their ratios, one of them can be set to unity. Here, $j_2 = 1$ is chosen which leads to

$$\tilde{J} = \begin{pmatrix} j_3 & 0 & j_3 \\ -j_1 & 8 + \varepsilon j_1 & -4 \\ 0 & -2 & 1 \end{pmatrix}. \quad (2.20)$$

To check, whether a Hopf bifurcation can occur, one can now either calculate the eigenvalues of \tilde{J} and check, if two of them can become complex conjugate with positive real parts or one can use a necessary and sufficient condition given in [41]. It is based on a modified Routh scheme [29] and arranges the coefficients a_i of the characteristic polynomial $p_{\tilde{J}}(\lambda) = \lambda^3 + a_1\lambda^2 + a_2\lambda + a_3$ of \tilde{J} in a specific manner (see, e.g. [120]). The criterion for the occurrence of a Hopf bifurcation turns out to be a change of sign in the expression $a_1a_2 - a_3$.

For the reduced Jacobian as given in Eq. (2.20), the coefficients of the characteristic polynomial are

$$a_1 = 9 + j_3 + j_1\varepsilon, \quad a_2 = 9j_3 + j_1\varepsilon + j_1j_3\varepsilon, \quad a_3 = 2j_1j_3 + j_1j_3\varepsilon. \quad (2.21)$$

With those, the condition for a Hopf bifurcation becomes $a_1a_2 - a_3 = 81j_3 + 9j_3^2 + \varepsilon(j_1j_3^2 + 9j_1 + 18j_1j_3) - 2j_1j_3 < 0$. For this condition to be fulfilled, $j_1 \gg j_3 \gg \varepsilon$, i.e. the flux going through the subnetwork E_1 must be much larger than the flux through the other two subnetworks and the kinetic exponent of the pump must be small. The latter point is a quite severe condition. Oscillations can only be expected, if the pumps (or exchangers) work near saturation (constant pumping, i.e. kinetic exponent zero). From this, a statement for the phenomenological constant K_{Ca} in the Hill-type term in Eq. (2.8) can be made. It should be much smaller than the typical peak calcium concentration during oscillations.

By applying SNA to slightly modified networks, it could further be found out, that the kinetic exponent of the reaction between calcium and calmodulin does not influence the occurrence of a Hopf bifurcation when varied between the experimentally reasonable values one and four (see Appendix A.1 for a numerical investigation of this point).

2.2.3 Numerical solution, comparison to experiments

After analytical considerations such as the SNA described above proved that the system of four coupled nonlinear ordinary differential equations (2.7)–(2.10) is capable of showing oscillatory solutions and narrowed the ranges for some of the parameters, this set of equations is integrated numerically using the stiff solver `ode15s` from `matlab` [149]¹⁰. The results are presented as time traces of concentrations of the different species for a variety of stimulus presentation patterns. The initial values for the four species were usually zero and before varying the stimulus, the system was evolved into a stationary state. Throughout this subsection the same model parameters were used as presented in Tab. 2.2. For most of the concentrations and kinetic constants, rough quantitative measurements exist, for some only qualitative statements have been found in the literature. The only 'true' phenomenological parameters k_{Ca} , K_{Ca} and k_{act}^+ were chosen in such a way that the resulting steady state concentrations (of Ca^{2+} , ...) are within reasonable ranges. The choice of the kinetic parameters for the binding of calcium to calmodulin is detailed in Appendix A.1. A quadratic relation is assumed between the stimulus parameter k_{act}^+ and the odourant concentration, based on an assumed Hill coefficient of two for the gating of the CNG channels by cAMP (see footnote on page 11).

¹⁰A simple self-written but much slower Euler forward algorithm in C++ was used for some of the runs to verify the validity of the results regarding parameters of the solver `ode15s`.

parameter	unit	value	literature
σ	dm	$5 \cdot 10^{-7}$	$(2.5 \dots 6.3) \cdot 10^{-7}$ [133] ^a
$[\text{CNG}^{\text{tot}}]_s$	$\frac{\text{mol}}{\text{dm}^2}$	$1.3 \cdot 10^{-13}$	$1.3 \cdot 10^{-13}$ [121] (rat); $1.2 \cdot 10^{-12}$ [86] (frog)
$[\text{CaM}^{\text{tot}}]$	$\frac{\text{mol}}{\text{dm}^3}$	$2 \cdot 10^{-5}$	10^{-5} [2]
$k_{\text{CNG}^{\circ}}^{-}$	$\frac{1}{\text{s}}$	10^{-2}	very slow [13] ^b
k_{CaM4}^{-}	$\frac{1}{\text{s}}$	2.5	10...40 [32] ^c ; slow [111] ^d
k_{CaM4}^{+}	$\frac{1}{\text{s}} \frac{\text{dm}^6}{\text{mol}^2}$	$1.1 \cdot 10^9$	"too fast to be measured" [32] ^e
$k_{\text{CNG}_1^{\text{i}}}^{+}$	$\frac{1}{\text{s}} \frac{\text{dm}^3}{\text{mol}}$	$2.1 \cdot 10^6$	$1.7 \cdot 10^7$ [13] ^f ; $1.5 \cdot 10^6$ [111] ^g
$k_{\text{CNG}_2^{\text{i}}}^{+}$	$\frac{1}{\text{s}} \frac{\text{dm}^3}{\text{mol}}$	$2.1 \cdot 10^6$	$= k_{\text{CNG}_1^{\text{i}}}^{+}$ [13]
$k_{\text{CNG}^{\text{i}}}^{-}$	$\frac{1}{\text{s}}$	$3.4 \cdot 10^{-1}$	$> 2.2 \cdot 10^{-1}$ [111] ^h
i_{Ca}	$\frac{1}{\text{s}}$	$2 \cdot 10^4$	$7.8 \cdot 10^4$ [121]
k_{Ca}	$\frac{1}{\text{s}} \frac{\text{mol}}{\text{dm}^2}$	10^{-10}	see text
K_{Ca}	$\frac{\text{mol}}{\text{dm}^3}$	$1.2 \cdot 10^{-7}$	see text
k_{act}^{+}	$\frac{1}{\text{s}}$	rest. state: $1.6 \cdot 10^{-5}$ (corresponds to $[\text{Ca}^{2+}] = 5 \cdot 10^{-9} \frac{\text{mol}}{\text{dm}^3}$)	see text $5 \cdot 10^{-8}$ [133]

^avolume-area ratio for an infinitely long cylinder of diameter 0.1...0.25 μm

^bFig. 1A inset, assuming PDE destroys remaining cAMP fast

^cslowest rate in the cooperative binding of the four Ca^{2+}

^dFig. 3B

^ethe value is an order of magnitude estimate based on the dissociation constants for the four binding sites given in [32, 36] and the value for k_{CaM4}^{-} ; see also Appendix A.1

^fFig. 3D, assuming CNGA2A4B1b is equivalent to native CNG

^gestimated from τ_1 in Fig. 3D

^hestimated from τ for +/+ in Fig. 3E assuming fast opening of CNG^c

Tab. 2.2: Parameters used in the deterministic model together with the available literature values. Appendix A.1 discusses the reaction of calmodulin and calcium (k_{CaM4}^{-} and k_{CaM4}^{+}) in greater detail and gives alternative parameters.

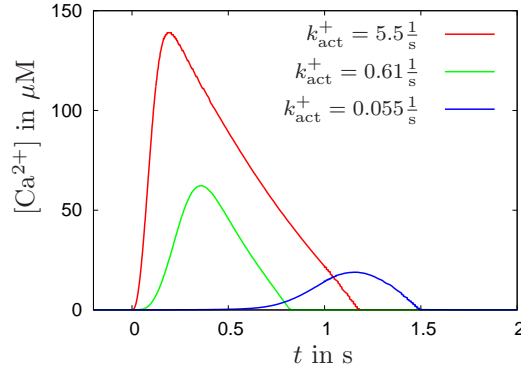


Fig. 2.10: Calcium concentration in the model as response to an increase of k_{act}^+ between $t = 0$ s and $t = 1$ s. Three different pulse strengths were used.

Single, short pulse

Fig. 2.10 shows the calcium concentration as a response to a 1s long increase in k_{act}^+ to three different values. Baseline k_{act}^+ was $1.6 \cdot 10^{-5} \frac{1}{\text{s}}$ and 'excitation' k_{act}^+ $5.5 \cdot 10^{-2} / 0.61 / 5.5 \frac{1}{\text{s}}$, which correspond, using the quadratic relation, to a ratio of odourant concentrations of roughly 1:3.3:10. k_{act}^+ was increased for $0 \text{ s} < t \leq 1 \text{ s}$.

The values reached for the calcium concentration (10–150 μM) are reasonable considering the extracellular concentration of 3–7 mM [102] or the results of a model for the steady state concentrations of a fully activated cilium [92]. Looking at the amplitude ratios of the response and comparing it to Fig. 2.5, this system comes closer to the cell with low sensitivity (A in Fig. 2.5). Since, in the simulations, the stimulus directly opens the CNG channels, for strong stimuli, the response follows immediately. In the experiment, however, time consuming steps before the opening of the channel (diffusion and reaction steps) lead to a latency of about 1s for the onset of the calcium signal. Taking this into account, the simulations show, as in the experiment, an increased latency for lower stimuli, although much more pronounced. Due to the noise in the experimentally observed curves, it is difficult to compare the shapes of the time traces, but as a common feature of both experiment and simulation, the response curves grow less steep with weaker stimuli. Quantitative comparison of the experimental data and the results from the model is difficult, because in the experiment the calcium concentration is not measured directly but through the fluorescence of a dye, whose reaction dynamics with the calcium ions might alter the response curves to some extent.

Single, long pulse

Stimulating the system for a longer time produces qualitatively different behaviours depending on the stimulus strength. For an intermediate stimulus strength $k_{\text{act}}^+ = 0.055 \frac{1}{\text{s}}$, spiky oscillations are observed (Fig. 2.11) for the duration of the stimulus (30s). The frequency is about $0.4 \frac{1}{\text{s}}$, which agrees with the experimentally observed oscillations in Fig. 2.6. In the simulations, the shape of the oscillations is much more spiky than in the experiment, which again might to some extent be an effect of the dynamics of the calcium-dye reaction.

When the system is simulated with a stronger stimulus, an increased oscillation frequency is observed with smaller amplitude, which is in qualitative agreement with experiment [124]. Increasing the stimulus above some threshold, the stable oscillations turn into damped oscillations (Fig. 2.11 top right). For decreasing stimuli, oscillation frequency decreases and again, passing through a specific threshold stimulus, the system produces damped oscillations as a response (Fig. 2.11 bottom right). In Subsec. 2.2.4, the occur-

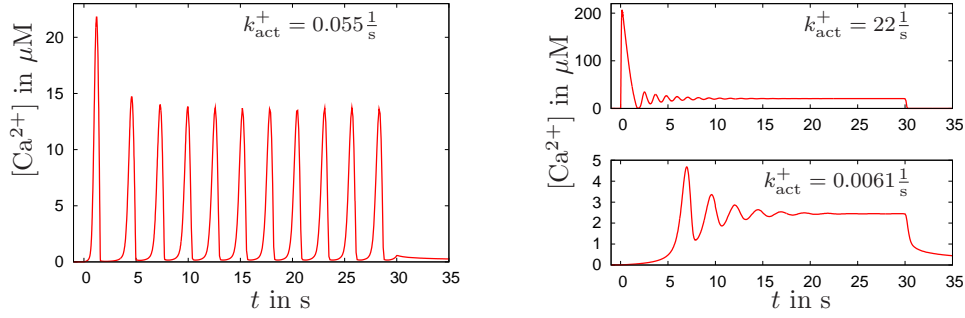


Fig. 2.11: Result of the simulation for a single, long (30s) stimulus-pulse. **Left:** Oscillating calcium concentration as a response to an intermediate stimulus strength k_{act}^+ . **Right:** Damped oscillations occur in the case of high or low stimulus strength.

rence of oscillations will be investigated more thoroughly. There is yet no experimental data available from fluorescence measurements that would relate to this result of the simulations, only current measurements are presented in [124]. Here, the shape of the non-oscillating case for strong stimulus looks similar to the result of the simulations, whereas this is not the case for the weak stimulus. An approximative quantitative agreement consists between the stimulus range, in which oscillations are observed. In the experiment, this range covers roughly 1–2 decades in odourant concentration, which corresponds to roughly 2–4 decades of stimulus strength (k_{act}^+) in the simulations (see the beginning of this subsection). In [126], the frequency of the oscillations is found to decrease roughly by a factor of two when the cell is bathed in a sodium free solution. Since the main extrusion mechanism for calcium appears to be $\text{Na}^+/\text{Ca}^{2+}$ -exchange, the reduction of extracellular sodium can be captured in the simulation by decreasing the calcium pump rate k_{Ca} . This indeed leads to a decrease in oscillation frequency, although by far not as pronounced (a decrease of k_{Ca} by a factor of seven leads to a decrease of oscillation frequency of only about ten percent).

A close-up view of Fig. 2.11 of approximately two periods is shown in Fig. 2.12. All four dynamical variables are shown to oscillate and the temporal order of peaks is the same as the order in the signal transduction cascade: An increase in the open channel fraction above the value $\frac{k_{\text{Ca}}}{i_{\text{Ca}}[\text{CNG}^{\text{tot}}]} \approx 0.038$ (horizontal dashed line in Fig. 2.12) leads to very fast accumulation of calcium. Calcium binds to calmodulin which then leads after a certain time lag to the maximum of the inhibited channel fraction, which corresponds to the minimum of the open channel fraction. Calcium is then pumped out of the system rapidly.

Two short pulses

The double pulse experiments investigating short time adaptation are usually done with high odourant concentrations. Fig. 2.13 shows the results of simulations of such double pulse experiments. As in the experiment (Fig. 2.7), the first short 100ms-pulse increase in the stimulus was followed by a second, identical pulse after a certain waiting time of 2,4,6,8,10 or 12 s, respectively. k_{act}^+ was increased to a value of $5.5 \frac{1}{\text{s}}$, which is one hundred times the value used for the single long pulse in which oscillations were observed, i.e. odourant concentration is now assumed to be higher by a factor of ten.

For the double pulse experiments, no experimental data for the calcium concentration has been measured yet, so comparison can only be made to current measurements as the ones in Fig. 2.7. The amplitude ratios of the second pulses for the different waiting times agree roughly between simulations and experiment.

Fig. 2.14 shows a close-up view of the run with 4s waiting time including all dynamical

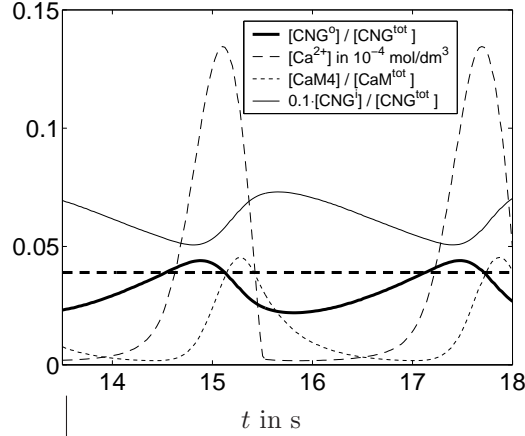


Fig. 2.12: Time courses of all dynamical variables in the simulation presenting a prolonged stimulus. Except for $[\text{Ca}^{2+}]$, fractions of the total concentrations are plotted as indicated in the legend. The values for $[\text{CNG}^1]/[\text{CNG}^{\text{tot}}]$ are divided by a factor of 10 for convenience of plotting. The dashed horizontal line indicates the open fraction $\frac{k_{\text{Ca}}}{i_{\text{Ca}}[\text{CNG}^{\text{tot}}]} \approx 0.038$ at which the pumps are no longer able to compensate the influx through channels.

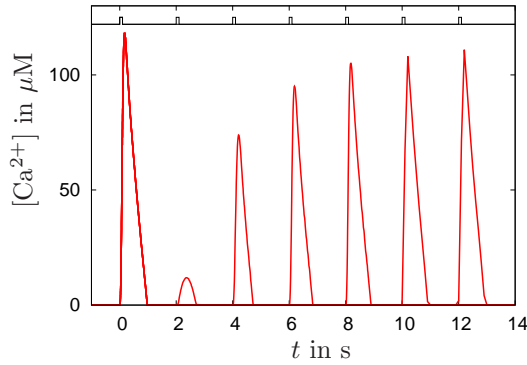


Fig. 2.13: Superimposed time traces for the simulation of the double pulse experiment. The upper row shows the stimulus (pulse increase in k_{act}^+ to $5.5 \frac{1}{\text{s}}$ for 0.1s), the lower one calcium concentration. The first pulse is the same for all six time traces, the second pulse is given after 2, 4, 6, 8, 10 or 12 s, respectively.

variables. As can be seen, it is only the species $[\text{CNG}^1]$ that has not returned close to its stationary state level after this waiting time. After 4s, still approximately 50% of all CNG channels have CaM4 bound and can therefore not respond to a new stimulus by opening and letting Ca^{2+} in.

As a variant of the double pulse experiment modelled above, the second pulse can be applied after a fixed time but for a different duration. In Fig. 2.15 such a protocol was applied to the model and the outcome can be compared to experiments (e.g. [84]). Qualitatively, the model shows the correct behaviour, namely an increase in the intensity of the response to the second pulse with stimulus duration. However, the ratio between the three response amplitudes does not agree with the experimental result.

Step-step

The experimental results obtained in [123] after a step-step adaptation protocol (a 4 s weak stimulus followed directly by a 1 s stimulus of varying strength) can not be reproduced consistently with the model and the parameter set as presented above (data not shown).

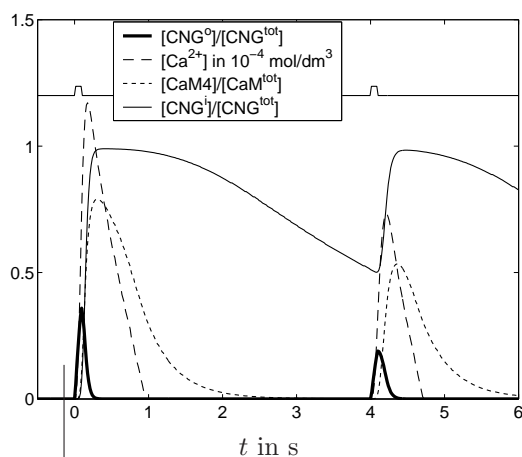


Fig. 2.14: Time courses of all dynamical variables in the simulation of the double-pulse experiment. Except for $[\text{Ca}^{2+}]$, fractions of the total concentrations are plotted as indicated in the legend.

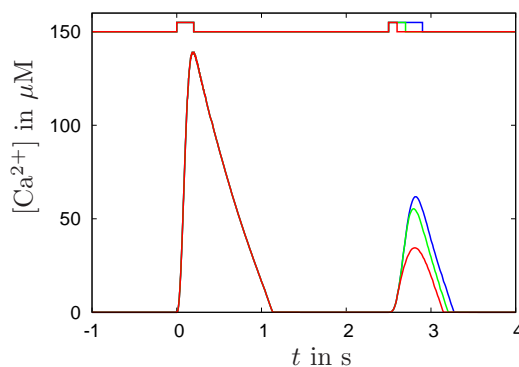


Fig. 2.15: Modified double-pulse experiment, where the first pulse was applied for 0.2 s and the second after a fixed time of 2.5 s for a varying duration (0.1 s (red), 0.2 s (green) and 0.4 s (blue) – see upper row). Pulse strength was for both pulses $k_{\text{act}}^+ = 5.5 \frac{1}{\text{s}}$.

Most probably, either a missing long time adaptation for small concentrations is the reason for this drawback or an odourant concentration-stimulus relation (e.g. only for small concentrations) that is different from the quadratic one used so far.

2.2.4 Explicit bifurcation analysis

When a complex system is numerically modelled and a desired dynamical behaviour (e.g. oscillations) is obtained using a set of experimentally maybe not very well-known parameters, an important and interesting question is always how robust this behaviour is produced when using a different parameter set that still might be within experimentally justifiable limits. A good way to deal with this question is a bifurcation analysis, that in addition leads to predictions and suggestions for the experimentalists to check the validity of the model proposed. Distinct from the stoichiometric network analysis (SNA) presented in Subsec. 2.2.2, the bifurcation analysis is now done with the full system and for the untransformed set of parameters, the kinetic constants. Whereas SNA was used to find the correct reactions that generally can produce oscillating solutions, here, the exact conditions under which the full system can oscillate will be derived for each of the parameters.

For a simplified version (using $k_{\text{CNG}^i_1}^+ = k_{\text{CNG}^i_2}^+$ as experiments suggest (see Tab. 2.2)) of the four coupled ordinary differential equations (2.7)–(2.10), the Jacobian is easily calculated to be

$$J \equiv \frac{\partial f}{\partial(u, v, w, x)} = \begin{pmatrix} J_{11} & J_{12} & 0 & J_{14} \\ 0 & J_{22} & J_{23} & J_{24} \\ J_{31} & J_{32} & J_{33} & J_{34} \\ 0 & J_{42} & 0 & J_{44} \end{pmatrix}, \quad (2.22)$$

with $u \equiv [\text{CNG}^o]_s$, $v \equiv [\text{CaM4}]$, $w \equiv [\text{Ca}^{2+}]$, $x \equiv [\text{CNG}^i]_s$ and

$$\begin{aligned} J_{11} &= -k_{\text{act}}^+ - k_{\text{CNG}}^- - k_{\text{CNG}^i}^+ v, & J_{12} &= -k_{\text{CNG}^i}^+ u, & J_{14} &= -k_{\text{act}}^+, \\ J_{22} &= -k_{\text{CaM4}}^+ w^2 - k_{\text{CaM4}}^- - \sigma k_{\text{CNG}^i}^+ ([\text{CNG}^{\text{tot}}]_s - x), \\ J_{23} &= 2k_{\text{CaM4}}^+ w ([\text{CaM}^{\text{tot}}] - v - \sigma x), & J_{24} &= \sigma (k_{\text{CNG}^i}^- + k_{\text{CNG}^i}^+ v - k_{\text{CaM4}}^+ w^2), \\ J_{31} &= i_{\text{Ca}} \sigma, & J_{32} &= 4k_{\text{CaM4}}^+ w^2 + 4k_{\text{CaM4}}^-, \\ J_{33} &= -8k_{\text{CaM4}}^+ w ([\text{CaM}^{\text{tot}}] - v - \sigma x) - \frac{k_{\text{Ca}} K_{\text{Ca}}}{(w + K_{\text{Ca}})^2}, & J_{34} &= 4k_{\text{CaM4}}^+ \sigma w^2, \\ J_{42} &= k_{\text{CNG}^i}^+ ([\text{CNG}^{\text{tot}}]_s - x), & J_{44} &= -k_{\text{CNG}^i}^- - k_{\text{CNG}^i}^+ v. \end{aligned} \quad (2.23)$$

By setting the time derivatives in Eqs. (2.7)–(2.10) to zero the following set of equations for the stationary states can be obtained:

$$v_{\text{ss}}(x_{\text{ss}}) = \frac{k_{\text{CNG}^i}^- x_{\text{ss}}}{k_{\text{CNG}^i}^+ [\text{CNG}^{\text{tot}}]_s - x_{\text{ss}}}, \quad (2.24)$$

$$w_{\text{ss}}(x_{\text{ss}}) = \sqrt{\frac{k_{\text{CaM4}}^- k_{\text{CNG}^i}^- x_{\text{ss}}}{k_{\text{CaM4}}^+ (k_{\text{CNG}^i}^+ ([\text{CNG}^{\text{tot}}]_s - x_{\text{ss}}) ([\text{CaM}^{\text{tot}}] - \sigma x_{\text{ss}}) - k_{\text{CNG}^i}^- x_{\text{ss}})}}, \quad (2.25)$$

$$u_{\text{ss}}(x_{\text{ss}}) = \frac{k_{\text{act}}^+ ([\text{CNG}^{\text{tot}}]_s - x_{\text{ss}})^2}{(k_{\text{act}}^+ + k_{\text{CNG}}^-) ([\text{CNG}^{\text{tot}}]_s - x_{\text{ss}}) + k_{\text{CNG}^i}^- x_{\text{ss}}}, \quad (2.26)$$

$$0 = i_{\text{Ca}} \sigma u_{\text{ss}} - \frac{\sigma k_{\text{Ca}} w_{\text{ss}}}{w_{\text{ss}} + K_{\text{Ca}}} - 4k_{\text{CaM4}}^+ w_{\text{ss}}^2 ([\text{CaM}^{\text{tot}}] - v_{\text{ss}} - \sigma x_{\text{ss}}) + 4k_{\text{CaM4}}^- v_{\text{ss}}. \quad (2.27)$$

Putting Eqs. (2.24)–(2.26) into Eq. (2.27) gives an algebraic equation for the stationary values of x , for which an analytical solution does not exist. Numerically (using the `FindRoot` function of `Mathematica` [163]), approximative solutions of Eq. (2.27) can be obtained and checked if they are physically meaningful (real and larger than zero). The stability of this stationary state is determined by the eigenvalues of the Jacobian (2.22) after substituting u, v, w, x by the numerically obtained $u_{\text{ss}}, v_{\text{ss}}, w_{\text{ss}}, x_{\text{ss}}$. The following Figs. 2.16(a)–2.16(k) show results of this bifurcation analysis represented as 2D-sections through the statespace of the system as functions of k_{act}^+ and another parameter of the model (i.e. all parameters are kept constant except k_{act}^+ and one other). White regions represent stable fixed points (i.e. all four eigenvalues of the Jacobian have negative real parts), black indicates oscillatory solutions (i.e. two eigenvalues have negative real parts and the other two eigenvalues are complex conjugate numbers with positive real part) and in grey areas the system has no physically reasonable stationary state (e.g. unlimited increase of $[\text{Ca}^{2+}]$). A cross marks the parameter set as of Tab. 2.2 together with the intermediate k_{act}^+ for which the system was found to oscillate (Fig. 2.11).

The region of stable oscillations in Figs. 2.16 spans approximately 2–3 decades in the stimulus parameter k_{act}^+ . Using the quadratic relation between stimulus strength and odourant concentration, this transforms into 1–2 decades of concentration range, where oscillations should be observed, which is consistent with the experimental findings cited and described in Subsec. 2.1.2 (cf. also Fig. 2.11).

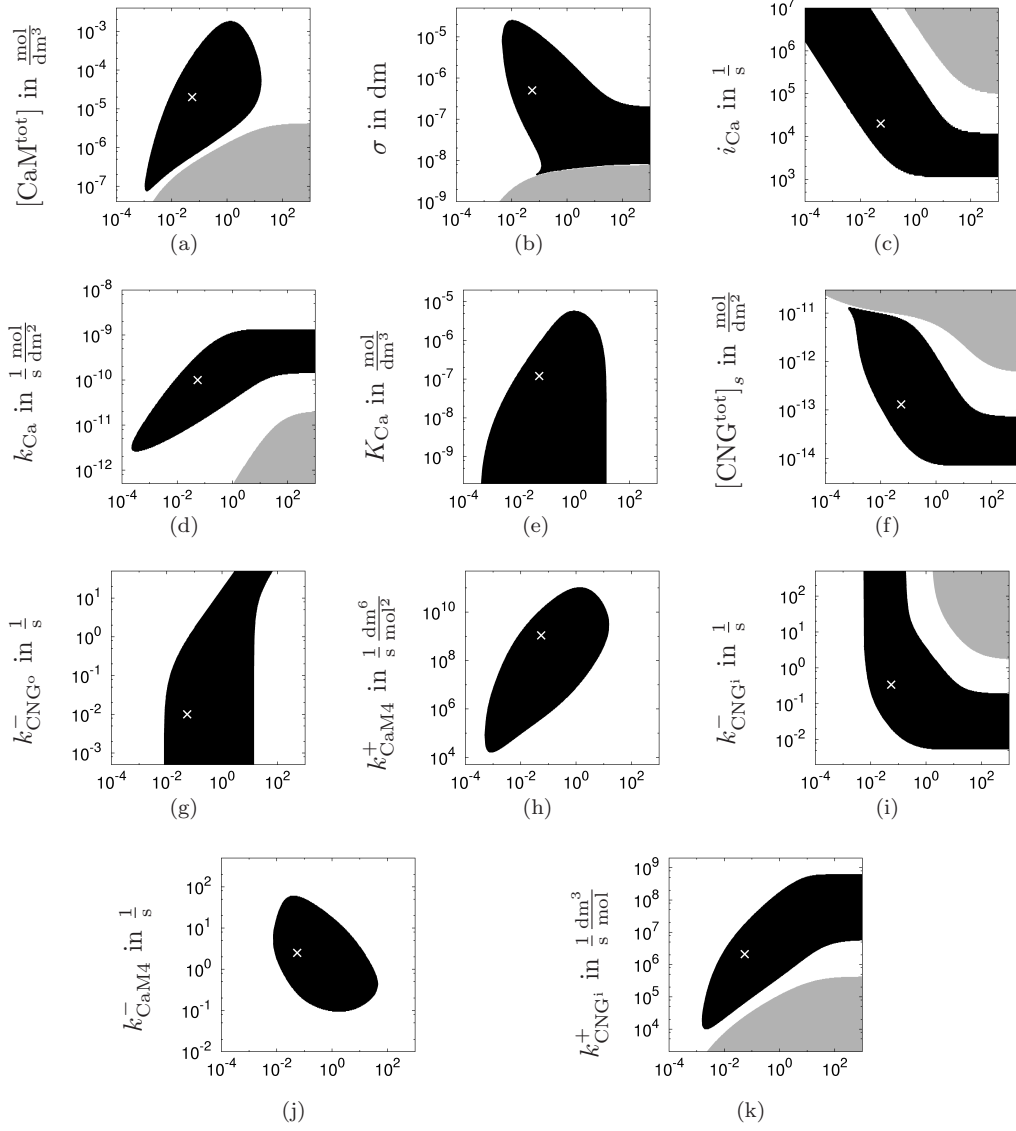


Fig. 2.16: Sections through the state space of the model (Eqs. (2.7)–(2.10)) with $k_{\text{CNG}_1^i}^+ = k_{\text{CNG}_2^i}^+ \equiv k_{\text{CNG}^i}^+$ using the parameters from Tab. 2.2. The parameter on all x -axes is k_{act}^+ in $\frac{1}{s}$. White regions indicate stable fixed points, black oscillatory solutions and in grey regions, no stationary state could be found. The white crosses indicate the parameters used (Tab. 2.2) together with $k_{\text{act}}^+ = 5.5 \cdot 10^{-2} \frac{1}{s}$.

The occurrence of oscillatory behaviour is, according to Figs. 2.16, robust in a sense that all parameters can be varied individually within a region of at least 1.5 decades and oscillations would still be observed. The most sensible parameters in this respect appear to be the calcium extrusion rate k_{Ca} and the rate for the generation of the calmodulin-channel complex k_{CNGi}^+ . Other parameters like K_{Ca} , k_{CNGo}^- and k_{CNGi}^- can be varied over more than four decades and would not destroy the oscillatory dynamics of the model. The occurrence of oscillations therefore is robust against the variation of one or two parameters from the set in Tab. 2.2, however, their frequency, shape and amplitude (e.g. peak calcium concentration) might be not in accordance with experiment.

A few of the parameters of the model might be experimentally accessible, which gives this bifurcation analysis predictive power. The volume-surface ratio σ , e.g., is naturally varied in the cells. Fig. 2.16(b) suggests that oscillations of calcium concentration can only be observed for $\sigma \lesssim 1 \mu\text{m}$. Approximating a cilium by a cylinder of constant diameter d , this condition is well fulfilled for experimentally measured $d \approx 0.1 \mu\text{m}$ (see Tab. 2.2), whereas in the cell body, this condition is not met (taking the soma as a sphere with radius $5 \mu\text{m}$ (Fig. 1.2)). This corresponds to experimental observations¹¹. In principle, experimentally variable are parameters connected to an expression level of genes coding for a specific protein, such as $[\text{CaM}^{\text{tot}}]$, $[\text{CNG}^{\text{tot}}]_s$ or k_{Ca} (through a change in the concentration of calcium pumps or the $\text{Na}^+/\text{Ca}^{2+}$ -exchanger). Genetic techniques exist (e.g. [60]) that can lead to an over- or underexpression of the respective gene and therefore might change the respective protein concentration. Accordingly, experiments could be conducted with genetically altered animals and it could be checked, whether oscillations still occur or not. However, this would be a quite involved experiment, and results would never be able to completely verify or falsify the model, since other, non-controllable facts like the type of receptor expressed or suchlike might bias the results. A parameter easier to be varied is the calcium current i_{Ca} through the CNG channels, which could be, e.g. decreased by lowering extracellular calcium concentration. A variation that was already done experimentally, is the lowering of the calcium extrusion (through a decrease of sodium concentration outside the cell), which is (most probably in a quite complex way) connected to the parameter k_{Ca} .

The grey areas in Figs. 2.16 indicate parameter ranges, where the model does not have a stable fixed point, i.e. the solution 'explodes', meaning that there is an unlimited increase in calcium. This can, e.g., be simply due to i_{Ca} being much too large to be compensated by an outflux k_{Ca} that is always constant for high calcium concentrations. The occurrence of these grey regions is clearly a result from the model being too simple. Increasing the complexity of the model, e.g. by using a more sophisticated term for the calcium extrusion or making the calcium current through the channels concentration-dependent, would decrease the grey areas in the state space plots.

2.2.5 Synchronisation between the cilia of an ORN

Although the signal transduction as described so far takes place entirely in the 5–40 [133] cilia of the ORN, stable oscillations in the transmembrane current of the whole cell are observed. The fluorescence signal related to the calcium concentration from Fig. 2.6 was measured as the average fluorescence of a number (probably ~ 5) of cilia that happen to lie within the laser spot (black circle in Fig. 2.4). Since, certainly, parameters like concentrations of the involved chemicals, reaction constants or activation of the signal transduction cascade vary slightly from cilium to cilium, for stable, phase-constant oscillations to be observed as a sum of the signals from the single cilia, some phase-synchronising mechanism has to be at work. Slightly different parameter sets lead to slightly different oscillation frequencies, which lead – by adding e.g. 5 of these time traces – to an output signal beats that quickly turn into damped oscillations for larger number of single, independent oscil-

¹¹Additionally, the surface density of CNG channels in the soma is much lower than in the cilia [75].

lators. A synchronising mechanism could be the voltage, since that spreads most rapidly through the whole cell, faster than, e.g. diffusion of calcium ions from one cilium into the dendritic knob and into a neighbouring cilium. Ion currents through channels are generally voltage-dependent, which would provide a mechanism to synchronise the single oscillators and produce stable oscillations of just one frequency as a common output. The possibility of the voltage being such a phase-synchronising variable that provides the coupling between different cilia, is currently investigated.

It has been suggested that there exist other coupling mechanisms between different cilia, namely intercilary diffusion of nitric oxide (NO) [136].

2.3 Summary and comparison to other theoretical approaches

The detailed dynamical properties of the signal transduction taking place in the cilia of the olfactory receptor neurons were analysed in this chapter. A brief review of experimental techniques as well as relevant measurements on the cells were given, which served as a starting point for the theoretical modelling. Instead of modelling 'all at once', i.e. setting up differential equations for all involved chemical species and their reactions with a large number of mostly unknown parameters (kinetic constants, concentrations), the goal was to find a minimal system, that is able to reproduce the experimentally observed behaviour of the cells, namely oscillations in calcium concentration and short time adaptation to repeated strong stimulus pulses. For that, stoichiometric network analysis was used, an analysis that checks whether a given chemical reaction network is capable of showing a desired dynamical behaviour merely from its topology. With that, an experimentally well established negative feedback from calcium on the calcium-conducting channels could be identified as the ingredient that can produce both oscillations and short time adaptation. Instead of putting in complicated kinetic terms that try to capture a broad range of stimulus strength, very simple, partly phenomenological assumptions were made, e.g. for the calcium current or the extrusion of calcium from the cilium. The four coupled nonlinear differential equations obtained with the help of stoichiometric network analysis were numerically integrated and tested with different stimulus patterns. Good and partly even quantitative agreement was found between the results of the model and experimental data from the literature when using reasonable choices for the parameters. A further explicit bifurcation analysis served both as a test of the robustness of the model against single parameter variations and as a predictive tool for further experiments. This might be of interest in the future, since other modelling approaches were published recently that identify another negative feedback acting in the cilia as the most important ingredient for the generation of, e.g. the oscillations.

Since the number of published theoretical approaches towards a better understanding of olfactory signal transduction is still quite small, most of them will be discussed briefly in the following. One of the conclusions drawn in [39, 144] is, that – different to the model presented in this chapter – the main reason for the occurrence of oscillations is the feedback of calcium on the adenylate cyclase (see Fig. 2.2) which leads to coupled cAMP-Ca²⁺ oscillations. A proof of principle for this mechanism was given in [33]. In [125], experimental evidence is given for this suggestion, but the results in [84] show that at least the adaptation works fully without involving the adenylate cyclase. This point appears to be undecided and further experiments might provide enough data to compare the two different claims made by the different modelling approaches.

In both papers [39, 144], the idea of the approach is quite different to the one presented in the present work. In [39], simulation results are presented for single pulses, oscillations and adaptation that fit very nicely to experimentally obtained data. Their model includes almost all chemicals involved in the signal transduction starting from the dynamics of the

receptor and ending in a change in transmembrane voltage. This concept leads to a much more complicated set of coupled differential equations with many more constants and parameters for which in most cases only rough estimates are available from experiment. They fit their model to experimentally observed time traces and use different sets of parameters (with single parameters varying by a factor of up to ten) for different experiments. A clear advantage of the results presented in the present work is, that the qualitative features of the different experiments were obtained using just one set of parameters. However, the agreement between theoretical and experimentally measured curves is better in [39].

In [144], a similar but even more extended 'brute-force' modelling approach is made (12 coupled nonlinear differential equations with 44 parameters), making it difficult to really draw conclusions or compare to other models. They find damped oscillations after short stimuli of only 25ms but fail to produce sustained oscillations for longer pulses of >5 s. Through changing single parameters of their model, they also come to the conclusion that the feedback loop generating the (damped) oscillations is the one from calcium on the adenylyl cyclase.

Another model containing essentially the same feedback loops is presented in [137]. It is based on some neural simulator toolkit (for which no further rate constants or equations are given) and produces bursts of spikes.

In [92], spatially dependent profiles of the different ion concentrations are calculated based on complicated equations for the currents. No dynamical features are considered there but when setting up the model of the present work, suggestions and parameter estimates were taken from [92].

There exist quite a few very phenomenological mathematical models for taste and smell reception, e.g. [100] and references cited therein.

A mathematical proof of the existence of periodic solutions in specific systems with negative feedback is given in [65]. In subsequent models, a common ingredient that comes with the negative feedback is often a time delay [151] or a large Hill coefficient. Another work [82] comes to the conclusion that for oscillations to occur, a saturated degradation is necessary, similar to the result from the stoichiometric network analysis in Subsec. 2.2.2 regarding the effective power ε .

As an open question remains the purpose of the oscillatory behaviour of the receptor neurons within specific stimulus regimes. Until now, it can only be speculated about the purpose, e.g. that oscillations might enhance the sensitivity of the system towards an oscillating stimulus pattern [83, 119]. Actually, the stimulus of the olfactory sense does oscillate with the frequency of respiration, which for mouse, e.g., lies roughly in the same range as the internal oscillations observed in separated receptor cells as well as in the model presented here.

As a possible extension of the model, the inclusion of the transmembrane voltage as a further dynamical variable was discussed in the context of synchronised oscillations between different cilia of the same cell. As further extensions, other feedback loops could be included, e.g. to produce adaptation on time scales much longer than the ones considered so far. Since experimentalists constantly improve the measurements of the kinetic relations and the concentrations found in vivo, the model parameters can be easily updated, and it can be checked if the model solely based on the negative feedback on the calcium-conducting channels still is able to reproduce the observed dynamics.

Most of the work presented in this chapter has been published before [120].

Chapter 3

Ion Channel Dynamics in Olfactory Signal Transduction: A Stochastic Signalling Module

3.1 From a deterministic to a stochastic description

In the preceding chapter, the signal transduction in the cilia of the olfactory receptor neurons (ORNs) was described completely deterministically, i.e. no stochastic (random) effects were considered. Such a description is valid only under specific circumstances:

- The mean numbers of molecules per species taking part in the signal transduction is much larger than the fluctuations of these numbers.
- The time scales considered in the deterministic description are much larger than the timescales of the molecular events and of the diffusion (on the length scale of the small compartments like the cilia and cells).

These circumstances are most likely met, if medium or strong stimuli (i.e. intermediate or high odourant concentrations) are presented to the system and one is interested in the whole cell output dynamics on relatively long time scales (milliseconds and longer) rather than the dynamics of a single chemical species in a single compartment as, e.g. one cilium. To get a feeling for the number of molecules involved in the signal transduction, one can assume a homogeneous distribution (cf. footnote p. 17) of the cyclic-nucleotide-gated (CNG) channels along the cilium and compartmentalise the cilium in parts, where roughly 1–10 CNG channels can be found¹. With the values from Tab. 2.2, such a compartment would be around $1\ \mu\text{m}$ long and within this compartment, roughly 200 calmodulin (CaM) molecules could be found as well as ~ 2000 calcium ions when the system is strongly excited (cf. Fig. 2.10). However, in the resting state (no odourant, i.e. no stimulus), the calcium concentration is very low and in such a $1\ \mu\text{m}$ -section of the cilium, only approximately one calcium ion and four second messenger molecules cAMP² [118] would be found. Therefore, the conditions for a deterministic description stated above do no longer hold in the case of no or very weak stimulus. The interesting questions in this context are:

1. What is the detection threshold, i.e. how many odourant molecules are needed to produce a reliable signalling event (cf. footnote on p. 7)?

¹No experimental data for the surface concentrations of the receptors or the adenylate cyclase was found in the literature (cf. Subsec. 2.1.1).

²Cyclic adenosin monophosphate

2. How does the cell make a distinction between real odourant-binding events and the ever-present noise?
3. What mechanisms does the cell use to achieve a low threshold and reliable signalling? Are, e.g. the signalling elements clustered in the membrane?

For approaching questions like these, as well as if one is interested in shorter time scales and intermediate steps of the signal transduction, the influence of (thermal) noise on the system has to be considered. Possible stochastic effects in this signal transduction system are

- the thermal (spontaneous) opening and closing of ion channels,
- the thermal (spontaneous) activation and deactivation of the involved enzymes (including the receptor),
- fluctuations in the number of molecules of involved species due to
 - thermal effects in the reactions,
 - reactions not considered in this scheme,
 - spatial effects,
- temporal and spatial fluctuations of the stimulus (odourant concentration).

Thermal effects in chemical reactions – and the opening and closing of an ion channel can be seen as such – are illustrated in the left panel of Fig. 3.1. Ion channels are large transmembrane proteins, whose conformational state (the tertiary structure) determines, if the channel is permeable to specific ions. Typical energy differences ΔU between different conformational states are usually quite small and comparable to typical thermal energies³ $k_B T$ with the Boltzmann constant k_B and body temperature of the animal $T \approx 300$ K. In thermodynamic equilibrium, the channel therefore has a non-vanishing probability of $e^{-\frac{\Delta U}{k_B T}}$ to be found in the energetically higher state. The rates of switching between the two states additionally depend on a potential energy barrier in between those. Activation, deactivation or inhibition of the channel can be seen as changes in the conformational energies or the energy barrier between them, e.g. due to a second messenger molecule binding to the channel protein.

The right panel of Fig. 3.1 shows a current measurement from a single ion channel as it is found in the cilia of ORNs. The discrete nature of the channel conformations is clearly seen ('o'/'c'). With higher stimulus concentration, the open conformation of the channel becomes more probable but not in such a way that the typical dwelling time in the open state is increased but rather the channel switches more often from 'c' to 'o' (increased R_+).

In the present chapter, the effect of a stochastic switching of the channel on the signalling properties of a simplified signalling module will be considered. In this module, the feedback on the channel introduced and dwelled on in the last chapter is implemented in a simple way and its influence on the signalling properties of the module are investigated. First, the view of the cilium consisting of many compartments (described above) will be taken, and the signalling properties of such a single compartment with a single channel will be looked at. Later (in Sec. 3.6), as an extension, the description of coupled compartments (towards a full cilium) within this framework will be outlined. The results obtained in this chapter are not restricted to olfactory signal transduction. They rather have to be seen as the signalling properties of an abstract building block (i.e. module) found in many instances in biology. Sec. 3.7 describes the general applicability by giving examples from other systems as well as discusses the idea behind this modular approach towards complex biological networks.

³The free enthalpy of a hydrogen bond lies in the range of 5–10 $k_B T$ at $T = 300$ K [56].

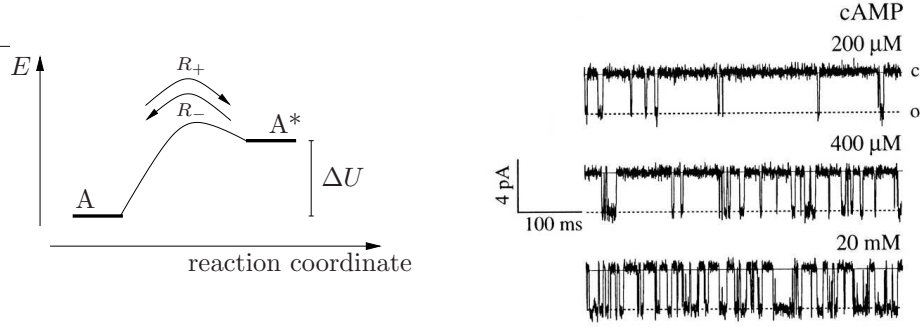


Fig. 3.1: **Left:** A very simple energy diagram of the conformational states A (closed) and A* (open) of an ion channel. The protein changes conformation spontaneously due to thermal activation with the rates R_+ and R_- , respectively. **Right:** Current recordings from a single olfactory cyclic-nucleotide-gated channel in a membrane patch exposed to different concentrations of cyclic adenosine monophosphate (cAMP). 'c'/o' indicates the closed/open state (modified from [52]).

3.2 A two-state signalling module with negative feedback

As a start, the thermal effect on the opening and closing of a single ion channel will be considered. The ion channel in this very much simplified picture is described as a two state system that can be either opened or closed. The channel variable S captures these two states by taking the values 1 if the channel is open and 0 if it is closed. Thermal effects lead to a switching between these two states with the rates R_+ and R_- :



The stimulation of the system, i.e. the external signal, is built in as a temporal variation of the opening rate $R_+(\bar{t})$ (cf. right panel of Fig. 3.1 and preceding text).

Only through the open state of the channel, ions (Ca^{2+} in the case of the olfactory signal transduction) can flow into the small compartment of volume V . In the simplest approximation this happens with a constant current J (independent of voltage difference and concentration difference). The number of calcium ions is supposed to be high enough and their dynamics fast enough to consider only the calcium concentration instead of discrete ions. For the removal of calcium from the volume V considered, a first order approximation is appropriate, making this term proportional to the concentration in the volume (pumping rate $\bar{\lambda}$). The differential equation for the calcium concentration \bar{c} therefore becomes

$$\frac{d\bar{c}}{dt} = \frac{J}{V} S(\bar{t}) - \bar{\lambda} \bar{c}(\bar{t}). \quad (3.2)$$

Fig. 3.2 illustrates the two different states of the system considered.

The negative feedback that calcium exerts onto the channel via the protein calmodulin and the binding of CaM4 to the channel (see Sec. 2.1) is built into this model by up-regulating the closing rate $R_- = R_-(\bar{c})$ with increasing concentration \bar{c} . As the simplest dependence, a linear relation (with the feedback parameter $\bar{\alpha}$) is considered here⁴:

$$R_-(t) = R_-^0 + \bar{\alpha} \bar{c}(t). \quad (3.3)$$

⁴This linear relation can also be seen as an expansion of a monotonically increasing function $R_- = R_-(\bar{c})$ around $c = 0$.

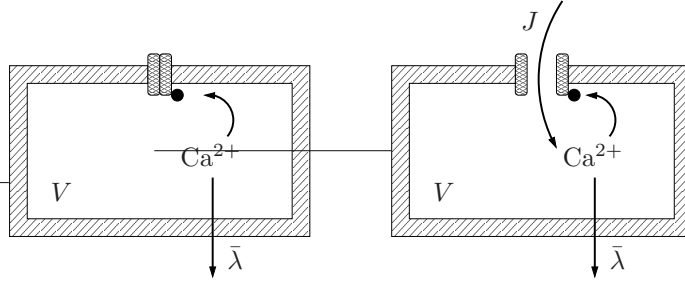


Fig. 3.2: The system considered. **Left:** closed state ($S = 0$), **right:** open state ($S = 1$).

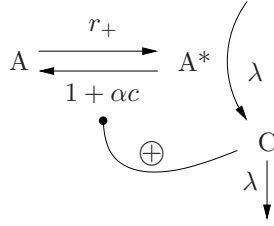


Fig. 3.3: The system considered in dimensionless units: The element A switches stochastically between an inactive and active state with the rates r_+ and $r_- = 1 + \alpha c$. In the active state, the component C is produced with a rate λ . It is removed with the same rate and exerts negative feedback on the switching of element A.

Eqs. (3.1)–(3.3) fully define the problem that will be worked with in this chapter. In order to minimise the number of parameters, the equations are made dimensionless by expressing time in units of $\frac{1}{R_-^0}$ and concentration in units of $\frac{J}{\lambda V}$ such that in the new units the maximally achievable calcium concentration is $c_{\max} = 1$. Using the following relations between the original parameters and the dimensionless ones:

$$\begin{aligned} r_-^0 &= 1, & t &= R_-^0 \bar{t}, & c &= \frac{\bar{\lambda} V}{J} \bar{c}, & r_+ &= \frac{1}{R_-^0} R_+, \\ \lambda &= \frac{1}{R_-^0} \bar{\lambda}, & \alpha &= \frac{J}{V \lambda R_-^0} \bar{\alpha}, & \frac{\partial}{\partial t} &= \frac{1}{R_-^0} \frac{\partial}{\partial \bar{t}}, \end{aligned}$$

Eqs. (3.1)–(3.3) can be rewritten with only three parameters (the opening rate r_+ , the pump rate λ and the feedback parameter α):

$$S(t) : \quad 0 \xrightleftharpoons[r_-]{r_+} 1, \quad (3.4)$$

$$\frac{dc}{dt} = \lambda(S(t) - c(t)), \quad (3.5)$$

$$r_-(t) = 1 + \alpha c(t). \quad (3.6)$$

Fig. 3.3 depicts this setup of the system as a chemical reaction diagram.

Eq. (3.5) can immediately be solved [19]:

$$c(t) = \lambda \int_{-\infty}^t e^{-\lambda(t-t')} S(t') dt', \quad (3.7)$$

i.e. the dynamics of the calcium concentration is fully determined by the opening and closing dynamics of the channel. The difficulty of the computation of statistical quantities

of S lies within the dependence of the closing rate on the calcium dynamics, which makes the effective dynamics of $S(t)$ non-Markovian. Fig. 3.4 shows two typical time traces with $\alpha = 0$ obtained from a numerical simulation. For $\alpha \neq 0$, the time evolution of S would depend on $c(t)$ and therefore would be different for different λ .

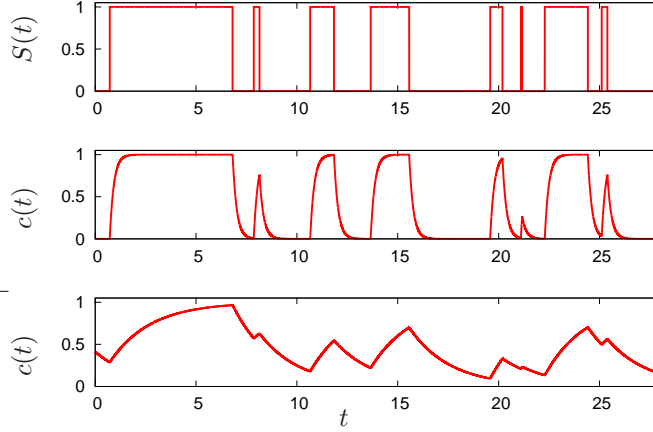


Fig. 3.4: Examples of a single time trace with no feedback. Middle row: $\lambda = 5$, Lower row: $\lambda = 0.5$. Since $\alpha = 0$, $S(t)$ is not affected by $c(t)$ and therefore the same for both λ -values.

3.2.1 Definition of the relevant quantities

The dynamics of the system introduced above can be characterised by the set of n -point functions of the channel variable S ($n \geq 1$):

$$\langle S(t_0)S(t_1) \cdots S(t_{n-1}) \rangle. \quad (3.8)$$

The angular brackets $\langle \cdots \rangle$ represent ensemble averages over all possible time evolutions of the system. The corresponding n -point functions for c are then determined by Eq. (3.7) and can be computed with

$$\begin{aligned} \langle c(t_0)c(t_1) \cdots c(t_{n-1}) \rangle &= \lambda^n e^{-\lambda(t_0+t_1+\cdots+t_{n-1})} \\ &\cdot \int_{-\infty}^{t_0} d\tau_0 \int_{-\infty}^{t_1} d\tau_1 \cdots \int_{-\infty}^{t_{n-1}} d\tau_{n-1} e^{\lambda(\tau_0+\tau_1+\cdots+\tau_{n-1})} \langle S(\tau_0)S(\tau_1) \cdots S(\tau_{n-1}) \rangle. \end{aligned} \quad (3.9)$$

In the following sections, both the mean values ($n = 1$) and the correlation functions ($n = 2$) in the steady state and for time-independent external signal r_+ will be calculated using three different methods. For the mean value of $\langle c \rangle$ in the steady state, one sees immediately from Eq. (3.7):

$$\langle c \rangle = \langle S \rangle. \quad (3.10)$$

The auto-correlation functions in the steady state are defined with the 2-point functions from Eq. (3.8):

$$\mathcal{C}_S(t) = \lim_{t_0 \rightarrow \infty} \langle S(t_0)S(t_0 + t) \rangle - \langle S \rangle^2, \quad (3.11)$$

$$\mathcal{C}_c(t) = \lim_{t_0 \rightarrow \infty} \langle c(t_0)c(t_0 + t) \rangle - \langle c \rangle^2. \quad (3.12)$$

Similarly, the two cross-correlation functions are defined as

$$\mathcal{C}_{Sc}(t) = \lim_{t_0 \rightarrow \infty} \langle S(t_0)c(t_0 + t) \rangle - \langle S \rangle \langle c \rangle, \quad (3.13)$$

$$\mathcal{C}_{cS}(t) = \lim_{t_0 \rightarrow \infty} \langle c(t_0)S(t_0 + t) \rangle - \langle c \rangle \langle S \rangle. \quad (3.14)$$

Equivalent to the auto-correlation functions in steady state is the description of the system in terms of the power spectra – the Fourier transform of the auto-correlation functions [19]. Here, the real cosine-Fourier transform is chosen:

$$P_S(\omega) = 2 \int_0^\infty \mathcal{C}_S(t) \cos(\omega t) dt, \quad P_c(\omega) = 2 \int_0^\infty \mathcal{C}_c(t) \cos(\omega t) dt = \frac{\lambda^2}{\lambda^2 + \omega^2} P_S(\omega). \quad (3.15)$$

The latter equality can be obtained from Eq. (3.7).

As described in the preceding subsection, an external signal is implemented as a temporal variation of r_+ . Naturally in a stochastic system, this temporal variation happens on top of a constant (thermal) r_+^0 :

$$r_+(t) = r_+^0 + \phi(t). \quad (3.16)$$

The response of the system towards this stimulus in both the channel variable S and the concentration c can then be defined as

$$\mathcal{R}_S(t) = \langle S(t) \rangle^\phi - \langle S \rangle, \quad \mathcal{R}_c(t) = \langle c(t) \rangle^\phi - \langle c \rangle. \quad (3.17)$$

The superscript ϕ indicates that the ensemble averages have to be evaluated in the presence of the time-dependent perturbation $\phi(t)$. If this perturbation is small ($\phi(t) \ll r_+^0$), the response of the system can be defined through the linear response functions $\chi(t)$:

$$\mathcal{R}_S(t) \approx \int_{-\infty}^t \chi_S(t-t') \phi(t') dt', \quad \mathcal{R}_c(t) \approx \int_{-\infty}^t \chi_c(t-t') \phi(t') dt', \quad (3.18)$$

where the two χ 's are related through Eq. (3.7):

$$\chi_c(t) = \lambda \int_0^t \chi_S(t') e^{-\lambda(t-t')} dt'. \quad (3.19)$$

One way of calculating the linear response functions is to analyse the response to a step-stimulus $r_+(t) = r_+^0 + \phi_0 \Theta(t)$ with the Heaviside function $\Theta(t)$ [19] and take the limit of infinitesimal small ϕ_0 :

$$\chi_S(t) = \lim_{\phi_0 \rightarrow 0} \frac{1}{\phi_0} \frac{d\mathcal{R}_S(t)}{dt} = \left. \frac{\partial}{\partial t} \frac{\partial \langle S(t) \rangle^{\phi_0}}{\partial \phi_0} \right|_{\phi_0=0}. \quad (3.20)$$

Different methods can be used to obtain insight into the problem defined by Eqs. (3.4)–(3.6) and calculating the aforementioned quantities. In Sec. 3.3, a fully (for all α) valid expression for the mean value of S will be computed using a master equation. In the subsequent section, a path-integral method is introduced with which approximative expressions for the auto-correlation functions and the response functions are obtained. Both are valid in the limit of weak feedback (small α). For later extensions of the signalling module, a computationally easier self-consistent method is explained and mean values and auto-correlation functions are computed that are only valid in specific parameter regimes.

After the analytical part, the results of all three methods are compared to numerical simulations of the system in Sec. 3.5. Simulations also provide results in parameter ranges where no analytical solutions could be found.

3.3 Channel open probability in the steady state

In the following subsection an expression for the mean open probability of the channel in the steady state, $\langle S \rangle$, (and therefore the mean calcium concentration $\langle c \rangle$ – Eq. (3.10)) of the system described by the Eqs. (3.4)–(3.6) will be derived for the whole parameter range using a master equation.

3.3.1 Solution using a master equation

If $p_i(c, t)$ is the probability density to find the system at time t in state $S(t) = i$ with concentration c , the following two equations can be set up for the fluxes between these two probability densities:

$$\begin{aligned}\frac{\partial}{\partial t}p_1(c, t) &= -\lambda\frac{\partial}{\partial c}((1-c)p_1(c, t)) - (1+\alpha c)p_1(c, t) + r_+p_0(c, t), \\ \frac{\partial}{\partial t}p_0(c, t) &= \lambda\frac{\partial}{\partial c}(cp_0(c, t)) - r_+p_0(c, t) + (1+\alpha c)p_1(c, t).\end{aligned}\quad (3.21)$$

The last two terms in Eqs. (3.21) describe the jumps between the different states of S , whereas the respective first terms on the right hand side are the drift terms in c due to an in- and outflux of ions.

For the two probability distributions, the following norm must hold:

$$\int_0^1 (p_1(c, t) + p_0(c, t)) dc = 1. \quad (3.22)$$

Since no probability is allowed to flow into or out of the system, the following boundary conditions must be met (they correspond to the boundaries of c : $0 \leq c \leq 1$):

$$\begin{aligned}(1-c)p_1(c, t)|_{c=0} &= p_1(0, t) = 0, \\ cp_0(c, t)|_{c=1} &= p_0(1, t) = 0.\end{aligned}\quad (3.23)$$

Setting the time derivatives in Eqs. (3.21) to zero, one obtains two equations for the stationary state:

$$0 = -\lambda\frac{d}{dc}((1-c)p_{1,ss}) - (1+\alpha c)p_{1,ss} + r_+p_{0,ss}, \quad (3.24)$$

$$0 = \lambda\frac{d}{dc}(cp_{0,ss}) - r_+p_{0,ss} + (1+\alpha c)p_{1,ss}. \quad (3.25)$$

Combining (adding) Eqs. (3.24) and (3.25) gives $\frac{d}{dc}((1-c)p_{1,ss} - cp_{0,ss}) = 0$, which leads to

$$p_{1,ss} = \frac{c}{1-c}p_{0,ss}. \quad (3.26)$$

A possible integration constant must be zero because of Eqs. (3.23).

Putting Eq. (3.26) into Eq. (3.25) gives

$$\lambda c \frac{dp_{0,ss}}{dc} = \left(r_+ - \lambda - \frac{(1+\alpha c)c}{1-c} \right) p_{0,ss}, \quad (3.27)$$

which can be transformed through separation of variables to

$$\frac{dp_{0,ss}}{p_{0,ss}} = \left(\frac{r_+ - \lambda}{\lambda c} - \frac{1}{\lambda(1-c)} - \frac{\alpha}{\lambda} \frac{c}{1-c} \right) dc. \quad (3.28)$$

Integration of Eq. (3.28) leads to

$$\ln p_{0,ss} = \left(\frac{r_+}{\lambda} - 1 \right) \ln c + \frac{1}{\lambda} \ln(1-c) + \frac{\alpha}{\lambda} c + \frac{\alpha}{\lambda} \ln(1-c) + \text{const.}, \quad (3.29)$$

which gives, exponentiated,

$$p_{0,ss} = N_0 c^{\frac{r_+}{\lambda} - 1} (1-c)^{\frac{1}{\lambda}(1+\alpha)} e^{\frac{\alpha}{\lambda} c}, \quad (3.30)$$

and with Eq. (3.26)

$$p_{1,ss} = N_0 c^{\frac{r_+}{\lambda}} (1-c)^{\frac{1}{\lambda}(1+\alpha-\lambda)} e^{\frac{\alpha}{\lambda} c}. \quad (3.31)$$

Despite the possible poles at $c = 0$ and $c = 1$, the integral in Eq. (3.22) can still be calculated and from that one obtains the normalisation constant N_0 as

$$N_0 = \frac{\Gamma\left(\frac{1}{\lambda}(1 + \alpha + r_+)\right)}{\Gamma\left(\frac{r_+}{\lambda}\right)\Gamma\left(\frac{1+\alpha}{\lambda}\right)} \frac{1}{F\left(\frac{r_+}{\lambda}; \frac{1}{\lambda}(1 + \alpha + r_+); \frac{\alpha}{\lambda}\right)}. \quad (3.32)$$

$F(a; c; x)$ is the confluent hypergeometric function (or Kummer's function) [18] and $\Gamma(x)$ the Gamma function.

Fig. 3.5 shows plots of the probability distribution functions $p_{0,ss}(c)$ and $p_{1,ss}(c)$.

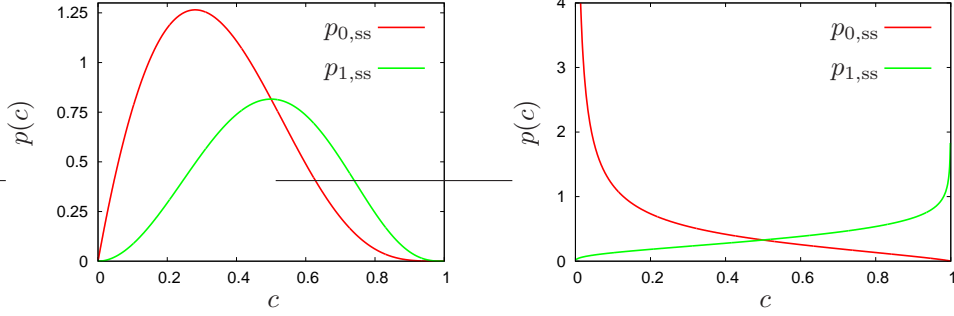


Fig. 3.5: Probability distribution functions $p_{0,ss}(c)$ and $p_{1,ss}(c)$ as obtained from the master equation approach for the two different $\lambda = 0.5$ (left) and $\lambda = 2.5$ (right); $r_+ = 1$, $\alpha = 1$. Mathematica [163] was used to evaluate the functions F and Γ .

Integrating $p_{1,ss}$ over all possible values of c gives the mean steady state open probability of the system:

$$\langle S \rangle_{ss} = \int_0^1 p_{1,ss} dc = \frac{r_+}{1 + r_+ + \alpha} \frac{F\left(\frac{r_+}{\lambda} + 1; \frac{1}{\lambda}(1 + r_+ + \alpha) + 1; \frac{\alpha}{\lambda}\right)}{F\left(\frac{r_+}{\lambda}; \frac{1}{\lambda}(1 + r_+ + \alpha); \frac{\alpha}{\lambda}\right)}. \quad (3.33)$$

Using the series representation of the confluent hypergeometric function [18], one can Taylor-expand $\langle S \rangle_{ss}$ around $\alpha = 0$, which gives

$$\langle S \rangle_{ss} = \frac{r_+}{1 + r_+} - \frac{r_+(r_+ + \lambda)}{(1 + r_+)^2(1 + r_+ + \lambda)} \alpha + \mathcal{O}(\alpha^2). \quad (3.34)$$

The same result will be found later using a path-integral technique (Subsec. 3.4.1).

In Fig. 3.6, the full expression from Eq. (3.33) is plotted against the opening rate r_+ . The right panel of Fig. 3.6 shows $\langle S \rangle$ for different values of λ . $\langle S \rangle$ only becomes λ -dependent for $\alpha \neq 0$ (for small α , see Eq. (3.34)), which is why only the results for high values of feedback are shown. If one defines r_+ as the input and $\langle c \rangle = \langle S \rangle$ as the output signal of the system, one can define a reception range as the interval of input signal r_+ that is transduced into a specific interval of output signal $\langle c \rangle$, say, e.g. from 0.1 to 0.9. A reduced slope of the $\langle c(r_+) \rangle$ curves on this logarithmic scale therefore increases the reception range which can be seen to happen for increasing feedback strength (left panel of Fig. 3.6). From the right panel of Fig. 3.6 one sees that for strong feedback, decreasing λ further broadens the reception range. Another observation is the shift of the reception range towards higher stimuli (r_+) with increasing feedback, which is simply due to the enhanced value of the back-flipping rate r_- .

Fig. 3.17 in the later Subsec. 3.5.2 plots the mean open fraction $\langle S \rangle$ of the channel against the feedback parameter α . There, it serves as a test for the quality of numerical results presented later.

The results from this subsection are contained in a previous study by others [101] focusing on the steady state properties of a more general module.

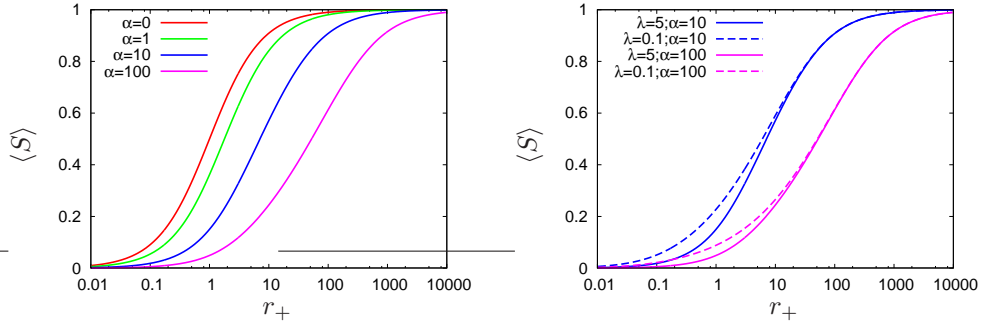


Fig. 3.6: Mean open fraction of the channel in the steady state (from Eq. (3.33)). **Left:** $\lambda = 5$; **Right:** curves for $\alpha = 10$ and 100 and $\lambda = 5$ and 0.1 .

Since the channel variable S can only take the values 0 and 1, the variance of it can be directly calculated from the mean value through

$$(\delta S)^2 = \langle S^2 \rangle - \langle S \rangle^2 = \langle S \rangle(1 - \langle S \rangle) \quad (= C_S(0)). \quad (3.35)$$

Its maximum is always $\frac{1}{4}$ and appears at $\langle S \rangle = \frac{1}{2}$, independent of feedback. For the concentration c , this relation does not hold and the two-point function has to be calculated in order to get the variance. The plots of the variance (and also the normalised standard deviation) will be shown later in Subsec. 3.5.2 presenting the numerical results together with an interpretation.

3.4 Correlation and response functions

In the last section, only steady state properties of the system as described by Eqs. (3.4)–(3.6) were calculated. In order to characterise also the dynamical properties, in this section, the correlation and response functions (as defined in Eqs. (3.11), (3.12) and (3.20)) will be calculated perturbatively for small values of the feedback parameter α . First, a powerful but computationally involved path-integral method will be described in detail and the relevant quantities calculated. From the auto-correlation functions, further quantities describing the statistics of the system are derived. Since both auto-correlation and response functions are calculated, the validity of the fluctuation dissipation theorem valid in thermal equilibrium can be shown to be broken by the present system. Due to the extensive algebra connected to the path-integral method, it is not the ideal starting point for extensions and modifications of the signalling module as introduced in Sec. 3.2. For this purpose, a less complicated but only approximative self-consistent method to calculate the auto-correlation functions is introduced in Subsec. 3.4.2, the results of which are valid only in specific parameter regimes and again only for weak feedback. In order to test the validity of the results, in both approaches also perturbative expressions for the mean values are calculated that are compared to the results from the master equation method in the preceding section together with numerically obtained results in Subsec. 3.5.1. Perturbative expressions for the auto-correlation functions that agree with the results from the path-integral method can also be obtained from a modified master equation similar to Subsec. 3.3.1 (not shown).

3.4.1 Path-integral formalism

More common in quantum theory, path integrals are not very often employed as mathematical tools in statistical physics, although this technique was developed for the investigation of Brownian motion (see, e.g. [23]). In the following, path integrals are used to

obtain insight into the dynamics of a stochastic system and actually compute its statistical properties. Together with other work [62] this subsection provides a further example of the potential of this method. First, the propagator of the system described by Eqs. (3.4)–(3.6) will be defined. Using path integrals, a reduced propagator (the ‘Green’s function’) will actually be calculated perturbatively to linear order in the feedback parameter α . From that, expressions for the different quantities as defined in Subsec. 3.2.1 are obtained.

Propagator

The general propagator $\Pi_{ij}(t_0, c_0; t, c)$ with $i, j = \{0, 1\}$ gives the probability density to find the system in state $S(t) = j$ and $c(t) = c$ given that it was in state $S(t_0) = i$ and $c(t_0) = c_0$ at some earlier time $t_0 \leq t$. With that, all the relevant quantities introduced in the preceding subsection can be calculated:

$$\langle S \rangle = \int_0^1 \Pi_{i1}(-\infty, c_0; 0, c) dc, \quad (3.36)$$

$$\langle S(0)S(t) \rangle = \int_0^1 dc \int_0^1 dc_1 \Pi_{i1}(-\infty, c_0; 0, c_1) \Pi_{11}(0, c_1; t, c), \quad (3.37)$$

$$\langle S(0)c(t) \rangle = \sum_j \int_0^1 dc \int_0^1 dc_1 \Pi_{i1}(-\infty, c_0; 0, c_1) \Pi_{1j}(0, c_1; t, c) c, \quad (3.38)$$

$$\langle c(0)S(t) \rangle = \sum_j \int_0^1 dc \int_0^1 dc_1 \Pi_{ij}(-\infty, c_0; 0, c) c \Pi_{j1}(0, c; t, c_1), \quad (3.39)$$

$$\chi_S(t) = \frac{\partial}{\partial t} \frac{\partial}{\partial \phi_0} \sum_j \int_0^1 dc \int_0^1 dc_1 \Pi_{ij}(-\infty, c_0; 0, c_1) \Pi_{j1}^{\phi_0}(0, c_1; t, c). \quad (3.40)$$

Since for the first propagators in the integral expressions above, $-\infty$ was used as a starting time, all of those quantities are steady state expressions.

Path integral

There are infinitely many ways (‘paths’) the system can evolve from one state at time t_0 (characterised by S_0 and c_0) to another state at time t_1 (with S_1 and c_1). Three of these are shown for $S_0 = 0$ and $S_1 = 1$ in Fig. 3.7. Since $c(t)$ is completely determined by $S(t)$ (Eq. (3.7)), already only $S(t)$ as shown in Fig. 3.7 fully characterises one possible trajectory (‘path’) of the system.

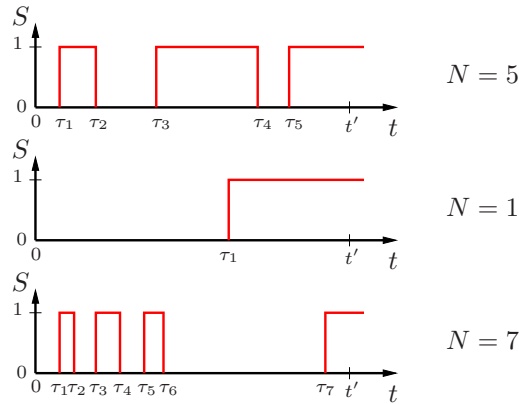


Fig. 3.7: Three different of the infinitely many ways (‘paths’) the system can evolve from state $S_0 = 0, c_0$ at time $t_0 = 0$ to $S_1 = 1$ at time t' . N gives the number of channel state changes and τ_i are the flip times.

$S(t)$ is most conveniently described in a given time interval by the set of flip times $\{\tau_i\}$ at which the channel changes its state. With that, a probability density $\mathcal{P}_{ij}[t_0, t; \{\tau_k\}_{k=1}^N; c_0; N]$ can be defined that describes one specific trajectory of the system evolving from $S(t_0) = i$ and $c(t_0) = c_0$ to $S(t) = j$ making N channel state changes in between at the flip times $\{\tau_k\}$. If $i = j$, N is even, for $i \neq j$ N is odd. The concentration c at time t is determined by $S(t')$ with $t_0 \leq t' < t$ and c_0 through Eq. (3.7) and is therefore not a parameter for \mathcal{P}_{ij} . The propagator as introduced above can now be calculated as a path integral over all possible paths $S(t)$ that lead from a given state $S(t_0) = i$, $c(t_0) = c_0$ to the state $S(t) = j$, $c(t) = c$. Since $c(t)$ is not contained in the probability density \mathcal{P}_{ij} , the correct paths have to be singled out in the path integral with a delta function:

$$\Pi_{ij}(t_0, c_0; t, c) = \sum_N \int \mathcal{D}\tau \mathcal{P}_{ij}[t_0, t; \{\tau_k\}_{k=1}^N; c_0; N] \delta(c(t) - c). \quad (3.41)$$

$\mathcal{D}\tau$ is an abbreviation for the differential of the path integral. The first state flip of S can happen between t_0 and t ($t_0 < \tau_1 < t$), the second between τ_1 and t ($\tau_1 < \tau_2 < t$) and so on. Therefore, the full differential reads $\int \mathcal{D}\tau \equiv \int_{t_0}^t d\tau_1 \int_{\tau_1}^t d\tau_2 \dots \int_{\tau_{N-1}}^t d\tau_N$.

It is much easier to evaluate this path integral, when the additional delta functional is removed. The quantity obtained can be called a reduced propagator or the Green's function of the system:

$$G_{ij}(t_0, c_0; t) = \sum_N \int \mathcal{D}\tau \mathcal{P}_{ij}[t_0, t; \{\tau_k\}_{k=1}^N; c_0; N]. \quad (3.42)$$

$G_{ij}(t_0, c_0; t)$ gives the probability to find the system in state $S = j$ at time t , given that it started in $S = i$ with $c = c_0$ at time t_0 . It is connected to the full propagator by

$$G_{ij}(t_0, c_0; t) \equiv \int_0^1 \Pi_{ij}(t_0, c_0; t, c) dc. \quad (3.43)$$

Since the system must be either in state $S = 0$ or $S = 1$ at time t , the following relations must hold for all times:

$$G_{00} + G_{01} = 1 = G_{10} + G_{11}. \quad (3.44)$$

Probability density

For calculating the functional $\mathcal{P}_{ij}[t_0, t; \{\tau_k\}_{k=1}^N; c_0; N]$ it is easiest to start with the case $\alpha = 0$ and look at the specific case with $i = j = 0$. It is then straightforward to calculate the remaining expressions for $\{i, j\} = \{0, 1\}, \{1, 0\}, \{1, 1\}$. Starting in the closed state $S(0) = 0$ at time $t_0 = 0$, the probability that the channel remains in this state until the first flip at time τ_1 is $P_0(0, \tau_1) = e^{-r_+\tau_1}$. Similarly, the probability that the channel remains in the open state $S = 1$ in the time interval $[\tau_1, \tau_2]$ is $P_1(\tau_1, \tau_2) = e^{-(\tau_2-\tau_1)}$ (the closing rate in the dimensionless version of the system is $r_- = 1$). One obtains the differential probability for the whole trajectory by simply putting all N of these intervals in a row and since they are mutually independent, the according probabilities have to be multiplied. Additionally, the rates r_+ for the $\frac{N}{2}$ flips from $S = 0$ to $S = 1$ have to be considered (the respective backflipping rates are $r_- = 1$ and therefore do not appear):

$$\mathcal{P}_{00}^{(0)}[0, t; \{\tau_i\}_{i=1}^N; N] d\tau_1 d\tau_2 \dots d\tau_N = r_+^{\frac{N}{2}} \prod_{i=1}^N d\tau_i P_0(0, \tau_1) P_1(\tau_1, \tau_2) P_0(\tau_2, \tau_3) \dots P_0(\tau_N, t). \quad (3.45)$$

It is convenient to make a transformation of the time variables from the set of flip times $\{\tau_i\}_{i=1}^N$ to the two sets of time-intervals $\{T_j\}_{j=1}^{N/2}$ and $\{T'_j\}_{j=1}^{N/2}$ during which the channel

stays in the closed or the open state, respectively. This transformation is illustrated in Fig. 3.8 and mathematically expressed as

$$\begin{aligned}
\tau_1 &= T_1, \\
\tau_i &= \sum_{l=1}^{i/2} T_l + \sum_{l=1}^{i/2} T'_l \quad \text{even } i \geq 2, \\
\tau_j &= \sum_{l=1}^{(j+1)/2} T_l + \sum_{l=1}^{(j-1)/2} T'_l \quad \text{odd } j > 1 \\
\Leftrightarrow \quad T_k &= \tau_{2k-1} - \tau_{2k-2} \quad T'_k = \tau_{2k} - \tau_{2k-1}.
\end{aligned} \tag{3.46}$$

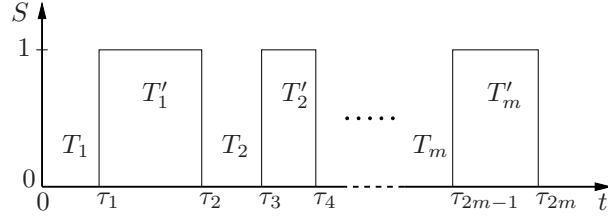


Fig. 3.8: The relation between the two different ways of describing the temporal dynamics of $S(t)$: the flip times $\{\tau_i\}_{i=1}^N$ vs. the time-intervals $\{T_j\}_{j=1}^{N/2}$ and $\{T'_j\}_{j=1}^{N/2}$.

The Jacobian of this transformation is $J = 1$ so that the differentials $d\tau$ directly transform into dT . Using this transformation, the probability functional (Eq. (3.45)) becomes ($2m = N$)

$$\mathcal{P}_{00}^{(0)}[0, t; \{T_i\}, \{T'_i\}; 2m] = r_+^m \prod_{i=1}^m e^{-r_+ T_i} e^{-T'_i} e^{-r_+ T_{m+1}}, \tag{3.47}$$

with $T_{m+1} = t - \tau_N$. This can be rewritten using $\sum_{i=1}^m (T_i + T'_i) + T_{m+1} = t$ as

$$\mathcal{P}_{00}^{(0)}[0, t; \{T_i\}, \{T'_i\}; 2m] = r_+^m e^{-F_{00}(0, t; \{T'_i\})}, \tag{3.48}$$

with the weight factor

$$F_{00}(0, t; \{T'_i\}) = r_+ t + (1 - r_+) \sum_{i=1}^m T'_i. \tag{3.49}$$

In the presence of feedback ($\alpha \neq 0$), the flipping rate from the open to the closed state of the channel becomes calcium-dependent ($r_-(t) = 1 + \alpha c(t)$), i.e. the probability for staying in the open state has to be modified (odd i):

$$P_1(\tau_i, \tau_{i+1}) = e^{-\int_{\tau_i}^{\tau_{i+1}} (1 + \alpha c(\tau')) d\tau'} = e^{-(\tau_{i+1} - \tau_i)} e^{-\alpha \int_{\tau_i}^{\tau_{i+1}} c(\tau') d\tau'}. \tag{3.50}$$

With that, the functional in Eq. (3.48) becomes

$$\mathcal{P}_{00}[0, t; \{T_i\}, \{T'_i\}; c_0; 2m] = r_+^m \left(\prod_{i=2}^{2m} \text{E} (1 + \alpha c(\tau_i)) \right) e^{-F_{00}} e^{-\alpha \sum_{j=1}^{2m-1} \text{O} \int_{\tau_j}^{\tau_{j+1}} c(\tau') d\tau'}, \tag{3.51}$$

where the symbols E and O on the product- or the sum-signs indicate multiplication/summation over all even, respectively odd indices.

The concentration $c(t)$ in Eq. (3.51) can (through Eq. (3.7)) be expressed in terms of the time intervals $\{T_i\}, \{T'_i\}$, which would lead to an expression containing a difficult

double-exponential. To circumvent this, in the following, the limit of weak feedback, i.e. small α , is considered. Expanding both the product as well as the exponential of Eq. (3.51) in powers of α yields

$$\mathcal{P}_{00}[0, t; \{T_i\}, \{T'_i\}; c_0; 2m] = r_+^m e^{-F_{00}} \left[1 + \alpha \left(\sum_{i=2}^{2m} c(\tau_i) - \sum_{j=1}^{2m-1} \int_{\tau_j}^{\tau_{j+1}} c(\tau') d\tau' \right) \right] + \mathcal{O}(\alpha^2). \quad (3.52)$$

This expansion is valid as long as the contribution of feedback to the dynamics is weak, i.e. $\alpha c \ll 1$. Since $c_{\max} = 1$, this condition reduces to $\alpha \ll 1$.

Computation of Green's function

Since two of the four G_{ij} are connected by the two Eqs. (3.44), only two remain independent. In the following, G_{00} will be calculated to first order in the feedback parameter α using the path-integral approach. After that, instead of doing a similar extensive calculation for G_{11} , a nontrivial relation between G_{00} and G_{11} will be derived, that is valid to first order in α .

First, a special Green's function is calculated for the system starting with $S(t=0) = 0$ and $c(t=0) = 0$. Putting Eq. (3.52) into Eq. (3.42) with $t_0 = 0$ and $c_0 = 0$ gives

$$G_{00}(0, 0; t) = \sum_{m=0}^{\infty} \left[\int \mathcal{D}\tau r_+^m e^{-F_{00}} + \alpha \left(\int \mathcal{D}\tau r_+^m e^{-F_{00}} \sum_{i=2}^{2m} c(\tau_i) - \int \mathcal{D}\tau r_+^m e^{-F_{00}} \sum_{j=1}^{2m-1} \int_{\tau_j}^{\tau_{j+1}} c(\tau') d\tau' \right) \right] + \mathcal{O}(\alpha^2). \quad (3.53)$$

Putting in the expression for F_{00} (Eq. (3.49)), this can be written as

$$G_{00}(0, 0; t) = e^{-r_+ t} \left(1 + \sum_{m=1}^{\infty} r_+^m [I_0(t; m) + \alpha(I_1(t; m) - I_2(t; m))] \right) + \mathcal{O}(\alpha^2), \quad (3.54)$$

with the three time-ordered integrals

$$I_0(t; m) = \int \mathcal{D}T e^{-(1-r_+) \sum_{i=1}^m T'_i}, \quad (3.55)$$

$$I_1(t; m) = \int \mathcal{D}T e^{-(1-r_+) \sum_{i=1}^m T'_i} \sum_{i=2}^{2m} c(\tau_i), \quad (3.56)$$

$$I_2(t; m) = \int \mathcal{D}T e^{-(1-r_+) \sum_{i=1}^m T'_i} \sum_{j=1}^{2m-1} \int_{\tau_j}^{\tau_{j+1}} c(\tau') d\tau'. \quad (3.57)$$

The first term in the parentheses in Eq. (3.54) (the '1'), gives the probability to stay in the closed state without switching ($m = 0$).

The time-ordered integrals of Eqs. (3.55)–(3.57) are series of convolutions in time. In Laplace space, convolutions turn into simple products of the Laplace transforms and in Appendix B.1.1, a general convolution theorem will be proven that makes the calculation of these integrals possible. Using the standard definition for the Laplace transform [19] $\hat{f}(s) = \int_0^{\infty} f(t) e^{-st} dt$, Eq. (3.54) becomes

$$\hat{G}_{00}(c_0 = 0; s) = \frac{1}{s + r_+} + \sum_{m=1}^{\infty} r_+^m \left[\hat{I}_0(s + r_+; m) + \alpha \left(\hat{I}_1(s + r_+; m) - \hat{I}_2(s + r_+; m) \right) \right] + \mathcal{O}(\alpha^2). \quad (3.58)$$

The quite involved calculation of the three integrals \hat{I}_0 , \hat{I}_1 and \hat{I}_2 is done in Appendix B.1. Putting the results into Eq. (3.58) gives

$$\begin{aligned} \hat{G}_{00}(0; s) &= \frac{1}{s + r_+} + \sum_{m=1}^{\infty} \frac{r_+^m}{(s + r_+)^{m+1}(s + 1)^m} \\ &+ \alpha \left[\frac{r_+ \lambda s}{(s + r_+)^2(s + 1)^2(s + 1 + \lambda)} + \sum_{m=2}^{\infty} \frac{r_+^m}{(s + r_+)^{m+1}(s + 1)^m} \right. \\ &\quad \left. \cdot \frac{s}{2s + 1 + r_+ + \lambda} \left(\frac{m(s + r_+ + \lambda)}{s + 1} + \frac{y'^m - 1}{1 - y'} \frac{s + r_+}{s + 1 + \lambda} \right) \right] + \mathcal{O}(\alpha^2), \end{aligned} \quad (3.59)$$

with

$$y' = \frac{(s + r_+)(s + 1)}{(s + r_+ + \lambda)(s + 1 + \lambda)}. \quad (3.60)$$

The sums over m can be evaluated and the inverse Laplace transform of the result is

$$\begin{aligned} G_{00}(0, c_0 = 0; t) &= \frac{1}{1 + r_+} \left(1 + r_+ e^{-(1+r_+)t} \right) + \alpha \frac{r_+}{(1 + r_+)^2} \left[\frac{r_+ + \lambda}{1 + r_+ + \lambda} \right. \\ &\quad \left. - e^{-\lambda t} \frac{r_+(1 + r_+)}{(1 + r_+ - \lambda)^2} - e^{-(1+r_++\lambda)t} \frac{1 + r_+}{\lambda(1 + r_+ + \lambda)} \right. \\ &\quad \left. + e^{-(1+r_+)t} \left(\frac{(1 + r_+)(\lambda - 1)t}{1 + r_+ - \lambda} + \frac{r_+^2 - (\lambda - 1)^3 + r_+(2 - 3\lambda + 2\lambda^2)}{\lambda(1 + r_+ - \lambda)^2} \right) \right] \\ &+ \mathcal{O}(\alpha^2). \end{aligned} \quad (3.61)$$

This is the Green's function G_{00} for the special initial condition $c_0(0) = 0$. Through Eq. (3.44), it is related to the time evolution of the open probability $\langle S(t) \rangle$ when starting in this initial condition by $\langle S(t) \rangle = 1 - G_{00}$. The corresponding equation for the time evolution of the mean value of c can be obtained through Eq. (3.7) and is given as Eq. (B.66) in Appendix B.5. Both of these quantities will be compared to numerically obtained results in Subsec. 3.5.1.

In order to get the general Green's function $G_{00}(0, c_0; t)$ for arbitrary initial concentration c_0 , one puts the expression of Eq. (3.52) (with $t_0 = 0$ and the general solution $c(t) = \lambda \int_0^t S(t') e^{-\lambda(t-t')} dt' + c_0 e^{-\lambda t}$ from Eq. (3.7)) into Eq. (3.42). From that it becomes obvious that the full Green's function depends only linearly on the initial concentration c_0 :

$$G_{00}(0, c_0; t) = G_{00}(0, c_0 = 0; t) + \alpha c_0 f(t) + \mathcal{O}(\alpha^2) \quad (3.62)$$

with $G_{00}(0, c_0 = 0; t)$ from Eq. (3.61). $f(t)$ can be either calculated as part of the path integral or using the rate equation

$$\frac{\partial}{\partial t} G_{00} = r_- - (r_- + r_+) G_{00} \quad (3.63)$$

with the time dependent rate $r_-(t) = 1 + \alpha c_0 e^{-\lambda t}$ and the initial condition $G_{00}(0, c_0; 0) = 1$ (i.e. the system evolves with an initial concentration c_0 but no influx ($J \equiv 0$)). In Appendix B.2 the rate equation is solved and gives:

$$f(t) = \frac{r_+}{\lambda} \left(\frac{-1}{1 + r_+ - \lambda} e^{-(1+r_+)t} + \frac{1}{1 + r_+} e^{-(1+r_++\lambda)t} + \frac{\lambda}{(1 + r_+)(1 + r_+ - \lambda)} e^{-\lambda t} \right). \quad (3.64)$$

Relation between G_{11} and G_{00}

In principle, the second (so far) independent Green's function G_{11} or G_{10} can be calculated using path integrals the same way as described for G_{00} . There is, however, a faster way of finding this relation valid up to linear order in α . It uses expressions of the Green's functions $G_{01}(t', c'; t)$ and $G_{11}(t', c'; t)$ similar to Eq. (3.62):

$$\begin{aligned} G_{01}(t', c'; t) &= G_{01}(t', c' = 0; t) + \alpha c' f_1(t - t') + \mathcal{O}(\alpha^2), \\ G_{11}(t', c'; t) &= G_{11}(t', c' = 0; t) + \alpha c' f_2(t - t') + \mathcal{O}(\alpha^2). \end{aligned} \quad (3.65)$$

Again, the two functions $c' f_1(t)$ and $c' f_2(t)$ are the $\mathcal{O}(\alpha)$ terms in $G_{01}(0, c'; t)$ and $G_{11}(0, c'; t)$, respectively, when the channel is closed and there is no influx of ions ($J \equiv 0$). $f_1(t)$ can be obtained from Eq. (3.44) and is just

$$f_1(t) = -f(t), \quad (3.66)$$

with $f(t)$ from Eq. (3.64). $f_2(t)$ is the $\mathcal{O}(\alpha)$ solution of the rate equation for G_{11} with the time dependent rate $r_-(t) = 1 + \alpha c' e^{-\lambda t}$. In appendix B.2 it is computed to be

$$f_2(t) = \frac{1}{\lambda} \left(\frac{\lambda - 1}{1 + r_+ - \lambda} e^{-(1+r_+)t} + \frac{1}{1 + r_+} e^{-(1+r_++\lambda)t} - \frac{\lambda r_+}{(1 + r_+)(1 + r_+ - \lambda)} e^{-\lambda t} \right). \quad (3.67)$$

With that, in appendix B.3 the relation between G_{11} and G_{00} is shown to be

$$G_{11}(t' = 0, c' = 0; t) \approx 1 - G_{00}(0, 0; t) + \frac{\frac{\partial G_{00}(0, 0; t)}{\partial t}}{\frac{\partial G_{00}(0, 0; t)}{\partial t} \Big|_{t=0}}. \quad (3.68)$$

The explicit expression for $G_{11}(0, 0; t)$ is given as Eq. (B.55) in appendix B.3.

Mean values

Since the steady state properties of the system do not depend on the initial conditions, the mean open probability of the channels can be found, e.g. by applying the limit

$$\langle S \rangle = \lim_{t \rightarrow \infty} (1 - G_{00}(0, c_0 = 0; t)) = \frac{r_+}{1 + r_+} \left(1 - \alpha \frac{r_+ + \lambda}{(1 + r_+)(1 + r_+ + \lambda)} \right) + \mathcal{O}(\alpha^2). \quad (3.69)$$

Due to the special choice of dimensions, the steady state limits of S and c are the same (see Eq. (3.7)):

$$\langle c \rangle = \lim_{t \rightarrow \infty} \langle c(t) \rangle = \langle S \rangle. \quad (3.70)$$

Eq. (3.69) is the same as the Taylor expansion around $\alpha = 0$ of the full result obtained with the master equation (Eq. (3.34)).

Auto-correlation functions and power spectra

Putting the definition of the Green's function from Eq. (3.43) into Eq. (3.37), one obtains for the auto-correlation function of S

$$\langle S(0)S(t) \rangle = \int_0^1 dc_1 \Pi_{i1}(-\infty, c_0; 0, c_1) G_{11}(0, c_1; t). \quad (3.71)$$

Using Eq. (3.65) and Eq. (3.36), this can be written as

$$\langle S(0)S(t) \rangle = \langle S \rangle G_{11}(0, 0; t) + \alpha \langle c \rangle_1 f_2(t) + \mathcal{O}(\alpha^2), \quad (3.72)$$

where $\langle c \rangle_1$ is the mean steady state value of the concentration, when the channel is in the open state. It is defined in Eq. (B.52) and calculated in Appendix B.4.

Using Eqs. (3.69), (B.55), (B.65) and (3.67), as well as the definition of Eq. (3.11), one gets for the auto-correlation function of the channel variable S

$$\mathcal{C}_S(t) = \frac{r_+}{(1+r_+)^2} e^{-(1+r_+)t} + \alpha \left[B_1 e^{-(1+r_+)t} + C_1 e^{-\lambda t} + D_1 e^{-(1+r_++\lambda)t} + E_1 t e^{-(1+r_+)t} \right] + \mathcal{O}(\alpha^2). \quad (3.73)$$

The coefficients B_1, C_1, D_1, E_1 are functions of the two parameters r_+ and λ and are given in Appendix B.6.

Using Eq. (3.9) with $n = 2$ and the definition of Eq. (3.12) one can directly calculate the auto-correlation function for the variable c :

$$\mathcal{C}_c(t) = \frac{r_+ \lambda}{(1+r_+)^2((1+r_+)^2 - \lambda^2)} \left[e^{-\lambda t}(1+r_+) - \lambda e^{-(1+r_+)t} \right] + \alpha \left[B_2 e^{-(1+r_+)t} + C_2 e^{-\lambda t} + D_2 e^{-(1+r_++\lambda)t} + E_2 t e^{-(1+r_+)t} + F_2 t e^{-\lambda t} \right] + \mathcal{O}(\alpha^2). \quad (3.74)$$

Again, the coefficients B_2, C_2, D_2, E_2, F_2 are given in Appendix B.6.

The power spectrum for S is easily obtained from Eq. (3.15):

$$P_S(\omega) = 2 \frac{r_+}{(1+r_+)^3 + (1+r_+)\omega^2} + 2\alpha \left(\frac{1+r_+}{(1+r_+)^2 + \omega^2} B_1 + \frac{\lambda}{\lambda^2 + \omega^2} C_1 + \frac{1+r_++\lambda}{(1+r_++\lambda)^2 + \omega^2} D_1 + \frac{(1+r_+)^2 - \omega^2}{((1+r_+)^2 + \omega^2)^2} E_1 \right) + \mathcal{O}(\alpha^2). \quad (3.75)$$

It is important to note, that also the term of $P_S(\omega)$ linear in α decays as ω^{-2} for large ω . This can be seen after some rearrangements when putting the coefficients of Eq. (B.69) into the expression above.

Accordingly, the power spectrum for the concentration can be obtained. It is given in Appendix B.5 as Eq. (B.67).

Fluctuation measures

According to Eq. (3.35), the mean squared fluctuation (or variance) of the channel variable S can be obtained both through the correlation function or the mean. For the root mean squared fluctuations (the standard deviation), one gets

$$\delta S = \frac{\sqrt{r_+}}{1+r_+} \left(1 - \frac{\alpha}{2} \frac{(1-r_+)(r_++\lambda)}{(1+r_+)(1+r_++\lambda)} \right) + \mathcal{O}(\alpha^2). \quad (3.76)$$

For c , one has to calculate the two-point function:

$$(\delta c)^2 = \langle c^2 \rangle - \langle c \rangle^2 = \mathcal{C}_c(0), \quad (3.77)$$

which gives the root mean squared fluctuations (using Eq. (3.74) with the coefficients from Eqs. (B.70))

$$\delta c = \sqrt{\frac{r_+ \lambda}{(1+r_+)^2(1+r_++\lambda)}} \left(1 + \frac{\alpha}{2} \cdot \frac{r_+^3 + r_+^2(3\lambda - 2) + r_+(2\lambda^2 - 4\lambda - 3) - \lambda(2\lambda + 3)}{(1+r_+)(1+r_++\lambda)(1+r_++2\lambda)} \right) + \mathcal{O}(\alpha^2). \quad (3.78)$$

As a measure of the precision of the system, one can calculate the relative fluctuations (normalised standard deviation, noise-to-signal ratio or coefficient of variation). Using Eqs. (3.76), (3.69) and Eqs. (3.78), (3.70), respectively, one gets

$$\frac{\delta S}{\langle S \rangle} = \sqrt{\frac{1}{\langle S \rangle} - 1} = \frac{1}{\sqrt{r_+}} \left(1 + \alpha \frac{\lambda + r_+}{2(1 + r_+ + \lambda)} \right) + \mathcal{O}(\alpha^2), \quad (3.79)$$

$$\frac{\delta c}{\langle c \rangle} = \sqrt{\frac{\lambda}{r_+(1 + r_+ + \lambda)}} \left(1 + \alpha \frac{(r_+ + \lambda)(-1 + r_+ + 2\lambda)}{2(1 + r_+ + 2\lambda)(1 + r_+ + \lambda)} \right) + \mathcal{O}(\alpha^2). \quad (3.80)$$

Cross-correlation functions

The two cross-correlation functions are defined in Eqs. (3.13), (3.14) and the respective 2-point functions using the propagator in Eqs. (3.38), (3.39).

Doing the integral over c and the sum over j in Eq. (3.38) gives the time evolution of the mean concentration with special initial conditions (cf. Eq. (B.52)):

$$\begin{aligned} \langle S(0)c(t) \rangle &= \int_0^1 dc_1 \Pi_{i1}(-\infty, c_0; 0, c_1) \langle c(t) \rangle_{S(0)=1, c(0)=c_1} \\ &= \langle S \rangle \langle c(t) \rangle_{S(0)=1, c(0)=0} + \langle c \rangle_1 e^{-\lambda t}. \end{aligned} \quad (3.81)$$

For the last equality, Eq. (3.5) was solved with the initial concentration $c(0) = c_1$. Further, Eq. (3.36) and the steady state limit of Eq. (B.52) were used. $\langle c(t) \rangle_{S(0)=1, c(0)=0}$ can be obtained by using Eq. (3.7):

$$\langle c(t) \rangle_{S(0)=1, c(0)=0} = \lambda \int_0^t e^{-\lambda(t-t')} \langle S(t') \rangle_{S(0)=1, c(0)=0} dt' = \lambda \int_0^t e^{-\lambda(t-t')} G_{11}(0, 0; t') dt'. \quad (3.82)$$

For $\langle S(0)c(t) \rangle$ to be valid to $\mathcal{O}(\alpha)$, $\langle c(t) \rangle_{S(0)=1, c(0)=0}$ is needed to $\mathcal{O}(\alpha)$ which can be easily obtained using Eq. (B.55). The mean value of the concentration when the channel is open, $\langle c \rangle_1$, is also needed to $\mathcal{O}(\alpha)$ which can be straightforwardly done following appendix B.4. In the present work, however, $\langle c \rangle_1$ is only calculated to $\mathcal{O}(\alpha^0)$ and no analytical expression is computed for $\mathcal{C}_{Sc}(t)$. Numerical results, however, are presented in Subsec. 3.5.2.

The integration over c_1 in Eq. (3.39) gives (using Eqs. (3.43) and (3.65)),

$$\langle c(0)S(t) \rangle = \sum_j \int_0^1 dc \Pi_{ij}(-\infty, c_0; 0, c) c (G_{j1}(0, 0; t) + \alpha f_{j+1}(t)). \quad (3.83)$$

With the steady state version of Eqs. (B.52) and the similar relations for the second moments, one gets

$$\langle c(0)S(t) \rangle = \sum_j (G_{j1}(0, 0; t) \langle c \rangle_j + \alpha f_{j+1}(t) \langle c^2 \rangle_j). \quad (3.84)$$

Again, $\langle c \rangle_j$ is needed to $\mathcal{O}(\alpha)$ and $\langle c^2 \rangle_j$ to $\mathcal{O}(\alpha^0)$ for $\langle c(0)S(t) \rangle$ being valid to first order in α . Both can in principle be calculated similarly to appendix B.4 but this is not done here. Rather, also the second cross-correlation function will be investigated numerically in Subsec. 3.5.2.

Linear response functions

The linear response function for S is calculated using a step stimulus $r_+(t) = r_+ + \phi_0 \Theta(t)$ (see Eq. (3.20)). At $t = 0$, when the input of the system changes, the channel can be

either in the closed or in the open state, dependent on that it will evolve differently and both cases have to be treated and 'weighted' by the factor $\langle S \rangle$ or $1 - \langle S \rangle$, respectively:

$$\langle S(t) \rangle^{\phi_0} = G_{11}^{\phi_0}(0, c_0; t) \langle S \rangle + G_{01}^{\phi_0}(0, c_0; t) (1 - \langle S \rangle). \quad (3.85)$$

The superscript ϕ_0 indicated that the functions have to be evaluated with the substitution $r_+ \rightarrow r_+ + \phi_0$. With Eqs. (3.65), this leads to (cf. also Eq. (3.40))

$$\langle S(t) \rangle^{\phi_0} = G_{11}^{\phi_0}(0, 0; t) \langle S \rangle + G_{01}^{\phi_0}(0, 0; t) (1 - \langle S \rangle) + \alpha \left(\langle c \rangle_0 f_1^{\phi_0}(t) + \langle c \rangle_1 f_2^{\phi_0}(t) \right) + \mathcal{O}(\alpha^2). \quad (3.86)$$

The functions $f_1(t)$ and $f_2(t)$ are given in Eqs. (3.66) and (3.67), the conditional c averages to $\mathcal{O}(\alpha^0)$ in appendix B.4 and the Green's functions in Eqs. (3.44) (with Eq. (3.61)) and (B.55). Putting all that together with Eq. (3.69) into Eq. (3.20) gives:

$$\begin{aligned} \chi_S(t > 0) &= \frac{1}{1 + r_+} e^{-(1+r_+)t} \\ &+ \alpha \left(B_3 e^{-(1+r_+)t} + C_3 e^{-\lambda t} + D_3 e^{-(1+r_++\lambda)t} + E_3 t e^{-(1+r_+)t} \right) + \mathcal{O}(\alpha^2). \end{aligned} \quad (3.87)$$

The coefficients B_3, C_3, D_3, E_3 are functions of r_+ and λ and are given in Appendix B.6.

The response function of c can be obtained using Eq. (3.19) and Eq. (3.87):

$$\begin{aligned} \chi_c(t > 0) &= \frac{\lambda}{(1 + r_+)(1 + r_+ - \lambda)} \left[e^{-\lambda t} - e^{-(1+r_+)t} \right] \\ &+ \alpha \left(B_4 e^{-(1+r_+)t} + C_4 e^{-\lambda t} + D_4 e^{-(1+r_++\lambda)t} + E_4 t e^{-(1+r_+)t} + F_4 t e^{-\lambda t} \right) \\ &+ \mathcal{O}(\alpha^2). \end{aligned} \quad (3.88)$$

Again, the coefficients B_4, C_4, D_4, E_4, F_4 are given in Appendix B.6.

As an application of the linear response functions, in appendix B.7, the linear response to a sinusoidal stimulus $r_+(t) = r_+^0 + a \sin \omega t$ is calculated.

Fluctuation dissipation theorem

Since perturbative expressions for both the auto-correlation functions $\mathcal{C}_{S/c}(t)$ and the linear response functions $\chi_{S/c}(t)$ have been calculated, one can now check the validity of the fluctuation dissipation theorem (FDT) for this system. The FDT in frequency space reads (with the Boltzmann constant k_B) and the $\tilde{}$ indicating the Fourier transform [85]

$$\tilde{\mathcal{C}}(\omega) = \frac{2k_B T}{\omega} \text{Im}(\tilde{\chi}(\omega)). \quad (3.89)$$

This relation is only fulfilled for systems in thermal equilibrium with temperature T . To quantify the violation of this FDT for systems out of equilibrium, one can introduce an effective temperature T_{eff} in the following way [98]:

$$\frac{T_{\text{eff}}(\omega)}{T} = \frac{\omega \tilde{\mathcal{C}}(\omega)}{2k_B T \text{Im}(\tilde{\chi}(\omega))}. \quad (3.90)$$

If the system characterised by the two functions \mathcal{C} and χ is in thermal equilibrium, the ratio on the left side of Eq. (3.90) is one. A frequency-dependent ratio or a ratio different to one is found for systems out of thermal equilibrium.

In the system described here, both the correlation functions and the response functions are dimensionless (as well as their Fourier transforms). In order to apply Eq. (3.89), one needs to transform the dimensionless response functions (e.g. $\chi_S(t)$) to response functions

with the dimension of an inverse energy. For that, one has to find a relation between the stimulus ϕ (a change in the opening rate) with which $\chi_S(t)$ has been calculated, and an energy h . Assuming an energy difference between the open and the closed conformation of the channel of ΔU (cf. left panel of Fig. 3.1) as well as thermal equilibrium, the ratio of the transition rates follow a Boltzmann statistics:

$$\frac{R_+}{R_-} \equiv r_+ = e^{-\frac{\Delta U}{k_B T}}. \quad (3.91)$$

A stimulus to the system means a change h in the energy difference: $\Delta U \rightarrow \Delta U + h$ which leads to new rates $r'_+ = r_+ e^{-\frac{h}{k_B T}}$. If $h \ll k_B T$, this can be expanded to give $r'_+ \approx r_+ (1 - \frac{h}{k_B T})$. In order to produce a change ϕ in r_+ (on which the computation of χ is based) one therefore needs an energy change of $h = -\frac{k_B T}{r_+} \phi$. The according response functions with dimensions of an inverse energy are connected to the dimensionless ones in Eqs. (3.87) and (3.88) by multiplication with $\frac{r_+}{k_B T}$ and Eq. (3.89) turns (for the channel variable S) into

$$\tilde{C}_S(\omega) = -2 \frac{r_+}{\omega} \text{Im} \tilde{\chi}_S(\omega). \quad (3.92)$$

Equally transformed, one can derive two expressions for the two effective temperatures for the S and the c variable:

$$\frac{T_{\text{eff},S}(\omega)}{T} = -\frac{\omega \tilde{C}_S(\omega)}{2r_+ \text{Im} \tilde{\chi}_S(\omega)}, \quad \frac{T_{\text{eff},c}(\omega)}{T} = -\frac{\omega \tilde{C}_c(\omega)}{2r_+ \text{Im} \tilde{\chi}_c(\omega)}. \quad (3.93)$$

For the computation of the exponential Fourier transforms, one has to consider that the response functions are zero for $t < 0$. For the channel variable (Eq. (3.87)) one gets

$$\begin{aligned} \tilde{\chi}_S(\omega) = \int_{-\infty}^{\infty} e^{-i\omega t} \chi_S(t) dt = & \frac{1}{(1+r_+)^2 + \omega^2} \left(1 - i \frac{\omega}{1+r_+} \right) \\ & + \alpha \left[\frac{1+r_+}{(1+r_+)^2 + \omega^2} B_3 + \frac{\lambda}{\lambda^2 + \omega^2} C_3 + \frac{1+r_++\lambda}{(1+r_++\lambda)^2 + \omega^2} D_3 \right. \\ & + \frac{(1+r_+)^2 - \omega^2}{((1+r_+)^2 + \omega^2)^2} E_3 - i\omega \left(\frac{1}{(1+r_+)^2 + \omega^2} B_3 + \frac{1}{\lambda^2 + \omega^2} C_3 \right. \\ & \left. \left. + \frac{1}{(1+r_++\lambda)^2 + \omega^2} D_3 + 2 \frac{1+r_+}{((1+r_+)^2 + \omega^2)^2} E_3 \right) \right]. \quad (3.94) \end{aligned}$$

The corresponding expression for c can be found as Eq. (B.68) in Appendix B.5.

Since the auto-correlation functions are even functions, the exponential Fourier transforms are the same as the power spectra as defined in Eqs. (3.15). The respective expressions for $\tilde{C}_S(\omega) = P_S(\omega)$ and $\tilde{C}_c(\omega) = P_c(\omega)$ are given in Eqs. (3.75) and (B.67).

Putting $\tilde{\chi}_{S/c}(\omega)$ and $\tilde{C}_{S/c}(\omega)$ into Eqs. (3.93) one finds the following:

$\alpha = 0$: $T_{\text{eff},S} = T$, $T_{\text{eff},c} \neq T$, i.e. even for no feedback, the whole system can not be described by an equilibrium system. Both effective temperatures are constant (not ω -dependent) but they are different. The partial system S is in equilibrium.

$\alpha \neq 0$: Both effective temperatures become frequency-dependent. Fig. 3.9 shows plots of the effective temperatures. For high frequencies, the partial system S becomes equilibrated, whereas the partial system c never is in equilibrium with the same temperature as S .

The violation of the fluctuation dissipation theorem underscores that the system considered is an active system that never reaches an equilibrium state. The 'microscopic' reason for that is the pump-term in the dynamic equation for c that works independent of an outside concentration.

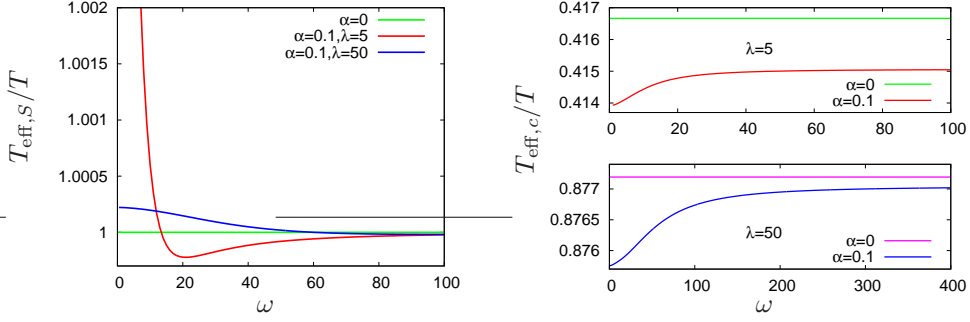


Fig. 3.9: Effective temperatures for S (left) and c (right) as defined in Eq. (3.93). Curves are plotted for two different values of λ . $r_+ = 6$ in all figures. $T_{\text{eff},S}/T = 1$ independent of λ or r_+ for $\alpha = 0$.

3.4.2 Self-consistent feedback model

In the preceding subsection, the mean values and the correlation functions of the two variables S and c of the system described by Eqs. (3.4)–(3.6) were calculated to linear order in the feedback parameter α using a computationally quite involved path-integral method. The expressions obtained are valid in the complete parameter range of r_+ and λ . In this subsection, now, a less involved approximative method will be introduced and expressions with limited validity in the parameter range will be obtained, again for the mean values and the correlation functions. The results of both approaches are compared in Subsec. 3.5.1. The method introduced in the following goes one step beyond a mean-field approximation.

The difficulty of the path-integral approach presented in Subsec. 3.4.1 arises, when the full $S(t)$ -dependent history of $c(t)$ is put into Eq. (3.51). In the self-consistent approach in this subsection, a new variable $\psi(t)$ is introduced, that is independent of $S(t)$ but is assumed to have the same statistics as $c(t)$. This statistics (the n -point functions of the distribution of $\psi(t)$) can, as will be shown in the following, be calculated using successive orders in an expansion around $\alpha = 0$. In the end, $\psi(t)$ will be replaced by $c(t)$ self-consistently.

The starting idea is to ‘prescribe’ a specific time evolution of $\psi(t)$ to the system and calculate the probability $P_{01}(t_0, t; \{\psi\})$ to find the system in the state $S(t) = 1$ after it has started in $S(t_0) = 0$ given an S -independent evolution of $\psi(t)$. From that, ensemble quantities can later be calculated by averaging the $P_{01}(t_0, t; \{\psi\})$ over all possible realisations of $\psi(t)$. Since S and ψ are assumed to be independent (e.g. $\langle c\psi \rangle = 0$), Eq. (3.5) is not used anymore and a simple master equation can be set up for the probability P_{01} from Eqs. (3.4) and (3.6):

$$\begin{aligned} \frac{d}{dt}P_{01} &= r_+(1 - P_{01}) - (1 + \alpha\psi(t))P_{01} \\ &= r_+ - (1 + r_+)P_{01} - \alpha\psi(t)P_{01}. \end{aligned} \quad (3.95)$$

This ordinary differential equation has the solution [19] (using the initial condition $P_{01}(t_0, t_0; \{\psi\}) = 0$)

$$P_{01}(t_0, t; \{\psi\}) = r_+ \int_{t_0}^t e^{-(1+r_+)(t-T) - \alpha \int_T^t \psi(t')dt'} dT. \quad (3.96)$$

For the complementary functional $P_{11}(t_0, t; \{\psi\})$ (the probability to find $S(t) = 1$ given $S(t_0 < t) = 1$ and ‘prescribing’ a certain $\psi(t)$), the same differential equation (Eq. (3.95)) holds but with the initial condition $P_{11}(t_0, t_0; \{\psi\}) = 1$. The result, then, is

$$P_{11}(t_0, t; \{\psi\}) = e^{-(1+r_+)(t-t_0) - \alpha \int_{t_0}^t \psi(t')dt'} + P_{01}(t_0, t; \{\psi\}). \quad (3.97)$$

Mean value to first order in α

The mean open probability of the channel in the steady state is the open probability under the condition of a specific history $\psi(t)$ averaged over all possible realisations of $\psi(t)$:

$$\langle S \rangle = \langle P_{01}(-\infty, 0; \{\psi\}) \rangle_{\psi}. \quad (3.98)$$

The brackets represent the average $\langle \dots \rangle_{\psi} \equiv \int \mathcal{D}\psi \dots \mathcal{P}[\psi(t)]$ with the (unknown) probability distribution $\mathcal{P}[\psi(t)]$.

Putting Eq. (3.96) into Eq. (3.98) gives

$$\langle S \rangle = r_+ \int_{-\infty}^0 dT e^{(1+r_+)T} \langle e^{-\alpha \int_T^0 \psi(t') dt'} \rangle_{\psi}. \quad (3.99)$$

Expanding the exponential leads to

$$\begin{aligned} \langle S \rangle &= r_+ \int_{-\infty}^0 dT e^{(1+r_+)T} \left(1 - \alpha \int_T^0 \langle \psi \rangle dt' \right) + \mathcal{O}(\alpha^2) \\ &= \frac{r_+}{1+r_+} - \alpha \frac{r_+}{(1+r_+)^2} \langle \psi \rangle + \mathcal{O}(\alpha^2). \end{aligned} \quad (3.100)$$

A self-consistent equation for $\langle S \rangle$ can now be obtained by replacing the average value of ψ by the average value of c (both quantities were assumed to have the same statistics) and using Eq. (3.10). In order to have Eq. (3.100) valid up to first order in α , for $\langle \psi \rangle$ the zeroth order ($\langle c \rangle = \langle S \rangle = \frac{r_+}{1+r_+} + \mathcal{O}(\alpha)$) has to be put in. This yields

$$\langle S \rangle = \frac{r_+}{1+r_+} - \alpha \frac{r_+^2}{(1+r_+)^3} + \mathcal{O}(\alpha^2). \quad (3.101)$$

Up to this point, the calculation is basically a mean-field approach and the result from Eq. (3.101) can also be obtained simply by setting $r_- = 1 + \alpha \langle c \rangle$, i.e. assume the variables S and c to be uncorrelated. In the following, the self-consistent approach goes beyond a mean-field calculation.

Auto-correlation functions to first order in α

Using the definition of the two probability functionals P_{01} and P_{11} , the auto-correlation function of S can be written in the steady state as

$$\begin{aligned} \mathcal{C}_S(t) &= \langle S(0)S(t) \rangle - \langle S(0) \rangle \langle S(t) \rangle \\ &= \langle P_{01}(-\infty, 0; \{\psi\}) P_{11}(0, t; \{\psi\}) \rangle_{\psi} - \langle P_{01}(-\infty, 0; \{\psi\}) \rangle_{\psi} \langle P_{01}(-\infty, t; \{\psi\}) \rangle_{\psi}. \end{aligned} \quad (3.102)$$

Putting in the results from Eqs. (3.96) and (3.97) and expanding the exponentials around $\alpha = 0$ to first order leads to

$$\begin{aligned} \mathcal{C}_S(t) &\approx \left\langle r_+ \int_{-\infty}^0 e^{(1+r_+)T} \left(1 - \alpha \int_T^0 \psi(t') dt' \right) dT \left[e^{-(1+r_+)t} \left(1 - \alpha \int_0^t \psi(t') dt' \right) \right. \right. \\ &\quad \left. \left. + r_+ \int_0^t e^{-(1+r_+)(t-T')} \left(1 - \alpha \int_{T'}^t \psi(t') dt' \right) dT' \right] \right\rangle_{\psi} - \langle S \rangle^2. \end{aligned} \quad (3.103)$$

Keeping only the terms of first order in α and replacing $\langle \psi \rangle$ by $\langle c \rangle = \langle S \rangle$ gives

$$\begin{aligned} \mathcal{C}_S(t) \approx & \frac{r_+}{1+r_+} \left[e^{-(1+r_+)t} + \frac{r_+}{1+r_+} \left(1 - e^{-(1+r_+)t} \right) \right] \\ & + \alpha \langle S \rangle \left\{ r_+ \int_{-\infty}^0 e^{(1+r_+)T} T dT \left[e^{-(1+r_+)t} + \frac{r_+}{1+r_+} \left(1 - e^{-(1+r_+)t} \right) \right] \right. \\ & \quad \left. + \frac{r_+}{1+r_+} \left[-e^{-(1+r_+)t} t - r_+ \int_0^t e^{-(1+r_+)(t-T')} (t-T') dT' \right] \right\} \\ & - \frac{r_+^2}{(1+r_+)^2} + \alpha \frac{2r_+^3}{(1+r_+)^4}. \end{aligned} \quad (3.104)$$

Since $\langle S \rangle$ on the right hand side of Eq. (3.104) is already multiplied by α , only the zeroth order of Eq. (3.101) has to be put in to keep Eq. (3.104) valid up to $\mathcal{O}(\alpha)$. Doing this and solving the integrals gives for the correlation function of S in the steady state

$$\mathcal{C}_S(t) = \frac{r_+}{(1+r_+)^2} e^{-(1+r_+)t} + \alpha \frac{r_+^2}{(1+r_+)^3} e^{-(1+r_+)t} \left(\frac{r_+ - 1}{1+r_+} - t \right) + \mathcal{O}(\alpha^2). \quad (3.105)$$

The correlation function for c is obtained using Eq. (3.9) with $n = 2$:

$$\begin{aligned} \mathcal{C}_c(t) &= \lim_{t_0 \rightarrow \infty} \langle c(t_0)c(t_0+t) \rangle - \langle c \rangle^2 \\ &= \lim_{t_0 \rightarrow \infty} \lambda^2 e^{-\lambda(2t_0+t)} \int_{-\infty}^{t_0} e^{\lambda\tau_1} d\tau_1 \int_{-\infty}^{t_0+t} d\tau_2 e^{\lambda\tau_2} (\mathcal{C}_S(\tau_2 - \tau_1) + \langle S \rangle^2) - \langle c \rangle^2. \end{aligned} \quad (3.106)$$

Since the correlation function as given in Eq. (3.105) was derived only for $t > 0$, the last integral in Eq. (3.106) has to be split. The integrals over the constant $\langle S \rangle^2$ gives $\langle c \rangle^2$, which therefore cancels and one gets

$$\begin{aligned} \mathcal{C}_c(t) &= \lim_{t_0 \rightarrow \infty} \lambda^2 e^{-\lambda(2t_0+t)} \int_{-\infty}^{t_0} e^{\lambda\tau_1} d\tau_1 \left(\int_{-\infty}^{\tau_1} d\tau_2 e^{\lambda\tau_2} \mathcal{C}_S(\tau_1 - \tau_2) \right. \\ & \quad \left. + \int_{\tau_1}^{t_0+t} d\tau_2 e^{\lambda\tau_2} \mathcal{C}_S(\tau_2 - \tau_1) \right). \end{aligned} \quad (3.107)$$

Putting in Eq. (3.105) and applying the limit for t_0 one ends up with

$$\begin{aligned} \mathcal{C}_c(t) &= \frac{\lambda r_+}{(1+r_+)^2((1+r_+)^2 - \lambda^2)} \left((1+r_+)e^{-\lambda t} - \lambda e^{-(1+r_+)t} \right) \\ & \quad + \alpha \frac{\lambda r_+^2}{(1+r_+)^4((1+r_+)^2 - \lambda^2)^2} \left[((1+r_+)^3(r_+ - 2) - (1+r_+)r_+\lambda^2) e^{-\lambda t} \right. \\ & \quad \left. - \lambda(r_+((1+r_+)^2 - \lambda^2) - (3r_+^2 - \lambda^2) - (1+r_+)((1+r_+)^2 - \lambda^2)t) \right]. \end{aligned} \quad (3.108)$$

The same expression is found if one uses cosine Fourier transform and the relation $P_c(\omega) = \frac{\lambda^2}{\lambda^2 + \omega^2} P_S(\omega)$ (Eq. (3.15)).

The fluctuations are easily obtained as the auto-correlation functions at time zero:

$$(\delta S)^2 = \mathcal{C}_S(0) = \frac{r_+}{(1+r_+)^2} + \alpha \frac{r_+^2(r_+ - 1)}{(1+r_+)^4} + \mathcal{O}(\alpha^2), \quad (3.109)$$

$$\begin{aligned} (\delta c)^2 = \mathcal{C}_c(0) &= \frac{\lambda r_+}{(1+r_+)^2(1+r_+ + \lambda)} + \alpha \frac{\lambda r_+^2}{(1+r_+)^4(1+r_+ + \lambda)^2} \\ & \quad \cdot [(1+r_+)(r_+ - 2) + \lambda(r_+ - 1)]. \end{aligned} \quad (3.110)$$

Again, due to S taking only the values 0 and 1, $(\delta S)^2$ can also be calculated using only the mean value $\langle S \rangle$ (Eq. (3.35)).

Mean value to second order in α

To go one step further in the perturbative calculation of $\langle S \rangle$, one has to expand the exponential in Eq. (3.99) to second order in α . Using the definition of the brackets $\langle \dots \rangle_\psi$ (see above), one gets

$$\langle e^{-\alpha \int_T^t dt' \psi(t')} \rangle_\psi = 1 - \alpha \int_T^t dt' \langle \psi(t') \rangle_\psi + \frac{\alpha^2}{2} \int \mathcal{D}\psi \int_T^t dt' \int_T^t dt'' \psi(t') \psi(t'') \mathcal{P}[\psi(t''')]. \quad (3.111)$$

The last term can be written as

$$\begin{aligned} & \int_T^t dt' \int_T^{t'} dt'' \langle \psi(t') \psi(t'') \rangle_{\psi; t'' < t'} + \int_T^t dt' \int_{t'}^t dt'' \langle \psi(t') \psi(t'') \rangle_{\psi; t'' \geq t'} \\ &= \int_T^t dt' \int_T^{t'} dt'' \langle \psi(t') \psi(t'') \rangle_{\psi; t'' < t'} + \int_T^t dt'' \int_T^{t''} dt' \langle \psi(t') \psi(t'') \rangle_{\psi; t'' \geq t'} \\ &= 2 \int_T^t dt' \int_T^{t'} dt'' \langle \psi(t'') \psi(t') \rangle_{\psi; t' \geq t''}, \end{aligned} \quad (3.112)$$

where the last step uses the fact that the correlation function is an even function with respect to the exchange of the two times. With Eq. (3.112) in Eq. (3.111), the expansion of the open probability of the channel to second order in α can be written as

$$\langle S \rangle = r_+ \int_{-\infty}^0 dT e^{(1+r_+)T} \left(1 - \alpha \int_T^0 dt' \langle \psi \rangle + \alpha^2 \int_T^0 dt' \int_T^{t'} dt'' \langle \psi(t'') \psi(t') \rangle \right) + \mathcal{O}(\alpha^3). \quad (3.113)$$

For this equation to be valid up to second order in α , $\langle \psi \rangle$ has to be replaced by the first order expression for $\langle c \rangle = \langle S \rangle$ and $\langle \psi(t'') \psi(t') \rangle$ by the zeroth order term of $\langle c(t'') c(t') \rangle$ (ψ and c are assumed to have the same statistics). Using Eq. (3.101) and $\langle c(t'') c(t') \rangle = \mathcal{C}_c(t' - t'') + \langle c \rangle^2$ together with the $\mathcal{O}(\alpha^0)$ term from Eq. (3.108), one gets

$$\langle S \rangle = \frac{r_+}{1+r_+} - \alpha \frac{r_+^2}{(1+r_+)^3} + \alpha^2 \frac{r_+^2}{2(1+r_+)^5} \left(1 + 4r_+ - \frac{(1+r_+)^2}{(1+r_+ + \lambda)^2} \right) + \mathcal{O}(\alpha^3). \quad (3.114)$$

From Eq. (3.113), the structure of this self-consistent method becomes clear. With each further step in the perturbation calculation in α , a higher n -point function of $\psi(t)$ (i.e. $c(t)$) comes in. As the next step, the second order expression of $\mathcal{C}_S(t)$ could be calculated, from which $\mathcal{C}_c(t)$ can easily be obtained to $\mathcal{O}(\alpha^2)$. For a third order term in $\langle S \rangle$, the three-point function $\langle c(0)c(t')c(t) \rangle$ would have to be calculated to zeroth order in α , and so on.

Validity of the results

The self-consistent method presented in this subsection is an extension of a mean-field calculation. This implies that the range of validity of the results obtained with the self-consistent method is (at most) the same as for the mean-field approach. For the $\mathcal{O}(\alpha)$ -results, that means that the fluctuations of c have to be negligible compared to its mean: $\frac{\delta c}{\langle c \rangle} \ll 1$. Using Eqs. (3.101) and (3.110), this leads to

$$\frac{\delta c}{\langle c \rangle} = \sqrt{\frac{\lambda}{r_+(1+r_+ + \lambda)}} + \mathcal{O}(\alpha). \quad (3.115)$$

For small α , the condition $\frac{\delta c}{\langle c \rangle} \ll 1$ therefore is fulfilled for the two cases

$$\lambda \ll 1 + r_+ \quad \text{or} \quad r_+ \gg 1. \quad (3.116)$$

In Subsec. 3.5.1, the results of the self-consistent approach will be compared to the results from the path-integral as well as the master equation approach. The criterions stated above will be verified, there.

3.5 Numerical results

To check the validity of the analytical results as well as to analyse the system in parameter ranges, where no analytical results were obtained, the system as described by Eqs. (3.4)–(3.6) is simulated numerically using a discrete time step Δt . To minimise errors induced by this discretisation, Δt has to be chosen much smaller than all timescales present in the system: $\Delta t \ll \min\{\frac{1}{r_+}, \frac{1}{1+\alpha}, \frac{1}{\lambda}\}$ ⁵.

At the beginning of each time step, the momentary flipping rates r_+ if $S(t) = 0$ or r_- if $S(t) = 1$ are calculated and a pseudo-random number from the interval (0,1) is drawn (random number generator `ran2` from [117]). The random number multiplied by the time step Δt gives the probability for a state flip of the channel. The dynamics of the concentration $c(t)$ is computed using a simple Euler forward algorithm. Ensemble averages are calculated by running the simulation many⁶ times with equal initial conditions but different sets of independent pseudo-random numbers. Before steady state quantities are calculated, the system is first evolved until its mean values (averaged over many runs) show no significant trend (in time) anymore. For the mean values and fluctuation measures, the respective quantities are additionally averaged over many⁷ consecutive time points.

The history dependence of the system is the reason, why an exact Gillespie-type algorithm [55] most probably does not significantly decrease computation time. Simple algorithms where the duration until the next state flip is calculated, are not appropriate, since the flipping probability changes through $c(t)$ in time (cf. [101])⁸.

In the following, the results of the numerical simulations will be presented in two parts: First, results for weak feedback (small α) will be shown and compared to the analytical results from the path-integral approach (referred to as 'PI' in the following; Subsec. 3.4.1) and the self-consistent method ('SC'; Subsec. 3.4.2). In the second part, the numerical results for intermediate and large α will be shown and with that the range of strong feedback explored. Where appropriate, also comparison to the results from the master equation approach ('ME'; Subsec. 3.3.1) is made.

Throughout this section, the dimensionless version of the system is considered, so no units are given on the axes of the plots. The only source of errors in the numerically obtained data is the random switching of the channel. In the simulations, single runs were repeated (see footnote) until the errors of the curves were smaller or of the order of the point sizes or the line widths in the following plots. The only quantities that have significant errors are the linear response functions and the response. Also in these cases, error bars are not shown for reasons of clearness and because this error could be reduced simply by letting computers run longer.

⁵Depending on the parameters, Δt was chosen to be 10^{-2} , 10^{-3} , 10^{-4} or 10^{-5} .

⁶For the plots over time, frequency and α , 10^5 , 10^6 or 10^7 independent runs were simulated, for the response functions and the plot of $f_1(t)$, $5 \cdot 10^8$ or 10^9 and for the plots over r_+ , 10^4 , $5 \cdot 10^4$, 10^5 or $5 \cdot 10^5$.

⁷Between $5 \cdot 10^3$ and $2 \cdot 10^5$.

⁸If the channel is closed and r_+ a constant, a Gillespie algorithm could be used instead of a constant time step method. The probability for the system to stay in the closed state for time t is $P_0(t) = e^{-r_+t}$. So, a random number could be drawn from an exponential distribution and used for the time $t = \tau_{j+1} - \tau_j$ until the next flip occurs at time τ_{j+1} . The concentration at time τ_{j+1} would then be calculated by $c(\tau_{j+1}) = c(\tau_j)e^{-\lambda(\tau_{j+1}-\tau_j)}$. In the open state, however, the probability to remain in $S = 1$ for a time t becomes more complicated. The concentration evolves according to $c(t) = (c(\tau_j) - 1)e^{-\lambda t} + 1$ for $\tau_j \leq t \leq \tau_{j+1}$. This gives for the concentration- and therefore time-dependent rate $r_-(t) = 1 + \alpha c(t) = 1 + \alpha [1 + (c(\tau_j) - 1)e^{-\lambda t}]$. Solving the differential equation for the probability to stay in the open state, $\frac{dP_1(t)}{dt} = -r_-(t)P_1(t)$ (with $P_1(0) = 1$), using this $r_-(t)$, gives

$$P_1(t) = e^{-\frac{\alpha(c(\tau_j)-1)}{\lambda}t} e^{-(1+\alpha)t} e^{\frac{\alpha(c(\tau_j)-1)}{\lambda}t} e^{-\lambda t}. \quad (3.117)$$

The inverse of this equation (which is needed to produce an accordingly distributed random number distribution [117, 131]) can not be expressed in elementary functions. Since $P_1(t)$ is continuous, in principle a Gillespie-type algorithm is possible [101]. It is, however, not clear if such an algorithm would save computer time compared to a constant time step algorithm, since the inverse would have to be computed numerically in each step with a new parameter $c(\tau_i)$.

3.5.1 Weak feedback

Fig. 3.10 shows the ensemble averages of $S(t)$ and $c(t)$ for the specific initial condition $S(t=0) = 0$, $c(t=0) = 0$ for no feedback ($\alpha = 0$) and the three weak feedback strengths $\alpha = 0.1, 0.2$ and 0.5 . For $\alpha = 0$ the system decouples and fully valid expressions for all relevant quantities can be calculated analytically. The more interesting results from the analytical derivations in the last section are therefore the changes in the quantities due to feedback. To extract only those from the plots, in the remainder of this subsection, only the differences between the cases with $\alpha \neq 0$ and $\alpha = 0$ will be shown and compared to the terms linear (or to second order) in α from the path-integral ('PI') and the self-consistent ('SC') approach. The insets in Fig. 3.10 show these differences and the linear order terms of the analytical expressions from the path-integral results (Eqs. (3.61) (with Eq. (3.44)) and (B.66)).

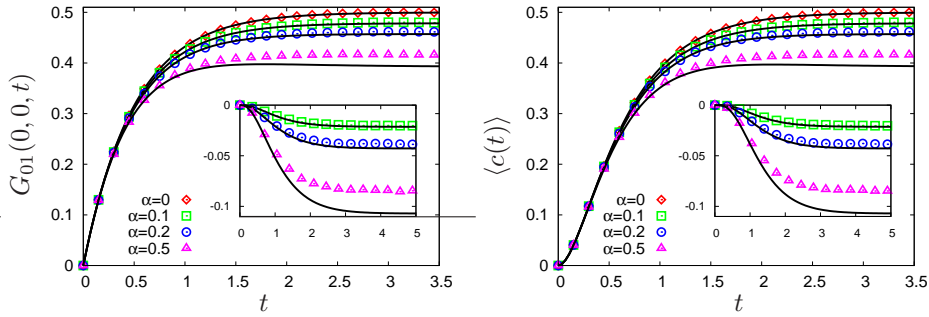


Fig. 3.10: The ensemble averages $\langle S(t) \rangle$ (left) and $\langle c(t) \rangle$ (right) for the initial condition $S(0) = 0$, $c(0) = 0$ for different feedback strengths ($r_+ = 1$, $\lambda = 5$). **Insets:** The differences between the results for $\alpha \neq 0$ and $\alpha = 0$. The black curves are the results from the path-integral (PI) approach (Eqs. (3.61) (with Eq. (3.44)) and (B.66)).

From both Figs. 3.10, it can be seen that the PI approach gives good results for α up to approximately 0.2. For $\alpha = 0.5$, the deviation is already quite big and higher order terms in α would have to be used to describe the system well. Fig. 3.11 underscores this statement. Here, the mean open probability of the channel in the steady state is plotted against different values of α for two different sets of $\{\lambda, r_+\}$ and compared to the results from the three analytical approaches. Whereas the result from the master equation approach agrees very well with the numerical result for all α , the approximative path-integral method works fine up to $\alpha \approx 0.1$. Depending on the parameters, the self-consistent method to first order in α is very close to the PI-result ($r_+ \gg \lambda$) or quite off (see also later in this subsection). The second order term in the SC-result improves the agreement with numerics to higher α of approximately 0.5 in the right panel of Fig. 3.11.

The agreement of the PI-result with the numerics for $\alpha \lesssim 0.1$ is consistent with the setup of the dimensionless model: For the contribution of feedback to be small, $\alpha \ll \frac{1}{c}$ and since c is bounded from above by 1, the linear expansion in α should work for $\alpha \ll 1$. In the following, for the comparison between simulations and analytical results, α will always be 0.1.

Fig. 3.12 shows the steady state mean open probability of the channel depending on r_+ (which is the same as the mean calcium concentration $\langle c \rangle$ – Eq. (3.70)) for two different values of λ . Here, both results of the PI (Eq. (3.69)) and the SC (Eq. (3.101)) approach are plotted against numerics. Since the feedback only acts on the closing rate r_- , the contribution of it to the mean open fraction of the channel is always negative. For both parameter sets, the PI-result comes quite close to the numerical result, whereas the SC-approach gives only correct results for either high r_+ or small λ (right panel of Fig. 3.12). This is in accordance with the two constraints derived in Subsec. 3.4.2.

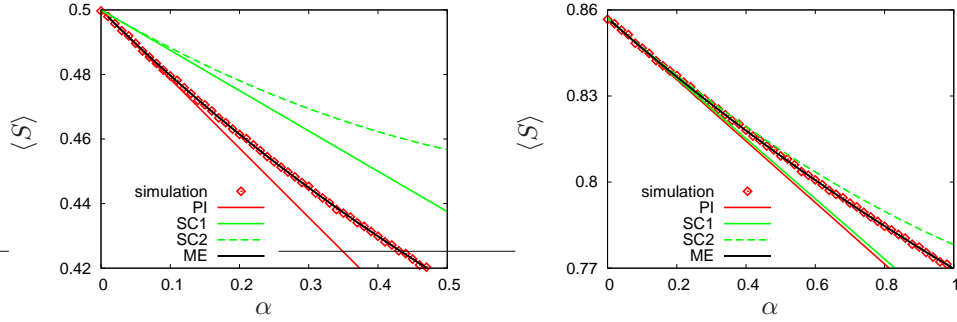


Fig. 3.11: The mean open probability of the channel plotted against the feedback parameter α together with the results from all three analytical approaches: The path-integral method (PI) (Eq. (3.69)), the self-consistent method to first (SC1) (Eq. (3.101)) and second (SC2) (Eq. (3.114)) order in α and the master equation result (ME) (Eq. (3.33)). **Left:** $r_+ = 1$, $\lambda = 5$, **Right:** $r_+ = 6$, $\lambda = 1$.

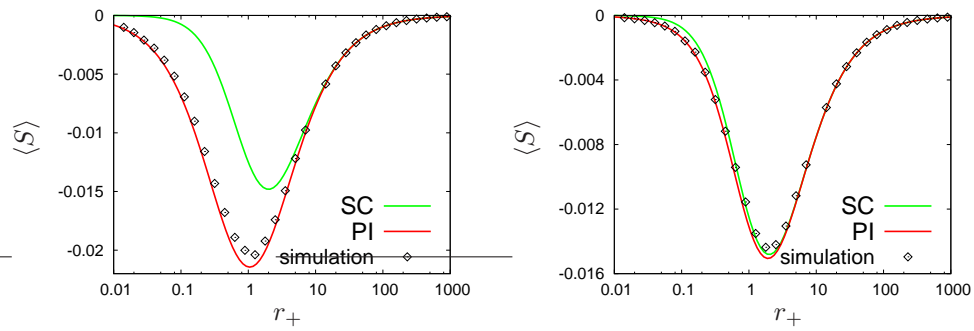


Fig. 3.12: Contribution of weak feedback to the mean open probability of the channel in steady state. **Left:** $\lambda = 5$; **Right:** $\lambda = 0.1$.

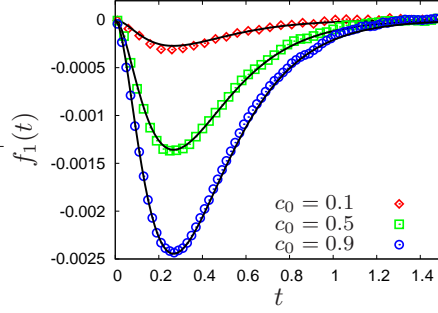


Fig. 3.13: The influence of an initial calcium concentration $c(t=0) = c_0$ on the Green's function $G_{01}(0, c_0; t)$. Plotted is the difference between $\langle S(t) \rangle$ for a simulation with $c_0 \neq 0$ and $c_0 = 0$ for $\alpha = 0.1$ ($r_+ = 6$, $\lambda = 5$). The analytical result (black curves) is $f_1(t)$ from the path-integral approach (Eq. (3.66)).

The basic quantity of the path-integral approach – the Green's function – has already been plotted and compared to the numerical results in Fig. 3.10. Another basic result that was needed for the derivation of further quantities and should be checked against numerics is the contribution of an initial calcium concentration c_0 to the Green's function, $f(t)$ as given in Eq. (3.64). Fig. 3.13 shows the difference between the time traces with $c_0 \neq 0$ and the one for $c_0 = 0$ for $\alpha = 0.1$. The agreement between the result from the path-integral approach ($f_1(t)$ from Eq. (3.66)) and the numerical result is very good.

In Fig. 3.14, the contribution of weak feedback to the correlation function $\mathcal{C}_S(t)$ of the channel variable is plotted for four different sets of r_+ and λ . The results from the PI-approach (Eq. (3.73)) and the SC-approach (Eq. (3.105)) are compared to numerics. Again, the PI-approach provides a fairly good description, whereas the SC-result fails for the left figures (small r_+ and/or large λ). Feedback is found to either decrease or increase correlations, depending on parameters.

Also for the correlation function \mathcal{C}_c of the calcium concentration, the effect of feedback can be either decreasing or increasing, as Fig. 3.15 shows (the same parameters are used as in Fig. 3.14). The PI-result (Eq. (3.74)) fits well, but the SC-result (Eq. (3.108)) does not give as nice results, even for the parameters that gave the correct correlation function of S .

In order to numerically obtain the response function of the system, it was evolved with a 'base-line' r_+ until it reached a steady state. At some time point t_0 , r_+ was increased to $r_+ + \phi_0$ (step-function stimulus) with $\phi_0 = 0.1$ and the resulting $S(t)$ and $c(t)$ were averaged over a large number of runs (10^9). For noise-reduction, the data was then averaged over a certain number of time points (10–100) and the temporal derivative was calculated numerically (cf. Eq. (3.20)). The left panel of Fig. 3.16 shows the result of that as the contribution of weak feedback to the response function of S for a given parameter set r_+ and λ . The data still shows fluctuations but the result from the PI-approach (Eq. (3.87)) agrees well with the simulations. Feedback in this case increases the response function for short times and decreases it for longer times. The linear response function of the concentration c (right panel of Fig. 3.16) looks similar, except that it goes to zero for small t . Again, the PI-result (Eq. (3.88)) agrees well with numerics.

Since for the mean values, correlation and response functions the PI-result was shown to describe the numerical results correctly, the agreement to relevant quantities derived from these basic ones (as, e.g. the power spectrum, the variance or the coefficient of variation) will be equally good and therefore no plots will be shown for that. These quantities will be discussed in the next subsection on strong feedback.

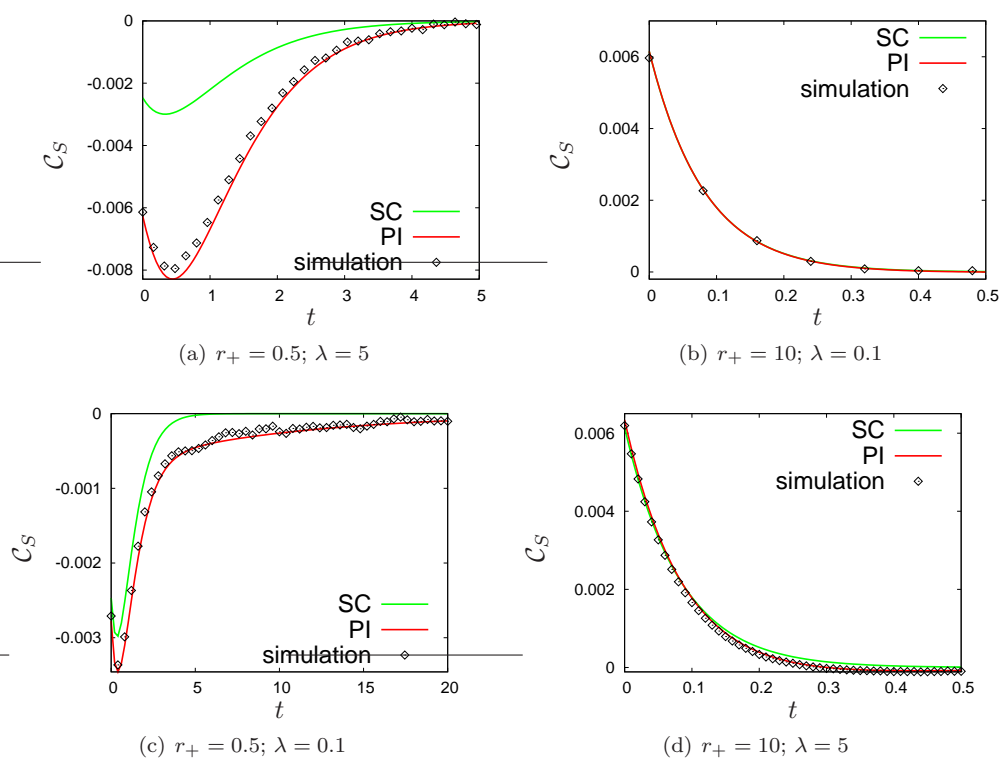


Fig. 3.14: Contribution of feedback to the auto-correlation function $C_S(t)$ of S in the steady state. In the right figures, the curves from the two different analytical approaches lie on top of each other.

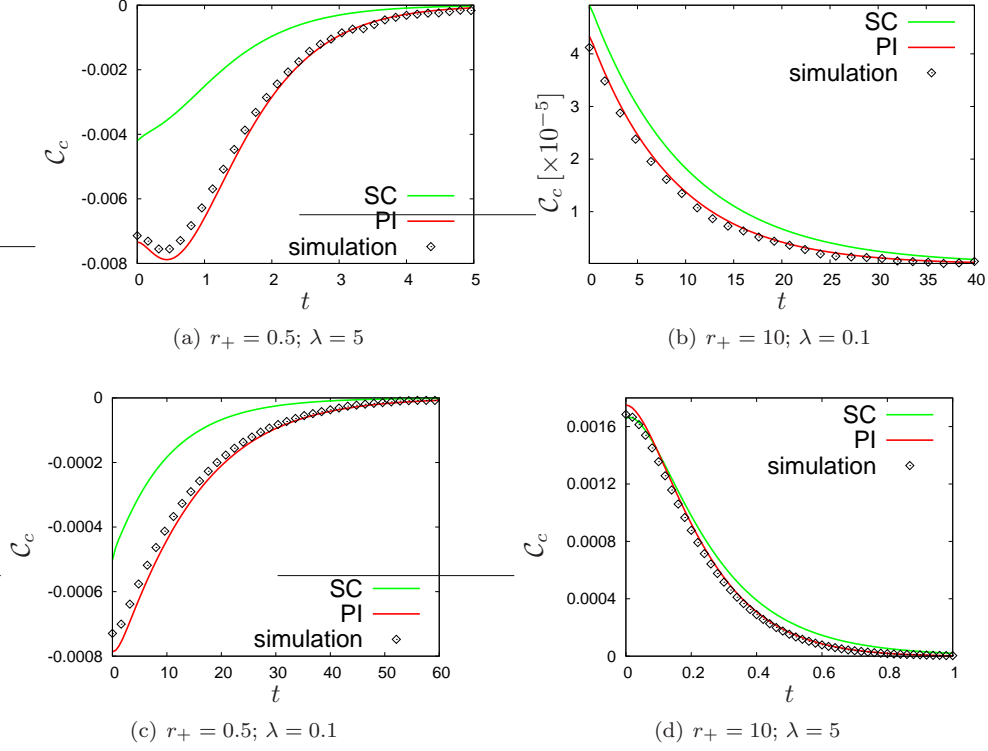


Fig. 3.15: The same figures as in Fig. 3.14 but for the contribution of feedback to the correlation function $C_c(t)$ of c .

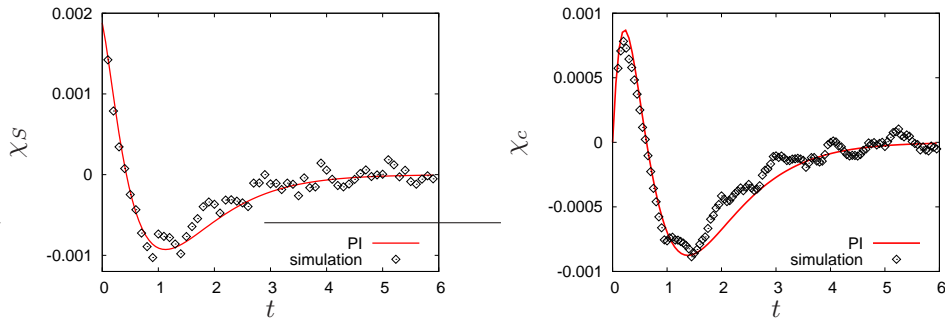


Fig. 3.16: Contribution of feedback to the linear response function χ_S (left) and χ_c (right) in the steady state ($r_+ = 0.5, \lambda = 5$). The time step for the simulation was $\Delta t = 10^{-3}$ and the calculation of the temporal derivative included an averaging over $100\Delta t$ for χ_S and $50\Delta t$ for χ_c .

3.5.2 Strong feedback

For intermediate ($0.1 \lesssim \alpha \lesssim 1$) and strong ($\alpha > 1$) feedback, analytical results were only derived for the mean values in the master equation ('ME') approach. In the following, the numerical results will be shown for different parameter values and different $\alpha > 1$.

Mean values

Fig. 3.17 shows the equivalent of Fig. 3.11 for larger values of α . The result from the ME approach for the mean open fraction $\langle S \rangle$ in the steady state agrees perfectly with the numerical results.

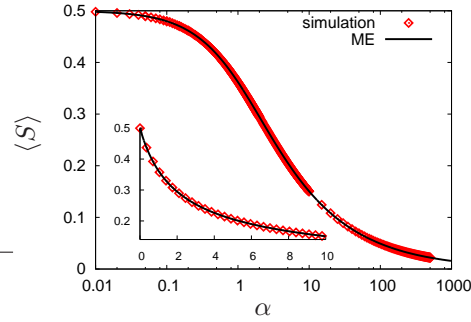


Fig. 3.17: The mean open probability of the channel plotted against the feedback parameter α ($r_+ = 1$, $\lambda = 5$) together with the result from the master-equation approach (ME) Eq. (3.33) on a logarithmic (main figure) and a linear scale (inset).

Fig. 3.18 shows the time evolution of the mean values of the channel variable S and the concentration c for a specific set of parameters and a special initial condition. $\langle S(t) \rangle$ in this case is the Green's function $G_{01}(0, 0; t)$. For larger feedback ($\alpha = 10$), the propagator

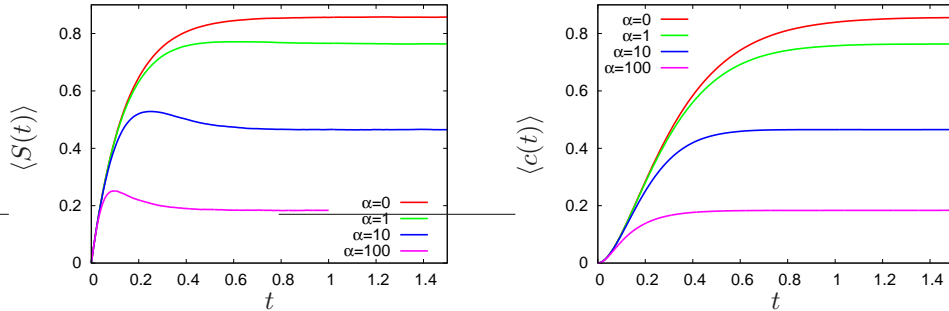


Fig. 3.18: The time evolution of the mean values $\langle S(t) \rangle$ (left) and $\langle c(t) \rangle$ (right) for $r_+ = 6$, $\lambda = 5$ and the initial condition $S(0) = c(0) = 0$.

shows an overshoot before it reaches its steady state. This specific behaviour will reappear in quantities considered in the remainder of this subsection. An overshoot is never seen for the time evolution of $\langle c(t) \rangle$.

The steady state mean open probability of the channel $\langle S \rangle = \langle c \rangle$ depending on r_+ was already shown as a result from the master equation approach in Subsec. 3.3.1. Agreement with numerical results was checked and found to be equally good as in Fig. 3.17.

Auto-correlation functions and power spectra

In Fig. 3.19, the auto-correlation function \mathcal{C}_S (as defined in Eq. (3.11)) for the channel variable S is plotted for different feedback strengths for intermediate r_+ and λ . Here,

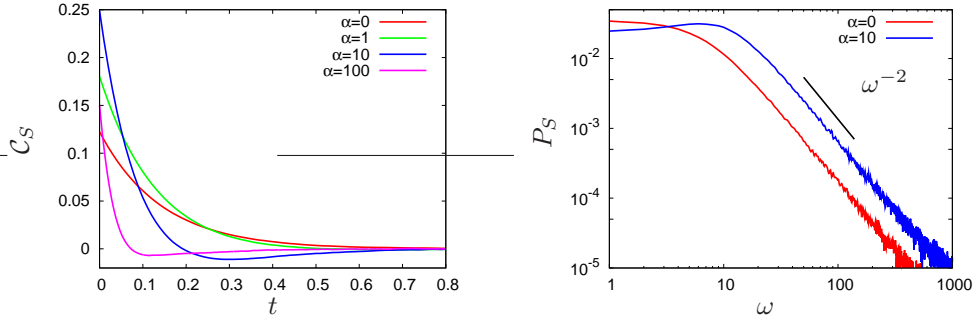


Fig. 3.19: Correlation function $C_S(t)$ (**left**) and power spectrum $P_S(\omega)$ (**right**) of S in the steady state for $r_+ = 6$ and $\lambda = 5$. In order to get data also for high frequencies, the simulations for the power spectrum were run with a small time step $\Delta t = 10^{-5}$.

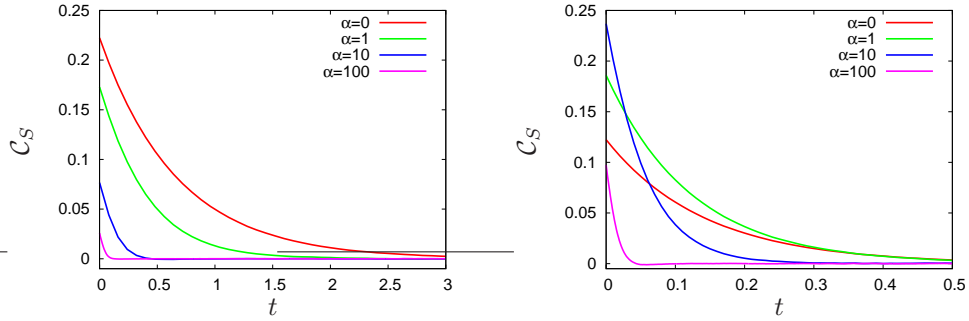


Fig. 3.20: Correlation function $C_S(t)$ of S in the steady state for $r_+ = 0.5$ and $\lambda = 5$ (**left**) and $r_+ = 6$ and $\lambda = 50$ (**right**).

feedback up to $\alpha \lesssim 10$ enhances correlations at short times. For strong feedback ($\alpha \gtrsim 10$), the correlations become negative for an intermediate time interval. This drop in the correlation function is also seen as a peak in the power spectrum, which is plotted for the same parameters on the right panel of Fig. 3.19 (defined in Eq. (3.15)). Independent of feedback, the power spectrum of S decays as ω^{-2} . For weak feedback, this property can also be seen from the analytical expression in Eq. (3.75).

The negative correlations in S mostly disappear for r_+ too small or λ too big, as Fig. 3.20 shows. Also, the feedback-dependent increase in correlations in S at short times is not a conserved property of the system as the left panel of Fig. 3.20 shows, where feedback decreases correlations for all times.

The same analysis can be conducted for the auto-correlation function of the concentration c . Fig. 3.21 shows C_c and the corresponding power spectrum. Different to the channel variable S , negative correlations are never observed for the concentration c . Consequently, the power spectrum shows no peak. It decays as ω^{-4} , which, again, is also the case for the analytical expression (Eq. (B.67)). $C_c(t)$ behaves non-monotonically for short times with growing feedback.

For small r_+ , the correlation function of c decreases with growing feedback for all times (Fig. 3.22, left panel), but for large λ , the non-monotonous behaviour reappears for intermediate times (Fig. 3.22, right panel). Feedback generally leads to a faster decay of the auto-correlation functions.

Cross-correlation functions

In Fig. 3.23, the two cross-correlation functions C_{Sc} and C_{cS} are shown for different strengths of feedback. The function $C_{Sc}(t)$ shows independent of feedback a peak at an

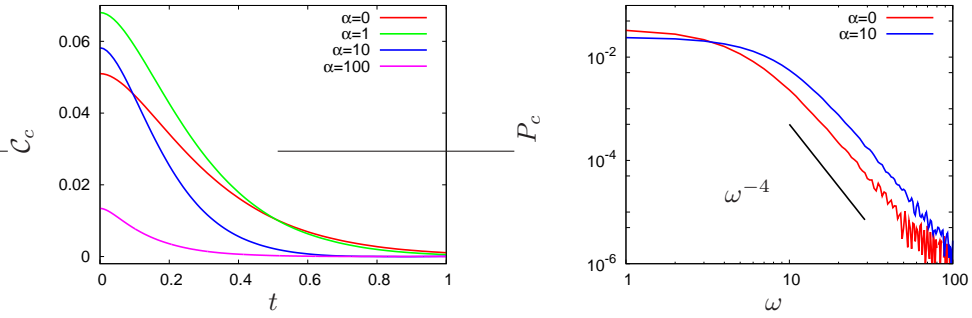


Fig. 3.21: Correlation function $C_c(t)$ of c (left) and the corresponding power spectrum $P_c(\omega)$ (right) for $r_+ = 6$ and $\lambda = 5$ in the steady state. As for the right panel of Fig. 3.19, a time step $\Delta t = 10^{-5}$ was used for the computation of the power spectrum.

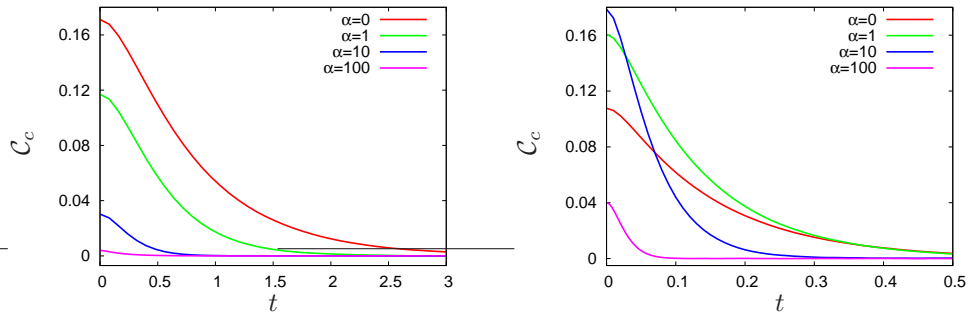


Fig. 3.22: Correlation function $C_c(t)$ of c in the steady state for $r_+ = 0.5$ and $\lambda = 5$ (left) and $r_+ = 6$ and $\lambda = 50$ (right).

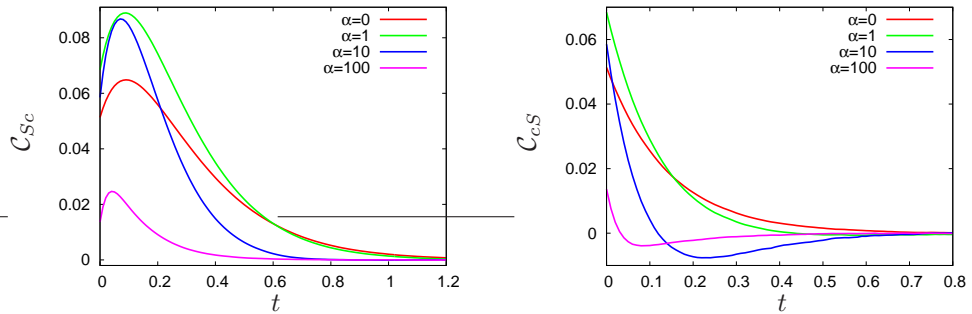


Fig. 3.23: Cross-correlation functions: $C_{Sc}(t)$ (left) and $C_{cS}(t)$ (right) for $r_+ = 6$ and $\lambda = 5$.

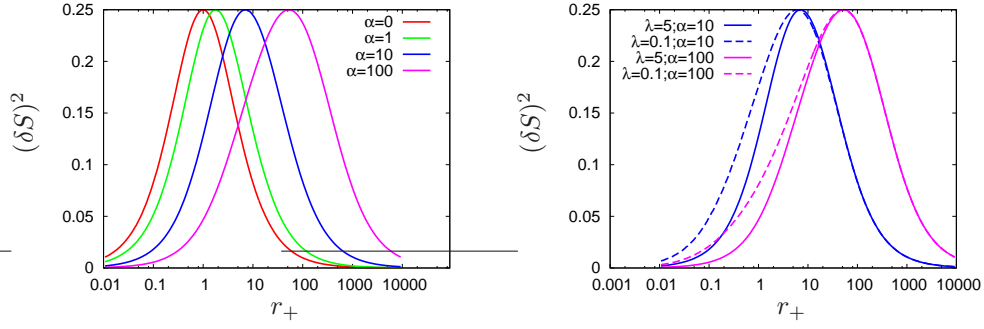


Fig. 3.24: Variance of S in the steady state. **Left:** $\lambda = 5$; **right:** curves for $\alpha = 10$ and 100 for $\lambda = 5$ and $\lambda = 0.1$.

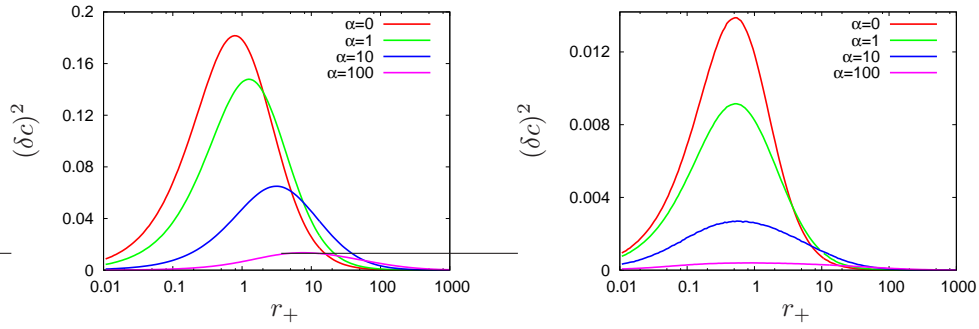


Fig. 3.25: Variance of c in the steady state. **Left:** $\lambda = 5$; **right:** $\lambda = 0.1$;

early time. This is due to the fact that the channel has a finite residence time that it stays, e.g. in the open state. During that time, calcium flows in until the channel flips states again, which produces the peak. For strong feedback, the other cross-correlation function $\mathcal{C}_{cS}(t)$ becomes negative for short times which is a result of high calcium concentrations lowering the chance of finding the channel in the open state.

Fluctuation measures

Fig. 3.24 plots the variance of the channel variable S in the steady state, which is the correlation function at time zero: $(\delta S)^2 = \mathcal{C}_S(0)$. Because S is a discrete variable with only the two values 0 and 1, the variance can also be obtained solely by the mean value (Eq. (3.35)). As in the case of $\langle S \rangle$ (Fig. 3.6), λ only has an effect on the variance for $\alpha \neq 0$, which is why in the right panel of Fig. 3.24 only two values of feedback strength are shown. As already explained in Subsec. 3.3.1, the maximum of $(\delta S)^2$ is always $\frac{1}{4}$ and appears at $\langle S \rangle = \frac{1}{2}$ independent of feedback, i.e. a shift in reception range due to feedback also shifts the maximum of the fluctuations to higher r_+ (cf. Fig. 3.6). Smaller λ increases the range, in which fluctuations might be relevant (right panel of Fig. 3.24).

The variance of the concentration c can not be obtained from the mean value as in the case of S . Fig. 3.25 plots $(\delta c)^2$ over r_+ for two different values of λ . A large value of λ (left panel of Fig. 3.25) is shown to shift the maximum of the fluctuations of c to higher r_+ for increasing feedback strength, which is not the case for a small λ (right panel). Looking at a line of constant r_+ in the left panel of Fig. 3.25, one again sees the non-monotonous behaviour of the correlation function $\mathcal{C}_c(0)$ as in Fig. 3.21. The decrease in fluctuations in c with increasing α suggests a positive effect of feedback on the signalling properties of the system which turns out to be a wrong conclusion in most cases when looking at the next quantity, the coefficient of variation.

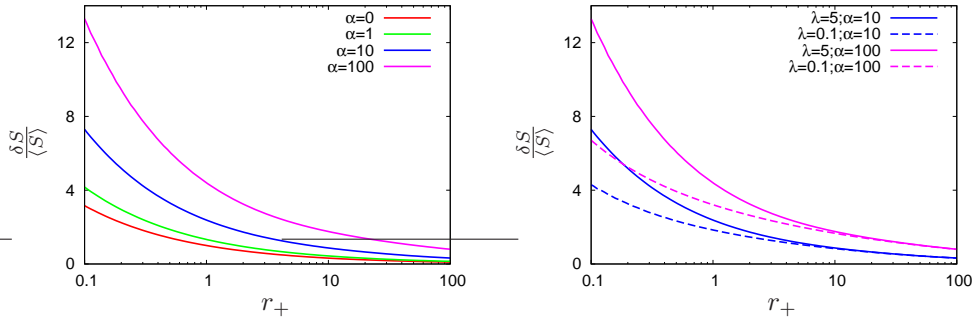


Fig. 3.26: Coefficient of variation of S in the steady state. **Left:** $\lambda = 5$; **right:** curves for $\alpha = 10$ and 100 for $\lambda = 5$ and $\lambda = 0.1$.

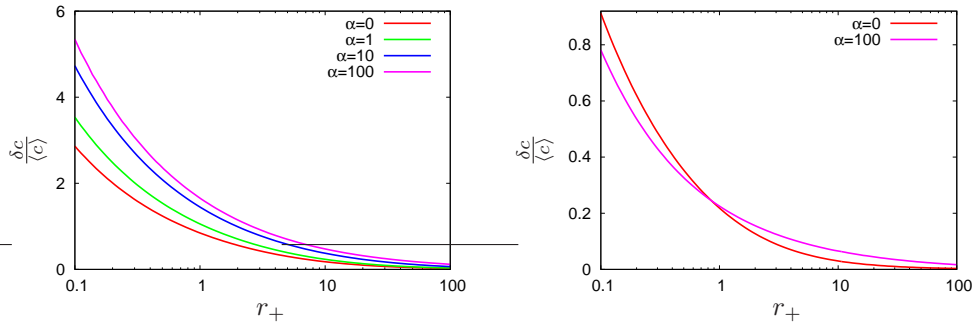


Fig. 3.27: Coefficient of variation of c in the steady state. **Left:** $\lambda = 5$; **right:** $\lambda = 0.1$. In the right panel, only the curves for $\alpha=0$ and 100 are shown for reasons of clarity. The data for $\alpha = 1$ and $\alpha = 10$ lies in between those two.

A quantity that describes the decreased reliability of a mean value due to fluctuations is the coefficient of variation, i.e. the standard deviation of the quantity divided by its mean (also called the relative standard deviation or the noise-to-signal ration). Fig. 3.26 shows this quantity for the channel variable S . According to Eq. (3.35), the coefficient of variation for S is $\frac{\delta S}{\langle S \rangle} = \sqrt{\frac{1}{\langle S \rangle} - 1}$ and since $\langle S \rangle$ decreases monotonically with α , the coefficient of variation increases monotonically, i.e. if S is treated as the output of the system, transmission of signals gets more noisy for stronger feedback. λ strongly increases the coefficient of variation for small r_+ and large α (right panel of Fig. 3.26).

For the concentration c , the coefficient of variation is found to increase in most cases (left panel of Fig. 3.27), but there are parameter regimes, where it decreases (right panel of Fig. 3.27), although not dramatically. A decrease of the coefficient of variation with increasing α is a positive effect of feedback on the faithful transduction of signals in this system. For small values of r_+ , the coefficient of variation becomes quite large (1 to 10), which means that fluctuations dominate the dynamics.

Linear response functions

Fig. 3.28 shows the linear response function of the channel variable S for different feedback strengths α . It was calculated numerically the same way as described in the preceding subsection on weak feedback results. According to the left panel of Fig. 3.28, increasing feedback makes the linear response function 'sharper', i.e. the decay time becomes shorter. The linear response function is – by definition – the response of the system to a δ -pulse in the stimulus. Increasing feedback therefore makes the shape of the output more closely related to the input, i.e. it gives a more reliable transmission of the input shape. This will

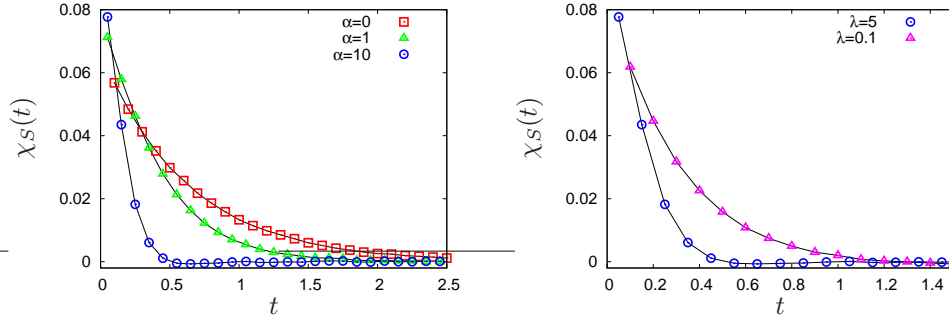


Fig. 3.28: The linear response function $\chi_S(t)$ for the channel variable S in the steady state computed for a step stimulus from $r_+ = 0.5$ to $r_+ = 0.6$. **Left:** $\lambda = 5$; **right:** $\alpha = 10$ and two different λ . The lines connect the data points and are guides to the eye. Before computing the time derivative, data was averaged over $10\Delta t$ ($\Delta t = 10^{-3}$).

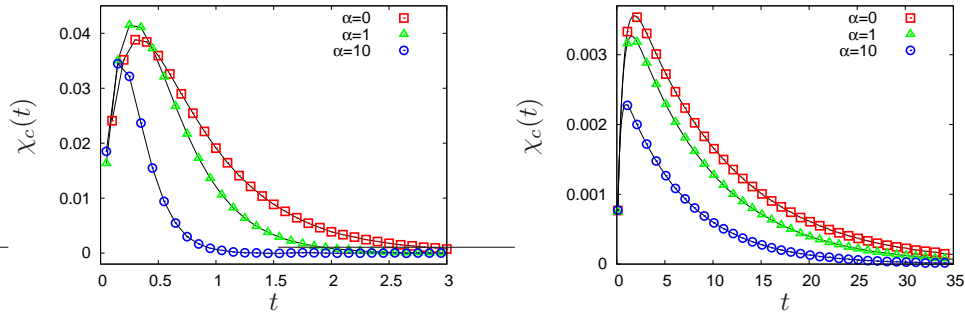


Fig. 3.29: The linear response function $\chi_c(t)$ for the concentration c in the steady state (cf. Fig. 3.28). **Left:** $\lambda = 5$; **right:** $\lambda = 0.1$. The lines connect the data points and are guides to the eye.

be confirmed by looking at the response towards a sinusoidal stimulus further down. The parameter λ shows only an effect on $\chi_S(t)$ for $\alpha \neq 0$, which is why in the right panel of Fig. 3.28 only the curves for strong feedback are shown. It is shown that an increasing λ has a similar effect on $\chi_S(t)$ as an increase in α .

In Fig. 3.29 the linear response function of the concentration c is plotted. With increasing feedback, the maximum of $\chi_c(t)$ clearly shifts towards shorter times. The effect of a decreasing λ is mainly a shift of the maximum towards longer times (right panel of Fig. 3.29).

As an example of a time-varying stimulus, a periodic input to the system is considered: $r_+(t) = r_+^0 + a \sin \omega t$. The system was evolved with $r_+^0 = 1$ until it reached a steady state and then the sinusoidal part with $a = 0.1$ was added to r_+ and the responses in S and c recorded: $\mathcal{R}_{S/c}(t)$ (cf. Eq. (3.17)). After some initial decay time, the response itself becomes sinusoidal with amplitude A and phase lag θ to the stimulus signal: $\mathcal{R}_{S/c}(t) = A_{S/c} \sin(\omega t + \theta_{S/c})$. Fig. 3.30 shows both these quantities⁹ for the response in the channel state S plotted over the stimulus frequency ω . The insets of the figures show the difference between the numerical results for $\alpha = 0.1$ and $\alpha = 0$ compared to the analytical result (cf. Subsec. 3.5.1) from the path-integral result computed in Appendix B.7 (Eqs. (B.74) and (B.75)).

Noticeable is a decrease of the amplitude of the response with increasing frequency

⁹The system was evolved numerically for some relaxation time after the sinusoidal stimulus was switched on. A sinusoidal curve was fitted to the response using the nonlinear fitting procedure of [58]. The amplitude and the phase lag were obtained as the two fitting parameters.

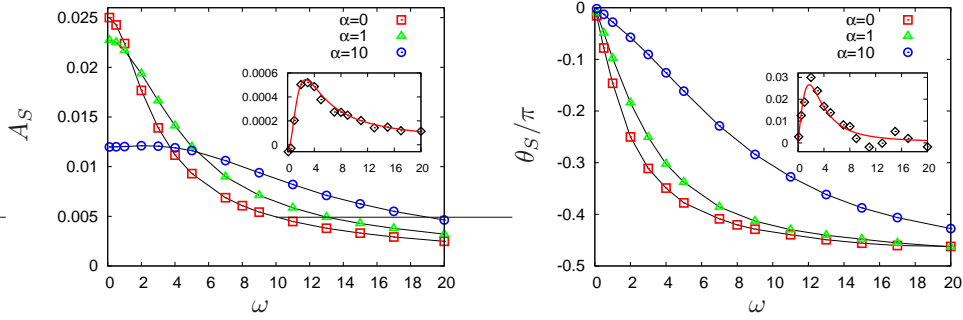


Fig. 3.30: Response of the channel variable S to a sinusoidal stimulus $r_+(t)$ ($\lambda = 5$). **Left:** amplitude; **right:** phase. The lines in the main figures are guides to the eye. The insets compare the result from the path-integral approach for $\alpha = 0.1$ (line) to numerics (points – difference between data obtained with $\alpha = 0.1$ and $\alpha = 0$ – cf. Subsec. 3.5.1).

of the stimulus (low-pass filter). Also, the amplitude at small frequencies decreases with increasing feedback. The horizontal plateau for strong feedback ($\alpha = 10$) that exists for small frequencies corresponds to the more δ -function like shape of the linear response function $\chi_S(t)$ for strong feedback (Fig. 3.28): As mentioned before, this leads to a more reliable transmission of the signal which in this case means a transmission of the property ‘constant amplitude’ over a wider range of frequencies. At high frequencies, feedback increases the amplitude of the transmitted signal, i.e. the frequency range detectable by the system is increased by feedback. The phase of the response signal decreases with frequency. Feedback leads to a more gradual decrease.

3.6 Extensions and outlook

3.6.1 Coupling of channels in a cilium

A single ion channel in a small compartment as it was described in the preceding sections is a very strong simplification and abstraction of nature. A system, where this simple model might serve as a constituent part is, e.g. a number of channels connected to the same – larger – compartment. An example of that are the cilia of the olfactory receptor neurons (ORNs), that, due to their geometry, can be approximately treated as one-dimensional objects. Not much is known about the distribution (or even the concentrations) of the relevant proteins (receptor, AC, CNG channels, pumps and exchangers) on the membrane of the cilium (cf. Subsec. 2.2.1 and the footnote on p. 17). Assuming a homogeneous distribution, the values in Tab. 2.2 suggest 2–30 CNG channels per $1\mu\text{m}$ segment of a thin (diameter $\sim 0.1\mu\text{m}$) cilium. These small numbers justify the consideration of a (nearly) separated compartment with a single channel, if the stimulus is very weak and single signalling events are of interest (cf. Sec. 3.1) [6]. However, if the stimulus is increased and many neighbouring channels have increased opening rates, coupling of these single compartments through different mechanisms becomes relevant.

There are several mechanisms that can couple the dynamics of the channels and the local calcium concentration in such an array of neighbouring compartments:

1. The diffusion of Ca^{2+} inside the cilium leads to different local Nernst potentials and therefore changes the ion flux J' through the channels.
2. Ca^{2+} entering through one channel can – through diffusion – alter the closing rate of a neighbouring channel (nonlocal feedback).

3. Local inhomogeneities in the stimulus (cAMP); spatial correlations of cAMP concentrations might lead to temporal correlations of the channel dynamics of different channels.
4. Since the transmembrane voltage spreads very quickly inside the cilium and since the currents through the channels depend on the voltage (cf. footnote on p. 18), the dynamics of the single-channel compartments are globally coupled (cf. Subsec. 2.2.5).

As a start and as a continuation of the analysis of the single channel compartment in the preceding sections, in the present work only the case of the nonlocal feedback (case 2 from above) will be looked at. Assumed is a one-dimensional system, in which calcium can diffuse freely. At the positions \bar{x}_i of the channels, calcium flows into the system with a rate J' if the respective channel is in the open state ($S_i = 1$). The extrusion of calcium is assumed to happen spatially continuous everywhere in the compartment with a constant rate $\bar{\lambda}$. The channel opening rates are assumed to be all the same, namely R_+ ¹⁰. The closing rates R_-^i of the channels are modified by the local feedback through the calcium concentration at the positions of the channels. The feedback parameter $\bar{\alpha}$ is assumed to be the same for all channels.

The modified Eqs. (3.1)–(3.3) together with a diffusion term in Eq. (3.2) read

$$S_i(\bar{t}) : \quad 0 \xrightleftharpoons[R_-^i]{R_+} 1, \quad (3.118)$$

$$\frac{\partial \bar{c}}{\partial \bar{t}} = \bar{D} \frac{\partial^2}{\partial \bar{x}^2} \bar{c}(\bar{x}, \bar{t}) + J' \sum_i S_i(\bar{t}) \delta(\bar{x} - \bar{x}_i) - \bar{\lambda} \bar{c}(\bar{x}, \bar{t}), \quad (3.119)$$

$$R_-^i = R_-^0 + \bar{\alpha} \bar{c}(\bar{x}_i, \bar{t}). \quad (3.120)$$

Fig. 3.31 shows four equally spaced channels together with the \bar{c} -profile that builds up after a while (for a specific history of channel state flips).

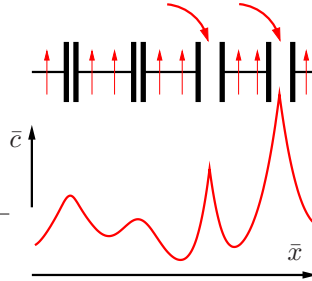


Fig. 3.31: Four equally spaced channels connected to the same one-dimensional compartment together with a snapshot of the \bar{c} -profile after some time and for a specific state of the system.

As before, it is convenient to work with a dimensionless version of these equations. The timescale remains the same as in the single channel case ($t \equiv \bar{t}R_-^0$) and the length scale d is chosen to be based on the diffusion constant \bar{D} :

$$x \equiv \frac{\bar{x}}{d} \quad \text{with} \quad d \equiv \sqrt{\frac{\bar{D}}{R_-^0}}. \quad (3.121)$$

The concentration scale c_0 is therefore altered to

$$c \equiv \frac{\bar{c}}{c_0} \quad \text{with} \quad c_0 \equiv \frac{J'}{R_-^0 d} = \frac{J'}{\sqrt{\bar{D}R_-^0}}. \quad (3.122)$$

¹⁰Later, a spatially heterogeneous stimulus could be introduced that leads to different opening rates for different channels.

The following scaling rules:

$$\begin{aligned}
r_-^0 &= 1, & r_+ &= \frac{R_+}{R_-^0}, & \lambda &= \frac{\bar{\lambda}}{R_-^0}, \\
D &= 1, & J' &= 1, & \alpha &= \frac{\bar{\alpha} \bar{J}'}{\sqrt{\bar{D} R_-^0 R_-^0}}, \\
\frac{\partial}{\partial t} &= \frac{1}{R_-^0} \frac{\partial}{\partial \bar{t}}, & \frac{\partial^2}{\partial x^2} &= \frac{\bar{D}}{R_-^0} \frac{\partial^2}{\partial \bar{x}^2}, & \delta(x - x_i) &= \sqrt{\frac{\bar{D}}{R_-^0}} \delta(\bar{x} - \bar{x}_i),
\end{aligned} \tag{3.123}$$

then lead to the rescaled equations:

$$S_i(t) : \quad 0 \stackrel{r_+}{\rightleftharpoons} 1, \tag{3.124}$$

$$r_-^i$$

$$\frac{\partial}{\partial t} c(x, t) = \frac{\partial^2}{\partial x^2} c(x, t) + \sum_i S_i(t) \delta(x - x_i) - \lambda c(x, t), \tag{3.125}$$

$$r_-^i = 1 + \alpha c(x_i, t). \tag{3.126}$$

As a special case, a one-dimensional lattice of N channels with equal distance a can be considered (N odd). Eq. (3.125) then turns into

$$\frac{\partial}{\partial t} c(x, t) = \frac{\partial^2}{\partial x^2} c(x, t) + \sum_{n=-\frac{1}{2}(N+1)}^{\frac{1}{2}(N-1)} S_n(t) \delta(x - an) - \lambda c(x, t). \tag{3.127}$$

In the limit of $N \rightarrow \infty$ (or using periodic boundary conditions), the solution for c in the steady state will be periodic:

$$c(x) = c(x + a). \tag{3.128}$$

Eq. (3.127) then has to be solved only in the range $0 \leq x \leq a$, with the right boundary conditions. The solution of this is

$$\langle c(x) \rangle = \frac{\langle S \rangle}{2\sqrt{\lambda}} \left(-\frac{1}{1 - e^{\sqrt{\lambda}a}} e^{\sqrt{\lambda}x} + \frac{1}{1 - e^{-\sqrt{\lambda}a}} e^{-\sqrt{\lambda}x} \right), \tag{3.129}$$

with the mean open probability $\langle S \rangle$ of the channels (all channels are equivalent).

Since Eqs. (3.124)–(3.126) are more complex than the 'zero-dimensional' problem of Sec. 3.2, the spatially extended system is only considered using the self-consistent method described in Subsec. 3.4.2.

Eq. (3.125) can be solved generally (similar to Eq. (3.7) in the zero-dimensional case):

$$c(x, t) = \sum_i \int_{-\infty}^t G(x - x_i, t - t') S_i(t') dt', \tag{3.130}$$

with the Green's function for the one-dimensional diffusion process with degradation:

$$G(x, t) = \frac{1}{\sqrt{4\pi t}} e^{-\frac{x^2}{4t} - \lambda t}. \tag{3.131}$$

The further procedure is equivalent to Subsec. 3.4.2. $c(x, t)$ is replaced by a variable $\psi(x, t)$ that is independent of S and has the same statistics as $c(x, t)$. Again, a specific realisation of $\psi(x, t)$ is 'prescribed' to the system and the probability to find the channel at x_i to be open at time t conditioned that it was closed at time t_0 and that $c(x, t)$ evolved

like $\psi(x, t)$ is defined as $P_{01}^i(t_0, t; \{\psi\})$. The master equation for this probability looks very similar to Eq. (3.95):

$$\frac{d}{dt} P_{01}^i = r_+ - (1 + r_+) P_{01}^i - \alpha \psi_i(t) P_{01}^i, \quad (3.132)$$

where $\psi_i(t)$ is $\psi(x, t)$ at the position of the channel i : $\psi_i(t) \equiv \psi(x_i, t)$. This master equation can be solved equivalently to Eq. (3.96). For the evolution of the mean open probability of the channel i , one gets after an expansion around $\alpha = 0$

$$\langle S_i(t) \rangle = r_+ \int_{t_0}^t dt' e^{-(1+r_+)(t-t')} \left(1 - \alpha \int_{t'}^t dt'' \langle \psi_i(t'') \rangle \right) + \mathcal{O}(\alpha^2) \quad (3.133)$$

(cf. Eq. (3.100)).

A self-consistent equation for $\langle S_i(t) \rangle$ now results when all the n -point functions of $\psi(x, t)$ are replaced by the n -point functions of $c(x, t)$ and Eq. (3.130) is used to express those in terms of the n -point functions of $S_i(t)$ (cf. Subsec. 3.4.2). The calculation of the mean values and correlation functions within this approach is the subject of future work.

3.6.2 Further extensions and modifications

Besides the spatial extension of the system as described in Subsec. 3.6.1, one can think of further modifications.

One could, e.g. instead of up-regulating the deactivation rate R_- , down-regulate the activation rate R_+ as a realisation of negative feedback. Depending on the definition of the stimulus, this would certainly alter the dynamical properties of the module. Within the picture developed in this chapter, a down-regulation of R_+ corresponds to a direct switch-off of the stimulus or a desensitisation of A (cf. Fig. 3.3) towards the stimulus. Certainly, such modules can be found in cellular mechanisms.

Switching to purely positive feedback, i.e. a down-regulation of R_- with c or an up-regulation of R_+ with c would lead to a self-amplification of the stimulus and make the system unstable. A stable positive feedback system could be produced by introducing nonlinearities into the model that compensate a linear dependence of the flipping rates on c . A natural way to do this is to make the current through the channel one step 'more realistic', i.e. make J' also c -dependent (cf. footnote on p. 18). The extrusion (or degradation) term of C can also be made more realistic by exchanging the linear term, e.g. by a Hill-type equation. Including nonlinearities into the model will certainly lead to richer dynamical properties, as, e.g. oscillatory solutions.

A central idea of the module-approach towards complex systems is the coupling of several modules such that the output of one module serves as the input of another one. In biology, signal transduction cascades can be viewed as realizations of such a coupling, which will be described in more detail in the following section.

3.7 The module aspect and other systems where this analysis may apply

The system considered in this chapter (and depicted again in the left panel of Fig. 3.32) can be viewed on a more abstract level than the example of an ion channel whose closing rate depends on the concentration of ions that it conducts. The left panel of Fig. 3.32 is an example of a signalling module, an abstract building block of signalling systems found in many more places than just the olfactory cilia. One approach towards the understanding of complex biological systems is to view them as consisting of many connected and in different instances reoccurring modules [64, 104, 162, 166]. A module in that sense is, e.g. a network of chemical species, interacting with each other and performing a specific task, e.g.

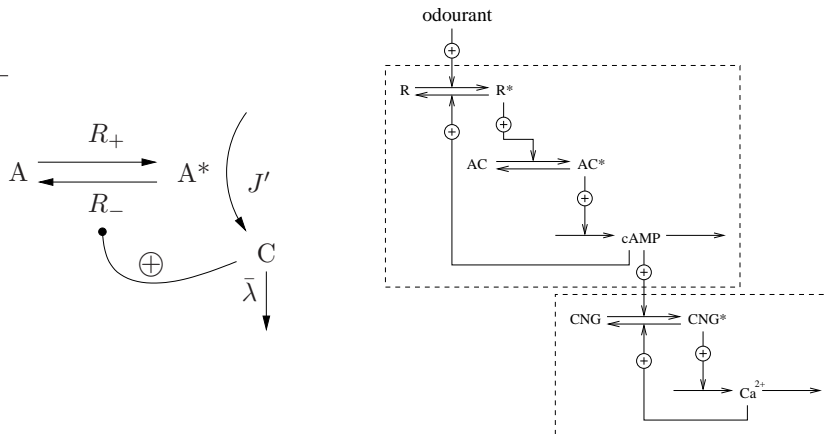


Fig. 3.32: Left: The stochastic signalling module with negative feedback (as already shown in Fig. 3.3). **Right:** A schematic representation of the modularity of signal transduction in olfactory receptor neurons. For a detailed description of the signal transduction as well as the abbreviations, see Subsec. 2.1.1. The lower of the two modules framed with a dashed line is the one treated as an example throughout this chapter. The upper one depicts a negative feedback loop of the second messenger cAMP through a kinase on the receptor. Instead of ion channel opening and closing, the stochastic element in this network is the receptor switching from an inactive into an active conformation.

transducing information from one type into another or providing adaptation mechanisms. What distinguishes a module from a general network is the fact, that a module to some extent can perform its tasks independently of the network that it is embedded in, i.e. the connections to the rest of the network are relatively simple. Ideally, modules are defined to be small enough, such that one has a chance to describe its properties and dynamics in terms of simple dynamical equations or statistical measures. In a larger biological network (as, e.g. a signal transduction pathway, a metabolic network or even a predator-prey network) a module is embedded into other modules and the output of one can be the input of the following. By that, one tries to get an understanding of the dynamics of the whole complex network 'bit by bit', i.e. by understanding each module's dynamics and then connect those. A catalogue of modules (i.e. building blocks) can be established [104], which might lead to a more intuitive understanding of some complex networks.

The modular approach lies somewhat in between strict bottom-up and top-down approaches. An analogy can to some extent be seen in electronics [64] (or engineering [34]): For the understanding of the important properties and the usual operating ranges of an integrated circuit (IC), one basically needs to know the input/output properties of the logical gates, the IC is built from. Depending on desired detailedness of the description of the dynamics of an IC, one might go one step deeper and look at the properties of the transistors, resistors and capacitors of which the logical gates consist. But one would hardly go into describing single electron dynamics or the detailed properties of the metals and semiconductors used in order to understand the whole system IC.

Looking at the module treated in this chapter (left panel of Fig. 3.32) from that perspective, further biological systems are obvious candidates where a description in terms of such a module might be successful:

1. Enzyme dynamics: 'A' is an enzyme (a large protein) that stochastically switches between an inactive and an activated form. Usually, this transition involves a conformational change of the protein very much the same way as a transmembrane ion channel changes conformation when switching between the open and the closed state. In the activated state A*, the enzyme catalyses a specific reactions which leads to the production of the chemical C. A very common [1] motif found in biochemical

regulation is that of feedback inhibition, where the accumulation of chemical C (or a subsequent molecule in the reaction cascade) leads to deactivation of the enzyme A. This deactivation can be seen as an up-regulation of the rate R_- .

An example from the olfactory signal transduction pathway discussed in the present work is the enzyme adenylate cyclase (AC) whose catalytic activity is down-regulated by an increase in calcium (through calmodulin and a kinase – see Subsec. 2.1.1 and Fig. 2.2)¹¹.

2. Transcription: 'A' could also be a gene that is stochastically 'switched on' by certain promoters. In the active state, the gene is transcribed and its mRNA produced. After translation, the protein C (or some molecule whose production is catalysed by C) for which the gene A coded, can act as a repressor on the transcription. An example is the operon in E.coli that codes for enzymes synthesising the amino acid tryptophan. If tryptophan is abundant in the cell, it binds to a protein, the tryptophan repressor, which shuts down the transcription of the operon [1].

Using the module depicted in the left panel of Fig. 3.32 for this kind of transcription would be a very coarse description since many steps in between are omitted. For the same reason, this would come closest to biology for prokaryotes, since there, the number of intermediate steps is smaller and the time scale between transcribing a gene and producing the respective protein is generally faster¹².

If one assumes the dynamics of the conformational change of the receptor to be similar to the dynamics of enzymes, one can identify another feedback module in the olfactory signal transduction (already described in Subsec. 2.1.1). The right panel of Fig. 3.32 shows this module as well as the one described in detail in this chapter. This is also an example of how modules can be connected with each other and how a larger reaction network can be decomposed into modules.

3.8 Summary

Motivated by a specific negative feedback loop identified in chapter 2 to be of great importance for the dynamics of the olfactory signal transduction, in this chapter, an abstract stochastic two-state signalling system with negative feedback was analysed in more general terms. In the olfactory transduction it is, e.g. realised by an ion channel that switches randomly between an open and a closed state. Negative feedback is provided by a closing rate of the channel that increases with the concentration of the conducted ion. The aim of the analysis was the characterisation of this system in terms of statistical quantities such as the mean values, correlation functions and the response functions and by that investigate the influence of both the intrinsic noise and the feedback on the signalling properties of the module.

Three different analytical approaches were applied to accomplish this task. A powerful but computationally involved path-integral method provided results for all the relevant quantities in the limit of weak feedback. Since both auto-correlation functions and response functions were obtained, it was possible to show that this specific system violates the fluctuation dissipation theorem. Setting up a master equation for the system, results for the mean values were obtained that hold for the whole parameter range, including strong feedback where the perturbative path-integral technique is difficult to use. The results from both these techniques agree in the limit of weak feedback. As a third method, a self-consistent calculation was presented, that can be seen as an extension of a mean field

¹¹Another example is the regulation of the enzyme ATCase by a product of the reaction cascade whose initial reaction it catalyses [156].

¹²In eukaryotes, the mRNA first has to be transferred from the nucleus to the ribosomes in the cytosol, whereas in prokaryotes both transcription and translation take place close to each other within the cytosol.

method. Due to this fact, the self-consistent method is only valid in specific parameter ranges, however the computational effort in the self-consistent approach is much smaller compared to the path-integral method. Also, the calculation of higher order terms in the expansion in feedback strength proves to be much less involved. This is the reason, why the self-consistent method is the most promising one for possible extensions of the system such as introducing a spatial dimension and diffusion or the coupling of a number of these modules to form a signal transduction cascade. Different to common methods of treating stochastic systems where noise is put in as an esemble property 'by hand' (e.g. Langevin equations [154]), in all of the analytical approaches described here, the intrinsic noise and its effects were derived from the dynamics of the system itself.

In order to compare the results from the three different method to each other and to check their validity within parameter space, careful and extended numerical simulations were conducted in the regime of weak feedback. For stronger influence of the feedback on the dynamics of the system, the simulations provide so far the only way to fully characterise the system. The feedback was found to have both positive and negative effects on the signalling properties of this specific module, depending on stimulus strength and parameters of the system. Parameter regimes were found in which strong feedback decreases the coefficient of variation. Generally, feedback increases the reception range of the module and it was found (by analysing the linear response function) that a module with strong feedback transfers the shape of a stimulus pulse more reliably. The correlation functions qualitatively change when feedback is included but an oscillatory behaviour (as, e.g. in chapter 2) has not been observed.

In the end, the stochastic two-state signalling module investigated in this chapter was put into a broader perspective and described in a more general context. Examples from other systems of cell biology were listed, where (variants of) this specific module are at work or might be found. The idea behind a modular (rather than a molecular) viewpoint on complex biological networks was explained. It constitutes one of the three theoretical approaches to complex biological systems used in the present dissertation. In the conclusions in chapter 5, the modular approach will be compared to the other two.

The path-integral method as well as some of the numerical data can also be found in [61].

Chapter 4

Axon Guidance in the Development of the Olfactory System

4.1 The olfactory map – a remarkable example of pattern formation

As already mentioned in Sec. 1.2, the axons of the few millions (in mice) olfactory receptor neurons (ORNs) connect to the glomeruli of the olfactory bulb (OB) in such a way that in each glomerulus only axons of one specific type of ORN (expressing a specific olfactory receptor (OR)) terminate. In Fig. 4.1, all the ORNs (including their axons) expressing a specific type of OR are labelled with a dye. The convergence is nicely seen for three different types of ORNs. In principle, figures like the three shown in Fig. 4.1 can be



Fig. 4.1: Convergence of axons of the ORNs on their way from the olfactory epithelium (OE) towards the olfactory bulb (OB). The three figures show the olfactory turbinates and the OB in mice heads (cf. left panel of Fig. 1.1), where ORNs (including their axons) expressing a specific type of receptor were labelled with a dye (ORs M71, P4 and P2; modified from [47]). The scale bar in the right figure is 0.5mm.

obtained for each of the ~ 1000 different types of ORNs. An overlay of these figures would give a full coverage of the surface of the OB, producing the mosaic-like pictures as in the left panel of Fig. 1.5 where the axons of all ORNs were labelled at the same time.

Through genetic labelling techniques it has been found out that the discrete spatial map generated on the surface of the OB is approximately the same in all animals of a given species. If a specific ORN is genetically labelled with a dye, and figures as the ones in Fig. 4.1 are analysed in different, e.g. mice, the respective glomerulus gathering all the axons of this type of ORN is always found within a region of roughly 30 glomeruli. When staining more than one type of ORN simultaneously with different dyes, it is found

that neither absolute nor relative positions of glomeruli seem to be conserved on the scale of a few diameters of glomeruli. Fig. 4.2 is a schematic drawing of the outcome of these experiments. On a coarse scale, the activity patterns as shown in Fig. 1.6 (and depicting

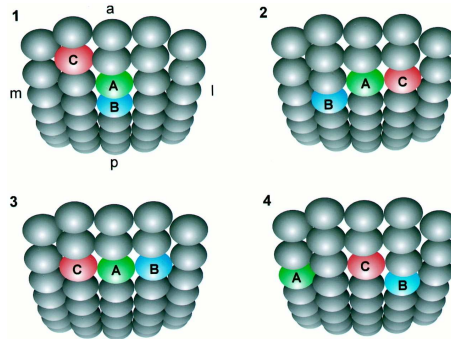


Fig. 4.2: Schematic drawing of the positions of three glomeruli (for three different ORs A,B,C) on a small part of the surface of the OBs of four different mice (from [143]). Absolute and relative positions of the glomeruli vary within a region of ~ 30 glomeruli [107].

the spatial map) are therefore the same for all animals of a given species. These patterns can be obtained and catalogued for many different odourants and in principle, one can tell what the animal smells by merely looking at the spatiotemporal activity pattern of its OB (or antennal lobe in insects [51]) and matching it with an entry of the catalogue (e.g [57]). The patterns are roughly the same on the two (left and right, cf. right panel of Fig. 1.5) OBs of an animal. Each OB possesses a symmetry plane itself, which divides it into two symmetrical half-bulbs (roughly lateral and medial). Most ORN types connect to one glomerulus in each half-bulb but there are some, for which connections to only one glomerulus per bulb are found [143]. The total number of glomeruli in one bulb (~ 1800 in mouse) is therefore a little less than twice the number of functioning OR genes (~ 1000 in mouse).

In mouse and rat, the ORNs that express a specific type of OR appear to be randomly distributed (spatially) on one of four different zones in the olfactory epithelium (OE) within the nasal cavity [127]¹. The same zones can be identified on the surface of the OB, meaning that if one looks only at the ORNs of one zone in the OE, one finds a closely packed region of corresponding glomeruli on the OB. These zones on the OB (each containing approximately 200 glomeruli) are much bigger than the scale of inter-animal variation of position of glomeruli (regions of ~ 30 glomeruli).

Not much is known about the mechanisms governing this remarkable pattern formation process during the development of the olfactory system, neither experimentally nor from a theoretical viewpoint. The two main questions that have to be answered in order to get a deeper understanding of this process are:

1. How do axons of the same type find each other, form bundles and accomplish the sorting within initially heterogeneous bundles?
2. How is the spatial map formed on the surface of the OB and which mechanisms lead to the specific properties of this map?

From the variety of different experiments conducted mostly within the last ten years, the picture emerges that these two questions are strongly connected and possible answers go beyond more simple neural pattern formation mechanisms found in other regions of the brain. In the following section, more experimental findings will be explained within the scope of possible mechanisms, partly known to contribute to similar ordering tasks

¹Recent studies [105] suggest a graded pattern rather than discrete zones.

in other neural systems. After that, theoretical concepts will be introduced, trying to capture the important features of these mechanisms. They are implemented in a number of numerical studies, focusing on the effects of guidance cues, axon-axon interactions and neural turnover.

4.2 The biology of the formation of the olfactory map

4.2.1 How axons grow

During axonal growth, at the further most end – the tip –, the axon extends and forms a structure called the growth cone (Fig. 4.3). This is the region, where the axon grows (is elongated) and determines the direction of growth due to the steady polymerisation of actin and microtubules [99]. At the same time, the growth cone is a sensing unit for its surrounding. Its membrane contains specific receptors that are able to sense concentration differences of external chemicals across the size of the growth cone as well as possible structures (e.g. other axons) in its vicinity, if it hits it.

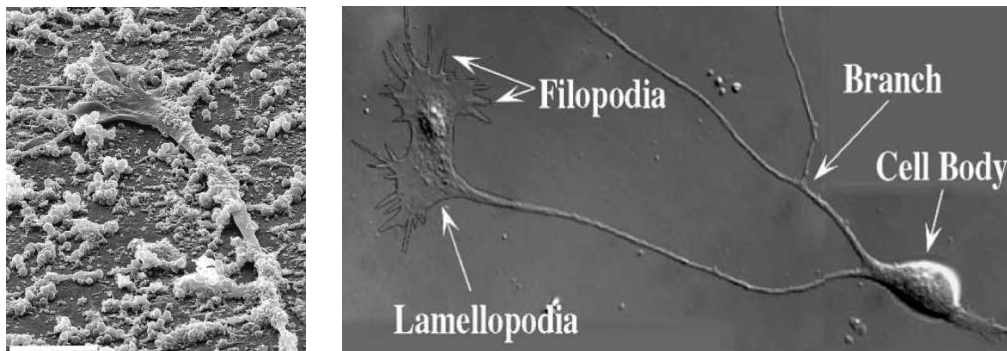


Fig. 4.3: Growth cones from sensory neurons on surfaces. **Left:** Scanning electron microscopic image (from [128]); scale bar: $5\mu\text{m}$. **Right:** Composite micrograph of a chick sensory neuron (from [99]). Branching is not observed in the axons of ORNs.

The axonal growth cone is very dynamic. It not only grows in one direction but it also changes shape constantly. Membrane protrusions are constantly formed, grow out of the growth cone, sense the environment, and either retreat back into the growth cone or steer the whole axon in its direction².

4.2.2 Chemical guidance cues

Axonal growth in many instances is known to be directed by concentration gradients of specific chemicals that act as ligands for receptors on the cell membrane of axonal growth cones. The reaction of the growth cone to these chemical guidance cues can be either attractive (it grows up the concentration gradient) or repulsive (it grows down the concentration gradient). The molecules acting as ligands can be both freely diffusing or fixed to a substrate or membrane [147]. Other forms of cues are also known, e.g. permissive cues [72] that tell the axon to grow or to stop, depending on concentration.

A prominent example for chemical guidance cues at work is the Eph/ephrine system operating during the formation of the retinotectal projection [94] (the neural map of the visual sense). Here, axons coming from nerve cells in the retina have to find their correct position in the target site (of the brain, the tectum opticum). Using (among other techniques) *in vitro* stripe-assays from different regions of the tectum opticum and letting the axons grow on these substrates, a family of membrane-bound receptor/ligand pairs could

²A movie showing this behaviour can be found at [66].

be found, that are expressed on the axons (with a concentration dependent on where they stem from) as well as the target tissue (in a spatially graded manner). This family of receptor tyrosine kinases ('Ephs') and their ligands ('ephrines'), appears also in other regions of the nervous system and stages of development. The exact mechanism of patterning in the retinotectal system is not yet completely understood, but one plausible hypotheses motivated by the law of mass action is, that axons with a given expression level $[R]$ of receptor find the target sites with a ligand concentration $[L]$ such that the product of both reaches some threshold value S that is the same in all axons: $[R][L] = S$.

Whereas in the visual system the formation of the neural map seems to be explainable in terms of simple chemical guidance cues, this process appears to be more complicated in the olfactory system. There is evidence for guidance cues in the olfactory bulb [80] but no conclusive experiment so far could show a similar simple rule as in the retinotectal projection. Instead of 'classical' cues (as, e.g. the Eph/ephrine's), olfactory receptors (rather than Eph receptors) play a vital role in establishing the olfactory map [109]. ORs are not only expressed on the cilia of the ORNs but also on their growth cones [4]. This finding immediately suggests that each axon 'smells' its way towards the correct position on the OB, however, such a simple picture seems unlikely, since a large number of guidance cues would be needed to operate as ligands for the ORs. Until now, there is no experimental evidence for this. Also, it is not clear in which way ORs influence the formation of the map, since genetically altered mice deficient of the most common signal transduction channel connected to the OR (as described in chapter 2) still develop an almost perfect neural map [91, 168]³. In insects, ORs do not influence the axon targeting [80].

A possibility to resolve the problem of the large number of graded guidance cues is the type-specific reaction towards a smaller number of graded cues. A cue can be either specific for one specific type of axon or there can be one cue that is differently interpreted by different types of axons. Assuming an attractive cue such that the axons always grow up the concentration gradient, all axons that react to this cue would always end up at one point, the point of highest concentration of the cue chemical, probably near the source of the cue. By that, no spatial map can be generated (neglecting spatial exclusion and possible different arrival times of the axons at the point of highest concentration). For that – using these simple rules – ~ 2000 different cue chemicals would be needed on the two-dimensional surface of the olfactory bulb in order to correctly guide the ~ 1000 different types of axons. A more probable mechanism of guidance would be a type-specific 'interpretation' of concentration gradients of a small number of cue chemicals [54]. One possible way of how to guide axons towards a specific position with only two guidance cues in two dimension is the incorporation of the internal processing of these two cues. The interaction between the cue and the axons has to be mediated through some kind of receptor-ligand internal signal transduction mechanism. Experiments (see above) suggest, that this can not be the cAMP-mediated transduction as described in chapter 2. Since nothing further is known, a very simple description of a typical signal transduction mechanism is adopted: a second order inhibitory kinetics [54]. The two graded cues would in that case be transduced into a 'cell-internal cue' $p(x, y)$, where the parameters α and β are specific for a given receptor (axon type):

$$p(x, y) = \frac{\alpha f(x)}{1 + (\alpha f(x))^2} + \frac{\beta g(y)}{1 + (\beta g(y))^2}. \quad (4.1)$$

Fig. 4.4 illustrates the effect of this internal processing for different parameters α, β , i.e. axon species.

If now the axon uses its 'internal cue' $p(x, y)$ to adjust its direction of growth (towards increasing 'internal concentration') and each axon type uses a specific set $\{\alpha, \beta\}$, the formation of a map is possible.

³The receptor could still transduce its information through other signal transduction channels (e.g. through the one involving IP_3 (see Sec. 2.1)).

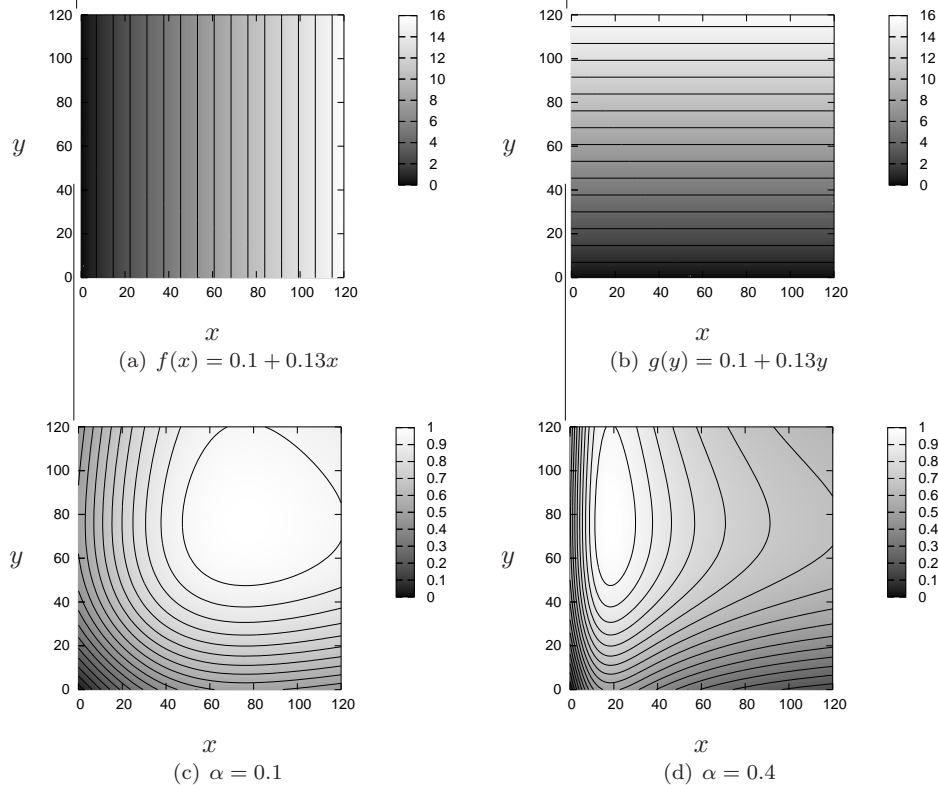


Fig. 4.4: A two-dimensional cue consisting of $f(x)$ (a) and $g(y)$ (b) and what two axons with different internal processing of this cue ($\beta = 0.1$, $\alpha = 0.1$ (c) and $\alpha = 0.4$ (d)) make out of it in terms of a 'cell-internal cue' $p(x, y)$ (Eq. (4.1); arbitrary units).

There are different sources of noise in this scheme of chemical guidance through internal processing. The guiding molecule numbers might be very low, such that temporal and spatial fluctuations across the length of a growth cone become too large to reliably measure a gradient on a sufficiently short time scale [7]. Other sources certainly lie within the internal processing of the external cue. The preceding chapter 3 showed that noise can play an important role in signal transduction.

In Sec. 4.3, possible realisations of axon-cue interaction are introduced and numerically investigated. The typical response of a growing axon to a cue is bending or turning. In the left panel of Fig. 4.5 single axons are shown near to a glomerulus. The goal of a more detailed analysis in Subsec. 4.3.2 is to reproduce such single trajectories and to check, whether an internal processing as described above is feasible.

4.2.3 Axon-axon interactions

When inspecting figures like Fig. 4.1 more closely and with a higher magnification, axons are often found to grow in bundles or fascicles of many axons (see also left panel of Fig. 4.5). Electronic micrographs of sections through the olfactory nerve show that within these bundles, axons are usually densely packed and the membranes of the axons attach to each other (right panel of Fig. 4.5). By staining axons of different types of ORNs with different colours, homotypic (consisting of a single type of axons) and heterotypic (consisting of more than one type) bundles were found.

It is a quite common property of axons (also in other systems) to grow along or together with other axons. For the olfactory system, experimental studies [47, 79] are available that

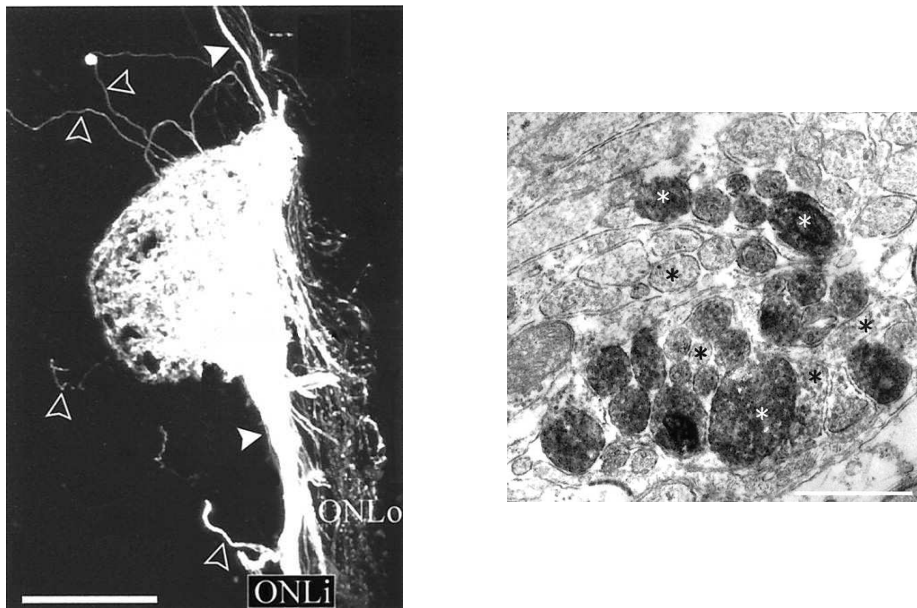


Fig. 4.5: **Left:** Stained axons of a specific type of ORNs near the respective glomerulus in the OB of an adult mouse. Single axons can be seen winding through the glomerular layer (*open arrowheads*) and olfactory nerve layer (ONL). Most axons, however, are fasciculated (*white arrowheads*). Scale bar is $50\mu\text{m}$ (modified from [153]). **Right:** Section through the inner olfactory nerve layer (which can be seen as a part of the OB). Axons of a specific type of ORNs are labelled (*white asterisks*) but others can be identified, too (*black asterisks*). Scale bar is $0.5\mu\text{m}$ (from [153]).

show the importance of axon-axon interactions for the correct formation of the neural map. These interactions are found to act between axons of the same type (homotypic) but also specific interactions between axons of different types can be concluded⁴.

Similar to the reaction of an axonal growth cone towards a chemical guidance cue, there is a quite straightforward picture of the microscopic mechanism leading to axons growing in bundles. In the membrane of axons, including their shafts, proteins are embedded that can serve as ligands for receptors in the membrane of growth cones of other axons. If now one of the filopodia of an axonal growth cone (Fig. 4.3) by chance hits the growth cone or the shaft of another axon, receptors on the one membrane might interact with ligands on the other, leading to a signalling event that can influence the direction of growth and steer the axon towards and along the other axon. Since the axonal growth cone is very dynamic, there is also a chance of detaching again from the other axon, e.g. if at some time point all filopodia of the growth cone extend in the direction away from the other axon.

An important concept connected to axon-axon interactions is that of the pioneering or pathfinding axons. If one axon starts growing (e.g. up a chemical guidance cue) earlier or faster than others, other axons might grow along this pioneering one rather than interpreting the chemical guidance cue by themselves. This can lead to more efficient targeting but it clearly increases the danger of all axons being mistargeted if just the first one made mistakes in the interpretation of the guidance cue.

In Sec. 4.3, axon-axon interactions will be implemented into numerical studies in different ways. Simple attachment/detachment rules will be set up as well as axon-axon interactions implemented by effective inter-axon forces or interaction energies between axons.

⁴In the experiments [47, 79], genetical modification of one type of ORN altered the targeting of a few other types of ORNs.

4.2.4 Axon turnover

The formation of the olfactory map already starts before birth. In mouse, the axons need a few days [139] to grow all the way from the nasal epithelium towards the OB. A remarkable property of the ORNs is, that there is a constant turnover of neurons during the whole life time of the animal. The average life time of an ORN (in mouse) lies in the range of 30–60 days [72] (in humans 2–6 months [67]). After that, the neuron dies but the total number of ORNs is roughly constant, since new ORNs are constantly generated by the basal cells in the olfactory epithelium.

In a recent study [169], the 'purity' of the glomeruli on the surface of the OB was studied during development of the animal. It has been found out, that the first map to be formed (roughly 10 days after birth) still contains some miswirings, meaning that ORNs that express a specific OR project not only to one ('their') glomerulus but a number of ORNs of this type also terminate in other glomeruli. During further development and after the first 1–2 generations of ORNs have died and have been renewed, this connectivity pattern gets sharpened and miswirings become less frequent. In Fig. 4.6, one of the results of this study [169] is plotted, namely the average number of glomeruli to which a specific type of ORN projects.

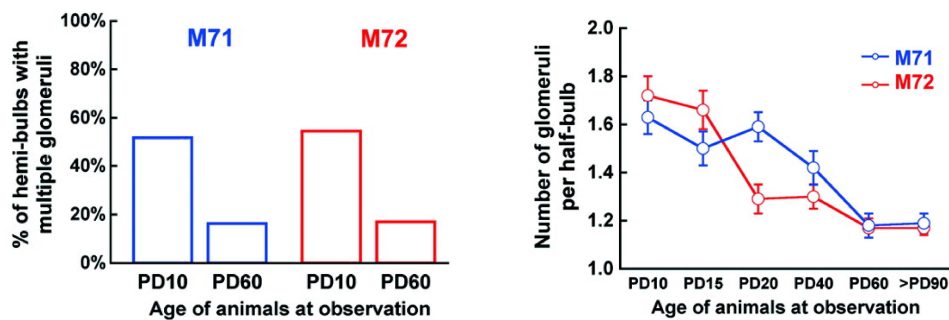


Fig. 4.6: **Left:** Percentage of animals in which two specific types of ORNs (expressing either the receptor M71 or M72) connect to more than one glomerulus in a half-bulb each (cf. Sec. 4.1). **Right:** Number of glomeruli per half-bulb to which the axons of the respective ORNs connect over time. 'PD' means postnatal day and is the age of the animal in days after birth (both figures modified from [169]).

In connection to axon-axon interactions as described in the preceding subsection, one can think of the axon turnover as a mechanism to refine the olfactory map. Assuming, e.g. a noisy guidance cue to which the first generation of axons reacts and forms a first, partly miswired neural map, the axons of later generations find already established paths along which they can grow. If the first map to be established already is quite good in terms of correct targeting (say, 90% of the axons connect to the correct glomerulus and the other 10% connect to glomeruli of different types), newborn ORNs have a much higher probability to grow their axons along the correctly connected axons of the mature ORNs (assuming random distribution of newborn ORNs in the epithelium). Due to axon turnover, the miswired ORNs will slowly die out and therefore it is just a question of time, that a refined neural map emerges. This effect can certainly be greatly enhanced, e.g. by a correct targeting increasing the life time of an ORN and miswiring letting them die earlier.

Axon turnover is implemented in one of the numerical investigations described in the following section. Its effect on the targeting and interplay with the axon-axon interaction will be examined.

4.2.5 Other possible mechanisms

The role neural activity plays in forming or sharpening the olfactory map remains unclear. There is evidence that at least correlated neural activity is not needed for a coarse formation of the map [91] but is needed for the 'fine-tuning' [169]. Other experiments suggest that spontaneous activity of the neurons is needed [167]. A theoretical model exists [152] that is solely based on neural activity but its applicability for the explanation of the formation of the olfactory map might be limited due to the stated experimental facts.

An important question to be asked is, whether the olfactory map is really established by the advancing axons of the ORNs or if it is formed 'from the other side', i.e. by the secondary neurons present in the olfactory bulb. In insects, e.g., the dendrites of the secondary neurons are located in the correct position even before the axons of the ORNs have reached the antennal lobe. Assuming an early structure on the OB, a guidance (possibly without graded cues) appears more likely since parts of the glomeruli would be already present, telling the respective axons where to grow. As in most of the effects described in this section, experiments in vertebrates are not fully conclusive. Axon sorting and convergence seems to be independent of the tissue [140] through which axons grow, i.e. axons of the same type find each other even if the OB was removed. However, spatial organisation on the level of mitral cells might be important also in mice [80].

4.3 Theoretical approaches to axon sorting and guidance

The preceding two sections describing the biology of the formation of the neural map in the olfactory system underscored the complexity of this biological pattern formation process. Experimental results suggest that the interplay of a few different mechanisms is needed for the correct formation of the map during the development of the animal. Theoretical considerations might help testing hypotheses of the biologists, gain deeper understanding of the processes and answering the two main questions as stated at the end of Sec. 4.1.

In this section, different aspects of the pattern formation process are investigated using numerical simulations ('in silico' experiments). Three main models are presented that focus on the different mechanisms as described in Sec. 4.2.

In the preliminary study presented in Subsec. 4.3.1, emphasis is put on the sorting of axons due to axon-axon interactions. Since the sorting of different types of axons can be seen in an abstract way as a phase separation problem, a well-studied system from statistical physics is used for the implementation, the Potts model. The effects of a simple realisation of a guidance cue are studied, as well. Due to the adopted geometry, the obtained results of this simple model are difficult to relate to the full pattern formation process of the biological system, nevertheless they might be relevant for specific aspects of it.

Subsec. 4.3.2 stays closer to biology by modelling the movement of single axons in a more realistic way. The focus in this subsection is put on chemical guidance of axons with axon-axon interactions put in in a very simple way as a modification. The main results here are axon trajectories that can be compared to pictures from single axon paths as seen in experiment. Only small numbers of axons are considered in this approach and due to two spatial dimensions being treated as a continuum, an upscaling to high numbers of axons becomes computationally ineffective.

In the last Subsec. 4.3.3, the same geometry as in the preceding model is used with the spatial variables discretised. This model comes closest to a simulation of the whole biological pattern formation and studies with high numbers of axons can be conducted. Single axons are simulated as interacting directed random walks with a specific life time. The focus lies on the axon-axon interactions as well as axon turnover leading to a refinement

of the neural map. The results can be related to experimental findings and the relatively easy structure of this model makes it possible to start analytical considerations regarding sorting and bundling.

4.3.1 Axon sorting through interacting growth cones – a generalised Potts model

The sorting of axons during growth, i.e. the transition from a random, mixed configuration of axons to a configuration where axons of the same type attach to each other and separate from different types, can be accomplished by different means. An external cue can guide axons individually to type-specific fixed position or homotypic axon-axon interactions can provide the sorting. In the simplest versions of the latter case, no conserved map will be formed, rather, after bundles of axon types have sorted out, their positions will still vary in time. Both mechanisms will be investigated in this subsection, using a well-studied system from statistical physics, the Potts model [164]. By that, axon sorting becomes related to the general problem of phase separation (e.g. [14, 35]). A similar but spatially continuous model based on the same geometry introduced below, is described in Appendix C.1.

Geometry

For a first study of axon sorting, in this subsection, a severe simplification regarding the geometry of the setup is made. All axons start at the same time and grow with the same speed. Their growth cones are all situated in one two-dimensional layer and form one advancing front in which they are able to move, interact with other growth cones and sense a possible guidance cue. They can only react to it by a change of growth direction in the x - z -plane (Fig. 4.7). Due to all axons advancing together in the y -direction, axon turnover cannot be considered within this framework. Fig. 4.7 illustrates the respective geometry.

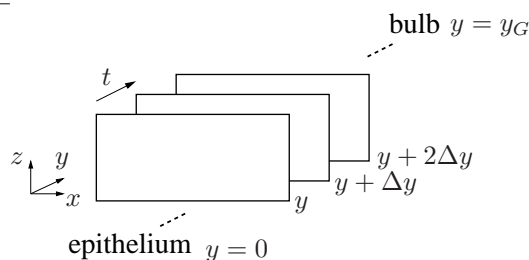


Fig. 4.7: Illustration of the geometry of the system where all axonal growth cones grow in one advancing two-dimensional plane.

$N = \sum_{i=1}^M n_i$ axons of M different types start randomly distributed on a sheet at $y = 0$. In each time step of the simulation the whole front moves one step Δy in the y -direction towards the future position of the glomeruli at $y = y_G$. Within such a time step, each axon can interact with other axons and/or can respond to a guidance cue established by a gradient towards the according position of the future glomerulus.

Axon-axon interactions and guidance cues

Adopting the picture described in Subsec. 4.2.3, an axon interacts with other axons in its neighbourhood through the filopodia of its growth cone. Especially if there are many other axons around, the filopodia will hit more than one neighbouring axon and instead of attaching to a single (probably the nearest) one, in the model used in this subsection, it will grow along an intermediate path in between, the path of highest attraction according to the neighbouring axons. This type of interaction can be implemented, e.g. by assigning

an effective interaction energy to each neighbouring axon. The axon then tries to grow along a path of minimal energy.

If space in x and z is discretised, i.e. the axons move on a lattice, their dynamics can be described in terms of a Potts model [164], a generalisation of the Ising model. Simply speaking, the Potts model is an Ising model for spins that can exist in $N > 2$ different states. The different species of axons are represented by the different spin states and since the number of different axons should be conserved, the number of spins in each state (the 'magnetisation') should be constant. One can define an interaction energy between different states (species) and a 'temperature' that represents the random movement of the growth cones. A guidance cue can be implemented by introducing a (y -dependent) potential, to which the axons react, e.g. as described in Subsec. 4.2.2. One time step corresponds to an advancement of the front by one step Δy in the y -direction⁵. Axons should not disappear, so the elementary dynamical step is a spin exchange (Kawasaki kinetics) rather than a (Glauber) spin flip [26].

An effective interaction energy is assigned to neighbouring pairs of axons. If neighbouring axons are of the same type i , the homotypic interaction energy is E_{hom}^i , if they are from different types i and j , the interaction contributes a heterotypic energy E_{het}^{ij} . In what is commonly referred to as the Potts model, all $E_{\text{het}} = 0$. In the simulations presented further down, only one value for each the homo- and the heterotypic interaction energy is used:

$$E_{\text{hom}}^i \equiv E_{\text{hom}}; \quad E_{\text{het}}^{ij} \equiv E_{\text{het}} \quad \forall i, j. \quad (4.2)$$

In this special case, the interaction Hamiltonian of the system can be written as

$$\mathcal{H} = - \sum_{\langle ij \rangle} (E_{\text{het}} + (E_{\text{hom}} - E_{\text{het}}) \delta_{S_i S_j}), \quad (4.3)$$

where $\langle ij \rangle$ means that lattice points i and j are nearest neighbours and $\delta_{S_i S_j}$ is the Kronecker-delta that is only nonzero if the type S_i of the axon at position i is equal to the type S_j of the axon at the position j .

A Metropolis algorithm is used in the numerical simulation: A neighbouring pair of axons is chosen randomly and its effective interaction energy $E_{\text{int}}^{\text{before}}$ within the neighbours of both axons is calculated. Then, the two axons are exchanged with each other and the interaction energy is calculated again (which gives $E_{\text{int}}^{\text{after}}$). If the system energy after the axon exchange is lower or equal than before ($\Delta E = E_{\text{int}}^{\text{after}} - E_{\text{int}}^{\text{before}} \leq 0$), the latter configuration is kept. If it is higher ($\Delta E > 0$), the new configuration is kept with the probability $p = \exp(-\frac{\Delta E}{T})$, where T is a parameter of the simulation that in the case of spins can be referred to as the effective temperature. A pseudo-random number (random number generator `ran2` from [117]) is drawn in the latter case, upon which the decision for keeping the new configuration is made.

N^2 of these elementary steps (attempts) give one Monte Carlo time step (corresponding to an advancement of Δy), where N is the number of lattice points of the square lattice. Periodic boundary conditions are used.

Guidance cues can be put into the model by introducing spatially dependent potentials, such that the overall effective energies for calculating the energy differences upon axon exchange are altered:

$$E^{\text{before/after}} = E_{\text{int}}^{\text{before/after}} + E_{\text{pot}}^{\text{before/after}}. \quad (4.4)$$

E_{pot} can either be one out of many type-specific potentials (as realised later in this subsection) or it can be the result of a type-specific interpretation of a two-dimensional potential as introduced in Subsec. 4.2.2.

⁵A maximal bending angle of the axons could be introduced by allowing the axons to make only a limited number of steps in the x - z -plane during one step in the y -direction (one Monte-Carlo time step).

The model as described above is commonly called Potts model, if no spatial potential is used and the Hamiltonian of the system reads

$$\mathcal{H}_{\text{Potts}} = -E_{\text{hom}} \sum_{\langle ij \rangle} \delta_{S_i S_j}. \quad (4.5)$$

In the following, results will be presented using this 'common' Potts model (analysed also in [35]). After that, it will be generalised by introducing spatial potentials to which the axons react as well as heterotypic interactions using the Hamiltonian from Eq. (4.3).

Results

Fig. 4.8 shows the time evolution of a lattice of 64×64 sites with periodic boundaries, occupied fully by each 1024 axons of four different species. Parameters used are $E_{\text{het}} = 0$; $E_{\text{hom}} = 1$; $T = 0.77$ and there are no guidance potentials ('common' Potts model). The initial configuration was generated randomly. If the parameter T (the 'temperature')

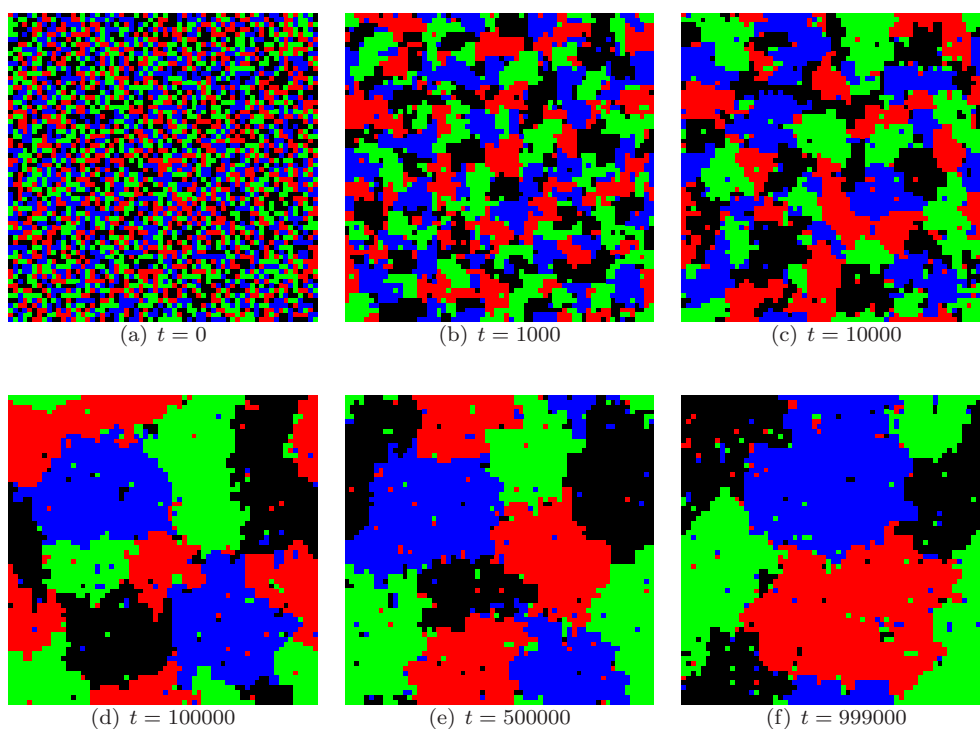


Fig. 4.8: The Potts model for 4 species on a fully occupied 64×64 grid at different times (x - z -plane (cf. Fig. 4.7) for $T = 0.77$ and $E_{\text{hom}} = 1$). Different colours depict different axon species. Very good sorting is observed at late times (note the periodic boundaries in both x and z).

is chosen within the right range (as it is done here), sorting ('bundling') is seen and after a sufficient number of time steps, one can observe what would be called almost perfect wiring in the context of the olfactory system. If one chooses T to be too high, the fluctuations of the system are too high to speak of 'good wiring', if T is too small, the time for the system to find its energetically lowest state increases and the system might get stuck in some local energy minimum that it is very unlikely to escape.

Fig. 4.9 tries to convey this effect of the 'temperature' T . The same system (same size, parameters and initial distribution) as in Fig. 4.8 was simulated using three different values for T . Shown are the configuration after 999000 time steps, a time, where the two systems with $T = 0.5$ and 0.77 are in a relatively stable steady state. The critical temperature for

the Potts model with q states is $(k_B = 1) T_c = \frac{E_{\text{hom}}}{\ln(1+\sqrt{q})}$ [35], i.e. for the case presented in Fig. 4.9, $T_c \approx 0.91$.

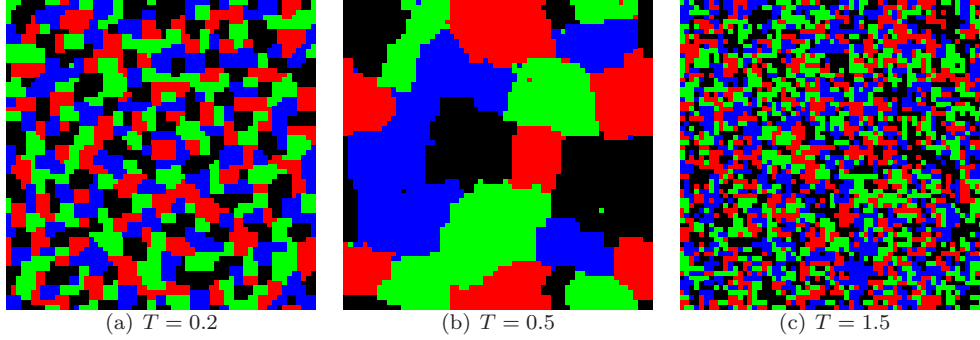


Fig. 4.9: The same system as in Fig. 4.8 after 999000 time steps simulated with the three different values for the temperature $T = 0.2; 0.5; 1.5$. The critical temperature for this system is $T_c \approx 0.91$.

Sorting of axons is observed in this model within specific parameter ranges (see Fig. C.5 in appendix C.2.1 for simulations with varying initial configurations), but for the generation of a spatial map with the same axon species appearing at the same position (independent of fluctuations and initial configurations), spatial symmetry has to be broken by some ingredient. This is easiest done by generalising the Potts model through the introduction of potentials that are specific for axon species (see further up in this subsection). In the simulations for Fig. 4.10, four potentials were included, and each axon felt its potential with the same space-dependent strength $E_{\text{pot}}(r) = -\frac{E_{\text{pot}}^0}{r}$ with $r = \sqrt{(x_A - x_G^i)^2 + (z_A - z_G^i)^2}$ ((x_A, z_A) is the position of the axon, and (x_G^i, z_G^i) the minimum of the respective potential – the future position of the glomerulus; periodic boundaries such that $0 \leq (x_A - x_G^i) \leq \frac{L}{2}$ and $0 \leq (z_A - z_G^i) \leq \frac{L}{2}$ with L being the linear size of the system). Now, the axons of a given type form a bundle at a conserved position independent of the initial configuration (not shown).

The Potts model can also be used for not fully occupied lattices, simply by treating vacancies as another spin state with effective interaction energy zero. Fig. 4.11 shows configurations at the late time $t = 999000$ for simulations with an axon occupancy of 50%, i.e. four species with each 512 axons on a 64×64 grid. Fig. 4.11(a) is the outcome of a diluted Potts model with $E_{\text{hom}} = 1$, in Fig. 4.11(b), the interaction energy between different types of axons is set to $E_{\text{het}} = 0.3$, which can be called a generalised Potts model. The heterotypic interaction leads to the attachment of bundles of different types.

There are a few analytical results available [164] for the thermal equilibrium state, but the more species are considered (and for a full simulation of the olfactory system this would be in the range of a few hundreds with each ~ 1000 axons), the less likely the system gets close to thermal equilibrium within reasonable simulation time. With more species it will be more likely trapped in local energy minima. To prevent this in numerical simulations and to reach equilibrium states in reasonable times, often specific techniques (as, e.g. the Monte Carlo renormalisation group [35]) are used. In the biological system, however, it is unlikely that the final connectivity pattern is close to a thermal equilibrium state and that the system could reach that solely by random fluctuations.

Due to the specific geometry (Fig. 4.7) used within this subsection (and in appendix C.1), the model lacks an important ingredient from the biological system, namely the fact that axonal growth cones are not restricted to one front in which they move. In reality, axons start growing at different times and are able to interact not only with the growth cones of other axons but with the full axons (including the shafts). In the model setup of this subsection, important concepts as, e.g. pioneering axons cannot be realised.

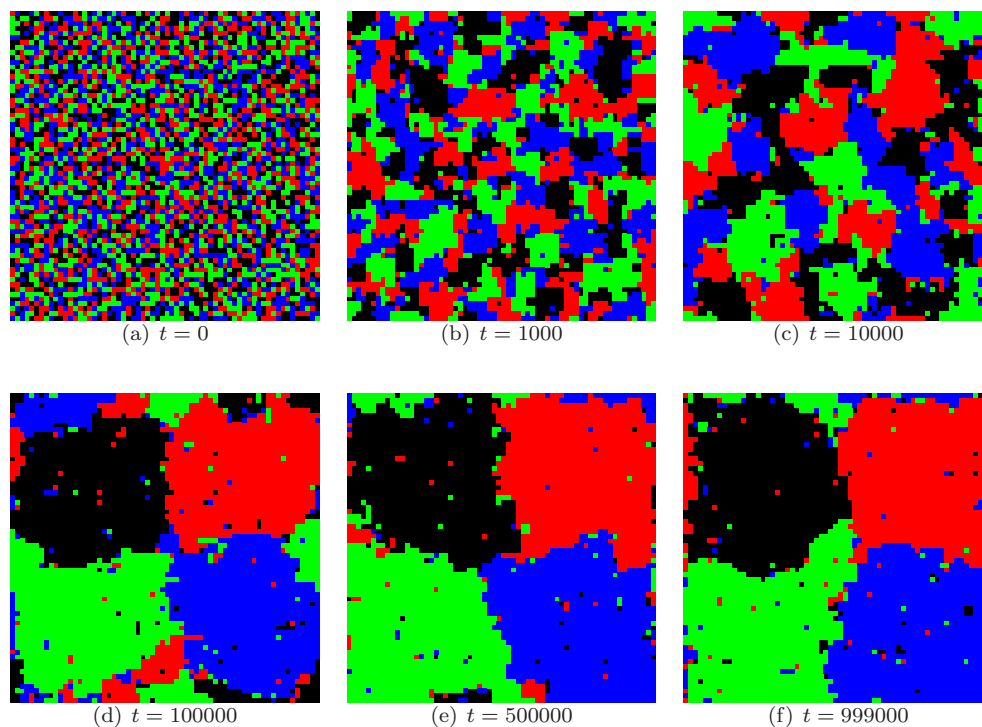


Fig. 4.10: The Potts model extended by four axon-type-specific potentials ($E_{\text{pot}}^0 = 1.5$) at different instants of time. The initial distribution is the same as in Fig. 4.8. The minima of the potentials are $(x_G^1, z_G^1) = (16, 16)$; $(x_G^2, z_G^2) = (16, 48)$; $(x_G^3, z_G^3) = (48, 16)$; $(x_G^4, z_G^4) = (48, 48)$ (grid size 64×64).

Also, axon turnover, i.e. removing of axons and putting in new ones cannot be naturally implemented. These facts make it difficult to interpret the obtained results in terms of the pattern formation process of the biological system. However, restricted applicability might be given in specific regions or stages of the development of the map, e.g. during the first stages, when a number of axons grow approximately at the same time into not occupied area.

In the following two subsections, another, more realistic geometry of the system will be used for the simulations. This will allow for both interactions between growth cones and shafts as well as the implementation of axon turnover.

4.3.2 Detailed model of the turning of axons in response to guidance cues

Whereas single axon paths produced by the preceding model lack some features of experimentally observed ones (e.g. loops as in the left panel of Fig. 4.5), the aim of this subsection is the simulation of more realistic single axon trajectories. For that, an idealised growth cone is introduced. Being a little bit more detailed than in [53] (for another model see [132]), here, the turning radius R of the axon depends on the concentration difference across the size of the growth cone⁶. For simplicity, axonal growth takes place on a two-dimensional sheet (x - y -plane – the flattened surface of the olfactory bulb (cf.

⁶The microscopic picture of this is a signalling apparatus on the membrane of the growth cone that transduces external concentrations into internal gradients of specific signalling molecules. These gradients then influence the polymerisation and depolymerisation of actin filaments and microtubules which steers the axonal growth.

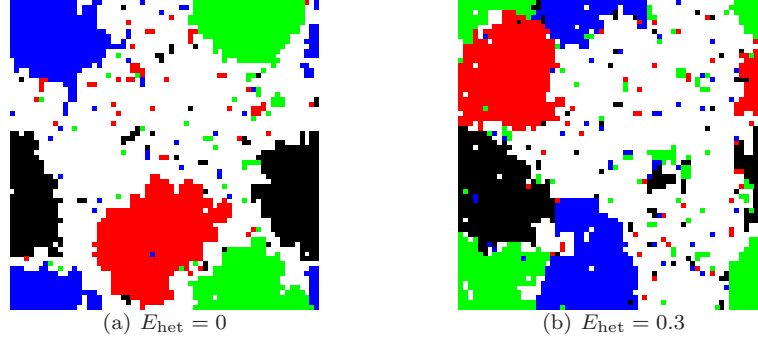


Fig. 4.11: The diluted Potts model (**left**) and the generalised Potts model (**right**) for an occupancy level of 50%. Configurations at $t = 999000$ with $E_{\text{hom}} = 1$ and periodic boundaries.

Fig. 4.7)) with a constant step size $\Delta L = \sqrt{\Delta x^2 + \Delta y^2}$ each time step Δt . At the tip of the growing axon (the growth cone), two 'sensing units' are extended in a distance L_c perpendicular to the momentary direction of growth⁷ (Fig. 4.12), where the concentration of the cue is measured. The positions of the points of guidance cue evaluation are (Fig. 4.12)

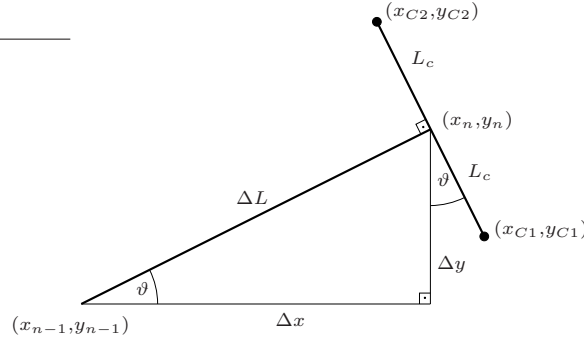


Fig. 4.12: The positions of the sensing points $C1$ and $C2$ with respect to the momentary (n) and former ($n - 1$) growth cone positions (idealised growth cone).

$$\begin{aligned} x_{C1} &= x_n + L_c \sin \vartheta, & y_{C1} &= y_n - L_c \cos \vartheta, \\ x_{C2} &= x_n - L_c \sin \vartheta, & y_{C2} &= y_n + L_c \cos \vartheta, \end{aligned} \quad (4.6)$$

with

$$\tan \vartheta = \frac{\Delta y}{\Delta x}, \quad (4.7)$$

where Δx and Δy represent the advancement of the growth cone during the previous time step.

At the sensing points $C1$ and $C2$, the guidance cue is measured (evaluated) to be c_{C1} and c_{C2} , respectively. To account for fluctuations in the distribution of guidance molecules and stochastic effects in the transduction of the cue, a random term is added to the concentrations c_{C1} and c_{C2} :

$$c'_{C1} = c_{C1} + f\sqrt{c_{C1}}a, \quad c'_{C2} = c_{C2} + f\sqrt{c_{C2}}a. \quad (4.8)$$

a is drawn from a set of equally distributed pseudo-random numbers between -0.5 and 0.5 everytime, a concentration is measured (random number generator `ran1` from [117]). The

⁷Since the step size ΔL of the axon is kept fixed, concentration differences in the direction of growth do not have to be considered.

difference between these two 'noisy' concentrations determines the radius R of turning. Since not much is known experimentally about this dependence, the following very simple relation is used:

$$R = \frac{R_0}{c'_{C1} - c'_{C2}}. \quad (4.9)$$

If the concentration difference is zero, the turning radius for the next step is infinity, i.e. the axon follows a straight path. A minimal turning radius can be accomplished by limiting the steepness of the gradient of the guidance cue in such a way that the possible concentration differences across the distance $2L_c$ is bounded from above.

The new position of the growth cone using the constant growth rate ΔL and the radius R from Eq. (4.9) is then calculated by (see Fig. 4.13)

$$\begin{aligned} x_{n+1} &= x_n + \Delta L \cos \left(\vartheta - \frac{\pi}{2} + \arccos \left(\frac{\Delta L}{2R} \right) \right), \\ y_{n+1} &= y_n + \Delta L \sin \left(\vartheta - \frac{\pi}{2} + \arccos \left(\frac{\Delta L}{2R} \right) \right). \end{aligned} \quad (4.10)$$

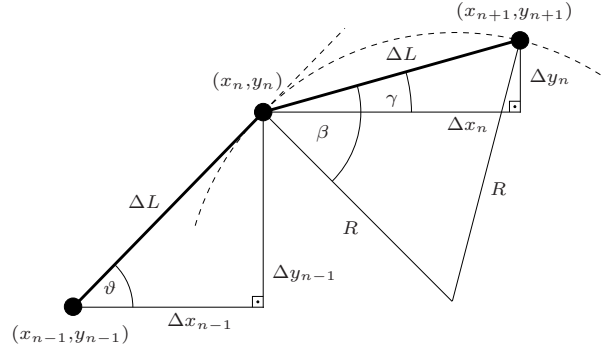


Fig. 4.13: New position (x_{n+1}, y_{n+1}) of the growth cone, if the axon turns with the radius R . Eqs. (4.10) are obtained using $\gamma = \vartheta - \frac{\pi}{2} + \beta$ and $\cos \beta = \frac{\Delta L}{2R}$.

As a proof of principle, Fig. 4.14 shows typical axon trajectories generated with the rules stated above. The axons all start at the same time, vertically aligned at $y = 0$ and during growth are allowed to cross each other.

A noticeable difference in the growth patterns of the red and blue axons in Fig. 4.14 is due to the different 'internal cues' that the two different types use for guidance. For the red axons ($\alpha = 0.1$, Fig. 4.4(c)), the internal cue is approximately symmetrical around its maximum in the region considered, which leads to relatively straight paths (except the loop in the right panel of Fig. 4.14). The internal cue of the blue axons ($\alpha = 0.4$, Fig. 4.4(d)), however, is very steep for small values of x and shallower for high values of x . This leads to the big bend the blue axons take when starting at high values of x . Since all axons start at the same time and have the same speed of growth, usually, the axons growing along straight paths reach the final position earlier than the ones that develop curved trajectories.

The results of this detailed modelling could be quantified in terms of

1. typical turning radii,
2. typical shapes of axon paths,
3. typical fluctuations in the direction of growth.

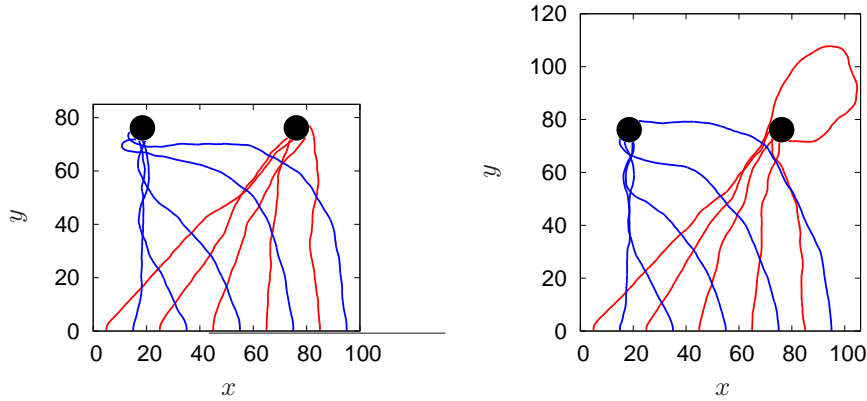


Fig. 4.14: Typical axon trajectories for the two two-dimensional cues depicted in Fig. 4.4. $L_c = 0.2$, $R_0 = 0.005$, $\Delta L = 0.1$, $f = 0.008$. The axons stop growing, if they come into a distance smaller or equal 5 to their respective glomerulus. The two figures are results for different sets of pseudo-random numbers (a similar figure can be found in [54]).

A comparison to experimentally obtained figures (e.g. left panel of Fig. 4.5) could then give reasonable ranges for the parameter values used in this model. By that, it could be tested if the assumptions made within this approach (the way the cue is interpreted, the relation between cue and turning radius, the way fluctuations are included) are sufficient to capture the relevant properties of a growing axon. Of particular interest for such a comparison are the big bends of the blue axons or the loop, one of the red axons forms in the right panel of Fig. 4.14 after it missed the glomerulus in the first attempt. Such loops are often observed in experimental figures with single axon resolution (left panel of Fig. 4.5 or figures in [46, 47, 116, 153, 155]).

Axon-axon interactions

Axon-axon interactions can easily be implemented in this model. In the simplest version, axonal growth cones have a certain circular area (radius L_c) that they explore. If the growth cone of an axon of type i finds another axon (growth cone or shaft) within this area, it will stick to it (it gets 'pinned' to the other axon) and from then on will grow along this axon. If the second axon is of the same type i , this 'pinning' is assumed to be irreversible. If the second axon is of different type j , in each time step, there is a probability p_{stay} that they stay together, otherwise the axon will detach and make a step according to the gradient that it senses⁸. Fig. C.6 in appendix C.2.2 shows a simplified version of the flowchart of the algorithm.

In Fig. 4.15, two examples of realizations of this algorithm are shown, where the same 2D-gradient of the guidance cue was used as in the example without axon-axon interaction above (Fig. 4.14). The probability $p_{\text{stay}} = 0.8$ (time step $\Delta t = 1$) to stay with an axon of a different type leads to short intervals of heterotypic bundling. Due to the homotypic interaction, the blue axon starting at the smallest x -value serves as a pathfinding axon for three other blue axons. This is the one that reaches the glomerulus first and grows almost in a straight line. The other axons attach to it and simply grow along. For the red axons, this is seen only for high y -values and it becomes clear that irreversible bundling can have positive and negative effects on the directness of the connections, depending only on the first trajectory formed by the pioneering axon. Assuming that axons generally stop growing whenever they hit a glomerulus, no matter if it is the correct one or the one belonging to another type, this implementation can certainly lead to miswiring, i.e. axons

⁸In order to escape the 'pinning', i.e. move out of the sensing region of the other axon, this gradient guided step is chosen to be four times the normal step size.

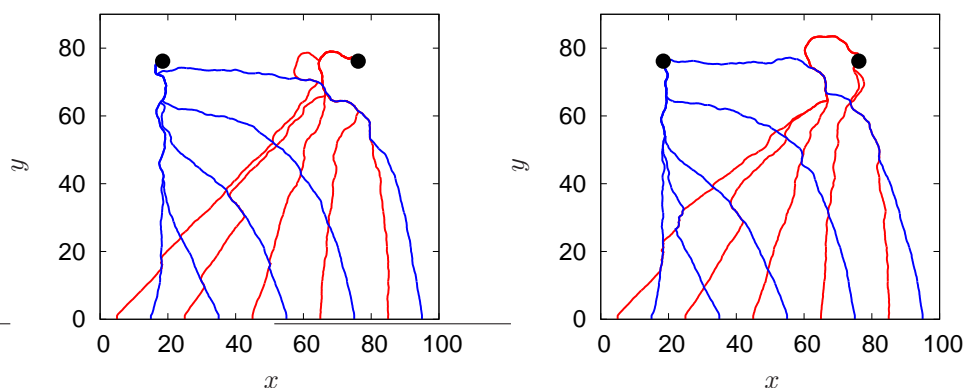


Fig. 4.15: Two examples for a system with axon-axon interactions and a two dimensional cue as shown in Fig. 4.4. Starting positions and parameters are the same as in Fig. 4.14, except $R_0 = 0.001$ and less fluctuations in the reading of the cue ($f = 0.005$). $p_{\text{stay}} = 0.8$. The two figures are results for different sets of pseudo-random numbers. The blue lines are plotted on top of the red ones, covering them within bundles. The algorithm prevents attachment of an axon to itself or to a bundle containing itself.

connecting to glomeruli of a different type. The biggest influence on the extent of miswiring has the parameter p_{stay} (in combination with Δt) but, e.g. the steepness of the guidance cue and the configurations of axons play a role, too. Heterotypic bundling can, however, contribute to a reliable map formation. Axons of one type might, e.g. meet each other in a bundle consisting mainly of axons of another type and from then on grow together. Since typically, less axons have to navigate very close to the glomerulus if bundling is allowed, the probability of 'unusual' excursions of axons (e.g. loops as in Fig. 4.14) becomes smaller compared to the case without bundling.

A big disadvantage of this algorithm is the search of the vicinity of each free axonal growth cone in each time step. Since no grid is used and since axonal growth cones can attach to all parts of all axons (including the shaft), for each search, the distances between the growth cone and all positions of all axons have to be calculated and compared to L_c (in the simplest possible algorithm). This needs a lot of computer time. The system introduced in the following subsection uses the same geometry but works much more efficiently by letting the axons grow on a grid.

4.3.3 Advancing axons as interacting directed random walks

In this last model of the development of the olfactory map, the influence of axon turnover is investigated. As in the preceding subsection, axons grow on a two-dimensional x - y -plane and are able to interact with each other. Different to the last model, here, axons grow on a lattice, which has big advantages concerning computing time. Axons are simulated as interacting directed random walks with turnover, i.e. each random walker has a given life time after which it dies and is replaced by a new one. Assuming the impossibility of synaptic rearrangements in the olfactory bulb, axon turnover is the only possible explanation of the experimental data presented in Fig. 4.6. A chemical guidance cue (as, e.g. described in Subsec. 4.2.2) is not implemented here yet for reasons of simplicity. The model described in the following is the one coming closest to a simulation of the whole pattern formation process in the olfactory system. It produces results that are qualitatively comparable to experimental observations while the assumptions being used are abstract enough to start analytical considerations.

Model

The axons grow on a tilted grid (Fig. 4.16), where in each time step, each axon grows one step in the y -direction and one step in the x -direction. The geometry used is the same

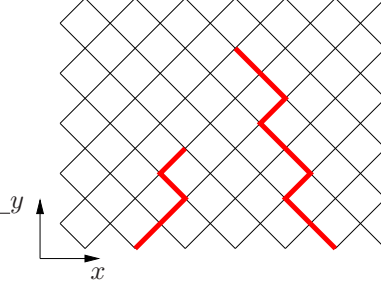


Fig. 4.16: A tilted quadratic grid with two axons growing in y -direction.

as in Subsec. 4.3.2 but since the axons can move only in the positive y -direction, axon paths will certainly look different as in the detailed model of Subsec. 4.3.2 (e.g. loops as in the right panel of Fig. 4.14 are not possible, here). The decision, if the tip of the axon moves one step to the left or to the right is made based on probabilities depending on the occupation on its future lattice position and its neighbourhood. Fig. 4.17 shows different possibilities of defining these neighbourhoods. If an axon of the same type is found on any

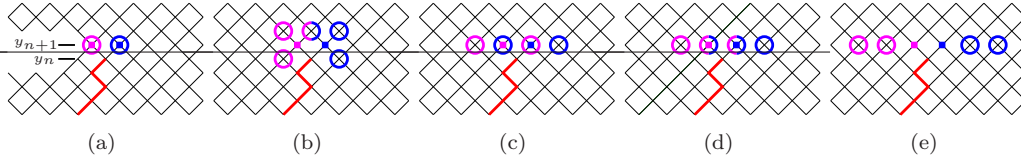


Fig. 4.17: Different ways of defining the neighbourhoods of a growth cone at y_n on the tilted grid. The two squares give the possible future positions at y_{n+1} (magenta – left, blue – right). The circles with the respective colour are the sites that the axon can interact with when growing to the left (magenta) or right (blue). (a) only the occupation of the possible future positions is considered; (b) nearest neighbours in two dimensions; (c) nearest neighbours at y_{n+1} ; (d) nearest neighbours and possible future position at y_{n+1} ; (e) nearest and next nearest neighbours at y_{n+1} only in one direction. (a) and (b) fail to follow a zig-zagging axon.

of the neighbouring positions (as defined in Fig. 4.17), an effective energy $E_{l/r} = E_{\text{hom}}$ is assigned to the left (l) or right (r) future position. If only an axon of a different type is found, the respective energy is $E_{l/r} = E_{\text{het}}$. Based on these energies, the probability for the axon to grow to the left/right is calculated as (cf. to the Potts model in Subsec. 4.3.1)

$$p_{l/r} = \frac{e^{-E_{l/r}}}{e^{-E_l} + e^{-E_r}}. \quad (4.11)$$

A pseudo-random number (random number generator `ran2` from [117]) then decides if the axon grows to the left or the right and before proceeding with the next axon, this one is moved to its new position ($x_{n+1} = x_n \pm 1, y_{n+1} = y_n + 1$). If $E_l = E_r$, e.g. for a pioneering axon without neighbours or for an axon that moves in a thick bundle, $p_{l/r} = 0.5$, i.e. the axon randomly 'diffuses' in x . Other ways of calculating the effective energies E_l and E_r might be designed, e.g. by making them proportional to the number of axons in the left/right neighbourhood.

The choice of the sites that are considered neighbours (i.e. that the axon interacts with – Fig. 4.17) strongly influences the shape of axon paths and the bundling properties of the model. An axon should certainly be able to follow another axon, independent of the shape

of the path of the pioneering one. The choices of interacting sites as given in Figs. 4.17(a) and 4.17(b) are only able to follow axons that grow straight (e.g. $x_{n+1} = x_n + 1 \forall n$) but lose the pioneering axon if it changes direction of growth (the extreme case is a zig-zagging pioneering axon that changes from left to right in every time step). Since lattice occupations greater than one are allowed (axons can cross each other and grow on top of each other), a too narrow definition of interacting sites can lead to very thin (in the y -direction, but 'high') bundles, which is difficult to relate to the biological system. Also, since the total area that is covered with axons decreases rapidly through this process, single axons that are still present at these high y values need an unrealistic long time to hit a bundle. Here, an effective 'penalty energy' E_{pen} is introduced, that is added to $E_{l/r}$, whenever an axon grows on an already occupied site⁹. Axons then prefer to stay on the margins of a bundle and therefore contribute to its extension in x .

In principle, also in this model, a guidance cue could be easily implemented. For reasons of simplicity, however, it is not done here. Therefore, only statements about sorting and bundling can be made, but none about positions of bundles.

Axons are inserted into the lattice at $y = 0$ (random x) with a certain rate. The first axon to grow therefore makes an one-dimensional random walk (in x), since there are no other axons yet to interact. Each axon has a specific life time, after which it dies and is completely removed from the system. The life time can be the same for all axons or it can be drawn from a Gaussian distribution of life times with mean $\langle T_{\text{life}} \rangle$ and standard deviation $\sigma_{T_{\text{life}}}$ ¹⁰. After the removal of the complete path of the axon, a new one of random type is put at a random x -position at $y = 0$ and starts growing, following the same rules of growth and interaction as described above.

The average life time of an axon is chosen following the biological system (cf. Subsec. 4.2.4). Since axons need a few days to grow all the way from the epithelium towards the bulb and since the average life time of the neurons is around 30–60 days, in the model, the average (or half-) life time is chosen to be ten times longer than the time, the axons need to travel the whole y -distance. After having reached the end position in y , the axons stay there until they die.

Results

Fig. 4.18 shows typical axon configurations for 100 axons from a single species (periodic boundaries in x) after $7.2 \cdot 10^6$ time steps for three different effective interaction energies E_{hom} . The relation between the extensions L_x and L_y of the system are chosen in such a way that a free and unbiased (in x) random walker typically explores a region of $\frac{L_x}{2}$ during its growth from $y = 0$ to $y = L_y$ ($L_y = (\frac{L_x}{2})^2$). Axons are inserted at $y = 0$ with the constant rate of one axon each 4000 time steps and after a life time (assigned to each axon with its birth; $\langle T_{\text{life}} \rangle = 4 \cdot 10^5$ and $\sigma_{T_{\text{life}}} = 4 \cdot 10^4$) are removed again. For this simulation, as well as for all the following, axons interact with the nearest neighbours on the same y_{n+1} of their future position as well as the future position itself (Fig. 4.17(d)). Fig. C.7 in appendix C.2.3 shows the time evolution of the configuration in Fig. 4.18(b) with $E_{\text{hom}} = -4.5$.

Depending on the absolute value of E_{hom} , different degrees of bundling are observed. The small absolute value of $E_{\text{hom}} = -2$ apparently is not enough to reliably form bundles. From Eq. (4.11), one can estimate the average number of 'false decisions' (i.e. moving away) an axon makes when growing along another axon or along the margin of a bundle (e.g. $E_l = E_{\text{hom}}$ and $E_r = 0$) during the 40000 time steps it needs to grow the whole distance. For $E_{\text{hom}} = -10$, this number is approximately 1.8. Almost no stray axons are therefore observed in Fig. 4.18(c). ~ 440 false decisions in the case with $E_{\text{hom}} = -4.5$

⁹Other solutions would be a space-narrowing towards high values of y , or the implementation of a general guidance cue attracting all axons towards a point at some high y -value.

¹⁰Any other distribution for the life times is also possible, e.g. an exponential one with half-life $T_{\frac{1}{2}}$.

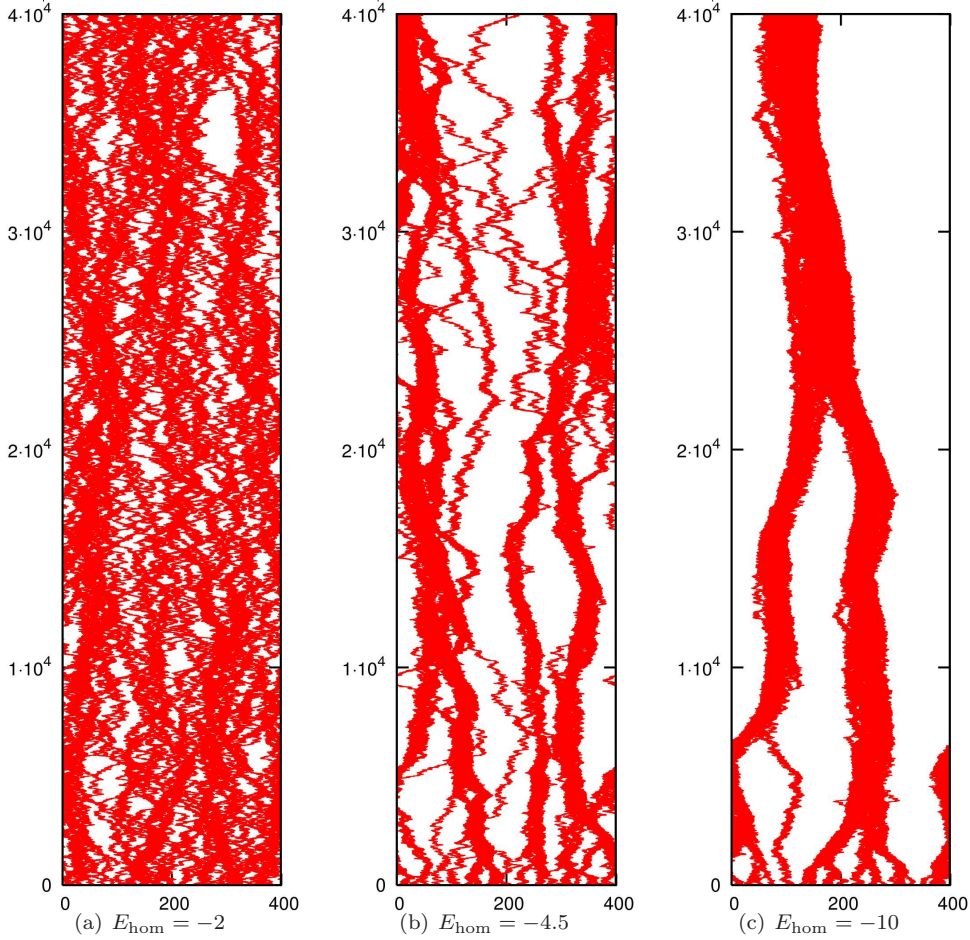


Fig. 4.18: Axon configurations obtained by simulating axonal growth as interacting directed random walks with three different effective interaction energies E_{hom} . x is plotted horizontally, y vertically and periodic boundaries are used in x . A single species with 100 axons is simulated and the figures represent snapshots of the dynamics at the late time $t = 7.2 \cdot 10^6$. The life times of the axons are Gaussian distributed with $\langle T_{\text{life}} \rangle = 4 \cdot 10^5$ and $\sigma_{T_{\text{life}}} = 4 \cdot 10^4$, and there was no 'penalty' energy E_{pen} in these cases. Fig. C.7 shows the time evolution of (b).

lead to quite a few bundle splittings and single axons wandering around and ~ 4800 ($E_{\text{hom}} = -2$), i.e. a 'debundling' every ~ 9 time steps, clearly is too much to form bundles.

In order to analyse the results more quantitatively, measures have to be found that capture the important features of the configurations and at the same time can be related to experiments on the biological system. One of these measures is the number of bundles at a given time t and position y . The definition of a bundle is to some extent subjective¹¹. Here, the configurations are coarse grained (over an x -window of 15 and y -window of 100) and the density of axons is calculated. Using a threshold value (larger than one axon per site), the number of bundles can then be counted. Fig. 4.19 shows these for the three coupling strengths used in Fig. 4.18.

For the weak interaction with $E_{\text{hom}} = -2$, there are strong fluctuations and already visual inspection of Fig. 4.18(a) suggests that it is difficult to define and count bundles here. With the definition used above, an increase in the number of bundles is observed

¹¹One has to decide, e.g. about a minimal distance between two bundles to be counted as two and not one.

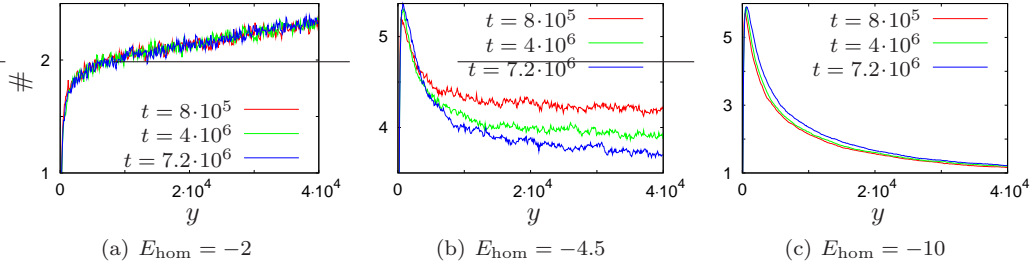


Fig. 4.19: The number of bundles (see text for details) plotted over y for different effective interaction energies E_{hom} and three different times each. $\langle T_{\text{life}} \rangle = 4 \cdot 10^5$, $\sigma_{T_{\text{life}}} = 4 \cdot 10^4$. The curves are averages over 1000 runs with independent sets of pseudo-random numbers. The subjectivity related to the definition of a bundle brings in that at very small y , no bundles are found (single axons are not counted as a bundle).

with growing y and during time evolution, no change is observed (Fig. 4.19(a)). When the effective interaction energy grows in absolute value, a decrease of number of bundles is observed both in y and in time (Fig. 4.19(b)). Both effects are also seen in experiments (for the temporal decrease, see, e.g. Fig. 4.6) so this looks like a reasonable parameter region. However, by numerical investigation, no set of parameters was found that would show a reduction of number of bundles in time and at the same time end in just a single bundle at high y and late t (cf. Fig. 4.6). Within these simulations, temporal decrease of the number of bundles always ended in 3–4 bundles at high y , even for very long runs. A further increase in interaction strength destroys the effect of temporal decrease in bundle numbers (Fig. 4.19(c)). Simulations usually end up in just a single bundle at high y (cf. Fig. 4.18(c)) but over time, the number of bundles stays constant or even increases slightly. One reason for the increase of number of bundles in time is the splitting of bundles due to the removal of axons that were growing roughly at the same time (and therefore die roughly at the same time, leaving back two separate bundles). Fig. 4.20 illustrates this effect with an example.

To study the effect of heterotypic interactions (between different types of axons), simulations were conducted using the same parameters as before but now with each 50 axons from two different types. Fig. 4.21(a) shows the decrease of the number of bundles of one type with both y and time if there is no heterotypic interaction (cf. to Fig. 4.19(b)). Putting in an effective interaction energy of $E_{\text{het}} = -2$ between the two types of axons increases the effect of reduction of bundle numbers over time (Fig. 4.21(b)). This, again, resembles qualitatively the experimental results from Fig. 4.6, however, since only bundles of one of the two types of axons were counted, a ‘purifying’ of bundles over time can not be observed and most probably does not happen. The nonzero heterotypic interaction energy probably just leads to bundles of different types growing together in larger heterogeneous bundles, however, there probably again is some optimal value of heterotypic interaction that enhances bundling and sorting.

As an illustration of the applicability of this model for higher numbers of different types of axons, Fig. 4.22 shows the time evolution of four different types with 25 axons each. The interaction strengths E_{hom} and E_{het} were chosen such that nice pictures with observable bundling are obtained. In order to get thicker bundles and weaken the tendency of bundles growing on top of each other, the ‘penalty’ energy was set to $E_{\text{pen}} = 0.5$. Fig. 4.22 shows a few qualitative features that are commonly observed in simulations with more than one type of axons. During time evolution, thick bundles tend to straighten especially for high y -values (see, e.g. the thick red bundle at $x \approx 350$). Another observation is, that bundles of different types that grew intermingled at early times, de-mix over time (e.g. the thick green and magenta bundles between $y \approx 2.1 \cdot 10^4$ and $3.5 \cdot 10^4$). It is obvious that it

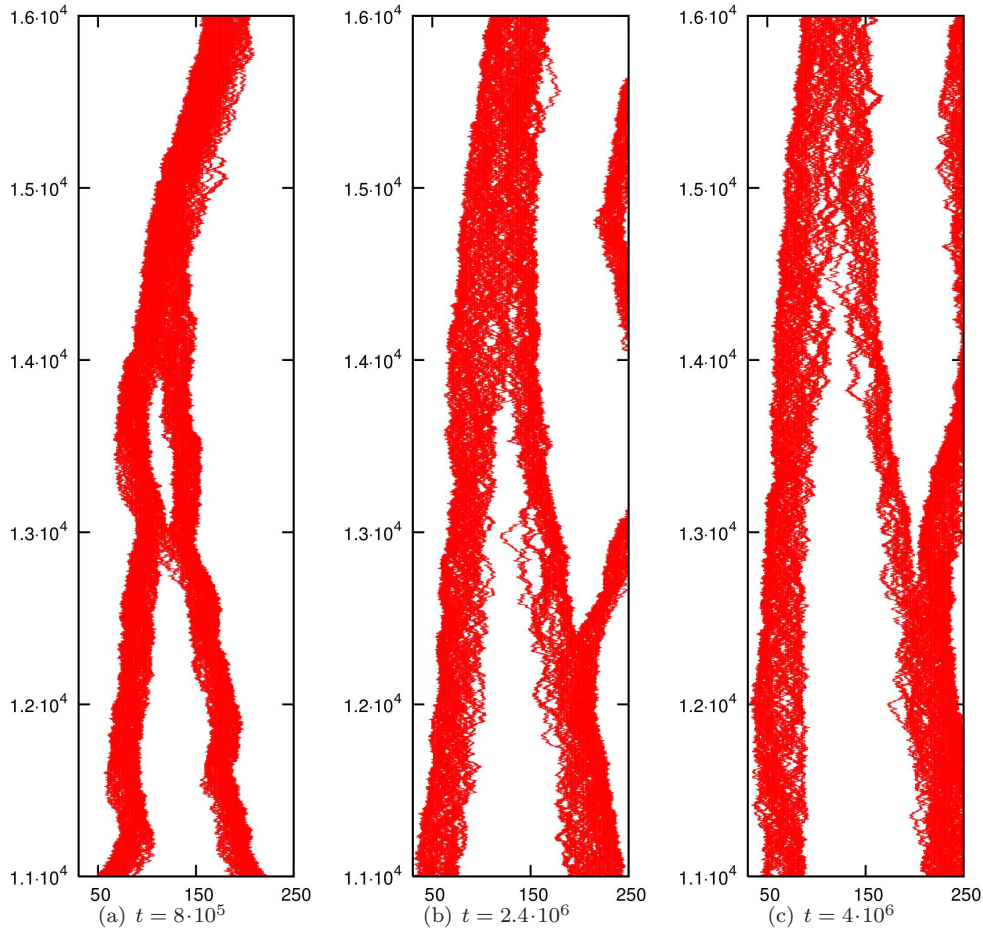


Fig. 4.20: The advancement (in y) of a splitting slit in a bundle due to the death and removal of several axons that grew roughly at the same time. Shown is the time evolution of a section of the simulation leading to the configuration in Fig. 4.18(c). The end of the slit moves upwards from $y \approx 1.4 \cdot 10^4$ to $y \approx 1.48 \cdot 10^4$. As another effect, this figures show the branching of a bundle due to a stray axon.

becomes increasingly difficult to describe the results quantitatively the more axon types and possible interaction between them are introduced.

Based on relatively simple rules and being quite close to the biological problem in terms of, e.g. geometry, the description of growing axons as interacting directed random walks on a grid is able to at least qualitatively capture some of the biological features of the pattern formation process during the development of the olfactory neural map. However, an analysis of the many differing set-ups of the model as well as a full characterisation based solely on numerical investigations seems ineffective. The goal, therefore, should be an analytical description of maybe even more simplified models, whose result then again serve as starting points of more detailed numerical work¹². Starting with a description (in terms of a zero-range process [44]) of a further simplified model, preliminary analytical results are obtained regarding the distribution of bundle sizes and its temporal change [106]. Investigations in this direction are in progress.

¹²Qualitatively similar results of path coalescence are obtained in studies, where independent particles are subjected to a common spatially and temporally random force field [38]. In these models, a phase transition is observed and analysed analytically [160].

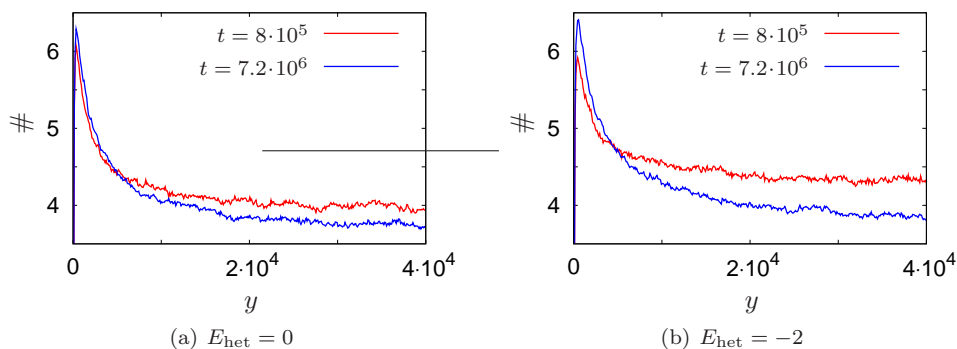


Fig. 4.21: The number of bundles (counted only for axons of one type) plotted over y for two different values of the heterotypic interaction energy E_{het} ($E_{\text{hom}} = -4.5$). Parameters are the same as in Fig. 4.19 except that two different types of axons were simulated with 50 axons each.

4.4 Summary and discussion

The formation of the neural map on the olfactory bulb during development of a mammal is a complex pattern formation process for which a consistent picture based on single axon dynamics does not exist yet. Most probable, not a single mechanism provides the observed sorting and placement of axons, but rather a complex interplay of a few different microscopic mechanisms. Only little experimental data is available describing the movement of single axons, most experiments focus on the patterning process of many thousands of axons as a whole, which renders a bottom-up approach to the problem more difficult. One important conclusion from these experiments is that the map formation can only be understood as a collective effect rather than single axons finding their way to the correct position independently and individually.

In this chapter, different mechanisms generally known to provide similar tasks in other biological systems, were implemented in *in silico* experiments and their effect on map formation and sorting was investigated. By using different geometries for the modelling as well as different levels of details in the descriptions, focus was put on respective effects that can be related to experimental observations. The results obtained are interesting from two perspectives. On the one hand, the detailed studies of the pattern formation process during the development of the olfactory system allow for statements regarding the applicability and importance of the different microscopic mechanisms considered. On the other hand, implementation of the models leads to extensions of well-known models from statistical physics that are interesting also in more general terms.

From a biological perspective, the main results from this chapter are the (mostly qualitative) reproductions of measurements and figures by *in silico* experiments. Simulating a front of advancing axonal growth cones as spins in a Potts model leads to the observations of axon sorting and placement (when a cue was implemented). In another model, growth of single axons was simulated with an idealised growth cone finding its way by interpreting a specifically designed chemical guidance cue. The axon trajectories obtained with these simple assumptions resemble pictures from single axons in the real system near the respective glomerulus. As an important concept, axon-axon interactions (both homo- and heterotypic) were included and their effect on the sorting of the axons investigated. When further implementing axon turnover, recently published experimental data of map refinement could be qualitatively reproduced. Especially this last model resembles the biological pattern formation process most and will be extended and enlarged in the future in order to use it as a tool for testing different hypotheses about map formation. Through extensions of this model, e.g. by considering the geometry of the olfactory bulb in greater

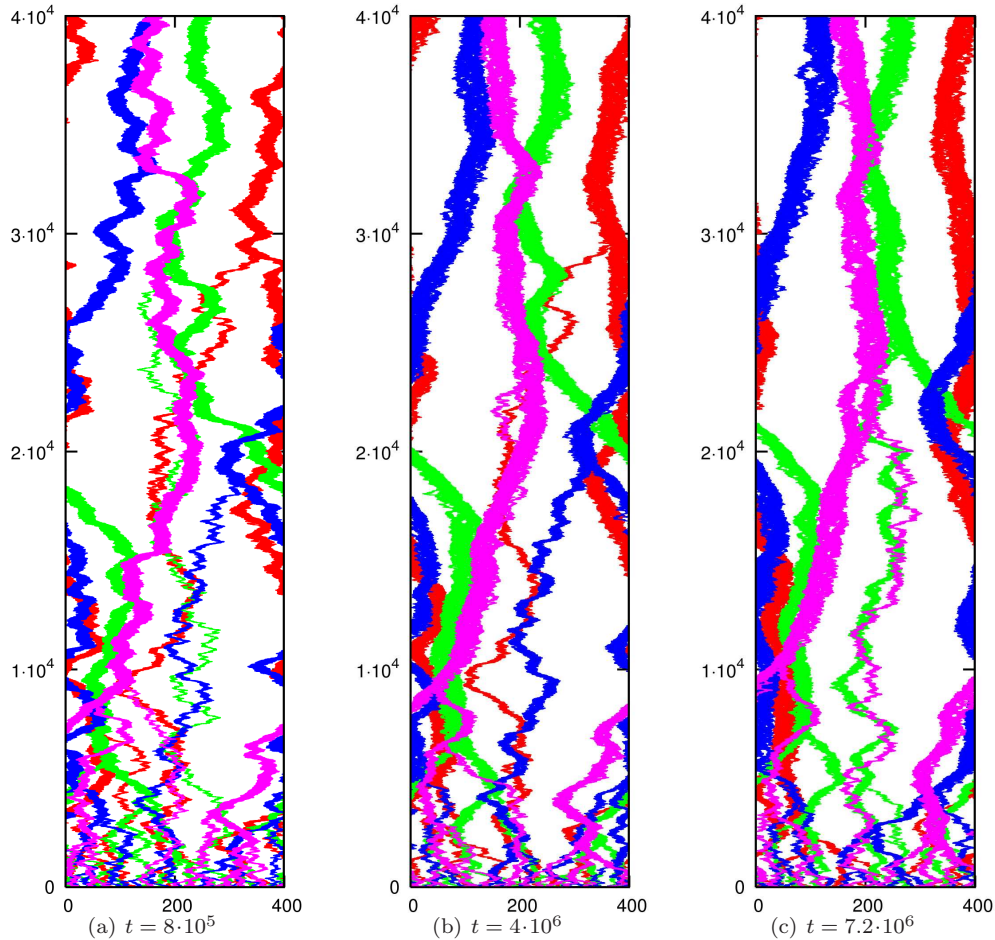


Fig. 4.22: Axon configurations at different times for 4 different types of each 25 axons. $E_{\text{hom}} = -10$, $E_{\text{het}} = -1$ and $E_{\text{pen}} = 0.5$. All remaining parameters are as in Fig. 4.19. The different types are plotted on top of each other in the order red - green - blue - magenta, so if a lattice site is occupied by more than one type, only the respective higher colour is shown.

detail or by giving axons of different types more distinguished properties, one can speculate that a reliable map formation might be possible with just a small number of 'general' guidance cues to which all axons react.

From a perspective focusing more on statistical physics, two well-known concepts were investigated and extended. In the last-mentioned model, advancing axons were simulated by interacting directed random walks. The concept of a random walk was extended by letting a large number of them interact and implementing turnover, i.e. each random walker has a specific life time after which it dies, its complete trajectory is removed from the system, and a new one is injected. The further analysis of this set-up – both numerically and analytically – promises interesting results in terms of path coalescence and phase separation. In a different model, axon interaction and sorting was mapped on the standard Potts model, a model commonly used for the study of phase separation. Extensions considered in this chapter include a specific choice of the Hamiltonian as well as the introduction of spatially dependent potentials to which the elements of the Potts model (the axons) react. Due to the adopted geometry, results obtained from the generalised Potts model might not be of great value for interpreting biological data, nevertheless the

described extensions introduce interesting dynamics that will be investigated further in the future.

In conclusion, the numerical models presented in this chapter provide a way to answer some aspects of the two main questions as stated in the introduction (Sec. 4.1). The quickly and continuously increasing knowledge about the biology of the pattern formation from experiments can be used to improve the presented theoretical approaches and make their results more reliable. To what extent general biological questions in this context can be answered using solely *in silico* experiments remains unclear. A bottom-up approach as it was aimed for in this chapter is most promising if there is a good knowledge of the microscopic properties. It appears that this is not the case for the problem of olfactory map formation, yet. However, enough data is available to go beyond pure phenomenological models. Precisely this gap between a pure microscopic description and a in some aspect always arbitrary phenomenological model makes this pattern formation process so interesting in terms of a theoretical analysis and challenges the development of new concepts and models.

Chapter 5

Conclusions and Perspective

Detailed experimental knowledge about how information is transmitted and processed in the olfactory sense has only emerged in the last 10–15 years. So far, this has happened to a great extent without the help of theoretical models that have proved to be beneficial in many other instances of cellular biology and other senses. The present work has to be seen as an early step in the direction of studying the complex biological task of sensing odourants by means of theoretical considerations. Various concepts and tools from theoretical physics were applied with the goal of a better understanding of some specific aspects of the olfactory system. A detailed model of parts of the olfactory signal transduction pathway was introduced and analysed as well as a more abstract general signalling module, whose statistical properties were evaluated. Further, different models were presented for a complex pattern formation process taking part during the development of the neural connections towards the brain. In each of these problems, different theoretical approaches to the complex biological processes and systems were used and each chapter provides a good example of how theoretical descriptions can contribute to a field of biology that is to a large extent still in the stage of descriptive, qualitative experiments.

The detailed quantitative description of the biochemistry of the olfactory signal transduction in chapter 2 is an example of the modelling part of what is commonly referred to as systems biology [76]. The aim of this (under this name) relatively new field is to understand dynamical processes in biology with the help of mathematics together with detailed biochemical measurements in a bottom-up approach. Here – as most commonly done in systems biology – this was achieved by describing the system of interest by a set of coupled non-linear differential equations. Usually, this very quickly leads to large numbers of parameters (kinetic constants, concentrations, . . .), whose precise choice, due to the nature of coupled nonlinear systems, can often affect the qualitative behaviour of the model quite severely. To reduce the number of parameters and to circumvent problems of this kind as much as possible, in chapter 2, extended analytical work was done, exploring the dynamical features of the underlying equations independently of the parameters. After it was analytically proven that the chosen network can in principle show oscillatory behaviour, it was numerically solved using experimental parameters from the literature. By that, specific whole-cell measurements on olfactory receptor neurons could be reproduced quantitatively. Due to the good agreement between the theory and experimental measurements, this model qualifies for making predictions regarding future experiments. The results from a detailed bifurcation analysis provide these predictions and show the robustness of the obtained results against the variation of single parameters.

In chapter 3, a part of the signalling pathway dealt with in chapter 2 is investigated in a more abstract way. The idea adopted in this chapter is that of a modular, rather than a molecular description of complex systems. One way of dealing with the complexity found in biological (e.g. signalling) systems is that of decomposing the system into smaller subsystems, the modules, whose dynamical properties can be calculated and are still to

some extent intuitive. In signalling systems, a module has specific input/output properties and the output of one module can be – within a larger system – the input of the subsequent one. The treatment of a small subnetwork as a module with just a few in- and output channels constitutes a kind of coarse graining, in the sense that not all possible dynamics are considered but only those relevant as an input for a subsequent module within the whole network. In chapter 3, a two-state signalling module with negative feedback was analysed that includes features of the pathway discussed in chapter 2. Different to the deterministic description in the latter, here, the magnitude and effects of intrinsic noise are considered and derived from stochastic differential equations. By using – among others – a path-integral technique described in detail, the relevant statistical quantities characterising the signalling properties (mean values, correlation and response functions) of the module were calculated and found to be in good agreement with the results of numerical studies.

Another – often preliminary – way of gaining understanding of biological systems is that of mostly phenomenological modelling, for which chapter 4 presented some examples in terms of numerical simulations. Often, in newly established fields or when considering macroscopic processes, mostly descriptive literature exists and the system as a whole proves to be too complicated for systematic quantitative experiments, using the current tools. Under these circumstances, hypotheses flourish but are usually on the same phenomenological level of description as the measurements themselves. Theory can contribute in such cases by setting up and conducting *in silico* experiments that serve mainly as a test of the general capabilities of different hypotheses. Microscopic mechanisms are modelled in simple ways, using effective parameters. The advantage compared to mere speculations is that quantitative models (no matter if analytical or numerical) have predictive power, can be adapted to new experimental findings and provide in general a more structured way of dealing with complex systems. The power and the diversity of this branch of modelling was shown in chapter 4 with three different simulation approaches that reproduce specific features of the convergence and targeting during the development of the neural connection between the olfactory receptor neurons and the brain. Focusing on different time- and length-scales of the system, different models were set up, analysed numerically and compared to experimental pictures and – where available – data. The level of detail that is adopted in this kind of approach is always a compromise between the variety of achievable results, the simplicity of the model and computation time.

All of these different approaches towards a better understanding of complex biological systems and processes work well and are important especially in 'softer' sciences as biology. The systems biology approach certainly is the one that grows fastest right now and due to extensive experimental efforts for obtaining better quantitative results in terms of *in vitro* biochemistry, will contribute considerably to the understanding of intracellular processes as well as biological design. How far the modular approach will get in terms of simple descriptions of the system, remains an open question. It certainly has the potential to severely simplify complex systems and classify them in terms of their dynamical properties. However, there is one condition for the applicability of the modular approach: The system as a whole has to be decomposable into subsystems that can be treated as modules, i.e. the degree of complexity of inter-module connections should be much lower than that of intra-module connections. This condition might be fulfilled in signalling or metabolic pathways but not necessarily in other biological systems. Purely phenomenological, numerical analyses remain a very important tool, too, mainly as a starting point for further studies on complex systems or for testing and comparing different hypotheses about these systems.

Regarding the more general questions raised in Sec. 1.3, some preliminary answers could be found. However, much more work has to be done until the system can be called 'understood' from the perspective of a physicist. It is the conviction of the author that only the development of new concepts and a new language, rather than just more detailed conventional modelling, will lead to a satisfying understanding of complex processes like olfaction.

Appendix

A.1 The reaction of calcium and calmodulin

In this appendix, the simple kinetic relation for the reaction of calcium and calmodulin that is used in Eq. (2.9) is compared to more complicated models with different parameters from different literature sources.

In [32] and [36], four dissociation constants are given for the four different binding sites of calmodulin. Writing the complex of calmodulin with i calcium ions as C_i ($0 \leq i \leq 4$), the four reaction steps towards the fully calcium-loaded calmodulin read ($0 \leq i \leq 3$)



Assuming mass action kinetics for each of the four steps, one gets for the kinetic constants $k_i^{-/+}$ different values from different literature sources. Some of them are given in Tab. A.1.

data set	A	B	C	D	E
reference	[32]	[36]	[138]	Subsec. 2.2.3	see text
k_0^- [$\frac{1}{\text{s}}$]	600	6.7	72		
k_1^- [$\frac{1}{\text{s}}$]	20	17		2.5	2.5
k_2^- [$\frac{1}{\text{s}}$]	600	60	10		
k_3^- [$\frac{1}{\text{s}}$]	20	90	10		
k_0^+ [$10^7 \frac{\text{dm}^3}{\text{mol}\cdot\text{s}}$]	1.8	10	$7.2 \cdot 10^{13} \frac{\text{dm}^6}{\text{mol}^2 \cdot \text{s}^2}$	$1.1 \cdot 10^9 \frac{\text{dm}^6}{\text{mol}^2 \cdot \text{s}}$	$2.2 \cdot 10^{11} \frac{\text{dm}^6}{\text{mol}^2 \cdot \text{s}}$
k_1^+ [$10^7 \frac{\text{dm}^3}{\text{mol}\cdot\text{s}}$]	2.9	10			
k_2^+ [$10^7 \frac{\text{dm}^3}{\text{mol}\cdot\text{s}}$]	2.4	10	36		
k_3^+ [$10^7 \frac{\text{dm}^3}{\text{mol}\cdot\text{s}}$]	5.0	10	46.5		

Tab. A.1: Kinetic constants from different sources for the reactions between calcium and calmodulin (another set of binding constants can be found in [93]).

In [138], the steps for $i = 0$ and $i = 1$ are combined to a second order reaction. Table A.1 also shows the kinetic constants from [138]. In Sec. 2.2 of the present work, one reaction of second order is assumed. The kinetic constants are given in Tab. 2.2 or as data set D in Tab. A.1.

Assuming mass action kinetics for the single steps of the full reaction, a constant calcium concentration, and the conservation constraint

$$\sum_{i=0}^4 [C_i] = [\text{CaM}^{\text{tot}}], \quad (\text{A.2})$$

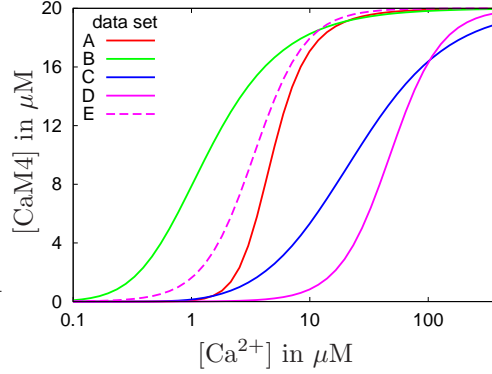


Fig. A.1: The concentration of the fully loaded calcium-calmodulin complex CaM4 in the steady state from the different models (Tab. A.1) according to Eqs. (A.3), (A.4) and (A.5).

one can easily calculate the steady state concentration of the fully loaded complex C_4 . For the four-step reaction scheme as of [32, 36], this turns out to be ($K_i^D = \frac{k_i^-}{k_i^+}$ is the dissociation constant)

$$[C_4^{A,B}]_{ss} = \frac{[CaM^{tot}]}{K_0^D + [Ca^{2+}]} \left[\frac{K_1^D K_2^D K_3^D}{[Ca^{2+}]^4} + \frac{1}{K_0^D + [Ca^{2+}]} \left(1 + \frac{K_3^D}{[Ca^{2+}]} + \frac{K_3^D K_2^D}{[Ca^{2+}]^2} \right) \right]^{-1}. \quad (A.3)$$

For the three-step reaction scheme of [138] one gets

$$[C_4^C]_{ss} = \frac{k_1^+ [Ca^{2+}]^4 [CaM^{tot}]}{K_2^D K_3^D (k_1^- + k_1^+ [Ca^{2+}]^2)} \left[1 + \frac{k_1^+ [Ca^{2+}]^4}{K_2^D K_3^D (k_1^- + k_1^+ [Ca^{2+}]^2)} \left(1 + \frac{K_3^D}{[Ca^{2+}]} \right) \right]^{-1}. \quad (A.4)$$

Those relations can be compared to the result for the simplified version used in the present model (from Eq. (2.9) if the terms related to channel-binding are dropped):

$$[C_4^{D,E}]_{ss} = [CaM^{tot}] \frac{k_{CaM4}^+ [Ca^{2+}]^2}{k_{CaM4}^+ [Ca^{2+}]^2 + k_{CaM4}^-}. \quad (A.5)$$

Fig. A.1 shows these different results plotted over constant calcium concentration.

To compare the kinetics of the different reaction schemes, the kinetic equations of each are simulated with a simple Euler forward step algorithm. A step increase in calcium concentration serves as the stimulus, where the magnitude of the step corresponds approximately to the two different time courses described in Subsec. 2.2.3 (long, single pulse: $[Ca^{2+}]$ grows from 1 to 25 μM ; double pulse: $[Ca^{2+}]$ grows from 1 to 150 μM). The results (the time evolution of the concentration of the fully calcium-loaded form of calmodulin) are presented in Fig. A.2.

As the figures show, experimental data from different sources for the reaction between calcium and calmodulin does not agree and allows for a broad range from which modelling parameters can be chosen. The simple, second order kinetics used in the modelling in the present work shows no big qualitative difference to the results from the more detailed and complicated reaction schemes. Concerning quantitative results, the model used here comes closest to the data of [138]. By increasing the effective association constant k_{CaM4}^+ by a factor of 200 (data set E in Tab. A.1), the result of the second order kinetics comes closer to the data from [32] and [36] (see Figs. A.1 and A.2). However, in order to get similar results for the calcium dynamics as presented in Subsec. 2.2.3 (based on the same set of equations), other parameters of the model have to be adjusted in a way that lead them further away from experimentally obtained values (see [120] for the full alternative parameter set).

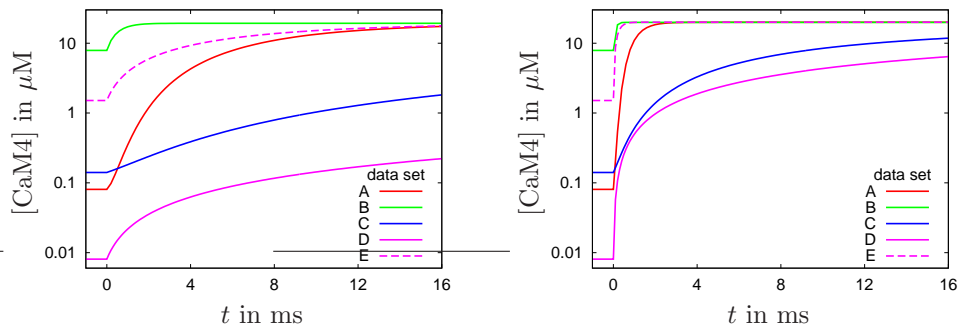


Fig. A.2: The time course of the concentration of the fully loaded calcium-calmodulin complex CaM4 after a step-increase in $[Ca^{2+}]$ (at $t = 0s$) roughly corresponding to the simulations depicted in the left panel of Fig. 2.11 (left) and in Fig. 2.13 (right). For the different data sets, see Tab. A.1.

B.1 Calculation of the integrals \hat{I}_0 , \hat{I}_1 , \hat{I}_2

B.1.1 Generalised convolution theorem

The following general result will be used in the calculations further down. If a function $g(t)$ has the form

$$g(t; n) = \int_0^t f_1(t_1) \int_0^{t-t_1} f_2(t_2) \int_0^{t-t_1-t_2} f_3(t_3) \cdots \int_0^{t-\sum_{i=1}^{n-1} t_i} f_n(t_n) dt_n \cdots dt_3 dt_2 dt_1, \quad (\text{B.6})$$

its Laplace transform can be shown to be

$$\hat{g}(s; n) = \frac{1}{s} \prod_{i=1}^n \hat{f}_i(s). \quad (\text{B.7})$$

To proof this, Eq. (B.6) is written as

$$g(t; n) = \int_0^t f_1(t_1) g_2(t - t_1) dt_1 \quad (\text{B.8})$$

with $g_i(\tau)$ recursively defined as

$$g_i(\tau) = \int_0^\tau f_i(t_i) g_{i+1}(\tau - t_i) dt_i, \quad 2 \leq i \leq n, \quad g_{n+1}(\tau) = 1. \quad (\text{B.9})$$

Eq. (B.8) is a convolution of the functions $f_1(\tau)$ and $g_2(\tau)$, whose Laplace transform is

$$\hat{g}(s) = \hat{f}_1(s) \hat{g}_2(s). \quad (\text{B.10})$$

Using this standard convolution theorem consecutively on the g_i 's together with $\hat{g}_n(s) = \frac{1}{s} \hat{f}_n(s)$, one arrives at Eq. (B.7).

B.1.2 Calculation of \hat{I}_0

Writing out the integrals in Eq. (3.55) gives

$$I_0(t; m) = \int_0^t \int_0^{t-T_1} e^{-(1-r_+)T_1'} \int_0^{t-T_1-T_1'} \cdots \int_0^{t-\cdots-T_m} e^{-(1-r_+)T_m'} dT_m' \cdots dT_2 dT_1' dT_1. \quad (\text{B.11})$$

Using the generalised convolution theorem from Subsec. B.1.1, one has $m+1$ functions $f(t) = 1$ and m times $f'(t) = e^{-(1-r_+)t}$. The Laplace transform of $I_0(t; m)$ therefore is

$$\hat{I}_0(s; m) = s^{-(m+1)} (s + 1 - r_+)^{-m}. \quad (\text{B.12})$$

B.1.3 Calculation of \hat{I}_1

In order to calculate the integrals \hat{I}_1 and \hat{I}_2 , one needs to express $c(t)$ in terms of the time interval variables T_i and T_i' . The solution of the differential equation Eq. (3.5) with $S(t=0) = c(t=0) = 0$ is ($j \geq 0$; $\tau_0 = 0$)

$$c(t) = \begin{cases} A_j e^{-\lambda t} & \tau_j \leq t \leq \tau_{j+1} \quad j \text{ even} \\ A_j e^{-\lambda t} + 1 & \tau_j \leq t \leq \tau_{j+1} \quad j \text{ odd} \end{cases}, \quad (\text{B.13})$$

where the coefficients A_j assure the continuity of $c(t)$ at the switching times τ_j . The initial condition $c(t=0) = 0$ gives $A_0=0$ and for the other A_j the following is found:

$$A_j = \sum_{i=1}^j (-1)^i e^{\lambda \tau_i}. \quad (\text{B.14})$$

For I_1 , the concentrations at the times when the channel switches from open to closed has to be known. This is ($i \geq 2$ and even)

$$c(\tau_i) = \sum_{j=1}^i (-1)^j e^{\lambda \tau_j} e^{-\lambda \tau_i}. \quad (\text{B.15})$$

The transformation to time interval variables (using Eq. (3.46)) requires a distinction between even and odd j . The case $j = i$ in Eq. (B.15) is treated separately and gives the '1':

$$\begin{aligned} c(\tau_i) &= 1 + \sum_{j=2; i \geq 4}^{i-2} \text{E} e^{\lambda \sum_{k=1}^{j/2} (T_k + T'_k) - \lambda \sum_{l=1}^{i/2} (T_l + T'_l)} - \sum_{j=1; i \geq 2}^{i-1} \text{O} e^{\lambda \left(\sum_{k=1}^{(j+1)/2} T_k + \sum_{k=1}^{j/2} T'_k \right) - \lambda \sum_{l=1}^{i/2} (T_l + T'_l)} \\ &= 1 + \sum_{j=2; i \geq 4}^{i-2} \text{E} e^{-\lambda \sum_{k=\frac{j}{2}+1}^{i/2} (T_k + T'_k)} - \sum_{j=1; i \geq 2}^{i-1} \text{O} e^{-\lambda \sum_{k=\frac{j+3}{2}}^{i/2} T_k} e^{-\lambda \sum_{k=\frac{j+1}{2}}^{i/2} T'_k}. \end{aligned} \quad (\text{B.16})$$

Putting this into the expression for I_1 (Eq. (3.56)), one gets

$$\begin{aligned} I_1(t; m) &= m I_0(t; m) + \sum_{i=4}^{2m} \text{E} \sum_{j=2}^{i-2} \int \mathcal{D}T e^{-(1-r_+) \sum_{i=1}^m T'_i} e^{-\lambda \sum_{k=\frac{j}{2}+1}^{i/2} T_k} e^{-\lambda \sum_{l=\frac{j+2}{2}}^{i/2} T'_l} \\ &\quad - \sum_{i=2}^{2m} \text{E} \sum_{j=1}^{i-1} \int \mathcal{D}T e^{-(1-r_+) \sum_{i=1}^m T'_i} e^{-\lambda \sum_{k=\frac{j+3}{2}}^{i/2} T_k} e^{-\lambda \sum_{l=\frac{j+1}{2}}^{i/2} T'_l}. \end{aligned} \quad (\text{B.17})$$

The path integrals can now be solved using the generalised convolution theorem from Subsec. B.1.1. E.g. contains the first path integral (even j) $\frac{i-j+2}{2} + 1$ times the functions $e^{-\lambda T_k}$ and $e^{-(1-r_+ + \lambda) T'_k}$ and $m - \frac{i-j+2}{2} + 1$ times the functions $e^{-(1-r_+) T'_k}$ and 1. The Laplace transform therefore is

$$\begin{aligned} \hat{I}_1(s; m) &= m \hat{I}_0(s; m) + \sum_{i=4}^{2m} \text{E} \sum_{j=2}^{i-2} s^{-1} [(s + \lambda)(s + 1 - r_+ + \lambda)]^{-\frac{i-j}{2}} [s(s + 1 - r_+)]^{-m + \frac{i-j}{2}} \\ &\quad - \sum_{i=2}^{2m} \text{E} \sum_{j=1}^{i-1} s^{-1} [(s + \lambda)(s + 1 - r_+ + \lambda)]^{-\frac{i-j-1}{2}} [s(s + 1 - r_+)]^{-m + \frac{i-j-1}{2}} \\ &\quad \cdot \frac{s + 1 - r_+}{s + 1 - r_+ + \lambda} \\ &= m \hat{I}_0(s; m) + s^{-(m+1)} (s + 1 - r_+)^{-m} \\ &\quad \cdot \left(\sum_{i=4}^{2m} \text{E} \sum_{j=2}^{i-2} y^{\frac{i-j}{2}} - \frac{s + 1 - r_+}{s + 1 - r_+ + \lambda} \sum_{i=2}^{2m} \text{E} \sum_{j=1}^{i-1} y^{\frac{i-j-1}{2}} \right), \end{aligned} \quad (\text{B.18})$$

using the abbreviation

$$y = \frac{s(s + 1 - r_+)}{(s + \lambda)(s + 1 - r_+ + \lambda)}. \quad (\text{B.19})$$

The two double geometric sums can easily be calculated ($y < 1$) and after some rearrangements one ends up with

$$\hat{I}_1(s; m) = s^{-(m+1)} (s + 1 - r_+)^{-m} \frac{\lambda}{s + 1 - r_+ + \lambda} \frac{1}{1 - y} \left(m + \frac{y}{1 - y} (y^m - 1) \right). \quad (\text{B.20})$$

B.1.4 Calculation of \hat{I}_2

For I_2 , the integrals over $c(t)$ over the open periods ($S = 1$: $\tau_j \leq t \leq \tau_{j+1}$ with odd j) are needed. Using the expression for odd j from Eq. (B.13) together with Eq. (B.14), one gets

$$\int_{\tau_j}^{\tau_{j+1}} c(t) dt = \tau_{j+1} - \tau_j + \frac{1}{\lambda} (e^{-\lambda\tau_j} - e^{-\lambda\tau_{j+1}}) \sum_{i=1}^j (-1)^i e^{\lambda\tau_i}. \quad (\text{B.21})$$

Putting this into the expression for I_2 (Eq. (3.57)) ($\tau_{j+1} - \tau_i = T'_{\frac{j+1}{2}}$; splitting the sum over i into even and odd i and treating the case $i = j$ separately), one gets

$$\begin{aligned} I_2(t; m) = \int \mathcal{D}T e^{-(1-r_+) \sum_{k=1}^m T'_k} & \left(\sum_{j=1}^{2m-1} T'_{\frac{j+1}{2}} + \frac{1}{\lambda} \left[- \sum_{j=1}^{2m-1} 1 \right. \right. \\ & - \sum_{j=3}^{2m-1} \sum_{i=1}^{j-2} e^{\lambda(\tau_i - \tau_j)} + \sum_{j=3}^{2m-1} \sum_{i=2}^{j-1} e^{\lambda(\tau_i - \tau_j)} \\ & \left. \left. + \sum_{j=1}^{2m-1} \sum_{i=1}^j e^{\lambda(\tau_i - \tau_{j+1})} - \sum_{j=3}^{2m-1} \sum_{i=2}^{j-1} e^{\lambda(\tau_i - \tau_{j+1})} \right] \right). \quad (\text{B.22}) \end{aligned}$$

Exchanging the flip time variables τ_i by the time interval variables T_i, T'_i , I_2 can be written as

$$I_2(t; m) = -\frac{m}{\lambda} I_0(t; m) + I_{2,1} + \frac{1}{\lambda} (-I_{2,2} + I_{2,3} + I_{2,4} - I_{2,5}), \quad (\text{B.23})$$

with

$$I_{2,1} = \sum_{j=1}^{2m-1} \int \mathcal{D}T e^{-(1-r_+) \sum_{k=1}^m T'_k} T'_{\frac{j+1}{2}}, \quad (\text{B.24})$$

$$I_{2,2} = \sum_{j=3}^{2m-1} \sum_{i=1}^{j-2} \int \mathcal{D}T e^{-(1-r_+) \sum_{k=1}^m T'_k} e^{-\lambda \sum_{l=\frac{i+3}{2}}^{\frac{j+1}{2}} T_l} e^{-\lambda \sum_{l=\frac{i+1}{2}}^{\frac{j-1}{2}} T'_l}, \quad (\text{B.25})$$

$$I_{2,3} = \sum_{j=3}^{2m-1} \sum_{i=2}^{j-1} \int \mathcal{D}T e^{-(1-r_+) \sum_{k=1}^m T'_k} e^{-\lambda \sum_{l=\frac{i+2}{2}}^{\frac{j+1}{2}} T_l} e^{-\lambda \sum_{l=\frac{i+2}{2}}^{\frac{j-1}{2}} T'_l}, \quad (\text{B.26})$$

$$I_{2,4} = \sum_{j=1}^{2m-1} \sum_{i=1}^j \int \mathcal{D}T e^{-(1-r_+) \sum_{k=1}^m T'_k} e^{-\lambda \sum_{l=\frac{i+3}{2}}^{\frac{j+1}{2}} T_l} e^{-\lambda \sum_{l=\frac{i+1}{2}}^{\frac{j+1}{2}} T'_l}, \quad (\text{B.27})$$

$$I_{2,5} = \sum_{j=3}^{2m-1} \sum_{i=2}^{j-1} \int \mathcal{D}T e^{-(1-r_+) \sum_{k=1}^m T'_k} e^{-\lambda \sum_{l=\frac{i+2}{2}}^{\frac{j+1}{2}} T_l} e^{-\lambda \sum_{l=\frac{i+2}{2}}^{\frac{j+1}{2}} T'_l}. \quad (\text{B.28})$$

$$(\text{B.29})$$

These path integrals are solved as described in the previous subsection (using the theorem from Subsec. B.1.1 and the abbreviation from Eq. (B.19)). Only $I_0, I_{2,1}$ and $I_{2,4}$ contribute to the case $m = 1$ and give for the Laplace transform

$$\hat{I}_2(s; 1) = s^{-2} (s + 1 - r_+)^{-1} \left(\frac{1}{s + 1 - r_+} - \frac{1}{s + 1 - r_+ + \lambda} \right). \quad (\text{B.30})$$

Calculating the (double) geometric sums, one gets for $m \geq 2$:

$$\hat{I}_{2,1}(s; m) = s^{-(1+m)}(s+1-r_+)^{-m} \frac{m}{s+1-r_+}, \quad (\text{B.31})$$

$$\hat{I}_{2,2}(s; m) = s^{-(1+m)}(s+1-r_+)^{-m} \frac{y}{1-y} \left(m + \frac{y^m - 1}{1-y} \right), \quad (\text{B.32})$$

$$\hat{I}_{2,3}(s; m) = s^{-(1+m)}(s+1-r_+)^{-m} \frac{y}{1-y} \left(m + \frac{y^m - 1}{1-y} \right) \frac{s+1-r_++\lambda}{s+1-r_+}, \quad (\text{B.33})$$

$$\hat{I}_{2,4}(s; m) = s^{-(1+m)}(s+1-r_+)^{-m} \frac{y}{1-y} \left(\frac{m}{y} + \frac{y^m - 1}{1-y} \right) \frac{s+1-r_+}{s+1-r_++\lambda}, \quad (\text{B.34})$$

$$\hat{I}_{2,5}(s; m) = s^{-(1+m)}(s+1-r_+)^{-m} \frac{y}{1-y} \left(m + \frac{y^m - 1}{1-y} \right). \quad (\text{B.35})$$

Using the Laplace transform of Eq. (B.23) and some rearrangements, this gives

$$\begin{aligned} \hat{I}_2(s; m) = & s^{-(1+m)}(s+1-r_+)^{-m} \left(\frac{m(s+\lambda)}{(s+1-r_+)(2s+1-r_++\lambda)} \right. \\ & \left. + \frac{y^m - 1}{1-y} \frac{s}{(s+1-r_++\lambda)(2s+1-r_++\lambda)} \right). \end{aligned} \quad (\text{B.36})$$

B.2 Solution of the rate equation: $f(t)$, $f_2(t)$

The rate equation

$$\frac{dG_{00}(t)}{dt} = r_-(t) - (r_-(t) + r_+)G_{00}(t) \quad (\text{B.37})$$

is an ordinary linear differential equation and has the solution [19]

$$G_{00}(t) = e^{-\int r_-(t)+r_+ dt} \left[\int r_-(t) e^{\int r_-(t)+r_+ dt} dt + C \right]. \quad (\text{B.38})$$

With $r_-(t) = 1 + \alpha c_0 e^{-\lambda t}$ this turns into

$$\begin{aligned} G_{00}(t) = & e^{-(1+r_+)t} e^{\frac{\alpha c_0}{\lambda} e^{-\lambda t}} \left[\int e^{(1+r_+)t} e^{-\frac{\alpha c_0}{\lambda} e^{-\lambda t}} dt \right. \\ & \left. + \alpha c_0 \int e^{-\lambda t} e^{(1+r_+)t} e^{-\frac{\alpha c_0}{\lambda} e^{-\lambda t}} dt + C \right]. \end{aligned} \quad (\text{B.39})$$

Taylor expansion around $\alpha c_0 = 0$ gives

$$\begin{aligned} G_{00}(t) \approx & G_{00}^{(0)}(t) + \alpha c_0 f(t) \approx e^{-(1+r_+)t} \left(1 + \frac{\alpha c_0}{\lambda} e^{-\lambda t} \right) \left[\int e^{(1+r_+)t} \left(1 - \frac{\alpha c_0}{\lambda} e^{-\lambda t} \right) dt \right. \\ & \left. + \alpha c_0 \int e^{(1+r_+-\lambda)t} dt + C_1 + C_2 \alpha c_0 \right], \end{aligned} \quad (\text{B.40})$$

which must be valid both for terms of $\mathcal{O}(\alpha^0)$ and $\mathcal{O}(\alpha^1)$. Using the initial condition $G_{00}(t=0) = 1$, the constants C_1 and C_2 can be calculated and after computing the integrals one finds

$$G_{00}^{(0)}(t) = \frac{1}{1+r_+} \left(1 + r_+ e^{-(1+r_+)t} \right), \quad (\text{B.41})$$

$$f(t) = \frac{r_+}{\lambda} \left(\frac{-1}{1+r_+-\lambda} e^{-(1+r_+)t} + \frac{1}{1+r_+} e^{-(1+r_++\lambda)t} + \frac{\lambda}{(1+r_+)(1+r_+-\lambda)} e^{-\lambda t} \right). \quad (\text{B.42})$$

The rate equation

$$\frac{dG_{11}(t)}{dt} = r_+ - (r_-(t) + r_+)G_{11}(t) \quad (\text{B.43})$$

is solved up to $\mathcal{O}(\alpha)$ in the same way. Taylor expansion around $\alpha c' = 0$ of the solution gives

$$G_{11}(t) \approx G_{11}^{(0)}(t) + \alpha c' f_2(t) \approx e^{-(1+r_+)t} \left(1 + \frac{\alpha c'}{\lambda} e^{-\lambda t} \right) \left[r_+ \int e^{(1+r_+)t} \left(1 - \frac{\alpha c'}{\lambda} e^{-\lambda t} \right) dt + C_1 + C_2 \alpha c' \right]. \quad (\text{B.44})$$

Again, separating between the terms of $\mathcal{O}(\alpha^0)$ and $\mathcal{O}(\alpha^1)$ and using the initial condition $G_{11}(t=0) = 1$, one can determine the constants C_1 and C_2 and finds

$$G_{11}^{(0)}(t) = \frac{1}{1+r_+} \left(r_+ + e^{-(1+r_+)t} \right), \quad (\text{B.45})$$

$$f_2(t) = \frac{1}{\lambda} \left(\frac{\lambda-1}{1+r_+-\lambda} e^{-(1+r_+)t} + \frac{1}{1+r_+} e^{-(1+r_++\lambda)t} - \frac{\lambda r_+}{(1+r_+)(1+r_+-\lambda)} \right). \quad (\text{B.46})$$

B.3 Relation between G_{11} and G_{00}

For $\alpha = 0$ (when the G_{ij} 's are independent of c), the theorem on the total probability [18] connects the Green's functions ($0 \leq t' \leq t$):

$$G_{01}^{(0)}(0, t) = G_{00}^{(0)}(0, t') G_{01}^{(0)}(t', t) + G_{01}^{(0)}(0, t') G_{11}^{(0)}(t', t). \quad (\text{B.47})$$

Using the Taylor expansions for small t' in the stationary state

$$\begin{aligned} G_{00}^{(0)}(0, t') &\approx 1 + \left. \frac{\partial G_{00}^{(0)}(0, t)}{\partial t} \right|_{t=0} t', \\ G_{01}^{(0)}(t', t) &= G_{01}^{(0)}(t-t') \approx G_{01}^{(0)}(0, t) - \frac{\partial G_{01}^{(0)}(0, t)}{\partial t} t', \\ G_{11}^{(0)}(t', t) &= G_{11}^{(0)}(t-t') \approx G_{11}^{(0)}(0, t) - \frac{\partial G_{11}^{(0)}(0, t)}{\partial t} t', \end{aligned} \quad (\text{B.48})$$

and $G_{01} = 1 - G_{00}$, and putting that into Eq. (B.47), one ends up with the following relation between the different Green's functions:

$$G_{11}^{(0)}(0, t) = (1 - G_{00}^{(0)}(0, t)) + \frac{\left. \frac{\partial G_{00}^{(0)}(0, t)}{\partial t} \right|_{t=0}}{\left. \frac{\partial G_{00}^{(0)}(0, t)}{\partial t} \right|_{t=0}}. \quad (\text{B.49})$$

For the G_{ij} instead of the $G_{ij}^{(0)}$, i.e. for $\alpha \neq 0$, Eq. (B.47) does not hold anymore. However, a corresponding expression can be written using the propagators Π_{ij} :

$$\begin{aligned} G_{01}(0, 0; t) &= \sum_j \int_0^1 dc' \int_0^1 dc \Pi_{0j}(0, 0; t', c') \Pi_{j1}(t', c'; t, c) \\ &= \int_0^1 dc' \Pi_{00}(0, 0; t', c') G_{01}(t', c'; t) + \int_0^1 dc' \Pi_{01}(0, 0; t', c') G_{11}(t', c'; t). \end{aligned} \quad (\text{B.50})$$

Putting the expressions from Eqs. (3.65) (Subsec. 3.4.1) in Eq. (B.50) together with the definition from Eq. (3.43), one gets

$$G_{01}(0, 0; t) = G_{00}(0, 0; t')G_{01}(t', 0; t) + G_{01}(0, 0; t')G_{11}(t', 0; t) \\ + \alpha f_1(t - t') \int_0^1 dc' c' \Pi_{00}(0, 0; t', c') + \alpha f_2(t - t') \int_0^1 dc' c' \Pi_{01}(0, 0; t', c'). \quad (\text{B.51})$$

The remaining integrals are the mean calcium concentrations, when the channel is in the closed or open state, and when the system started in the initial state $S(0) = 0$ and $c(0) = 0$:

$$\langle c(t') \rangle_0 \equiv \int_0^1 dc' c' \Pi_{00}(0, 0; t', c'), \quad \langle c(t') \rangle_1 \equiv \int_0^1 dc' c' \Pi_{01}(0, 0; t', c'). \quad (\text{B.52})$$

With that, Eq. (B.51) can be written as

$$G_{11}(t', c_0 = 0; t) = \frac{1}{G_{01}(0, 0; t')} (G_{01}(0, 0; t) - G_{01}(t', 0; t)G_{00}(0, 0; t') \\ - \alpha \langle c'(t') \rangle_0 f_1(t - t') - \alpha \langle c'(t') \rangle_1 f_2(t - t')) + \mathcal{O}(\alpha^2). \quad (\text{B.53})$$

Using Taylor expansions around $t' = 0$ equivalently to Eq. (B.48) as well as the fact that $\langle c'(t' = 0) \rangle_{0/1} = 0$ and Eq. (3.44), one can write the limit $t' \rightarrow 0$ of Eq. (B.53) as

$$G_{11}(0, 0; t) \approx 1 - G_{00}(0, 0; t) + \frac{1}{\left. \frac{\partial G_{00}(0, 0; t)}{\partial t} \right|_{t=0}} \left(\frac{\partial G_{00}(0, 0; t)}{\partial t} \right. \\ \left. - \alpha f_1(t) \left. \frac{\partial \langle c'(t') \rangle_0}{\partial t'} \right|_{t'=0} - \alpha f_2(t) \left. \frac{\partial \langle c'(t') \rangle_1}{\partial t'} \right|_{t'=0} \right). \quad (\text{B.54})$$

From Eq. (B.66) it can be seen that $\frac{d}{dt} \langle c(t) \rangle|_{t=0} = 0$ (for these initial conditions) and since none of the derivatives of $\langle c'(t') \rangle_{0/1}$ can be negative at time $t = 0$ ($0 \leq c \leq 1$), they both have to be zero. With that – equivalent to the case without feedback (Eq. (B.49)) – one ends up with Eq. (3.68) as the relation between the two Green's functions valid up to $\mathcal{O}(\alpha)$.

Using Eq. (3.61), G_{11} is obtained from Eq. (3.68) and the result is

$$G_{11}(0, 0; t) = \frac{1}{1 + r_+} \left(r_+ + e^{-(1+r_+)t} \right) + \alpha \frac{r_+}{(1 + r_+)^2} \left[-\frac{r_+ + \lambda}{1 + r_+ + \lambda} \right. \\ + \frac{(1 + r_+)(r_+ - \lambda)}{(1 + r_+ - \lambda)^2} e^{-\lambda t} - \frac{(1 + r_+)(1 + \lambda)}{\lambda r_+(1 + r_+ + \lambda)} e^{-(1+r_++\lambda)t} \\ + \left(\frac{\lambda^3 r_+ + \lambda^2(1 - r_+ - r_+^2) + \lambda(r_+^2 - r_+ - 2) + (1 + r_+)^2}{r_+ \lambda (1 + r_+ - \lambda)^2} \right. \\ \left. + \frac{(1 + r_+)(\lambda - 1)}{r_+(1 + r_+ - \lambda)} t \right) e^{-(1+r_+)t} \Big] + \mathcal{O}(\alpha^2). \quad (\text{B.55})$$

B.4 Calculation of $\langle c(t) \rangle_0$ and $\langle c(t) \rangle_1$

As mentioned in Subsec. 3.4.1 and defined in Sec. B.3, the quantities $\langle c(t) \rangle_0$ and $\langle c(t) \rangle_1$ are the mean calcium concentrations when the channel is in the closed or the open state, respectively. Since in this work they appear only in terms that are of $\mathcal{O}(\alpha)$ already, they need to be computed only up to $\mathcal{O}(\alpha^0)$. Putting Eq. (3.41) into the definition of $\langle c(t) \rangle_0$ (Eq. (B.52)), one finds

$$\langle c(t) \rangle_0 = \sum_{m=0}^{\infty} \int \mathcal{D}T\mathcal{P}_{00}[0, t; \{T_i\}, \{T'_i\}; 0; 2m] c(t). \quad (\text{B.56})$$

$c(t)$ in the closed state $S = 0$ (after an even number of flips) can be found from Eqs. (B.13) and (B.14) to be (not to be confused with the constant $c_0 \equiv c(t_0)$)

$$c_0(t) = e^{-\lambda t} \sum_{\mathcal{O}}^{2m-1} (e^{\lambda \tau_{j+1}} - e^{\lambda \tau_j}). \quad (\text{B.57})$$

Putting that into Eq. (B.56) together with the no-feedback version of \mathcal{P}_{00} from Eq. (3.48), one gets (the case $m = 0$ does not contribute, since $c(t = 0) = 0$ and $m = 0$ means no switch and therefore no opening of the channel)

$$\langle c(t) \rangle_0 = e^{-(r_+ + \lambda)t} \sum_{m=1}^{\infty} r_+^m I_3(t; m), \quad (\text{B.58})$$

with

$$I_3(t; m) = \sum_{\mathcal{O}}^{2m-1} \int \mathcal{D}T e^{-(1-r_+) \sum_{i=1}^m T'_i} (e^{\lambda \tau_{j+1}} - e^{\lambda \tau_j}). \quad (\text{B.59})$$

Using the transformation rules from Eqs. (3.46), this turns into

$$\begin{aligned} I_3(t; m) &= \sum_{\mathcal{O}}^{2m-1} \int \mathcal{D}T e^{-(1-r_+) \sum_{i=1}^m T'_i} e^{\lambda \sum_{i=1}^{\frac{j+1}{2}} (T_i + T'_i)} - \int \mathcal{D}T e^{-(1-r_+) \sum_{i=1}^m T'_i} e^{\lambda T_1} \\ &\quad - \sum_{\mathcal{O}}^{2m-1} \int \mathcal{D}T e^{-(1-r_+) \sum_{i=1}^m T'_i} e^{\lambda \sum_{i=1}^{\frac{j+1}{2}} T_i + \lambda \sum_{i=1}^{\frac{j-1}{2}} T'_i}. \end{aligned} \quad (\text{B.60})$$

Laplace transformation of Eq. (B.58) gives

$$\langle \hat{c}(s) \rangle_0 = \sum_{m=1}^{\infty} r_+^m \hat{I}_3(s + r_+ + \lambda; m). \quad (\text{B.61})$$

The Laplace transform of I_3 is now calculated in the same way as the expressions in Subsecs. B.1.2–B.1.4. The result is

$$\begin{aligned} \hat{I}_3(s; m) &= \sum_{\mathcal{O}}^{2m-1} (s + 1 - r_+ - \lambda)^{-\frac{j+1}{2}} (s + 1 - r_+)^{-m + \frac{j+1}{2}} (s - \lambda)^{-\frac{j+1}{2}} s^{-m + \frac{j+1}{2} - 1} \\ &\quad - (s + 1 - r_+)^{-m} (s - \lambda)^{-1} s^{-m} \\ &\quad - \sum_{\mathcal{O}}^{2m-1} (s + 1 - r_+ - \lambda)^{-\frac{j-1}{2}} (s + 1 - r_+)^{-m + \frac{j-1}{2}} (s - \lambda)^{-\frac{j+1}{2}} s^{-m + \frac{j+1}{2} - 1} \\ &= \frac{1}{\lambda + r_+ - 1 - 2s} \left[(s(s + 1 - r_+))^{-m} - ((s + 1 - r_+ - \lambda)(s - \lambda))^{-m} \right]. \end{aligned} \quad (\text{B.62})$$

Putting that into Eq. (B.58) and computing the geometric sum, one finds after some rearrangements

$$\langle \hat{c}(s) \rangle_0 = \frac{r_+ \lambda}{s(s + \lambda)(s + 1 + r_+)(s + 1 + r_+ + \lambda)}, \quad (\text{B.63})$$

which, after applying an inverse Laplace transform, gives

$$\langle c(t) \rangle_0 = \frac{r_+}{1 + r_+} \left(\frac{1}{1 + r_+ + \lambda} + \frac{e^{-(1+r_+)t}}{1 + r_+ - \lambda} - \frac{e^{-\lambda t}}{1 + r_+ - \lambda} - \frac{e^{-(1+r_++\lambda)t}}{1 + r_+ + \lambda} \right). \quad (\text{B.64})$$

From that one finds the two conditional steady state averages (with Eq. (3.70)):

$$\langle c \rangle_0 = \frac{r_+}{1 + r_+} \frac{1}{1 + r_+ + \lambda}, \quad \langle c \rangle_1 = \langle c \rangle - \langle c \rangle_0 = \frac{r_+}{1 + r_+} \frac{r_+ + \lambda}{1 + r_+ + \lambda}. \quad (\text{B.65})$$

B.5 Additional expressions

1. The time evolution of the mean value of the concentration c when starting in the initial state $S(0) = c(0) = 0$:

$$\begin{aligned}
\langle c(t) \rangle = & \frac{r_+}{1+r_+} \left(1 + \frac{\lambda}{1+r_+-\lambda} e^{-(1+r_+)t} - \frac{1+r_+}{1+r_+-\lambda} e^{-\lambda t} \right) \\
& - \alpha \frac{r_+\lambda}{(1+r_+)^2} \left[\frac{r_++\lambda}{\lambda(1+r_++\lambda)} + \frac{1}{\lambda(1+r_++\lambda)} e^{-(1+r_++\lambda)t} \right. \\
& \quad - \frac{(1+r_+)^2 - 4(1+r_+)\lambda + (4+3r_+)\lambda^2 - \lambda^3}{\lambda(1+r_+-\lambda)^3} e^{-(1+r_+)t} \\
& \quad + \frac{(1+r_+)(1+r_+-(2+r_+)\lambda + \lambda^2)}{(1+r_+-\lambda)^3} t e^{-(1+r_+)t} \\
& \quad - \frac{r_+(1+r_+)^2 + (1+r_+)(1-3r_+)\lambda - \lambda^2}{\lambda(1+r_+-\lambda)^3} e^{-\lambda t} \\
& \quad \left. - \frac{r_+(1+r_+)}{(1+r_+-\lambda)^2} t e^{-\lambda t} \right] + \mathcal{O}(\alpha^2). \tag{B.66}
\end{aligned}$$

2. The power spectrum for c :

$$\begin{aligned}
P_c(\omega) = & 2 \frac{r_+\lambda^2}{(\lambda^2 + \omega^2)[(1+r_+)^3 + (1+r_+)\omega^2]} \\
& + 2\alpha \left(\frac{1+r_+}{(1+r_+)^2 + \omega^2} B_2 + \frac{\lambda}{\lambda^2 + \omega^2} C_2 + \frac{1+r_++\lambda}{(1+r_++\lambda)^2 + \omega^2} D_2 \right. \\
& \quad \left. + \frac{(1+r_+)^2 - \omega^2}{[(1+r_+)^2 + \omega^2]^2} E_2 + \frac{\lambda^2 - \omega^2}{(\lambda^2 + \omega^2)^2} F_2 \right) + \mathcal{O}(\alpha^2). \tag{B.67}
\end{aligned}$$

Both the α -independent term and the term linear in α of $P_c(\omega)$ decay as ω^{-4} for large ω , which becomes clear after putting in the coefficients from Eq. (B.70) and some rearrangements.

3. The Fourier transform of the response function of c :

$$\begin{aligned}
\tilde{\chi}_c(\omega) = & \frac{\lambda}{(1+r_+)((1+r_+)^2 + \omega^2)(\lambda^2 + \omega^2)} [\lambda(1+r_+) - \omega^2 - i\omega(1+r_++\lambda)] \\
& + \alpha \left[\frac{1+r_+}{(1+r_+)^2 + \omega^2} B_4 + \frac{\lambda}{\lambda^2 + \omega^2} C_4 + \frac{1+r_++\lambda}{(1+r_++\lambda)^2 + \omega^2} D_4 \right. \\
& \quad + \frac{(1+r_+)^2 - \omega^2}{((1+r_+)^2 + \omega^2)^2} E_4 + \frac{\lambda^2 - \omega^2}{(\lambda^2 + \omega^2)^2} F_4 - i\omega \left(\frac{1}{(1+r_+)^2 + \omega^2} B_4 \right. \\
& \quad \quad \left. + \frac{1}{\lambda^2 + \omega^2} C_4 + \frac{1}{(1+r_++\lambda)^2 + \omega^2} D_4 \right. \\
& \quad \left. \left. + 2 \frac{1+r_+}{((1+r_+)^2 + \omega^2)^2} E_4 + 2 \frac{\lambda}{(\lambda^2 + \omega^2)^2} F_4 \right) \right] + \mathcal{O}(\alpha^2). \tag{B.68}
\end{aligned}$$

B.6 Coefficients of the correlation and response functions

In the following, the coefficients of the correlation and response functions are listed.

1. For the auto-correlation function of S , C_S from Eq. (3.73):

$$\begin{aligned}
B_1 &= -\frac{r_+}{(1+r_+)^3(1+r_+-\lambda)^2\lambda(1+r_++\lambda)} \\
&\quad \cdot [-(\lambda-1)r_+^4 - (\lambda-1)(2-\lambda)r_+^3 + \lambda(\lambda^2-2\lambda-1)r_+^2 \\
&\quad \quad + (-\lambda^4 + \lambda^3 - 3\lambda^2 + 3\lambda - 2)r_+ + (\lambda-1)^2(\lambda+1)(\lambda-1)], \\
C_1 &= -\frac{2r_+^2\lambda}{(1+r_+)^2(1+r_+-\lambda)^2(1+r_++\lambda)}, \\
D_1 &= \frac{r_+(r_+^2-1)}{(1+r_+)^3\lambda(1+r_++\lambda)}, \quad E_1 = \frac{r_+(\lambda-1)}{(1+r_+)^2(1+r_+-\lambda)}.
\end{aligned} \tag{B.69}$$

2. For the auto-correlation function of c , C_c from Eq. (3.74):

$$\begin{aligned}
B_2 &= -\frac{r_+\lambda}{(1+r_+)^3(1+r_+-\lambda)^3(1+r_++\lambda)^2} \\
&\quad \cdot [(\lambda-1)r_+^4 + (\lambda-1)(2-\lambda)r_+^3 - \lambda(\lambda^2-4\lambda+1)r_+^2 \\
&\quad \quad + (\lambda^4 - \lambda^3 + 7\lambda^2 - 7\lambda + 2)r_+ - (\lambda-1)(\lambda^3 - \lambda^2 - 3\lambda + 1)], \\
C_2 &= \frac{r_+\lambda}{(1+r_+)^3(1+r_+-\lambda)^3(1+r_++\lambda)^2(1+r_++2\lambda)} \\
&\quad \cdot [r_+^6 + (1+\lambda)r_+^5 - (3\lambda^2 - 5\lambda + 6)r_+^4 + (-\lambda^3 + 4\lambda^2 + 6\lambda - 14)r_+^3 \\
&\quad \quad + (2\lambda^4 + \lambda^3 + 18\lambda^2 - 2\lambda - 11)r_+^2 + (\lambda^4 + 3\lambda^3 + 12\lambda^2 - 7\lambda - 3)r_+ \\
&\quad \quad + \lambda(\lambda^3 + \lambda^2 + \lambda - 3)], \\
D_2 &= -\frac{r_+\lambda(r_+-1)}{(1+r_+)^3(1+r_++\lambda)(1+r_++2\lambda)}, \\
E_2 &= -\frac{r_+\lambda^2(\lambda-1)}{(1+r_+)^3(1+r_+-\lambda)^3(1+r_++\lambda)^2} (r_+^3 + 3r_+^2 + (3-\lambda^2)r_+ - (\lambda^2-1)), \\
F_2 &= -\frac{r_+^2\lambda^2}{(1+r_+)^2(1+r_+-\lambda)^2(1+r_++\lambda)}.
\end{aligned} \tag{B.70}$$

3. For the linear response function of S , χ_S from Eq. (3.87):

$$\begin{aligned}
B_3 &= -\frac{1}{\lambda(1+r_+)^2(1+r_+-\lambda)^2} [-(\lambda-1)r_+^3 + (2\lambda^2-4\lambda+1)r_+^2 \\
&\quad \quad + (-\lambda^3 + 2\lambda^2 - \lambda - 1)r_+ - (\lambda-1)^2], \\
C_3 &= -\frac{r_+\lambda}{(1+r_+)^2(1+r_+-\lambda)^2}, \quad D_3 = \frac{r_+^2 - \lambda - 1}{(1+r_+)^2\lambda(1+r_++\lambda)}, \\
E_3 &= \frac{\lambda-1}{(1+r_+)(1+r_+-\lambda)}.
\end{aligned} \tag{B.71}$$

4. For the linear response function of c , χ_c from Eq. (3.88):

$$\begin{aligned}
B_4 &= -\frac{1}{(1+r_+)^2(1+r_+-\lambda)^3} \left[r_+^3(\lambda-1) - r_+^2(1+2\lambda(\lambda-2)) \right. \\
&\quad \left. + r_+(1+\lambda^2(\lambda-1)) + \lambda(2\lambda-3) + 1 \right], \\
C_4 &= \frac{\lambda}{(1+r_+)^3(1+r_+-\lambda)^3(1+r_++\lambda)} \left[r_+^5 + r_+^4(-\lambda+2) + r_+^3(-\lambda^2+3\lambda) \right. \\
&\quad \left. + r_+^2(\lambda^3-2\lambda^2+8\lambda-2) + r_+(\lambda^3-\lambda^2+3\lambda-1) + \lambda^3-\lambda \right], \quad (\text{B.72}) \\
D_4 &= -\frac{r_+^2-\lambda-1}{(1+r_+)^3(1+r_++\lambda)}, \quad E_4 = -\frac{\lambda(\lambda-1)}{(1+r_+)(1+r_+-\lambda)^2}, \\
F_4 &= -\frac{r_+\lambda^2}{(1+r_+)^2(1+r_+-\lambda)^2}.
\end{aligned}$$

B.7 Computation of the linear response to a sinusoidal stimulus

Using $r_+(t) = r_+^0 + a \sin \omega t$ as a stimulus to the system, one can write the linear response (Eq. (3.17)) in both the channel variable S and the concentration c in the limit of large t as

$$\mathcal{R}_{S/c} = A_{S/c} \sin(\omega t + \theta_{S/c}). \quad (\text{B.73})$$

Putting $\phi(t) = a \sin \omega t$ and $\chi_S(t)$ from Eq. (3.87) together with the coefficients from Appendix B.6 into Eq. (3.18), one gets (after some rearrangements) for the channel variable S :

$$\begin{aligned}
A_S &= \frac{a}{1+r_+^0} \frac{1}{\sqrt{(1+r_+^0)^2 + \omega^2}} \\
&+ \alpha \frac{a}{(1+r_+^0)^2 ((1+r_+^0)^2 + \omega^2)^{\frac{3}{2}} (\lambda^2 + \omega^2) ((1+r_+^0 + \lambda)^3 + \omega^2(1+r_+^0 + \lambda))} \\
&\cdot \left[(1+r_+^0)^2 \lambda^2 (1+r_+^0 + \lambda) ((-2+r_+^0)r_+^0(1+r_+^0) + (-1+r_+^0)(1+2r_+^0)\lambda \right. \\
&+ (-1+r_+^0)\lambda^2) + \omega^2 ((-1+r_+^0)r_+^0(1+r_+^0)^4 + (1+r_+^0)^3(-1+r_+^0 + 3(r_+^0)^2)\lambda \\
&+ (1+r_+^0)^3(-2+5r_+^0)\lambda^2 + r_+^0(1+r_+^0)(4+5r_+^0)\lambda^3 + (1+3r_+^0(1+r_+^0))\lambda^4 + r_+^0\lambda^5) \\
&+ \omega^4 (2(r_+^0)^4 + \lambda + \lambda^2 + 2(r_+^0)^2\lambda(3+2\lambda) + (r_+^0)^3(3+4\lambda) \\
&+ r_+^0(-1+\lambda(3+\lambda(3+2\lambda)))) + \omega^6 r_+^0(r_+^0 + \lambda) \left. \right] + \mathcal{O}(\alpha^2), \quad (\text{B.74})
\end{aligned}$$

$$\begin{aligned}
\theta_s &= -\frac{\pi}{2} + \arctan\left(\frac{1+r_+^0}{\omega}\right) \\
&+ \alpha \frac{\omega}{(1+r_+^0 + \lambda) ((1+r_+^0)^2 + \omega^2) (\lambda^2 + \omega^2) ((1+r_+^0 + \lambda)^2 + \omega^2)} \\
&\cdot \left[(r_+^0)^4 \lambda + (r_+^0)^3(3\lambda + 5\lambda^2 + \omega^2) + (r_+^0)^2(6\lambda^3 + 10\lambda^2 + \lambda(3 + \omega^2) + 2\omega^2) \right. \\
&+ r_+^0(4\lambda^4 + 8\lambda^3 + \lambda^2(5 + 3\omega^3) + \lambda(1 + 3\omega^2) + \omega^2(1 + \omega^2)) \\
&\left. + \lambda(2 + 3\lambda + \lambda^2)(\lambda^2 + \omega^2) \right] + \mathcal{O}(\alpha^2). \quad (\text{B.75})
\end{aligned}$$

Doing the same for the concentration c ($\chi_c(t)$ from Eq. (3.88)) yields

$$A_c = \frac{\lambda}{\sqrt{\lambda^2 + \omega^2}} A_S, \quad (\text{B.76})$$

$$\theta_c = \arctan\left(\frac{\lambda(1+r_+) - \omega^2}{\omega(1+r_+ + \lambda)}\right) + \text{term linear in } \alpha \text{ from } \theta_S + \mathcal{O}(\alpha^2). \quad (\text{B.77})$$

C.1 Axon sorting and guidance through interacting growth cones – a continuum model

As a preliminary study to the generalised Potts model presented in Subsec. 4.3.1, axons are simulated using the same geometry (Fig. 4.7) but they are not restricted to the sites of a lattice, rather their coordinates in the x - z plane are continuous (y remains discrete).

Axons have a circular shape with radius r_A and the random initial distribution of axons is produced such that axons do not overlap. If an axon (at position (x_{A_1}, z_{A_1})) finds another axon within a certain circular 'sampling' range of radius L_c , they interact and an effective 'interaction force' F_{AA} is assigned to this pair of axons. In the simplest model, this force is defined as the inverse distance (D_{AA}) of the centre points of the axons multiplied by a factor f_{AA}^{ij} that can be different for different types i and j of interacting axons:

$$F_{AA} = \frac{f_{AA}^{ij}}{D_{AA}} \quad \text{with} \quad D_{AA} = \sqrt{(x_{A_1} - x_{A_2})^2 + (z_{A_1} - z_{A_2})^2}. \quad (\text{C.78})$$

The axon also feels a very simple guidance cue towards the future position of its glomerulus, exerting an 'attraction force' F_{AG} on it. For reasons of simplicity, for each axon type there exists one cue and the 'attraction force' is defined in a similar manner as the attraction between different axons:

$$F_{AG} = \frac{f_{AG}^i}{D_{AG}} \quad \text{with} \quad D_{AG} = \sqrt{(x_{A_1} - x_G^i)^2 + (y_{A_1} - y_G^i)^2 + (z_{A_1} - z_G^i)^2}, \quad (\text{C.79})$$

where (x_G^i, y_G^i, z_G^i) is the future position of the glomerulus of type i . Different to the potentials in the generalised Potts model in Subsec. 4.3.1, here, the attraction force is also y -dependent. In the simulations shown further down, only one value for f_{AG}^i was used and only two different ones for the axon-axon attraction, depending, if the two axons are of the same (f_{AA}^s) or different (f_{AA}^d) types:

$$f_{AA}^{ij} = f_{AA}^d + \delta^{ij}(f_{AA}^s - f_{AA}^d). \quad (\text{C.80})$$

In each time step, these effective 'attraction forces' both towards other axons (F_{AA}) and due to a cue (F_{AG}) are calculated for each axon. Then, a 'winner takes it all' strategy is implemented: The attraction strengths to all axons available within the radius L_c and the one due to the cue are compared and the highest force determines the next step. The axon then either makes a step of length ΔL towards the winner-axon (avoiding overlap, i.e. the minimum distance is $2r_A$) or towards the future position of the glomerulus of its type. The geometries of both steps are illustrated in Fig. C.1 and Eqs. (C.81) give the relations to calculate the positions of the axon in the next plane ($x_{A_1}(y_n) = x_{A_1}(y_n) + \Delta x_s, \dots$; Δx is the difference in the x -coordinates of the axon and the other axon or the future position of the glomerulus, respectively; Δy is kept fixed all the time for all axons),

$$\begin{aligned} D_{AA} > 2r_A : \quad \Delta x_s &= \frac{\Delta x \Delta L}{D_{AA}} & \Delta z_s &= \frac{\Delta z \Delta L}{D_{AA}} \\ D_{AA} \leq 2r_A : \quad \Delta x_s &= \frac{\Delta x (D_{AA} - 2r_A)}{D_{AA}} & \Delta z_s &= \frac{\Delta z (D_{AA} - 2r_A)}{D_{AA}} \\ & \Delta x_s &= \frac{\Delta x \Delta L}{D_{AG}} & \Delta z_s &= \frac{\Delta z \Delta L}{D_{AG}}. \end{aligned} \quad (\text{C.81})$$

The flowchart in Fig. C.2 summarises the algorithm used, leaving out some details. Axon positions at the next y -position $y + \Delta y$ are updated all at once.

Figs. C.3 show a typical time evolution of this algorithm with carefully chosen parameters. Each 25 axons of 21 different species (different colours and symbols) start in a random configuration with minimum distance $2r_A = 0.4$ (area occupancy $\sim 0.7\%$). Since in the

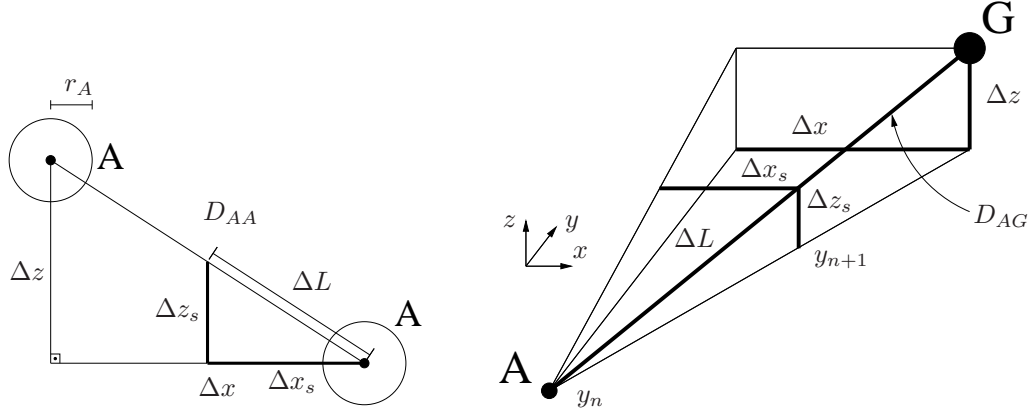


Fig. C.1: Geometry of the steps towards a neighbouring axon ('A' – left) and towards the glomerulus ('G' – right). D denotes a distance and ΔL is the step size.

first few time steps, there is typically no other axon within L_c , the axons can only react towards the guidance cue, which moves them small distances in the x - z -plane. Within less than 50 time steps, approximately 50% of the axons find another one within a distance L_c and form bundles (Fig. C.4). The bundles do not react to the cue and move straight forward in the y -direction. Only later, when the 'attraction force' of the cue becomes stronger (due to the shorter distance D_{AG}), a further sorting and movement of the axons towards their respective future glomeruli is observed. Finally, very near to the glomerular layer ($y_G = 310$), perfect bundling and positioning is seen.

More quantitative features of the simulation can be read from Fig. C.4. Two transitions can be observed, corresponding to the three plateaus of the curve depicting the total number of bundles (counting single axons as one bundle). The first plateau ($100 \lesssim t \lesssim 500$) is the region where mostly heterogeneous bundles exist. Latest at

$$y = D_{AG} = \frac{f_{AG}}{f_{AA}^d} 2r_A = 50 \quad \text{corresponding to } t = 500, \quad (\text{C.82})$$

the attraction towards the respective glomerulus becomes stronger than the attraction towards an axon of a different type, therefore heterogeneous bundles split and free axons move towards the glomerulus for some time. The second plateau in the blue curve is the region of many homogeneous bundles, which then leads to the third plateau with 21 homogeneous bundles at the correct positions. The last transition is completed at $y = 206$, which can be obtained from Eq. (C.82) by replacing f_{AA}^d with f_{AA}^s (for the parameters used, see the caption of Fig. C.3).

In the simplest realisation of the algorithm of Fig. C.2, in each time step for each axon the distance to all other axons has to be calculated, which makes this algorithm slow for large numbers of axons. If one discretises space also in the x - z -plane, the check if $D_{AA} < L_c$ is simply implemented by considering a limited (small) set of neighbouring lattice sites. The model described in Subsec. 4.3.1 uses this simplification and by that also comes closer to models known from other fields of statistical physics. Since the same geometry as in Subsec. 4.3.1 is used in the model presented above, the comments regarding the difficulties of relating this to the biological system do also apply here.

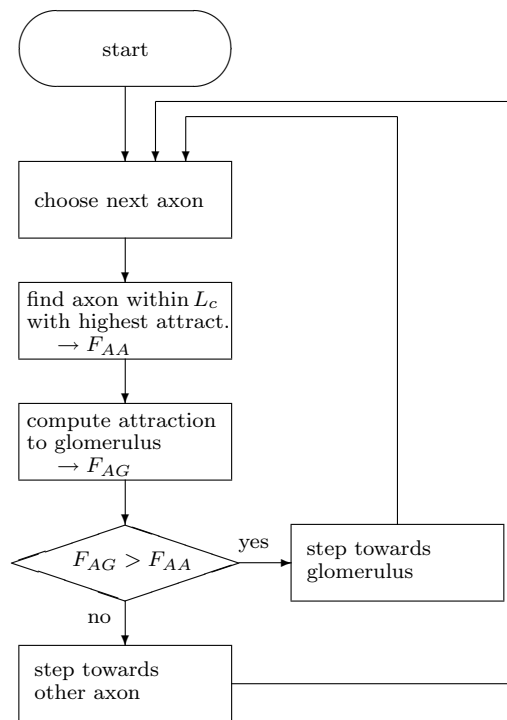


Fig. C.2: Flowchart of the algorithm used in the continuous model with all axonal growth cones growing in one plane (appendix C.1).

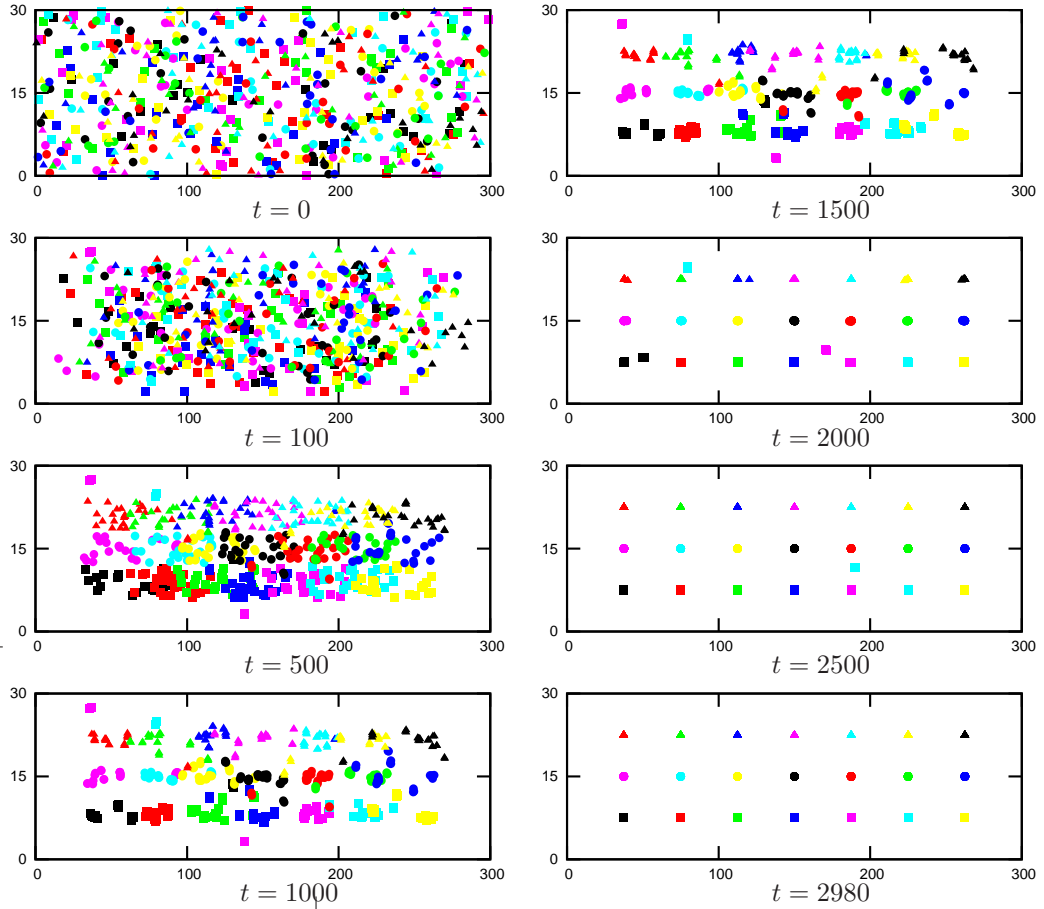


Fig. C.3: Time evolution of a random distribution ($t = 0$) of 525 axons (21 different species - depicted by different colours and symbols - with each 25 axons). The time step of $\Delta t = 1$ corresponds to a step in the y -direction of $\Delta y = 0.1$. The y -position of the attracting cues is $y_G = 310$. Other parameters used are $r_A = 0.2$, $L_c = 3$, $\Delta L = 1$, $f_{AA}^d = 2$, $f_{AA}^s = 5$ and $f_{AG} = 1300$.

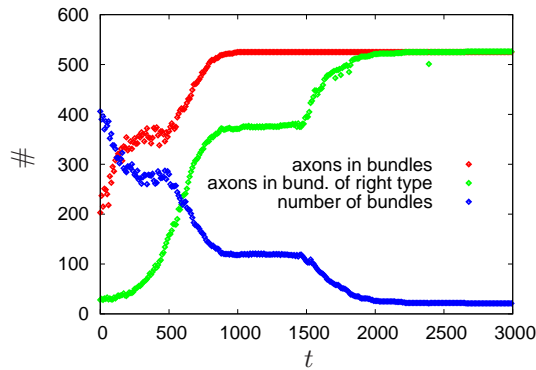


Fig. C.4: Three different quantities describing the evolution of the system of Fig. C.3. The red points depict the number of axons that are connected to at least one other axons. The blue points count the number of bundles (including free axons) and the green line is a measure of the 'purity' of the bundles. The first data point is at $t = 10$, i.e. already within the first ten time steps, approximately 200 axons find a partner and form a bundle.

C.2 Additional figures for chapter 4

C.2.1 Further plots from the generalised Potts model

Fig. C.5 shows the system of Fig. 4.8 at time $t = 999000$ when one starts the simulations with different (random) initial configurations. The results look quite the same in all three cases but the positions (absolute and relative) of the 'bundles' or 'glomeruli' are obviously varying. Similar results are obtained if one starts with the same initial distribution but uses different sets of pseudo-random numbers for the simulation.

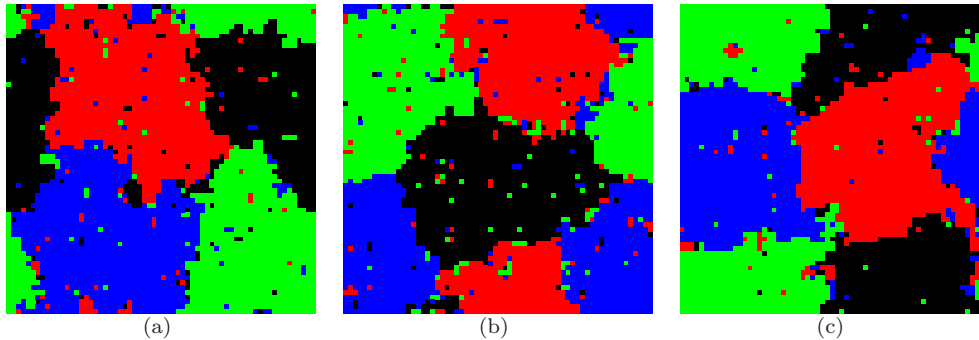


Fig. C.5: The same system as in Fig. 4.8 after 999000 time steps when started with different random initial configurations. The positions of the 'bundles' are not conserved.

C.2.2 Flowchart for the detailed turning-model including axon-axon interaction

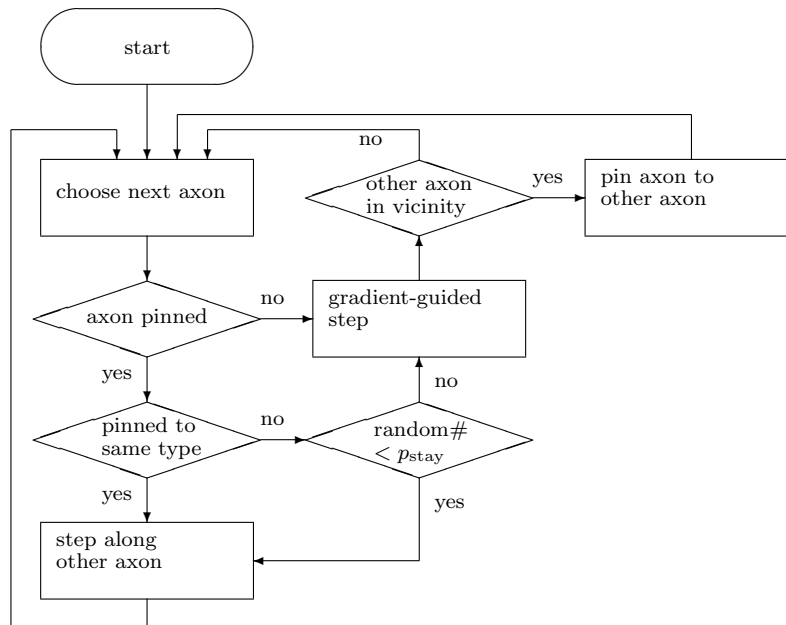


Fig. C.6: Flowchart for the algorithm of the turning-model from Subsec. 4.3.2 including axon-axon interactions (and therefore bundling).

C.2.3 Further configurations of the interacting directed random walks

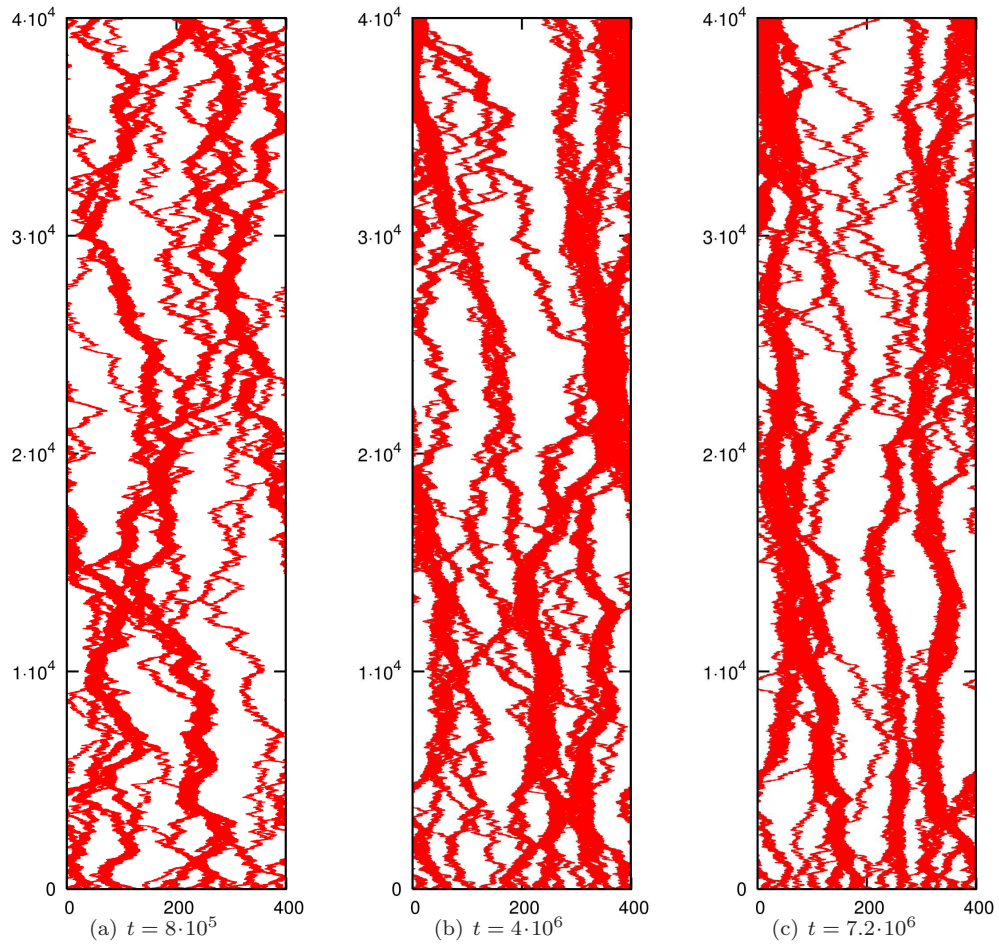


Fig. C.7: Time evolution of the axon configuration with $E_{\text{hom}} = -4.5$ from Fig. 4.18. Fig. (c) is the same as Fig. 4.18(b).

Bibliography

- [1] B. Alberts, D. Bray, and A. Johnson. *Essential Cell Biology*. Garland Science, 2nd edition, 2003. [72](#), [73](#)
- [2] R.R. Anholt and A.M. Rivers. Olfactory transduction: cross-talk between second-messenger systems. *Biochemistry*, 29(17):4049–4054, 1990. [23](#)
- [3] Aristoteles. De Anima. e.g. <http://classics.mit.edu/Aristotle/soul.html>, –350. [2](#)
- [4] G. Barnea, S. O’Donnell, F. Mancina, X. Sun, A. Nemes, M. Mendelsohn, and R. Axel. Odorant receptors on axon termini in the brain. *Science*, 304(5676):1468, 2004. [78](#)
- [5] U. Becker, S. Ganter, and C. Just. *Herder Lexikon der Biologie*. Spektrum Akad. Vlg., 1994. [12](#)
- [6] V. Bhandawat, J. Reisert, and K.-W. Yau. Elementary response of olfactory receptor neurons to odorants. *Science*, 308(5730):1931–1934, 2005. [14](#), [68](#)
- [7] W. Bialek. Physical limits to sensation and perception. *Annu.Rev.Biophys.Biophys.Chem.*, 16:455–478, 1987. [79](#)
- [8] W. Bialek. Thinking about the brain. In H. Flyvbjerg, F. Jülicher, P. Ormos, and F. David, editors, *Physics of Bio-Molecules and Cells. Les Houches Session LXXV, 2-27 July 2001*. Springer, 2002. arXiv:physics/0205030. [1](#)
- [9] W. Bialek, F. Rieke, R.R. de Ruyter van Steveninck, and D. Warland. Reading a neural code. *Science*, 252(5014):1854–1857, 1991. [12](#)
- [10] F. Bitter, O. Böttcher, A. Dahms, J. Kasche, B. Müller, and D. Müller. Handbuch zur Messung der empfundenen Luftqualität; Hermann-Rietschel-Institut, TU Berlin. http://www.tu-berlin.de/fb6/hri/dokumente/LQ-Handbuch/LQ_Handbuch_v08.pdf, 2004. [7](#)
- [11] I. Boekhoff and H. Breer. Termination of second messenger signaling in olfaction. *Proc.Natl.Acad.Sci. USA*, 89(2):471–474, 1992. [12](#)
- [12] F.F. Borisy, G.V. Ronnett, A.M. Cunningham, D. Juilfs, J. Beavo, and S.H. Snyder. Calcium/calmodulin-activated phosphodiesterase expressed in olfactory receptor neurons. *J.Neurosci.*, 12(3):915–923, 1992. [11](#)
- [13] J. Bradley, D. Reuter, and S. Frings. Facilitation of calmodulin-mediated odor adaptation by cAMP-gated channel subunits. *Science*, 294(5549):2176–2178, 2001. [11](#), [23](#)
- [14] A.J. Bray. Theory of phase-ordering kinetics. *Adv.Phys.*, 43(3):357–459, 1994. [83](#)
- [15] D. Bray. Reasoning for results. *Nature*, 412(6850):863, 2001. [1](#)
- [16] H. Breer, I. Boekhoff, and E. Tareilus. Rapid kinetics of second messenger formation in olfactory transduction. *Nature*, 345(6270):65–68, 1990. [12](#)
- [17] S. Brenner. Loose ends. *Curr.Biol.*, 5(3):332, 1995. [1](#)
- [18] I.N. Bronstein and K.A. Semendjajew. *Handbook of Mathematics*. Springer, 3rd edition, 1998. [40](#), [110](#)
- [19] I.N. Bronstein, K.A. Semendjajew, G. Musiol, and H. Mühlig. *Taschenbuch der Mathematik*. Harri Deutsch, 3rd edition, 1997. [36](#), [38](#), [45](#), [52](#), [109](#)
- [20] L.B. Buck. The molecular architecture of odor and pheromone sensing in mammals. *Cell*, 100(6):611–618, 2000. [5](#)

- [21] M. Canepari and F. Mammano. Imaging neuronal calcium fluorescence at high spatio-temporal resolution. *J.Neurosci.Methods*, 87(1):1–11, 1999. 13
- [22] CellNetAnalyzer. <http://www.mpi-magdeburg.mpg.de/projects/cna/cna.html>, 2006. 21
- [23] M. Chaichian and A. Demichev. *Path Integrals in Physics*, volume I. Institute of Physics Publishing, 2001. 41
- [24] C. Chen, T. Nakamura, and Y. Koutalos. Cyclic AMP diffusion coefficient in frog olfactory cilia. *Biophys.J.*, 76(5):2861–2867, 1999. 11, 17
- [25] T.Y. Chen and K.W. Yau. Direct modulation by Ca^{2+} -calmodulin of cyclic nucleotide-activated channel of rat olfactory receptor neurons. *Nature*, 368(6471):545–548, 1994. 11
- [26] D. Chowdhury and D. Stauffer. *Principles of Equilibrium Statistical Mechanics*. Wiley-VCH, 2002. 84
- [27] B.L. Clarke. Stability of complex reaction networks. *Adv.Chem.Phys.*, 43:1–215, 1980. 19, 21
- [28] B.L. Clarke. Complete set of steady-states for the general stoichiometric dynamical system. *J.Chem.Phys.*, 75(10):4970–4979, 1981. 21
- [29] B.L. Clarke. Stoichiometric network analysis. *Cell Biophys.*, 12:237–253, 1988. 19, 22
- [30] B.L. Clarke. Stoichiometric network analysis of the oxalate persulfate silver oscillator. *J.Chem.Phys.*, 97(4):2459–2472, 1992. 19
- [31] B.L. Clarke and W.M. Jiang. Method for deriving Hopf and saddle-node bifurcation hypersurfaces and application to a model of the Belousov-Zhabotinskii system. *J.Chem.Phys.*, 99(6):4464–4478, 1993. 19
- [32] P. Cohen and C.B. Klee. *Calmodulin (Molecular Aspects of Cellular Regulation)*. Elsevier Science Ltd., 1988. 23, 103, 104
- [33] D.M. Cooper, N. Mons, and J.W. Karpen. Adenylyl cyclases and the interaction between calcium and cAMP signalling. *Nature*, 374(6521):421–424, 1995. 31
- [34] M.E. Csete and J.C. Doyle. Reverse engineering of biological complexity. *Science*, 295(5560):1664–1669, 2002. 1, 72
- [35] S.K. Das and S. Puri. Dynamics of phase separation in multicomponent mixtures. *Phys.Rev.E*, 65(2):026141, 2002. 83, 85, 86
- [36] A. Delville, P. Laszlo, and D.J. Nelson. Calmodulin: calcium, potassium, and magnesium ion multiple equilibria and kinetics for interconversion, including the effect of repeated stimulation. *J.Theor.Biol.*, 112(1):157–175, 1985. 23, 103, 104
- [37] P.B. Detwiler, S. Ramanathan, A. Sengupta, and B.I. Shraiman. Engineering aspects of enzymatic signal transduction: photoreceptors in the retina. *Biophys.J.*, 79(6):2801–2817, 2000. 1
- [38] J.M. Deutsch. Aggregation disorder transition induced by fluctuating random forces. *J.Phys.A:Math.Gen.*, 18(9):1449–1456, 1985. 96
- [39] D.P. Dougherty, G.A. Wright, and A.C. Yew. Computational model of the cAMP-mediated sensory response and calcium-dependent adaptation in vertebrate olfactory receptor neurons. *Proc.Natl.Acad.Sci. USA*, 102(30):10415–10420, 2005. 31, 32
- [40] M. Eiswirth. Kagaku ni okeru fuanteisei to shindoo (Instability and oscillations in chemistry). *Suuri Kagaku*, 372:59–64, 1994. The english translation is available on request. 19, 21
- [41] M. Eiswirth, J. Burger, P. Strasser, and G. Ertl. Oscillating Langmuir-Hinshelwood mechanisms. *J.Phys.Chem.*, 100(49):19118–19123, 1996. 19, 22
- [42] R. Elsaesser and J. Paysan. Morituri te salutant? Olfactory signal transduction and the role of phosphoinositides. *J.Neurocytol.*, 34(1–2):97–116, 2005. 3, 10
- [43] I.R. Epstein and J.A. Pojman. *An Introduction to Nonlinear Chemical Dynamics: Oscillations, Waves, Patterns, and Chaos (Topics in Physical Chemistry)*. Oxford University Press, 1998. 19

- [44] M.R. Evans and T. Hanney. Nonequilibrium statistical mechanics of the zero-range process and related models. *J.Phys.A:Math.Gen.*, 38(19):R195–R240, 2005. 96
- [45] G.L. Fain. *Sensory Transduction*. Sinauer Associates, 2003. 4, 5, 6
- [46] P. Feinstein, T. Bozza, I. Rodriguez, A. Vassalli, and P. Mombaerts. Axon guidance of mouse olfactory sensory neurons by odorant receptors and the $\beta 2$ adrenergic receptor. *Cell*, 117(6):833–846, 2004. 90
- [47] P. Feinstein and P. Mombaerts. A contextual model for axonal sorting into glomeruli in the mouse olfactory system. *Cell*, 117(6):817–831, 2004. 75, 79, 80, 90
- [48] S. Firestein. How the olfactory system makes sense of scents. *Nature*, 413(6852):211–218, 2001. 4, 5, 10
- [49] R.J. Flannery, D.A. French, and S.J. Kleene. Clustering of cyclic-nucleotide-gated channels in olfactory cilia. *Biophys.J.*, 91:179–188, 2006. 17
- [50] Flavornet. <http://www.flavornet.org/>, 2006. 2
- [51] C.G. Galizia and R. Menzel. Odour perception in honeybees: coding information in glomerular patterns. *Curr.Opin.Neurobiol.*, 10(4):504–510, 2000. 76
- [52] P. Gavazzo, C. Picco, E. Eismann, U.B. Kaupp, and A. Menini. A point mutation in the pore region alters gating, Ca^{2+} blockage, and permeation of olfactory cyclic nucleotide-gated channels. *J.Gen.Physiol.*, 116(3):311–326, 2000. 35
- [53] A. Gierer. Directional cues for growing axons forming the retinotectal projection. *Development*, 101(3):479–489, 1987. 87
- [54] A. Gierer. Possible involvement of gradients in guidance of receptor cell axons towards their target position on the olfactory bulb. *Eur.J.Neurosci.*, 10(1):388–391, 1998. 78, 90
- [55] D.T. Gillespie. Exact stochastic simulation of coupled chemical reactions. *J.Phys.Chem.*, 81(25):2340–2361, 1977. 56
- [56] R. Glaser. *Biophysics*. Springer, Berlin, 2001. 34
- [57] Glomerular activity response archive. <http://leonservers.bio.uci.edu>, 2006. 7, 76
- [58] gnuplot. <http://www.gnuplot.info/>, 2004. Version 4.0. 67
- [59] A.L. Goldman, W. Van der Goes van Naters, D. Lessing, C.G. Warr, and J.R. Carlson. Coexpression of two functional odor receptors in one neuron. *Neuron*, 45(5):661–666, 2005. 3
- [60] C. Gomez-Diaz, F. Martin, and E. Alcorta. The cAMP transduction cascade mediates olfactory reception in *Drosophila melanogaster*. *Behav.Genet.*, 34(4):395–406, 2004. 5, 30
- [61] M. Gopalakrishnan, P. Borowski, F. Jülicher, and M. Zapotocky. Response and fluctuations of a two-state signaling module with feedback, 2006. *to be submitted to Phys.Rev.E*. 74
- [62] I. Goychuk and P. Hänggi. Stochastic resonance in ion channels characterized by information theory. *Phys.Rev.E*, 61(4 Pt B):4272–4280, 2000. 42
- [63] P. Hänggi. Stochastic resonance in biology. How noise can enhance detection of weak signals and help improve biological information processing. *ChemPhysChem*, 3(3):285–290, 2002. 7
- [64] L.H. Hartwell, J.J. Hopfield, S. Leibler, and A.W. Murray. From molecular to modular cell biology. *Nature*, 402(6761 Suppl):47–52, 1999. 71, 72
- [65] S. Hastings, J. Tyson, and D. Webster. Existence of periodic-solutions for negative feedback cellular control-systems. *J.Diff.Equat.*, 25(1):39–64, 1977. 32
- [66] C. Holt. In vivo timelapse imaging of retinotectal axon pathfinding in *xenopus laevis*. <http://www.pdn.cam.ac.uk/staff/holt/>, 2006. 77
- [67] T. Hummel. in Experten gehen dem Riechen auf den Nerv. *Dresdner Neueste Nachrichten*, 119:11, 2006. 81
- [68] T. Hummel, M.L. Vasconcelos, J.C. Clemens, Y. Fishilevich, L.B. Vosshall, and S.L. Zipursky. Axonal targeting of olfactory receptor neurons in *Drosophila* is controlled by Dscam. *Neuron*, 37(2):221–231, 2003. 5

- [69] D.E. Jaworsky, O. Matsuzaki, F.F. Borisy, and G.V. Ronnett. Calcium modulates the rapid kinetics of the odorant-induced cyclic AMP signal in rat olfactory cilia. *J.Neurosci.*, 15(1 Pt 1):310–318, 1995. [12](#)
- [70] D. Johnston and S.M.-S. Wu. *Foundations of Cellular Neurophysiology*. Bradford Books, 1999. [11](#)
- [71] K.E. Kaissling and E. Priesner. Die Riechschwelle des Seidenspinners. *Naturwissenschaften*, 57(1):23–28, 1970. [7](#)
- [72] E.R. Kandel, J.H. Schwartz, and T.M. Jessell. *Principles of neural science*. McGraw-Hill, 4th edition, 2000. [3](#), [77](#), [81](#)
- [73] H. Kaneko, I. Putzier, S. Frings, U.B. Kaupp, and T. Gensch. Chloride accumulation in mammalian olfactory sensory neurons. *J.Neurosci.*, 24(36):7931–7938, 2004. [11](#)
- [74] U.B. Kaupp and R. Seifert. Cyclic nucleotide-gated ion channels. *Physiol.Rev.*, 82(3):769–824, 2002. [11](#), [13](#)
- [75] R. Kaur, X.O. Zhu, A.J. Moorhouse, and P.H. Barry. IP₃-gated channels and their occurrence relative to CNG channels in the soma and dendritic knob of rat olfactory receptor neurons. *J.Membr.Biol.*, 181(2):91–105, 2001. [30](#)
- [76] H. Kitano. *Foundations of Systems Biology*. The MIT Press, 2002. [101](#)
- [77] S. Klamt and E.D. Gilles. Minimal cut sets in biochemical reaction networks. *Bioinf.*, 20(2):226–234, 2004. [21](#)
- [78] S.J. Kleene and R.C. Gesteland. Dissociation of frog olfactory epithelium with N-ethylmaleimide. *Brain Res.*, 229(2):536–540, 1981. [4](#)
- [79] T. Komiyama, J.R. Carlson, and L. Luo. Olfactory receptor neuron axon targeting: intrinsic transcriptional control and hierarchical interactions. *Nat.Neurosci.*, 7(8):819–825, 2004. [79](#), [80](#)
- [80] T. Komiyama and L. Luo. Development of wiring specificity in the olfactory system. *Curr.Opin.Neurobiol.*, 16(1):67–73, 2006. [5](#), [78](#), [82](#)
- [81] R.H. Kramer and S.A. Siegelbaum. Intracellular Ca²⁺ regulates the sensitivity of cyclic nucleotide-gated channels in olfactory receptor neurons. *Neuron*, 9(5):897–906, 1992. [11](#)
- [82] S. Krishna, M.H. Jensen, and K. Sneppen. Spiky oscillations in NF- κ B signalling. arXiv:q-bio.MN/0509017, 2005. [32](#)
- [83] K. Kruse and F. Jülicher. Oscillations in cell biology. *Curr.Opin.Cell Biol.*, 17(1):20–26, 2005. [32](#)
- [84] T. Kurahashi and A. Menini. Mechanism of odorant adaptation in the olfactory receptor cell. *Nature*, 385(6618):725–729, 1997. [14](#), [26](#), [31](#)
- [85] L.D. Landau and E.M. Lifschitz. *Lehrbuch der theoretischen Physik, Band V Statistische Physik Teil 1*. Akademie-Verlag, 8th edition, 1979. [50](#)
- [86] H.P. Larsson, S.J. Kleene, and H. Lecar. Noise analysis of ion channels in non-space-clamped cables: estimates of channel parameters in olfactory cilia. *Biophys.J.*, 72(3):1193–1203, 1997. [23](#)
- [87] Y. Lazebnik. Can a biologist fix a radio? – Or, what I learned while studying apoptosis. *Cancer Cell*, 2(3):179–182, 2002. [1](#)
- [88] T. Leinders-Zufall, C.A. Greer, G.M. Shepherd, and F. Zufall. Imaging odor-induced calcium transients in single olfactory cilia: specificity of activation and role in transduction. *J.Neurosci.*, 18(15):5630–5639, 1998. [14](#), [15](#), [16](#)
- [89] T. Leinders-Zufall, M. Ma, and F. Zufall. Impaired odor adaptation in olfactory receptor neurons after inhibition of Ca²⁺/calmodulin kinase II. *J.Neurosci.*, 19(14):RC19, 1999. [11](#)
- [90] T. Leinders-Zufall, M.N. Rand, G.M. Shepherd, C.A. Greer, and F. Zufall. Calcium entry through cyclic nucleotide-gated channels in individual cilia of olfactory receptor cells: spatiotemporal dynamics. *J.Neurosci.*, 17(11):4136–4148, 1997. [13](#), [14](#)
- [91] D.M. Lin, F. Wang, G. Lowe, G.H. Gold, R. Axel, J. Ngai, and L. Brunet. Formation of precise connections in the olfactory bulb occurs in the absence of odorant-evoked neuronal activity. *Neuron*, 26(1):69–80, 2000. [78](#), [82](#)

- [92] B. Lindemann. Predicted profiles of ion concentrations in olfactory cilia in the steady state. *Biophys.J.*, 80(4):1712–1721, 2001. [11](#), [24](#), [32](#)
- [93] S. Linse, A. Helmersson, and S. Forsen. Calcium binding to calmodulin and its globular domains. *J.Biol.Chem.*, 266(13):8050–8054, 1991. [103](#)
- [94] J. Löschinger, F. Weth, and F. Bonhoeffer. Reading of concentration gradients by axonal growth cones. *Phil.Trans.R.Soc.Lond.B*, 355:971–982, 2000. [77](#)
- [95] G. Lowe and G.H. Gold. The spatial distributions of odorant sensitivity and odorant-induced currents in salamander olfactory receptor cells. *J.Physiol.*, 442:147–168, 1991. [12](#), [14](#)
- [96] G. Lowe and G.H. Gold. Olfactory transduction is intrinsically noisy. *Proc.Natl.Acad.Sci.USA*, 92(17):7864–7868, 1995. [14](#), [15](#)
- [97] B. Malnic, J. Hirono, T. Sato, and L.B. Buck. Combinatorial receptor codes for odors. *Cell*, 96(5):713–723, 1999. [5](#)
- [98] P. Martin, A.J. Hudspeth, and F. Jülicher. Comparison of a hair bundle’s spontaneous oscillations with its response to mechanical stimulation reveals the underlying active process. *Proc.Natl.Acad.Sci. USA*, 98(25):14380–14385, 2001. [50](#)
- [99] S. Maskery and T. Shinbrot. Deterministic and stochastic elements of axonal guidance. *Annu.Rev.Biomed.Eng.*, 7:187–221, 2005. [77](#)
- [100] F. Maurin. A mathematical model of chemoreception for odours and taste. *J.Theor.Biol.*, 215(3):297–303, 2002. [32](#)
- [101] B. Mazzag, C.J. Tiganelli, and G.D. Smith. The effect of residual Ca^{2+} on the stochastic gating of Ca^{2+} -regulated Ca^{2+} channel models. *J.Theor.Biol.*, 235(1):121–150, 2005. [40](#), [56](#)
- [102] A. Menini. Calcium signalling and regulation in olfactory neurons. *Curr.Opin.Neurobiol.*, 9(4):419–426, 1999. [24](#)
- [103] A. Menini, C. Picco, and S. Firestein. Quantal-like current fluctuations induced by odorants in olfactory receptor cells. *Nature*, 373(6513):435–437, 1995. [14](#), [15](#)
- [104] R. Milo, S. Shen-Orr, S. Itzkovitz, N. Kashtan, D. Chklovskii, and U. Alon. Network motifs: simple building blocks of complex networks. *Science*, 298(5594):824–827, 2002. [1](#), [71](#), [72](#)
- [105] K. Miyamichi, S. Serizawa, H.M. Kimura, and H. Sakano. Continuous and overlapping expression domains of odorant receptor genes in the olfactory epithelium determine the dorsal/ventral positioning of glomeruli in the olfactory bulb. *J.Neurosci.*, 25(14):3586–3592, 2005. [76](#)
- [106] P.K. Mohanty, P. Borowski, and M. Zapotocky, 2006. unpublished. [96](#)
- [107] P. Mombaerts. How smell develops. *Nat.Neurosci.*, 4 Suppl:1192–1198, 2001. [3](#), [4](#), [76](#)
- [108] P. Mombaerts. Odorant receptor gene choice in olfactory sensory neurons: the one receptor-one neuron hypothesis revisited. *Curr.Opin.Neurobiol.*, 14(1):31–36, 2004. [3](#)
- [109] P. Mombaerts, F. Wang, C. Dulac, S.K. Chao, A. Nemes, M. Mendelsohn, J. Edmondson, and R. Axel. Visualizing an olfactory sensory map. *Cell*, 87(4):675–686, 1996. [6](#), [78](#)
- [110] E.E. Morrison and R.M. Costanzo. Morphology of the human olfactory epithelium. *J.Comp.Neurol.*, 297(1):1–13, 1990. [2](#), [9](#)
- [111] S.D. Munger, A.P. Lane, H. Zhong, T. Leinders-Zufall, K.W. Yau, F. Zufall, and R.R. Reed. Central role of the CNGA4 channel subunit in Ca^{2+} -calmodulin-dependent odor adaptation. *Science*, 294(5549):2172–2175, 2001. [23](#)
- [112] K. Narusuye, F. Kawai, and E. Miyachi. Spike encoding of olfactory receptor cells. *Neurosci.Res.*, 46(4):407–413, 2003. [12](#)
- [113] Y. Niimura and M. Nei. Comparative evolutionary analysis of olfactory receptor gene clusters between humans and mice. *Gene*, 346:13–21, 2005. [3](#)
- [114] T.C. Pearce. Computational parallels between the biological olfactory pathway and its analogue ‘the electronic nose’: Part II. Sensor-based machine olfaction. *Biosystems*, 41(2):69–90, 1997. [6](#)

- [115] S.L. Pomeroy, A.S. LaMantia, and D. Purves. Postnatal construction of neural circuitry in the mouse olfactory bulb. *J.Neurosci.*, 10(6):1952–1966, 1990. **6**
- [116] S.M. Potter, C. Zheng, D.S. Koos, P. Feinstein, S.E. Fraser, and P. Mombaerts. Structure and emergence of specific olfactory glomeruli in the mouse. *J.Neurosci.*, 21(24):9713–9723, 2001. **90**
- [117] W.H. Press, S.A. Teukolsky, W.T. Vetterling, and B.P. Flannery. *Numerical Recipes in C*. Cambridge University Press, 2nd edition, 1988. <http://library.lanl.gov/numerical/index.html>. **56, 84, 88, 92**
- [118] R.Y.K. Pun and S.J. Kleene. Contribution of cyclic-nucleotide-gated channels to the resting conductance of olfactory receptor neurons. *Biophys.J.*, 84(5):3425–3435, 2003. **33**
- [119] P.E. Rapp, A.I. Mees, and C.T. Sparrow. Frequency encoded biochemical regulation is more accurate than amplitude dependent control. *J.theor.Biol.*, 90(4):531–544, 1981. **32**
- [120] J. Reidl, P. Borowski, A. Senses, J. Starke, M. Zapotocky, and M. Eiswirth. Model of calcium oscillations due to negative feedback in olfactory cilia. *Biophys.J.*, 90(4):1147–1155, 2006. **22, 32, 104**
- [121] J. Reisert, P.J. Bauer, K.-W. Yau, and S. Frings. The Ca-activated Cl channel and its control in rat olfactory receptor neurons. *J.Gen.Physiol.*, 122(3):349–363, 2003. **11, 17, 23**
- [122] J. Reisert and H.R. Matthews. Na⁺-dependent Ca²⁺ extrusion governs response recovery in frog olfactory receptor cells. *J.Gen.Physiol.*, 112(5):529–535, 1998. **11**
- [123] J. Reisert and H.R. Matthews. Adaptation of the odour-induced response in frog olfactory receptor cells. *J.Physiol.*, 519 Pt 3:801–813, 1999. **14, 26**
- [124] J. Reisert and H.R. Matthews. Response properties of isolated mouse olfactory receptor cells. *J.Physiol.*, 530(Pt 1):113–122, 2001. **14, 15, 24, 25**
- [125] J. Reisert and H.R. Matthews. Responses to prolonged odour stimulation in frog olfactory receptor cells. *J.Physiol.*, 534(Pt 1):179–191, 2001. **14, 15, 31**
- [126] J. Reisert and H.R. Matthews. Simultaneous recording of receptor current and intraciliary Ca²⁺ concentration in salamander olfactory receptor cells. *J.Physiol.*, 535(3):637–645, 2001. **12, 13, 14, 15, 16, 25**
- [127] K.J. Ressler, S.L. Sullivan, and L.B. Buck. A zonal organization of odorant receptor gene expression in the olfactory epithelium. *Cell*, 73(3):597–609, 1993. **76**
- [128] S.M. Rosentreter, R.W. Davenport, J. Löschinger, J. Huf, J. Jung, and F. Bonhoeffer. Response of retinal ganglion cell axons to striped linear gradients of repellent guidance molecules. *J.Neurobiol.*, 37(4):541–562, 1998. **77**
- [129] J.-P. Rospars, P. Lansky, A. Duchamp, and P. Duchamp-Viret. Relation between stimulus and response in frog olfactory receptor neurons in vivo. *Eur.J.Neurosci.*, 18(5):1135–1154, 2003. **12**
- [130] J. Ross and M.O. Vlad. Nonlinear kinetics and new approaches to complex reaction mechanisms. *Annu.Rev.Phys.Chem.*, 50:51–78, 1999. **19**
- [131] S. Ross. *A first course in probability*. Pearson Education International, 7th edition, 2006. **56**
- [132] Y. Sakumura, Y. Tsukada, N. Yamamoto, and S. Ishii. A molecular model for axon guidance based on cross talk between rho GTPases. *Biophys.J.*, 89(2):812–822, 2005. **87**
- [133] D. Schild and D. Restrepo. Transduction mechanisms in vertebrate olfactory receptor cells. *Physiol.Rev.*, 78(2):429–466, 1998. **6, 9, 23, 30**
- [134] D. Schneider, G. Kasang, and K.E. Kaissling. Bestimmung der Riechschwelle von Bombyx mori mit Tritium-markiertem Bombykol. *Naturwissenschaften*, 55(8):395, 1968. **7**
- [135] E. Schrödinger, L. Mazurczak, and E. Schneider. *Was ist Leben*. Lehnen, 1951. **1**
- [136] G.M. Shepherd. *Neurobiology*. Oxford University Press, 3rd edition, 1994. **9, 31**
- [137] F.M. Simões-de Souza and A.C. Roque. Simulation of a vertebrate receptor cell of the olfactory epithelium for use in network models. *Neurocomp.*, 44-46:177–182, 2002. **32**

- [138] S. Sivakumaran, S. Hariharaputran, J. Mishra, and U.S. Bhalla. The Database of Quantitative Cellular Signaling: management and analysis of chemical kinetic models of signaling networks. *Bioinformatics*, 19(3):408–415, 2003. <http://doqcs.ncbs.res.in/>. 103, 104
- [139] R.K. Small and C.M. Leonard. Rapid fiber reorganization after early olfactory tract section and bullectomy in the hamster. *J.Comp.Neurol.*, 214(4):353–369, 1983. 81
- [140] J.A. St. John, H.J. Clarris, S. McKeown, S. Royal, and B. Key. Sorting and convergence of primary olfactory axons are independent of the olfactory bulb. *J.Comp.Neurol.*, 464(2):131–140, 2003. 82
- [141] L. Stowers and T.F. Marton. What is a pheromone? Mammalian pheromones reconsidered. *Neuron*, 46(5):699–702, 2005. 5
- [142] P. Strasser, J.D. Stemwedel, and J. Ross. Analysis of a mechanism of the chlorite iodide reaction. *J.Phys.Chem.*, 97(12):2851–2862, 1993. 19
- [143] J. Strotmann, S. Conzelmann, A. Beck, P. Feinstein, H. Breer, and P. Mombaerts. Local permutations in the glomerular array of the mouse olfactory bulb. *J.Neurosci.*, 20(18):6927–6938, 2000. 76
- [144] N. Suzuki, M. Takahata, and K. Sato. Oscillatory current responses of olfactory receptor neurons to odorants and computer simulation based on a cyclic AMP transduction model. *Chem.Senses*, 27(9):789–801, 2002. 14, 15, 31, 32
- [145] H. Takeuchi and T. Kurahashi. Photolysis of caged cyclic AMP in the ciliary cytoplasm of the newt olfactory receptor cell. *J.Physiol.*, 541(Pt 3):825–833, 2002. 13, 14
- [146] H. Takeuchi and T. Kurahashi. Mechanism of signal amplification in the olfactory sensory cilia. *J.Neurosci.*, 25(48):11084–11091, 2005. 14
- [147] M. Tessier-Lavigne and C.S. Goodman. The molecular biology of axon guidance. *Science*, 274(5290):1123–1133, 1996. 77
- [148] The digital anatomist. <http://www.digitalanatomist.com/>, 2006. 6
- [149] The MathWorks, Inc. Matlab, 2005. Version 7.1.0.183. 22
- [150] The mouse brain library. <http://www.mbl.org/>, 2006. 3
- [151] G. Tian, M.H. Jensen, and K. Sneppen. Time delay as a key to apoptosis induction in the p53 network. *Euro.Phys.J. B*, 29(1):135–140, 2002. 32
- [152] H. Tozaki, S. Tanaka, and T. Hirata. Theoretical consideration of olfactory axon projection with an activity-dependent neural network model. *Mol.Cell.Neurosci.*, 26(4):503–517, 2004. 82
- [153] H.B. Treloar, P. Feinstein, P. Mombaerts, and C.A. Greer. Specificity of glomerular targeting by olfactory sensory axons. *J.Neurosci.*, 22(7):2469–2477, 2002. 80, 90
- [154] N.G. van Kampen. *Stochastic Processes in Physics and Chemistry*. North-Holland Publishing, 1992. 74
- [155] A. Vassalli, A. Rothman, P. Feinstein, M. Zapotocky, and P. Mombaerts. Minigenes impart odorant receptor-specific axon guidance in the olfactory bulb. *Neuron*, 35(4):681–696, 2002. 90
- [156] D. Voet and J.G. Voet. *Biochemistry*. Wiley, 2nd edition, 1995. 18, 73
- [157] A.I. Vol’pert and S.I. Hudjaev. *Analysis in Classes of Discontinuous Functions and Equations of Mathematical Physics (Mechanics: Analysis 8)*. Martinus Nijhoff Publishers, 1985. 19
- [158] T.F. Weiss. *Cellular Biophysics, Vol. 1: Transport*. The MIT Press, 1996. 18
- [159] Wikipedia. <http://www.wikipedia.org/>, 2006. 11
- [160] M. Wilkinson and B. Mehlig. Path coalescence transition and its applications. *Phys.Rev.E*, 68(4):040101, 2003. 96
- [161] M. Witt and T. Hummel. Vomeronasal versus olfactory epithelium: is there a cellular basis for human vomeronasal perception? *Int.Rev.Cytol.*, 248:209–259, 2006. 5
- [162] D.M. Wolf and A.P. Arkin. Motifs, modules and games in bacteria. *Curr.Opin.Microbiol.*, 6(2):125–134, 2003. 71

-
- [163] Wolfram Research, Inc. Mathematica, 2005. Version 5.2. [28](#), [40](#)
- [164] F.Y. Wu. The Potts model. *Rev.Mod.Phys.*, 54(1):235–268, 1982. [83](#), [84](#), [86](#)
- [165] C. Yan, A.Z. Zhao, J.K. Bentley, K. Loughney, K. Ferguson, and J.A. Beavo. Molecular cloning and characterization of a calmodulin-dependent phosphodiesterase enriched in olfactory sensory neurons. *Proc.Natl.Acad.Sci. USA*, 92(21):9677–9681, 1995. [11](#)
- [166] E. Yeger-Lotem, S. Sattath, N. Kashtan, S. Itzkovitz, R. Milo, R.Y. Pinter, U. Alon, and H. Margalit. Network motifs in integrated cellular networks of transcription-regulation and protein-protein interaction. *Proc.Natl.Acad.Sci. USA*, 101(16):5934–5939, 2004. [71](#)
- [167] C.R. Yu, J. Power, G. Barnea, S. O’Donnell, H.E.V. Brown, J. Osborne, R. Axel, and J.A. Gogos. Spontaneous neural activity is required for the establishment and maintenance of the olfactory sensory map. *Neuron*, 42(4):553–566, 2004. [82](#)
- [168] C. Zheng, P. Feinstein, T. Bozza, I. Rodriguez, and P. Mombaerts. Peripheral olfactory projections are differentially affected in mice deficient in a cyclic nucleotide-gated channel subunit. *Neuron*, 26(1):81–91, 2000. [78](#)
- [169] D.-J. Zou, P. Feinstein, A.L. Rivers, G.A. Mathews, A. Kim, C.A. Greer, P. Mombaerts, and S. Firestein. Postnatal refinement of peripheral olfactory projections. *Science*, 304(5679):1976–1979, 2004. [81](#), [82](#)
- [170] F. Zufall and T. Leinders-Zufall. The cellular and molecular basis of odor adaptation. *Chem.Senses*, 25(4):473–481, 2000. [11](#), [14](#)

Index

- AC, *see* adenylyate cyclase
- ACTase, 73
- action potential, 3, 9, 11, 12
- adaptation, 7, 11, 13, 14, 24
- adenylyate cyclase, 10, 30, 73
- algorithm
 - Euler, 22, 56
 - Gillespie, 56
 - Metropolis, 84
- antenna, 4
- antennal lobe, 5, 82
- approach
 - bottom-up, 72
 - top-down, 72
- ATP, 10
- axon, 3, 4, 12, 75, 79
 - axon interaction, 79, 81
 - modelling of, 90
 - bundle, 79, 80, 93, 94
 - purifying of, 95
 - splitting of, 95
 - growth cone, *see* growth cone
 - growth of, 77
 - life time, 93
 - pathfinding, 80
 - pioneering, 80, 87
 - single, 80
 - speed of growth, 93
 - trajectory, 80, 90
 - simulation of, 87
 - turning, 87, 89
 - turnover, 81, 87, 91, 93
- axon hillock, 3, 11
- basal cell, 2, 81
- beats, 29
- bifurcation
 - analysis, 26
 - Hopf, 21
- biochemical measurements, 12
- brain, 3, 6
- building block, 71
- calcium, 13, 29, 35, 68, 73
- calmodulin, 11, 17, 19, 24, 35, 73
- CaM, *see* calmodulin
- CaM4, *see* calmodulin
- CaMKII, 11
- cAMP, 9, 11, 13, 16, 35, 69, 72
 - caged, 13
 - degradation of, 11
 - diffusion constant, 11
- cell membrane, 10
- cGMP, 11
- channel
 - calcium gated, 11
 - cationic, 10
 - chloride, 11
 - coupling between, 68
 - current recording, 35
 - current through, 18, 35
 - cyclic-nucleotide-gated, 9, 11, 17, 25
 - inhibited, 17, 19, 24
 - open probability, 38
 - single, 35, 68
- characteristic polynomial, 21
- chemical kinetics, 16
- chemical reaction
 - thermal effects in, 34
- cilia, 4, 9, 12, 29, 33, 68, 71
- cinetole, 14
- CNG, *see* cyclic-nucleotide-gated channel
- coarse graining, 94
- coefficient of variation, 49, 59, 66
- conformation, 72
 - energy differences between, 34
- convergence, 4, 75
- correlation function, 37, 41
 - auto-, 37, 42, 47, 50, 53, 60, 61, 63, 64
 - cross-, 37, 42, 49, 64
- correlations
 - spatial, 69
 - temporal, 69
- cytosol, 10
- degradation, 31
- dendrite, 4
- dendritic knob, 2, 9
- diffusion, 16, 30, 68, 69
- double pulse experiment, 14, 24

- double-exponential, 44
- dye, 23
 - calcium-sensitive, 13
- eigenvalue, 21, 27
- electronics, 72
- energy
 - barrier, 34
 - effective interaction, 84, 92, 93
 - penalty, 93, 95
 - thermal, 34
- ensemble, 37, 56
- enzyme, 10, 34, 72
- Eph, 77
- ephriane, 77
- evolution, 7
- exchanger
 - sodium-calcium, 11, 24
- extreme current, 20
- feedback
 - inhibition, 72
 - negative, 11, 71
 - parameter, 35, 41
 - positive, 71
- filopodia, 80, 83
- fitting, 67
- flow
 - passive, 11
- fluctuation dissipation theorem, 41, 50
- fluctuations, 33, 55
 - mean squared, *see* variance
 - relative, *see* coefficient of variation
 - root mean squared, *see* standard deviation
- fluorescence measurement, 13, 14
- flux
 - through extreme current, 21
- Fourier transform, 38, 50, 54
- frog, 12
- G-protein, 10
- Gamma function, 40
- gene, 73
 - expression level, 29
- genome, 3
- Glauber dynamics, 84
- glomerulus, 4, 6, 75, 80
 - number of, 4
 - purity of, 81
- Goldman-Hodgkin-Katz current equation, 18
- Green's function, 43, 45, 46, 57, 59, 62
- grid
 - tilted, 92
- growth cone, 77, 78, 80
 - idealised, 87
- guidance cue, 88
 - chemical, 77
 - in the olfactory bulb, 78
 - interpretation of, 78
 - modelling of, 84
- Hamiltonian, 84
- Heaviside function, 38
- Hill coefficient, 11, 22, 31
- Hill-type equation, 18, 20, 71
- hydrogen bond, 34
- hypergeometric function
 - confluent, 40
- IBMX, 13
- in silico, 82
- insects
 - axon targeting in, 78
 - olfactory system in, 4
- integrated circuit, 72
- interaction
 - heterotypic, 84, 90, 92, 95
 - homotypic, 84, 90, 92
- ion
 - calcium, 11, 18
 - chloride, 11
 - pump, 11, 21, 51
 - chloride, 11
 - sodium, 11, 24
- ion channel, *see* channel
- IP₃, 10, 78
- Ising model, 84
- Jacobian, 21, 27, 44
- Kawasaki dynamics, 84
- kinase, 72, 73
- kinetic
 - equation, 20
 - exponent, 21
 - parameters, 19
- Kummer's function, *see* hypergeometric function
- Langevin equation, 74
- Laplace transform, 45
- latency time, 14
- lattice, 84, 91
 - neighbouring positions, 92
- ligand, 11
- linear response function, *see* response function

- loo, 7
- mass action
 - kinetics, 20
 - law of, 17, 78
- master equation, 38, 39, 41, 52, 56, 62
- maxillary palp, 4
- ME, *see* master equation
- mean value, 37, 41, 42, 46, 47, 52, 54, 56, 58, 62
- mean-field, 52
- microelectrode, 12
- micropipette, 12, 13
- miswiring, 81, 91
- mitral cell, 4, 82
- modelling
 - different approaches, 30
- module, 71, 101
 - coupling of, 71
 - signalling, 34, 35
- Monte Carlo time step, 84
- moth, 7
- motif, 72
- mouse, 12
- mRNA, 73
- mucus, 2, 9

- n-point function, 37, 55
- nasal cavity, 2
- Nernst potential, 11, 68
- network, 71
 - chemical, 12, 19
 - diagram, 19
 - metabolic, 72
 - topology, 19
- neural activity
 - role in olfactory map formation, 82
- neural map, 7
- neuron, 3, 9
 - secondary, 4
- neurons
 - secondary, 82
- newt, 12
- nitric oxide, 30
- noise, 7, 23, 59, 74
 - in chemical guidance, 79, 88
- noise-to-signal ratio, *see* coefficient of variation
- non-Markovian dynamics, 37
- norm, 39
- nose, 2
 - electronic, 6
- odourant, 10
- odourant binding protein, 3, 5, 10
- olfactory
 - bulb, 3, 4, 75, 80
 - accessory, 5
 - epithelium, 2, 3, 12
 - map, 75
 - precision of, 76
 - refinement of, 81
 - receptor, 3, 10, 78
 - number of, 3
 - reception range, 3, 6
 - receptor neuron, 2, 12, 68
 - life time, 81
 - spatial distribution, 76
 - varying sensitivity, 15
 - sense, 2
- olfactory sensory neuron, *see* olfactory receptor neuron
- olfactory system
 - in insects, 4
- operon, 73
- oscillations, 23, 27, 29, 71
 - coupled cAMP-Ca²⁺, 30
 - damped, 24, 29

- path coalescence, 96
- path integral, 38, 41, 42, 56
- pattern formation, 75
- PDE, 11, 13
- periodic boundary conditions, 70
- phase separation, 82
- phase transition, 96
- pheromone, 5
- PI, *see* path integral
- pole, 40
- potential, 84
- Potts model, 84
 - critical temperature, 85
 - generalised, 85
 - vacancies, 86
- power spectrum, 38, 48, 51, 59, 63, 64
- probability density, 43
- procaryotes, 73
- promoter, 73
- propagator, 42
 - reduced, 43
- protein, 34, 72
- protein kinase, 12
- pump, *see* ion pump

- random number, 56, 84, 88, 92
- random walk
 - interacting directed, 91
- rat, 12

- reaction kinetics, 12
 reception range, 40, 65
 receptor, 72, 73
 deactivation of, 12
 repressor, 73
 response, 38, 68
 oscillatory, 14
 response function, 38, 41, 42, 49, 50, 61, 67
 retinotectal projection, 77
 Ringer solution, 12
 robustness, 18, 26, 29
 Routh scheme, 21
- salamander, 12, 13
 saturation, 21
 SC, *see* self-consistent
 second messenger, 11, 72
 self-consistent, 38, 51, 56, 70
 sense
 auditory, 1
 chemical, 2
 classical, 2
 of smell, *see* olfactory
 olfactory, 1, 2
 three stages of, 2
 visual, 1
 sensillia, 4
 sensitivity, 6
 signal transduction, 9, 33, 72, 78
 cascade, 3, 71
 pathway, 9
 cAMP-mediated, 10
 stochastic effects in, 34
 SNA, *see* stoichiometric network analysis
 soma, 4, 29
 sorting, 85
 of axons, 76
 spike train, 3
 information encoding in, 12
 stability, 27
 standard deviation, 48
 normalised, *see* coefficient of variation
 statespace, 27
 stimulus, 11–13, 23, 35, 50, 69
 periodic, 67
 stoichiometric matrix, 20
 stoichiometric network analysis, 16, 19
 structure
 tertiary, 10, 34
 tetrameric, 11
 suction pipette, 12
 synapse, 4
 synchronisation, 29
 systems biology, 101
- temperature, 34, 50
 effective, 50, 84, 85
 thermal effects, 34
 thermal equilibrium, *see* thermodynamic equilibrium, 86
 thermodynamic equilibrium, 34, 41
 time delay, 31
 transcription, 73
 transmembrane current, 12, 14
 trout, 12
 tryptophan, 73
 tufted cell, 4
- variance, 41, 48, 59, 65
 visual system, 12, 78
 voltage, 18, 30, 31
 transmembrane, 11
 vomeronasal organ, 5
- whole cell measurements, 12, 14
 zero-range process, 96

Versicherung

Hiermit versichere ich, dass ich die vorliegende Arbeit ohne unzulässige Hilfe Dritter und ohne Benutzung anderer als der angegebenen Hilfsmittel angefertigt habe; die aus fremden Quellen direkt oder indirekt übernommenen Gedanken sind als solche kenntlich gemacht. Die Arbeit wurde bisher weder im Inland noch im Ausland in gleicher oder ähnlicher Form einer anderen Prüfungsbehörde vorgelegt.

Die vorgelegte Arbeit wurde vom 1.4.2003 bis zum 30.6.2006 unter wissenschaftlicher Betreuung durch Prof. Dr. Frank Jülicher am Max-Planck-Institut für Physik komplexer Systeme in Dresden durchgeführt.

Ich versichere, dass ich bisher keine erfolglosen Promotionsverfahren unternommen habe. Ich erkenne die derzeit gültige Fassung der Promotionsordnung der Fakultät Mathematik und Naturwissenschaften an der Technischen Universität Dresden an.

Dresden, 28. September 2006,

Peter Borowski